Single Meson Production in Proton Diffraction at 190 GeV/c at COMPASS

Dissertation
zur Erlangung des Grades
"Doktor
der Naturwissenschaften"

am Fachbereich Physik, Mathematik und Informatik
der JOHANNES GUTENBERG-UNIVERSITÄT
in Mainz

TOBIAS WEISROCK

geboren in Mainz

Mainz, den 15. April 2015

Tobias Weisrock: *Single Meson Production in Proton Diffraction at* 190 GeV/c *at COMPASS*
Mainz **D77**

BERICHTERSTATTER:

TAG DER MÜNDLICHEN PRÜFUNG:

28. August 2015

Ein Pomeron ist, wenn man sich vorstellt, es gäbe ein Teilchen, das es aber gar nicht gibt,
und dann berechnet, wie es aussähe, wenn es es gäbe.

(Hans Graßmann in "Sperrt das DESY zu", Der Spiegel 44/1999)

ABSTRACT

The quark model successfully describes all ground state baryons as members of $SU(N)$ flavour multiplets. For excited baryon states the situation is totally different. There are much less states found in the experiment than predicted in most theoretical calculations. This fact has been known for a long time as the 'missing resonance problem'. In addition, many states found in experiments are only poorly measured up to now. Therefore, further experimental efforts are needed to clarify the situation.

At COMPASS, reactions of a 190 GeV/c hadron beam impinging on a liquid hydrogen target are investigated. The hadron beam contains different species of particles (π, K, p). To distinguish these particles, two Cherenkov detectors are used. In this thesis, a new method for the identification of particles from the detector information is developed. This method is based on statistical approaches and allows a better kaon identification efficiency with a similar purity compared to the method, which was used before.

The reaction $pp \to ppX$ with $X = (\pi^0, \eta, \omega, \phi)$ is used to study different production mechanisms. A previous analysis of ω and ϕ mesons is extended to pseudoscalar mesons. As the resonance contributions in $p\eta$ are smaller than in $p\pi^0$ a different behaviour of these two final states is expected as a function of kinematic variables. The investigation of these differences allows to study different production mechanisms and to estimate the size of the resonant contribution in the different channels.

In addition, the channel $pp \to ppX$ allows to study baryon resonances in the pX system. In the COMPASS energy regime, the reaction is dominated by Pomeron exchange. As a Pomeron carries vacuum quantum numbers, no isospin is transferred between the target proton and the beam proton. Therefore, the pX final state has isospin $\frac{1}{2}$ and all baryon resonances in this channel are N^* baryons. This offers the opportunity to do spectroscopy without taking Δ resonances into account.

To disentangle the contributions of different resonances a partial wave analysis (PWA) is used. Different resonances have different spin and parity $J^{\mathcal{P}}$, which results in different angular distributions of the decay particles. These angular distributions can be calculated from models and then be fitted to the data. From the fit the contributions of the single resonances as well as resonance parameters – namely the mass and the width – can be extracted. In this thesis, two different approaches for a partial wave analysis of the reaction $pp \to pp\pi^0$ are developed and tested.

ZUSAMMENFASSUNG

Das Quarkmodell beschreibt erfolgreich alle baryonischen Grundzustände in Multipletts einer Flavour-$SU(N)$. Für die angeregten Zustände ist die Situation eine andere. Die Zahl der experimentell gefundenen Baryonen ist viel kleiner als die Zahl der theoretisch vorhergesagten Zustände. Dies kennt man schon lange als das "missing resonance problem". Außerdem sind viele der experimentell gefundenen Baryonen bisher nur unzureichend gemessen worden. Weitere Experimente werden also benötigt, um die Situation zu klären.

Im COMPASS-Experiment werden Reaktionen von 190 GeV/c Hadronen mit einem Flüssigwasserstofftarget untersucht. Der Hadronstrahl beinhaltet verschiedene Teilchensorten (π, K, p). Zur Trennung der verschiedenen Teilchensorten werden zwei Cherenkovdetektoren verwendet. In dieser Arbeit wird eine neue Methode zur Identifikation von Teilchen mithilfe der Detektorinformation entwickelt. Diese Methode nutzt statistische Ansätze und erreicht eine höhere Identifikationseffizienz für Kaonen im Vergleich zur bisher verwendeten Methode. Die Reinheit der Kaonselektion ist dabei vergleichbar.

Die Reaktion $pp \to ppX$ mit $X = (\pi^0, \eta, \omega, \phi)$ wird verwendet, um unterschiedliche Reaktionsmechanismen zu untersuchen. Dabei wird die existierende COMPASS-Analyse auf pseudoskalare Mesonen erweitert. Da die resonanten Beiträge in $p\eta$ kleiner sind als in $p\pi^0$, wird erwartet, dass sich beide Endzustände in ihren kinematischen Abhängigkeiten unterscheiden. Die Untersuchung dieser Unterschiede gibt Hinweise auf verschiedene Produktionsmechanismen und die Größe der resonanten Beiträge.

Des weiteren erlaubt der Kanal $pp \to ppX$ die Untersuchung von Baryonresonanzen im pX System. Im betrachteten Energiebereich dominiert der Pomeronaustausch. Da das Pomeron Vakuumquantenzahlen besitzt, wird kein Isospin zwischen dem Targetproton und dem Strahlproton ausgetauscht. Daher hat der Endzustand pX immer Isospin $\frac{1}{2}$ und alle Resonanzen in diesem Kanal sind N^* Baryonen. Dies ermöglicht Spektroskopie ohne Berücksichtigung von Δ Resonanzen.

Um die Beiträge der einzelnen Resonanzen von einander zu trennen, wird eine Partialwellenanalyse (PWA) verwendet. Resonanzen mit unterschiedlicher Spin-Parität $J^{\mathcal{P}}$ führen zu unterschiedlichen Winkelverteilungen der Zerfallsteilchen. Diese Winkelverteilungen können mit Modellen berechnet und dann an die Daten angepasst werden. Aus dieser Anpassung können die Resonanzparameter, d. h. die Massen und die Zerfallsbreiten, der Resonanzen extrahiert werden. In der vorliegenden Arbeit werden zwei Ansätze für eine Partialwellenanalyse der Reaktion $pp \to pp\pi^0$ entwickelt und getestet.

CONTENTS

I BEAM PARTICLE IDENTIFICATION WITH STATISTICAL METHODS

II PRODUCTION OF SINGLE MESONS IN pp REACTIONS

III PARTIAL WAVE ANALYSIS OF $p\pi^0$ FINAL STATES

APPENDIX

INTRODUCTION

Dissertatio est omnis divisa in partes tres – this thesis contains three main parts, which cover three different topics. They can be read independently of each other and are introduced in the following. Prior to those three parts, chapter 1 gives an overview on the standard model of particle physics with an emphasis on strong interactions and quantum chromodynamics (QCD). In the end of that chapter, scattering processes will be discussed. Those cannot be calculated in QCD and therefore, they are discussed in the framework of Regge theory. With Regge theory, the process of diffractive dissociation, which is the dominant reaction mechanism at COMPASS, can be described as the exchange of a Pomeron. Diffractive dissociation processes will be investigated in parts II and III. The data used in this work were taken in 2009 with the COMPASS experiment. Components of the experimental set-up that are important for the presented analyses will be discussed in chapter 2.

I BEAM PARTICLE IDENTIFICATION WITH STATISTICAL METHODS

The negative hadron beam used for the COMPASS experiment mainly contains pions (97%) but also a small fraction of kaons (2.4%) and anti-protons. To perform physics analyses, the different particle species have to be separated. Two Cherenkov detectors are used to distinguish kaons from pions by selecting with a diaphragm the light ring of one species. The Cherenkov light is detected by a ring of eight photomultipliers. Until now, a multiplicity method was used to identify particles: If a certain number of photomultipliers produce a signal, the particle is identified as a kaon. This method relies on small angles between the particle path through the detector and the detector axis. However, the COMPASS hadron beam has a natural angular spread, which goes beyond the requirement for the multiplicity method. In this thesis, a new method for the identification of beam particles was developed. The method is based on a statistical approach and takes the beam divergence into account. This allows for a significant improvement in the kaon identification efficiency.

In chapter 3, the design and functional principle of the Cherenkov detectors is discussed. The new method is introduced in chapter 4. In chapter 5, the efficiency and purity for kaon selection as well as for pion selection are calculated and compared to the old multiplicity method.

II PRODUCTION OF SINGLE MESONS IN pp REACTIONS

The ratio of production cross sections for mesons contains information on production mechanisms and resonance contributions in the intermediate state. For this work, the reaction $pp \to ppM$ of $190\,\mathrm{GeV}/c$ protons impinging on a liquid hydrogen target is investigated, where M is a π^0, η, ω or ϕ meson. The presented analyis is an extension of a previous COMPASS analysis to pseudoscalar mesons. Up to now, the production of π^0 and η mesons was investigated only in very limited kinematic regions. In this work, a comparison of all four meson production cross sections will be performed in a wide kinematic range.

The event selection for the different final states is presented in chapter 6. In chapter 7, the experimental acceptance is determined with a Monte-Carlo simulation. Afterwards, kinematic distributions for the different channels are presented in chapter 8. Possible resonance contributions and the influence of the acceptance correction are discussed. The results for the cross section ratios as a function of kinematic variables are presented in chapter 9.

III PARTIAL WAVE ANALYSIS OF $p\pi^0$ FINAL STATES

The excitation spectrum of the proton contains several resonances, which have a difference in mass that is well below the decay width. To disentangle the contributions of such overlapping resonances, a partial wave analysis (PWA) is used. Different resonances have different spin and parity $J^{\mathcal{P}}$, which results in different angular distributions of the decay particles. These angular distributions can be calculated from models and then be fitted to the data. From the fit the contributions of the single resonances as well as resonance parameters – namely the mass and the width – can be extracted.

The original idea of this thesis was to develop a partial wave analysis for resonances that decay into a proton and a pseudoscalar meson (π^0 or η). The goal was to reproduce the well established $N^* \to p\pi^0$ decays and to perform an analysis of the still not very well known $N^* \to p\eta$ resonances afterwards. However, the $p\pi^0$ channel turned out to be much more complicated than expected due to the contributions of non-resonant reaction mechanisms. Thus, only the $p\pi^0$ final state is considered in this work. For the analysis, the data set from part II is used.

Chapter 10 gives an overview on previous experimental results as well as theoretical models for the baryon spectrum. The helicity formalism is introduced in chapter 11 to describe the two-body decay of resonances. In chapter 12 a partial wave analysis program based on the helicity formalism is developed and tested on pseudo data. Afterwards an analysis of the data is tried and different possibilities for background reduction are investigated. The form of the invariant mass spectrum of $p\pi^0$ will be discussed qualitatively based on theory calculations in chapter 13. The results will be used to estimate the background contribution in the reaction. Finally, an alternative approach for the partial wave analysis is presented in chapter 14. This approach allows for a proper inclusion of background processes.

1

QCD AND THE STRONG INTERACTION

1.1 STANDARD MODEL AND QCD

All known physics processes can be attributed to four basic interactions: gravitation, electromagnetic interaction, weak interaction and strong interaction. While gravitation is negligible in the short-distance interactions of particles, the other three are combined into the very successful standard model of particle physics.
The standard model describes fundamental fermions (quarks and leptons) and the fundamental interactions (electromagnetic, weak, strong), which are mediated by gauge bosons. The particle content of the standard model (without the Higgs boson) is given in figure 1.1, some more details are given in the following.

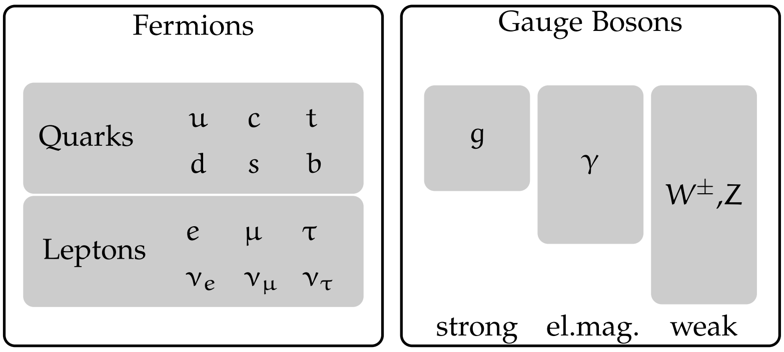

Figure 1.1: Particle content of the standard model. The box size of the gauge bosons denotes, which fermions participate in the single interactions: The strong interaction only acts on quarks, the electromagnetic interaction on quarks and charged leptons. Neutrinos only interact weakly.

QUARKS are spin-$\frac{1}{2}$ fermions that can interact strongly. There are six different quarks in three generations. Each generation contains an up-type quark with an electric charge of $\frac{2}{3}$e and a down-type quark with a charge of $-\frac{1}{3}$e. Some basic properties of the quarks are given in table 1.1.

LEPTONS are also spin-$\frac{1}{2}$ fermions but do not participate in the strong interaction. The six fermions are also grouped in three generations. Each generation contains an electrically charged fermion (with charge −e) and a neutrino, which only participates in weak interaction. The six leptons are summarised in table 1.2.

GAUGE BOSONS are spin-1 particles which mediate the interactions through gauge couplings. More details are given in sections 1.1.1 and 1.1.2. The gauge bosons for the different interactions are given in table 1.3.

THE HIGGS BOSON results from the electroweak symmetry breaking (see section 1.1.1). All other massive elementary particles acquire their masses via couplings to the Higgs boson. Although it was already predicted in 1964 [2–4] it was only recently found at the LHC [5, 6].

	charge	mass
up	$\frac{2}{3}e$	$2.3^{+0.7}_{-0.5}$ MeV/c^2
down	$-\frac{1}{3}e$	$4.8^{+0.7}_{-0.3}$ MeV/c^2
charm	$\frac{2}{3}e$	(1.275 ± 0.025) GeV/c^2
strange	$-\frac{1}{3}e$	(95 ± 5) MeV/c^2
top	$\frac{2}{3}e$	$(173.21 \pm 0.51 \pm 0.71)$ GeV/c^2
bottom	$-\frac{1}{3}e$	(4.18 ± 0.03) GeV/c^2

Table 1.1: The six quarks with their charges and masses. The only mass which can be directly measured is the mass of the top quark, the other masses are given in the $\overline{\text{MS}}$ renormalisation scheme with $\mu = 2\,\text{GeV/c}^2$ (for u,d,s) and $\mu = m_{b,c}$ (for c,b), respectively. For more details refer to [1].

		mass in MeV/c^2	life time in s
electron	e	0.510998928(11)	stable
electron neutrino	ν_e	0*	stable*
muon	μ	105.6583715(35)	$2.1969811(22) \times 10^{-6}$
muon neutrino	ν_μ	0*	stable*
tau	τ	1776.82(16)	$(290.6 \pm 1.0) \times 10^{-15}$
tau neutrino	ν_τ	0*	stable*

Table 1.2: The six fermions with their masses and life times. *In the standard model the neutrinos are massless and stable. However, the observation of neutrino oscillations (a review is given in [1]) requires the neutrinos to have small masses.

interaction	gauge boson	mass in GeV/c^2
electromagnetic	photon γ	0
weak	$W^\pm$	80.385(15)
	Z^0	91.1876(21)
strong	8 gluons	0

Table 1.3: The gauge bosons for the three interactions. While the photon and the gluons are massless, the weak gauge bosons are massive. They acquire their masses through the Higgs mechanism of electroweak symmetry breaking (see section 1.1.1).

1.1.1 Electroweak Interactions

The electromagnetic and weak interactions can be commonly described in one gauge theory [7–9], namely an $SU(2) \times U(1)$. The gauge bosons W^i_μ ($i = 1, 2, 3$) of $SU(2)$ and B_μ of $U(1)$ are connected to the observed gauge bosons by

$$\begin{aligned} W^\pm_\mu &= \frac{1}{\sqrt{2}}\left(W^1_\mu \mp W^2_\mu\right) \\ A_\mu &= \cos(\theta_W)B_\mu + \sin(\theta_W)W^3_\mu \\ Z^0_\mu &= -\sin(\theta_W)B_\mu + \cos(\theta_W)W^3_\mu \end{aligned} \tag{1.1}$$

where A_μ denotes the photon. The weak mixing angle θ_W connects the two couplings g of $U(1)$ and g' of $SU(2)$ via

$$\theta_W = \arctan\left(\frac{g'}{g}\right) = 0.23116(12)\,, \tag{1.2}$$

and relates g to the electric charge e of the electron as

$$e = g\sin(\theta_W)\,. \tag{1.3}$$

The mass of the gauge bosons is generated through a spontaneous symmetry breaking. A scalar Higgs doublet $\phi = \left(\begin{smallmatrix}\phi^+\\ \phi^0\end{smallmatrix}\right)$ with a potential

$$V(\phi) = \mu^2\phi^\dagger\phi + \frac{\lambda^2}{2}(\phi^\dagger\phi)^2 \tag{1.4}$$

is added to the Lagrangian. For $\mu^2 < 0$ and $\lambda^2 > 0$, the field ϕ has a vacuum expectation value $\frac{v}{\sqrt{2}}$ which breaks the electroweak symmetry. After the symmetry breaking only one neutral Higgs boson H remains in the theory. The masses of the gauge bosons and the Higgs boson can be expressed in terms of the vacuum expectation value

$$\begin{aligned} M_H &= \lambda v\\ M_W &= \frac{gv}{2} = \frac{ev}{2\sin(\theta_W)}\\ M_Z &= \frac{M_W}{\cos(\theta_W)}\\ M_\gamma &= 0\,, \end{aligned} \tag{1.5}$$

with $v = 246.22\,\text{GeV}$. λ is not fixed by theory and thus the mass of the Higgs boson is a free parameter of the standard model. The current value for the Higgs mass is $125.09 \pm 0.24\,\text{GeV}$ [10].

1.1.2 Strong Interactions and QCD

The strong interaction between quarks is described by an $SU(3)$ gauge theory, the so-called quantum chromodynamics (QCD). Quarks can carry three different kinds of QCD charges, which are called colours (antiquarks carry the corresponding anti-colour). The interaction between quarks is mediated by 8 gluons which – due to the non-abelian gauge group – also carry colour. The fact that no free quarks or gluons are observed lead to the *confinement* hypothesis: All asymptotic QCD states are colourless, i. e. only certain combinations of quarks and antiquarks, called hadrons, are allowed and described by colour-singlets. The simplest possibilities are mesons (quark-antiquark states) and baryons (three-quark states):

$$M = \frac{1}{\sqrt{3}}\delta^{\alpha\beta}|q_\alpha\overline{q}_\beta\rangle \qquad B = \frac{1}{\sqrt{6}}\epsilon^{\alpha\beta\gamma}|q_\alpha q_\beta q_\gamma\rangle \tag{1.6}$$

More details on the quark model and bound states of QCD are given in section 1.2.

The Structure of the Proton and Asymptotic Freedom

The cross section for elastic electron-proton scattering $e^-p \to e^-p$ in the proton rest frame is given by

$$\frac{d\sigma}{dQ^2} = \frac{\pi\alpha^2\cos\frac{\theta}{2}}{4E^2\sin^4\frac{\theta}{2}EE'}\left[\frac{\left|G_E(Q^2)\right|^2 + \frac{Q^2}{4M_p^2}\left|G_M(Q^2)\right|^2}{1+\frac{Q^2}{4M_p^2}} + \frac{Q^2}{2M_p^2}\left|G_M(Q^2)\right|^2\tan^2\frac{\theta}{2}\right]\,, \tag{1.7}$$

where E and E' are the energies of the incoming and scattered electron, respectively, θ the electron scattering angle, M_p the proton mass and

$$Q^2 \equiv -q^2 \approx 4EE' \sin^2 \frac{\theta}{2} \tag{1.8}$$

the squared four-momentum transfer by the virtual photon, where the lepton masses are neglected. The electric and magnetic form factors $G_E(Q^2)$ and $G_M(Q^2)$ describe the structure of the proton. For a point-like spin-$\frac{1}{2}$ particle they would be equal to $G_E = 1$ (electric charge in units of e) and $G_M = 5.59$ (magnetic moment in units of the nuclear magneton μ_N), respectively. This can be observed at very low energies ($Q^2 \ll 1\,\text{GeV}^2$) where the proton behaves like a point-like particle. For higher energies the form factors can be approximated by the dipole form

$$G_M(Q^2)/\mu_p \approx G_E(Q^2) \approx \left(1 + \frac{Q^2}{0.7\,\text{GeV}^2}\right)^{-2} . \tag{1.9}$$

Thus, the proton is an extended object with a size of approximately 1 fm.
For even higher energies, the inelastic process $e^-p \to e^-X$ becomes dominant. The one photon exchange differential cross section is given by

$$\frac{d\sigma}{dQ^2 d\nu} = \frac{\pi\alpha^2 \cos\frac{\theta}{2}}{4E^2 \sin^4 \frac{\theta}{2} EE'} \left[W_2(Q^2, \nu) + 2W_1(Q^2, \nu) \tan^2 \frac{\theta}{2}\right] , \tag{1.10}$$

with the energy transfer in the proton rest frame $\nu = E - E'$ and the structure functions $W_1(Q^2, \nu)$ and $W_2(Q^2, \nu)$. The behaviour of the structure functions at large Q^2 hints at the existence of point-like objects inside the proton. Assuming the proton to be made of spin-$\frac{1}{2}$ constituents (so-called partons), which carry a fraction ξ_i of the total proton momentum each, the structure functions of the single partons can be written as

$$\begin{aligned} W_1^{(i)}(Q^2, \nu) &= \frac{e_i^2}{2M_p} \delta(\xi_i - x) \\ W_2^{(i)}(Q^2, \nu) &= e_i^2 \frac{x}{\nu} \delta(\xi_i - x) . \end{aligned} \tag{1.11}$$

Here, e_i is the electric charge of the parton and $x = \frac{Q^2}{2M_p\nu}$ the Bjorken variable. Thus, the structure functions of the single partons only depend on x, which fixes the parton momentum fraction ξ_i. In the limit of large Q^2 and $\nu \to \infty$, where x is fixed and the transverse momenta of the partons can be neglected, the proton structure functions are given as an incoherent sum of the parton structure functions:

$$\begin{aligned} W_1(Q^2, \nu) &= \sum_i \int_0^1 d\xi_i f_i(\xi_i) W_1^{(i)}(Q^2, \nu) = \frac{1}{2M_p} \sum_i e_i^2 f_i(x) \equiv \frac{1}{M_p} F_1(x) \\ W_2(Q^2, \nu) &= \sum_i \int_0^1 d\xi_i f_i(\xi_i) W_2^{(i)}(Q^2, \nu) = \frac{x}{\nu} \sum_i e_i^2 f_i(x) \equiv \frac{1}{\nu} F_2(x) . \end{aligned} \tag{1.12}$$

In this model, the proton structure functions only depend on x. This behaviour is called Bjorken scaling [11]. In addition, the Callan-Gross relation [12]

$$F_2(x) = 2xF_1(x) \tag{1.13}$$

is a direct consequence of the assumption of spin-$\frac{1}{2}$ partons (spin-0 partons would have lead to $F_1(x) = 0$). The experimental confirmation of Bjorken scaling exhibits another property of the strong interaction: At high energies quarks are only weakly bound and behave like free particles. This behaviour is called *asymptotic freedom*.

The Running QCD Coupling

Similar to QED, renormalisation leads to a running coupling constant in QCD. On one-loop level the running coupling is given by

$$\alpha_s(Q^2) = \frac{\alpha_s(Q_0^2)}{1 - \frac{\beta_1 \alpha_s(Q_0^2)}{2\pi} \ln\left(\frac{Q^2}{Q_0^2}\right)}, \tag{1.14}$$

with the first coefficient of the β-function

$$\beta_1 = \frac{2N_f - 11N_C}{6}, \tag{1.15}$$

where N_f and N_C are the number of flavours and colours, respectively. For $N_C = 3$ and $N_f \leqslant 16$ the coupling decreases with increasing Q^2 leading to asymptotic freedom of QCD. For low energies, α_s rises and a perturbative approach is no longer valid for bound states. Figure 1.2 shows a collection of extractions of the QCD coupling constant as a function of Q. The world average for α_s at the mass of the Z boson is given by the PDG [1] as

$$\alpha_s(M_Z^2) = 0.1185 \pm 0.0006$$

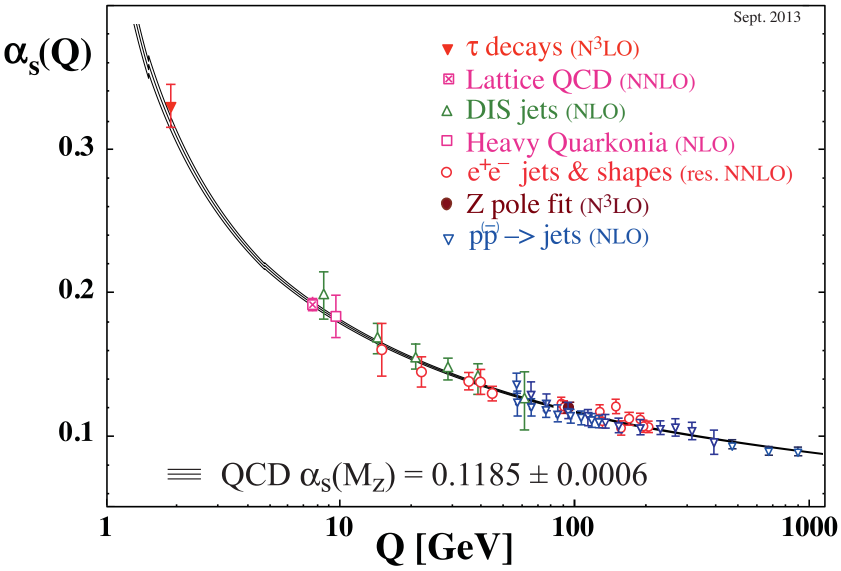

Figure 1.2: Summary of measurements [1] of α_s as a function of the momentum transfer Q using several channels and different orders of perturbation theory.

The QCD Lagrangian

QCD can be formulated as a non-abelian gauge theory with symmetry group $SU(3)_c$ in colour space. The fundamental degrees of freedom are the quarks. In the limit of massless quarks, QCD does not distinguish between different flavours. The non-abelian gauge group leads to self interactions among the gluons, which also carry colour charge. This self interaction influences the running of the coupling constant which results in asymptotic freedom at high energies.

In compact notation the Lagrangian of QCD, which is invariant under $SU(3)_c$ transformations in colour space, is given as

$$\mathcal{L}_{QCD} = -\frac{1}{4} G_a^{\mu\nu} G_{\mu\nu}^a + \sum_f \bar{q}_f (i\gamma^\mu D_\mu - m_f) q_f, \tag{1.16}$$

where $a = 1, \dots, 8$ counts the eight gluons, $f = u, d, s, c, b, t$ denotes the six quark flavours and μ, ν are Lorentz indices using the Einstein summation convention. The gluonic field strength tensor is given as

$$G_a^{\mu\nu} = \partial^\mu G_a^\nu - \partial^\nu G_a^\mu + g_s f^{abc} G_b^\mu G_c^\nu \tag{1.17}$$

and the covariant derivative as

$$D^\mu = \partial^\mu - i g_s \frac{\lambda^a}{2} G_a^\mu , \tag{1.18}$$

where the generators λ^a of $SU(3)$ and the corresponding structure constants f^{abc} are linked by[1]

$$[\lambda^a, \lambda^b] = 2 i f^{abc} \lambda^c . \tag{1.19}$$

With equations (1.17) and (1.18) the QCD Lagrangian can be decomposed in different terms

$$\begin{aligned} \mathcal{L}_{\text{QCD}} = & \sum_f \bar{q}_f^\alpha (i\gamma^\mu \partial_\mu - m_f) q_{f,\alpha} - \frac{1}{4} (\partial^\mu G_a^\nu - \partial^\nu G_a^\mu)(\partial_\mu G_\nu^a - \partial_\nu G_\mu^a) \\ & + g_s G_a^\mu \sum_f \bar{q}_f^\alpha \gamma_\mu \left(\frac{\lambda^a}{2} \right)_{\alpha\beta} q_f^\beta \\ & - \frac{g_s}{2} f^{abc} (\partial^\mu G_a^\nu - \partial^\nu G_a^\mu) G_\mu^b G_\nu^c - \frac{g_s^2}{4} f^{abc} f_{ade} G_b^\mu G_c^\nu G_\mu^d G_\nu^e , \end{aligned} \tag{1.20}$$

where $\alpha, \beta = r, g, b$ denote the three different colours. The first line describes the propagation of gluons and quarks, the second line the interaction of quarks with a gluon and the third line shows the self interaction of three and four gluons, respectively. Thus, the Lagrangian can symbolically written as

$\mathcal{L}_{\text{QCD}} =$

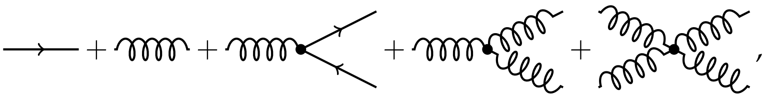

(1.21)

where a summation over all possible combination of flavours and colours is implied.
There is no analytic solution for QCD as a gauge theory. In the high energy regime, where the coupling constant is sufficiently small, a perturbation series expansion is possible. In the low energy regime, where quarks are confined into hadrons, the coupling constant is too large for a perturbative calculation. However, hadrons – the bound states of QCD – can be described by the quark model, which will be presented in the following.

1.2 QUARK MODEL AND QCD BOUND STATES

The large number of different particles which were discovered in the 1950s and 60s led to the development of the quark model, mainly driven by the work of Gell-Mann and Ne'emann [13]. The model only included the three light quarks (u,d,s) which were known at that time. Today, the model is well established and extended to six quarks. However, the following considerations will mainly focus on the three light quarks, which are well separated in mass from the heavier quarks (compare table 1.1).
Starting point is the experimentally well confirmed confinement hypothesis: Only colourless hadrons are observed in nature. Therefore, only certain combinations of quarks are possible. This can be achieved, if the three lightest quarks are in the fundamental representation **3** of an $SU(3)_f$ in flavour space. The three antiquarks belong to the adjoint representation $\bar{\mathbf{3}}$. In this model, the hadrons are part of different $SU(3)_f$ multiplets. This $SU(3)_f$ is not a perfect symmetry; it is broken by the difference in quark masses.

---

[1] Some more details on the group $SU(3)$ can be found in appendix A.1.

1.2.1 Flavour Quantum Numbers

The experimental observations on the formation and decay of hadrons led to the introduction of several quantum numbers, which are related to the quark flavours:

- The up and down quark, which have similar masses, fulfil a nearly perfect $SU(2)$ symmetry, which is called isospin I. The concept was originally introduced by Heisenberg [14] to explain the similar properties of protons and neutrons ($\frac{m_n - m_p}{m_p} \approx 0.14\%$), the name isospin was suggested by Wigner [15]. In strong interaction, isospin is conserved and no down quarks can be turned into up quarks. However, the decay of down quarks into up quarks is possible via weak interaction (e. g. neutron β decay $n \to pe\overline{\nu}_e$).

- The observation of particles with an unusual long life time led to the introduction of a new quantum number called strangeness S. Today, strangeness is associated with strange quarks which have $S = -1$ while anti-strange quarks have $S = 1$. Like isospin, strangeness is only conserved in strong interaction.

- Like strangeness, there are also quantum numbers for charm, bottom and top quarks.

- Experimental observations show, that the number of baryons $\mathcal{B}$ is conserved in all reactions. As baryons are three-quark states, each quark has a baryon number of $\mathcal{B} = \frac{1}{3}$ and each antiquark a baryon number of $\mathcal{B} = -\frac{1}{3}$.

	u	d	s	c	b	t
I – isospin	$\frac{1}{2}$	$\frac{1}{2}$	0	0	0	0
I_3 – isospin projection	$+\frac{1}{2}$	$-\frac{1}{2}$	0	0	0	0
S – strangeness	0	0	-1	0	0	0
C – charm	0	0	0	1	0	0
B – bottomness	0	0	0	0	-1	0
T – topness	0	0	0	0	0	1

Table 1.4: Additive flavour quantum numbers of quarks.

Those flavour quantum numbers for the six quarks are listed in table 1.4. They are chosen such that the sign of the flavour corresponds to the sign of the electric charge of the quark. This holds also for any charged meson. The flavour quantum numbers are connected to the electric charge through the Gell-Mann–Nishijima formula [16, 17]

$$Q = I_3 + \frac{\mathcal{B} + S + C + B + T}{2}\,, \tag{1.22}$$

which is also valid for any hadron.

1.2.2 Mesons

The simplest combination of quarks to colourless states is the combination of a quark with a certain colour with an antiquark of the corresponding anti-colour ($q\overline{q}'$), where the flavours of the two quarks might be different. These bound states are called mesons. They can have a spin of 0 (anti parallel quark spins) or 1 (parallel quark spins). For an angular momentum l of the $q\overline{q}'$ state, the total angular momentum J is in the range

$$|l - s| \leqslant J \leqslant |l + s|\ . \tag{1.23}$$

The parity of a meson is given by

$$P = (-1)^{l+1}\,, \tag{1.24}$$

the charge conjugation of a meson which is made of a quark and its own antiquark is

$$C = (-1)^{l+s}\,. \tag{1.25}$$

Mesons are members of $SU(3)_f$ multiplets for a given J^{PC}. For $l = 0$ those are pseudoscalars (0^{-+}) and vectors (1^{--}). Taking only the three light quarks (u,d,s) into account, nine possible $q\overline{q}'$ combinations form a singlet and an octet

$$\mathbf{3} \otimes \overline{\mathbf{3}} = \mathbf{8} \oplus \mathbf{1}\,. \tag{1.26}$$

The isoscalar states of the octet (ψ_8) and the singlet (ψ_1) mix into the physically observed states. Therefore, the octet and singlet are normally seen together as meson nonets, which are shown in figures 1.3 and 1.4 for the pseudoscalar and vector mesons, respectively.

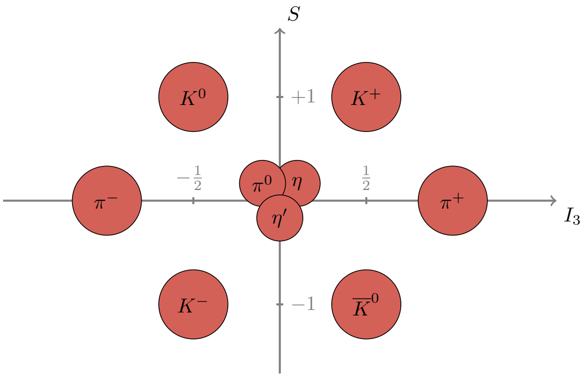

Figure 1.3: The pseudoscalar mesons.

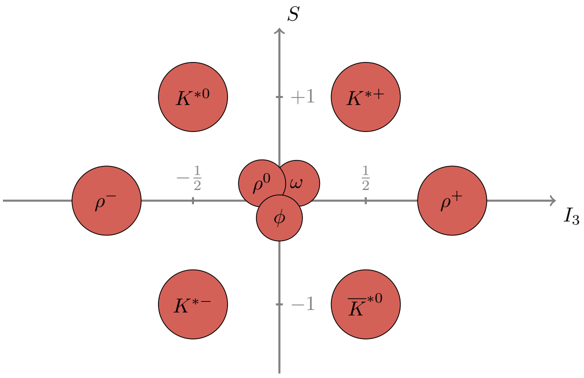

Figure 1.4: The vector mesons.

1.2.3 Baryons

Another possibility for colourless states is the combination of three quarks with different colours which are called baryons. Taking again only the three light quarks into account the 27 possible $q_1 q_2 q_3$ combinations decompose as

$$\mathbf{3} \otimes \mathbf{3} \otimes \mathbf{3} = \mathbf{10}_S \oplus \mathbf{8}_M \oplus \mathbf{8}_M \oplus \mathbf{1}_A\,, \tag{1.27}$$

where the subscripts denote the symmetry (S = symmetric, M = mixed symmetry, A = antisymmetric) of the multiplets. To obtain the experimentally observed states, flavour and spin are combined into a spin-flavour $SU(6)$ which decomposes as

$$\mathbf{6} \otimes \mathbf{6} \otimes \mathbf{6} = \mathbf{56}_S \oplus \mathbf{70}_M \oplus \mathbf{70}_M \oplus \mathbf{20}_A\,. \tag{1.28}$$

The ground states have to be symmetric in the spin-flavour wave function. The 56 possible states form a spin-$\frac{1}{2}$ octet ($8 \cdot 2$ states) and a spin-$\frac{3}{2}$ decuplet ($10 \cdot 4$ states). They are shown in figures 1.5 and 1.6, respectively. In the decuplet, in contrast to the octet, also states with three identical quark flavours are allowed, namely the $\Delta^{++} = |uuu\rangle$, the $\Delta^- = |ddd\rangle$ and the $\Omega^- = |sss\rangle$. These states led to the introduction of colour: The wave function in space, spin and flavour is symmetric for these particles. According to the spin-statistics theorem [18] the wave function of a fermion has to be antisymmetric. Thus, an additional degree of freedom with an antisymmetric wave function had to be introduced. The discovery of the Ω^- in 1964 [19] was a great success for the quark model, which this particles properties were predicted in.

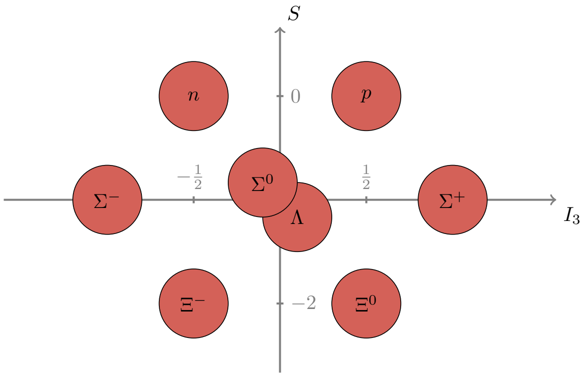

Figure 1.5: The octet of spin-$\frac{1}{2}$ baryons

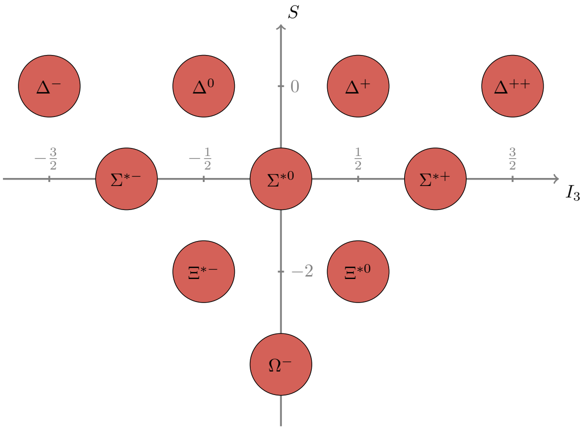

Figure 1.6: The decuplet of spin-$\frac{3}{2}$ baryons

1.2.4 Beyond Mesons and Baryons

Not only mesons and baryons, but also more complex combinations of quarks and gluons are allowed within the standard model. However, only a few of those states have been observed by now and are still controversially discussed. The “simplest” states beyond mesons and baryons are

- States with 4 quarks $|q\bar{q}q\bar{q}\rangle$, mostly assumed to be of a molecular type $|q\bar{q}\rangle|q\bar{q}\rangle$. Some high-mass states in the charmonium and bottomonium spectrum, such as the $X(3872)$ [20, 21], the $\Upsilon_b(10890)$ [22] and $Z_c(3900)$ [23, 24] are now assumed to be 4-quark states.
- States with gluonic degrees of freedom, such as hybrids $|q\bar{q}'g\rangle$ or glue balls $|gg\ldots\rangle$, can carry non-mesonic quantum numbers, i. e. J^{PC}-combinations that are not allowed in $|q\bar{q}'\rangle$-states. Candidates for those states where found, e. g. at COMPASS [25].

A summary and discussion on glue balls and other exotic mesons may be found in [26].

1.3 STRONG INTERACTIONS AND THE POMERON

Scattering processes involving strong interactions cannot be calculated from QCD due to the large coupling constant. Even before QCD was developed, those processes were described in a phenomenological way. This description was based on imposing reasonable properties of the scattering matrix (S-matrix) based on classical theories. The basic ideas and consequences of this approach are given in the following based on the first chapter of [27].

1.3.1 Properties of the S-Matrix

The ij-element of the S-matrix is the probability for an incoming state $|\psi_i^{\text{in}}\rangle$ to become the outgoing state $|\psi_j^{\text{out}}\rangle$

$$S_{ij} = \langle\psi_j^{\text{out}}|\psi_i^{\text{in}}\rangle\,. \tag{1.29}$$

The scattering amplitude A_{ij} is related to the S-matrix by

$$S_{ij} = \delta_{ij} + i(2\pi)^4\delta^4\left(\sum p_i - \sum p_j\right)A_{ij} \equiv \delta_{ij} + iT_{ij}\,, \tag{1.30}$$

with the T-matrix element T_{ij} describing the non-elastic scattering process.
The properties imposed on the S-matrix are:

1. The S-matrix is Lorentz invariant.
2. The S-matrix is unitary, i. e. $SS^\dagger = S^\dagger S = \mathbb{1}$.
3. The S-matrix is an analytic function of Lorentz-invariant variables which are taken as complex variables. Singularities have to be implied by unitarity.

Lorentz invariance implies that the S-matrix can be written as a function of Lorentz invariant variables. For a simple two-particle scattering process

$$a + b \to c + d$$

those are the Mandelstam variables [28]

$$\begin{aligned} s &= (p_a + p_b)^2 \\ t &= (p_a - p_c)^2 \\ u &= (p_a - p_d)^2 , \end{aligned} \tag{1.31}$$

which are connected to the invariant masses of the particles via

$$s + t + u = m_a^2 + m_b^2 + m_c^2 + m_d^2 . \tag{1.32}$$

Thus, the S-matrix can be written as a function of s and t only.

Unitarity of the S-matrix is connected to conservation of probability, i. e. the probabilities for an in-state to end up in a certain out-state must sum up to one. An important consequence of unitarity [29] is the optical theorem

$$2\mathfrak{Im}(A_{ii}) = \Psi\sigma_{\text{tot}} , \tag{1.33}$$

which connects the forward elastic amplitude A_{ii} to the total cross section σ_{tot}. Ψ is a flux factor with $\Psi \approx 2s$ for $\sqrt{s} \gg m_i$.

Analyticity is connected to causality and has some consequences:
Together with unitarity, analyticity implies the properties of s-plane singularities in the scattering Amplitude $A_{ij}(s,t)$. Every n-particle threshold leads to an s-plane cut, which contributes to the imaginary part of the scattering amplitude above threshold. Below threshold the amplitude is purely real and thus

$$A(s,t)^* = A(s^*,t) \tag{1.34}$$

is valid in the whole complex s-plane (Schwarz reflection principle). The imaginary part

$$\mathfrak{Im}(A(s,t)) = \frac{1}{2i} \lim_{\epsilon \to 0} \left[A(s + i\epsilon, t) - A(s - i\epsilon, t)\right] \tag{1.35}$$

is only non-zero if there is a cut along the real axis with a branch point at threshold. The right-hand side of (1.35) is then called s-channel discontinuity $\Delta_s(A(s,t))$.
Analyticity implies crossing symmetry, that means that the amplitude for the t-channel process

$$a + \bar{c} \to \bar{b} + d$$

is given by the s-channel amplitude by interchanging s and t

$$A_{a+\bar{c}\to\bar{b}+d}(s,t;u) = A_{a+b\to c+d}(t,s;u) . \tag{1.36}$$

Similarly, the amplitude for the u-channel process

$$a + \overline{d} \to \overline{b} + c$$

is given by

$$A_{a+\overline{d}\to\overline{b}+c}(s, t; u) = A_{a+b\to c+d}(u, t; s)\,. \tag{1.37}$$

Analyticity allows to connect the real and imaginary parts of the amplitudes via dispersion relations. Using the Cauchy integral formula for a contour not containing any singularities (see figure 1.7) yields

$$A(s, t) = \frac{1}{\pi}\int\limits_{+s_{\mathrm{th}}}^{+\infty} \frac{\mathfrak{Im}(A(s', t))}{s' - s}\mathrm{d}s' + \int\limits_{-\infty}^{-s_{\mathrm{th}}} \frac{\mathfrak{Im}(A(s', t))}{s' - s}\mathrm{d}s'\,. \tag{1.38}$$

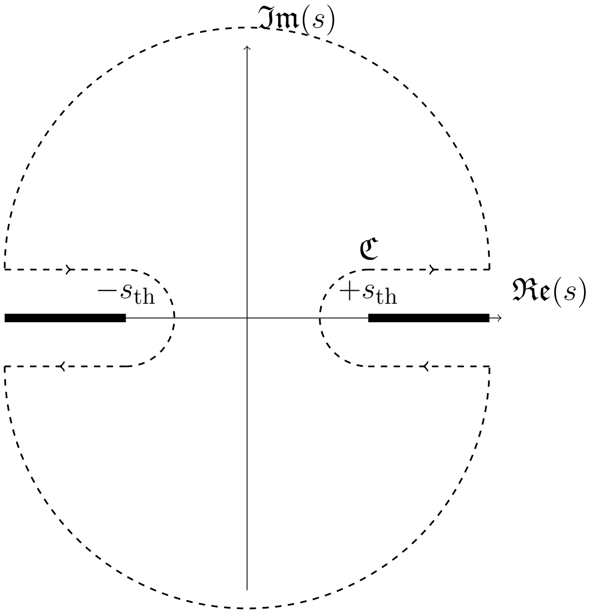

Figure 1.7: The contour $\mathfrak{C}$ does not contain the singularities, which are in this case cuts and denoted by thick lines.

Without any assumptions about the underlying theory, it is possible to construct conditions for the scattering amplitudes. To fully reconstruct amplitudes, their asymptotic behaviour is needed. The determination of this asymptotic behaviour of amplitudes is the goal of Regge theory [30, 31].

1.3.2 Regge Theory and the Pomeron

The two-particle scattering process in the t-channel

$$a + \overline{c} \to \overline{b} + d$$

for $\sqrt{s} \gg m_i$ can be expanded in a series of Legendre polynomials $P_\ell(\cos\theta)$, where θ is the scattering angle in the centre-of-mass frame and

$$\cos\theta = 1 + \frac{2t}{s}\,. \tag{1.39}$$

This expansion

$$A_{a+\bar{c}\to\bar{b}+d}(s,t) = \sum_{\ell=0}^{\infty}(2\ell+1)a_\ell(s)P_\ell\big(1+2\tfrac{2t}{s}\big) \tag{1.40}$$

is called a partial wave expansion and $a_\ell(s)$ are the partial wave amplitudes. By crossing symmetry this amplitude can be continued into the s-channel as

$$A_{a+b\to c+d}(s,t) = \sum_{\ell=0}^{\infty}(2\ell+1)a_\ell(t)P_\ell\big(1+2\tfrac{2s}{t}\big) \tag{1.41}$$

and rewritten [32, 33] as an integral in the complex angular-momentum plane (see figure 1.8)

$$A(s,t) = \frac{1}{2i}\oint_{\mathfrak{C}}(2\ell+1)\frac{a(\ell,t)}{\sin(\pi\ell)}P\big(\ell,1+\tfrac{2s}{t}\big)\,d\ell\,, \tag{1.42}$$

where the Legendre polynomials are expressed using hypergeometric functions[2] and analytically continued in ℓ. The function $a(\ell,t)$ is the analytic continuation of the partial wave amplitude $a_\ell(t)$.

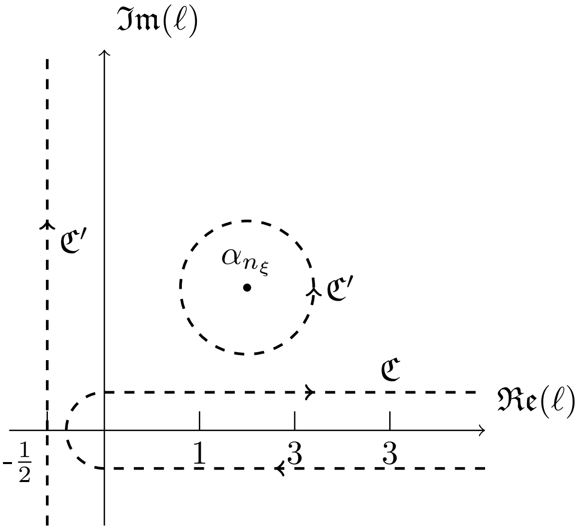

Figure 1.8: Contours $\mathfrak{C}$ and $\mathfrak{C}'$.

The expansion (1.42) is unique [34] as long as

$$a(l,t) < \exp(\pi|\ell|) \quad \text{for } |\ell| \to \infty\,. \tag{1.43}$$

As the amplitude contains terms proportional to $(-1)^\ell$, this condition is violated along the negative imaginary axis[3]. Therefore, two analytic functions $a^{(+1)}(\ell,t)$ and $a^{(-1)}(\ell,t)$ are introduced, which are analytic continuations of even and odd partial waves, respectively. The partial wave expansion (1.42) can then be rewritten

$$A(s,t) = \frac{1}{2i}\oint_{\mathfrak{C}}\frac{2\ell+1}{\sin(\pi\ell)}\sum_{\xi=\pm1}\frac{\xi+e^{-i\pi\ell}}{2}a^{(\xi)}P\big(\ell,1+\tfrac{2s}{t}\big)\,d\ell\,, \tag{1.44}$$

---

[2] $P_\ell(x) = F\begin{pmatrix} -\ell,\ \ell+1 \\ 1 \end{pmatrix}, \tfrac{1-x}{2}\Big)$, see `http://dlmf.nist.gov/15.9` (called August 30, 2015).

[3] $(-1)^{-\alpha i} = \exp(\alpha\pi)$ for $\alpha \in \mathbb{R}^+$ violating the inequality.

with the signature ξ of the partial wave. The contour $\mathfrak{C}$ is deformed to the contour $\mathfrak{C}'$ parallel to the imaginary axis at $\mathfrak{Re}(\ell) = -\frac{1}{2}$. To restore analyticity, any poles that the functions $a^{(\xi)}(\ell, t)$ might have at a given $\ell = \alpha_{n_\xi}(t)$ have to be circled by the contour (see figure 1.8). The integral in eq. (1.44) can then be calculated using the residue theorem

$$\begin{aligned} A(s,t) =& \frac{1}{2i} \int\limits_{-\frac{1}{2}-i\infty}^{-\frac{1}{2}+i\infty} \frac{2\ell+1}{\sin(\pi\ell)} \sum_{\xi=\pm1} \frac{\xi + e^{-i\pi\ell}}{2} a^{(\xi)} P\big(\ell, 1+\tfrac{2s}{t}\big)\, d\ell \\ &+ \sum_{\xi=\pm1} \sum_{n_\xi} \frac{\xi + e^{-i\pi\alpha_{n_\xi}(t)}}{2} \frac{\hat{\beta}_{n_\xi}(t)}{\sin\big(\pi\alpha_{n_\xi}(t)\big)} P\big(\alpha_{n_\xi}(t), 1+\tfrac{2s}{t}\big)\,, \end{aligned} \tag{1.45}$$

where $\alpha_{n_\xi}(t)$ are even- and odd-signature Regge poles and

$$\hat{\beta} = \pi\big(2\alpha_{n_\xi}(t)\big)\mathrm{Res}\big(A(s,t), \alpha_{n_\xi}(t)\big)\,. \tag{1.46}$$

In the so-called Regge region ($s \gg |t|$) the Legendre polynomials are dominated by the leading term

$$P_\ell\big(1+\tfrac{2s}{t}\big) \xrightarrow{s \gg |t|} \frac{\Gamma(2\ell+1)}{\Gamma^2(\ell+1)} \left(\frac{s}{2t}\right)^\ell\,, \tag{1.47}$$

with Euler's gamma function $\Gamma(x)$. For $s \to \infty$ the integral in eq. (1.45) vanishes and the asymptotic behaviour of the amplitude is dominated by the leading Regge pole (the one with the largest real part of $\alpha_{n_\xi}(t)$) and given by

$$A(s,t) \xrightarrow{s \to \infty} \frac{\xi + e^{-i\pi\alpha(t)}}{2} \beta(t) s^{\alpha(t)}\,, \tag{1.48}$$

where $\alpha(t)$ is the leading Regge pole with its signature ξ and $\beta(t)$ contains all remaining factors.

The amplitude (1.48) describes the t-channel exchange of an object with "angular momentum" $\alpha(t)$. This object is not a particle (as its "angular momentum" is a function of t and thus not (half-)integer) and called a Reggeon. The exchange of a Reggeon is a superposition of all possible particle exchanges in the t-channel. The amplitude (1.48) of the process shown in figure 1.9 can be factorised into the two couplings γ_{ab} and γ_{bd} of two particles to the Reggeon

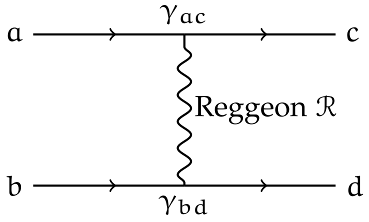

Figure 1.9: A t-channel Reggeon exchange diagram.

$$A(s,t) \xrightarrow{s \to \infty} \frac{\xi + e^{-i\pi\alpha(t)}}{2\sin\big(\pi\alpha(t)\big)} \frac{\gamma_{ab}\gamma_{bd}}{\Gamma\big(\alpha(t)\big)} s^{\alpha(t)}\,. \tag{1.49}$$

For integer values of $\alpha(t)$, the factor $\sin\big(\pi\alpha(t)\big)$ in the denominator leads to a pole in the amplitude which corresponds to a t-channel exchange of a resonance with integer spin, where the gamma function cancels so-called nonsense poles at negative integer values of $\alpha(t)$. The mass and spin of the resonances are connected via $\alpha(m_i^2) = J_i$. In the Chew-Frautschi plot [35, 36] in figure 1.10, the lightest meson resonances for each spin are plotted against their squared mass. All resonances lie on a straight line, thus $\alpha(t)$ is a linear function of t

$$\alpha(t) = \alpha(0) + \alpha' t \tag{1.50}$$

with $\alpha(0) = 0.55$ and $\alpha' = 0.86\,\text{GeV}^{-2}$, which is called Regge trajectory, or – as it includes the ρ meson – also ρ-trajectory.

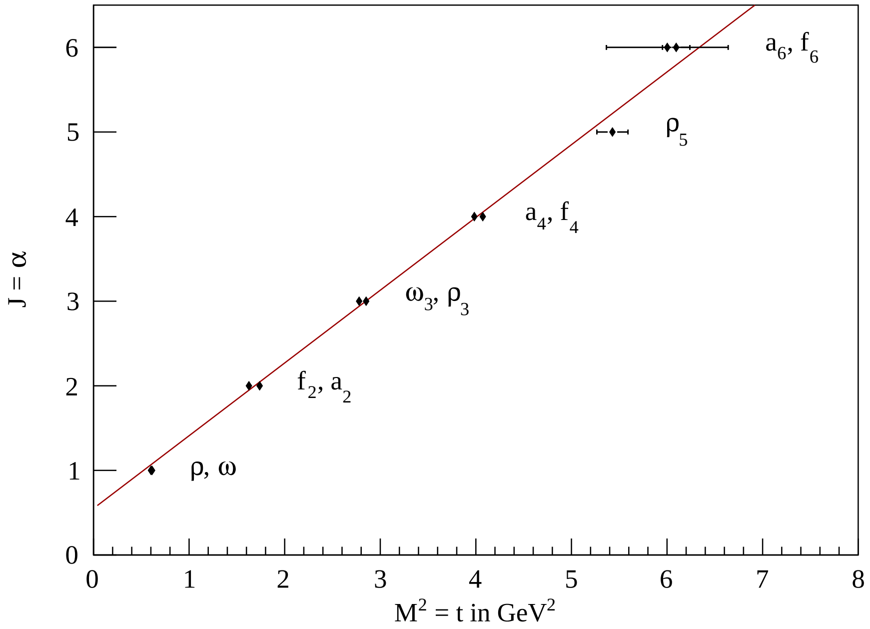

Figure 1.10: The Chew-Frautschi plot using the newest masses taken from the PDG [1].

The intercept $\alpha(0)$ together with the optical theorem (1.33) lead to the asymptotic behaviour of the cross section

$$\sigma_{\text{tot}} \propto s^{\alpha(0)-1}\,. \tag{1.51}$$

For the ρ-trajectory described above $\alpha(0) < 1$, which leads to a falling cross section ($\propto s^{-0.45}$) with increasing centre-of-mass energy. The Pomeranchuk theorem [37, 38] states, that any charge-exchange cross section vanishes asymptotically. Experimental observations show that the total cross section for pp- and $p\bar{p}$-scattering, which is shown in figure 1.11, only falls with increasing s for small s and then rises slightly for higher values of s. For such a behaviour, the process must be dominated by the exchange of vacuum quantum numbers ($I = 0$, $C = +$) [39]. The slow rising of cross sections for increasing s can be attributed to a Regge trajectory with intercept $\alpha(0) > 1$ that carries vacuum quantum numbers. This trajectory is called the Pomeron. The particles on the Pomeron trajectory have so far not been discovered and would be candidates for glue balls.

The total cross sections for pp- and $p\bar{p}$-scattering shown in figure 1.11 can be fitted as [40]

$$\begin{aligned} \sigma_{pp} &= 21.7 s^{0.08} + 56.1 s^{-0.45}\,\text{mb} \\ \sigma_{p\bar{p}} &= 21.7 s^{0.08} + 98.4 s^{-0.45}\,\text{mb}\,. \end{aligned} \tag{1.52}$$

The first term in (1.52) is due to the Pomeron, which does not distinguish between protons and antiprotons, the second term is due to the Regge trajectory with $\alpha(0) = 0.55$, which

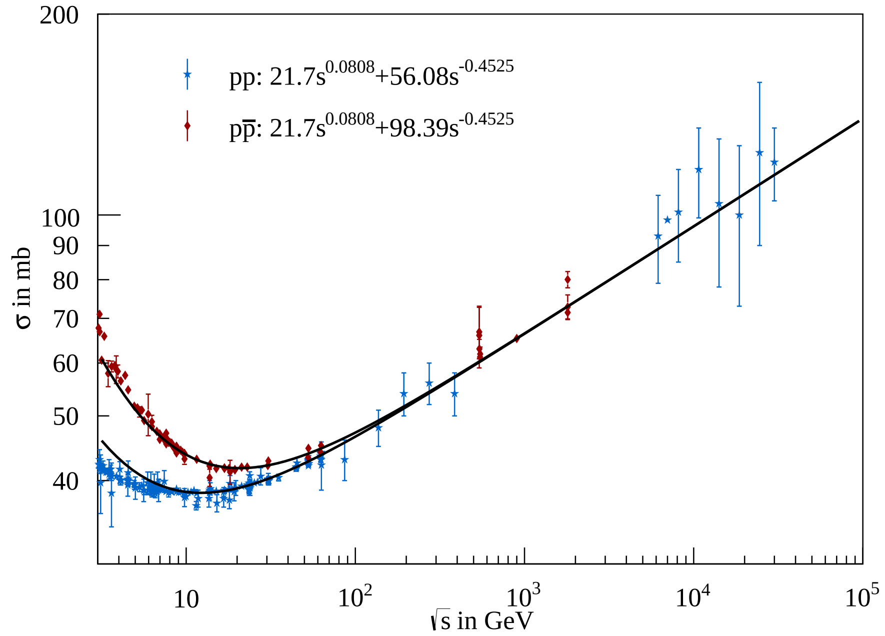

Figure 1.11: The total cross sections for pp- and $p\bar{p}$-scattering together with the fits taken from [40]. The cross section data are taken from the PDG at `http://pdg.lbl.gov/current/xsect` (called August 30, 2015, courtesy of the COMPAS group, IHEP, Protvino).

has different couplings to particles and antiparticles. Similar fits containing the same trajectories can be done for $\pi^\pm$- and γp-scattering. The intercept of the Pomeron trajectory can be extracted from the fit and equation (1.51) to $\alpha_{\mathbb{P}}(0) = 1.08$, the slope can be extracted from differential cross section measurements [41–43] as $\alpha'_{\mathbb{P}} = 0.25\,\mathrm{GeV}^{-2}$. In figure 1.12 the Pomeron

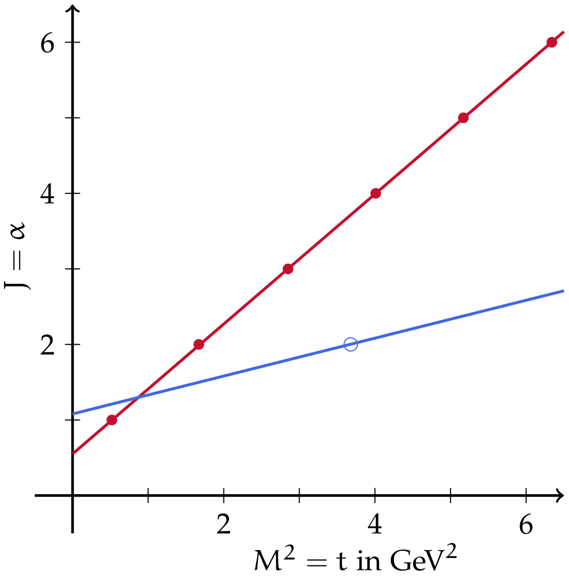

Figure 1.12: The ρ-trajectory (red) together with the Pomeron trajectory (blue). The red dots denote the intersections with integer spins, where real particles are present. The blue circle shows the intersection of the Pomeron trajectory with J = 2, where a real particle is expected.

trajectory is shown in blue together with the ρ-trajectory in red. The Pomeron trajectory intersects $J = 2$ at $t = 3.68\,\mathrm{GeV}^2$. Therefore, a particle with a mass of roughly $1.9\,\mathrm{GeV}/c^2$ with spin

2 and vacuum quantum numbers is expected. Indeed, the $f_2(1950)$ [1] has vacuum quantum numbers with a spin of $J = 2$ and is discussed as a glue ball candidate.

1.3.3 Diffractive Dissociation

Another process, in which the Pomeron plays in important role, is diffractive dissociation. In this hadron-hadron scattering process, one of the hadrons gains enough energy to either break up and produce a cluster of hadrons due to hadronisation, or to be exited into a resonance that decays into hadrons. This process can be described as a Pomeron emission by one hadron followed by a (resonant) Pomeron-hadron scattering into a hadronic final state. This process is depicted in figure 1.13.

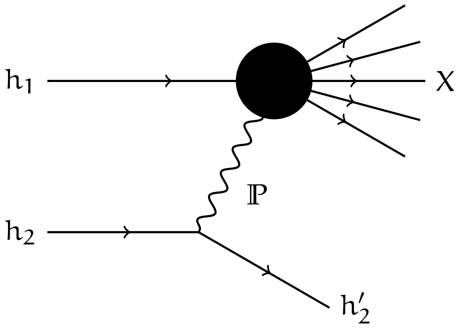

Figure 1.13: Diffractive dissociation of the hadron h_1 into the hadronic final state X through a Pomeron exchange with hadron h_2.

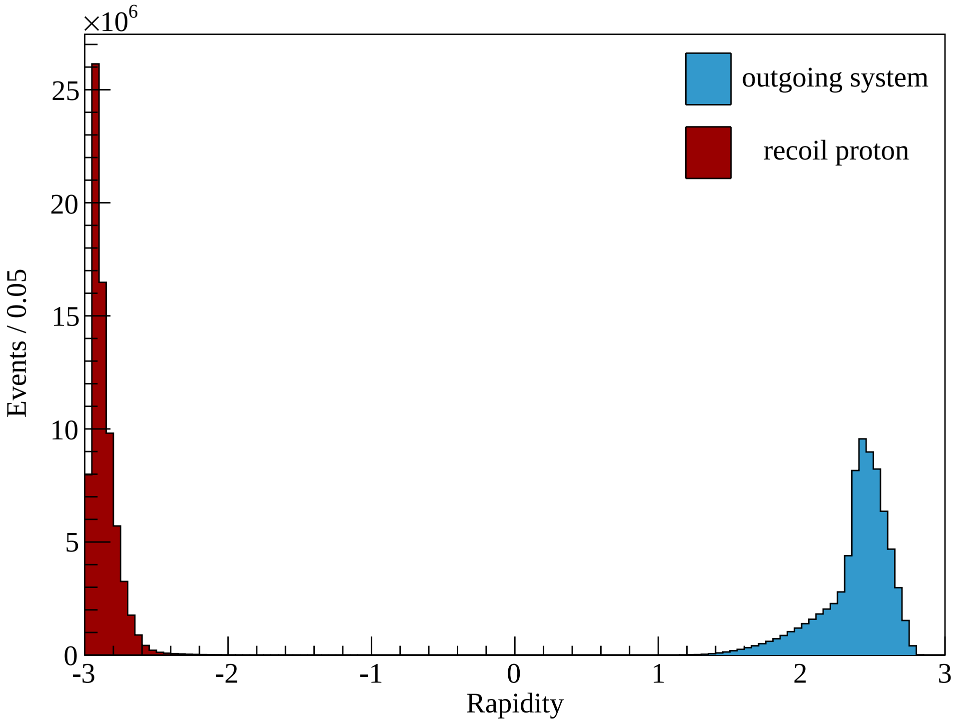

Figure 1.14: Rapidity of outgoing $p\pi^0$ system (blue) and recoil proton (red) for $pp \to pp\pi^0$. A large rapidity gap can be observed which is typical for diffractive dissociation. Details on the data used in this plot can be found in chapter 6.

Diffractive dissociation events are characterised by a large gap in rapidity between the hadron h_2 providing the Pomeron and the outgoing hadronic system X, where rapidity is defined as

$$y = \frac{1}{2} \ln \left(\frac{E + p_z}{E - p_z} \right) , \tag{1.53}$$

with the z-axis in the direction of the beam (h_1 in figure 1.13). In figure 1.14 the rapidity distributions are shown for the reaction $pp \to pp\pi^0$, which will be discussed in detail in the following. The large rapidity gap between the recoiling proton (red) and the outgoing $p\pi^0$ system (blue) shows the dominance of diffractive dissociation in this channel.

2

THE COMPASS EXPERIMENT AT CERN

The goal of the COMPASS (COmmon Muon and Proton Apparatus for Structure and Spectroscopy) experiment is to study QCD in a large range of momentum transfers covering perturbative as well as non-perturbative regions. The experimental set-up is shown in figure 2.1. COMPASS is a two-stage fixed-target spectrometer. The spectrometer magnet SM1 for the large angle spectrometer (LAS) has an integrated field strength up to 1 Tm, the magnet SM2 for the small angle spectrometer (SAS) an integrated field strength up to 4.4 Tm. The original set-up for data taking with muon beams is described in [44], the modifications for hadron beams in [45]. In the following a short overview is given over the components essential for the analyses presented in this work.

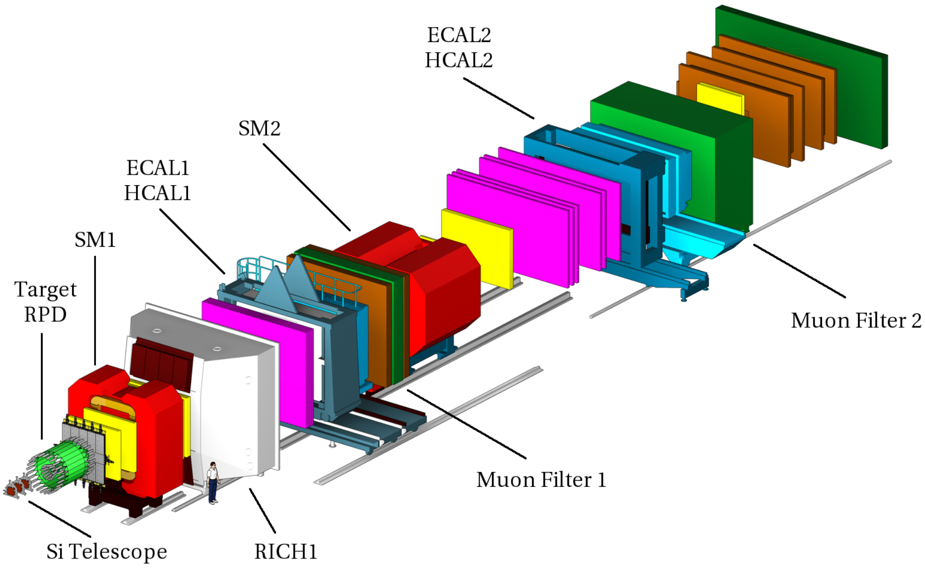

Figure 2.1: The COMPASS set-up for physics with hadron beams [45]. Different colours denote the different types of components.

Coordinate System

The z-axis of the COMPASS coordinate system points along the beam axis. The origin $z = 0$ is roughly the position of the target[1], the axis points in the direction of the beam, thus, the spectrometer components have positive z values, elements in front of the target have negative z values. The y-axis points upwards with $y = 0$ on the beam line. The x-axis completes the right-handed coordinate system.

2.1 THE M2 BEAM LINE AND HADRON BEAMS FOR COMPASS

The hadron beams used at COMPASS are secondary beams. Protons from the Super Proton Synchrotron (SPS) with a momentum of 400 GeV/c impinge on a production target consisting

---

[1] The centre of the liquid hydrogen target is at −49 cm.

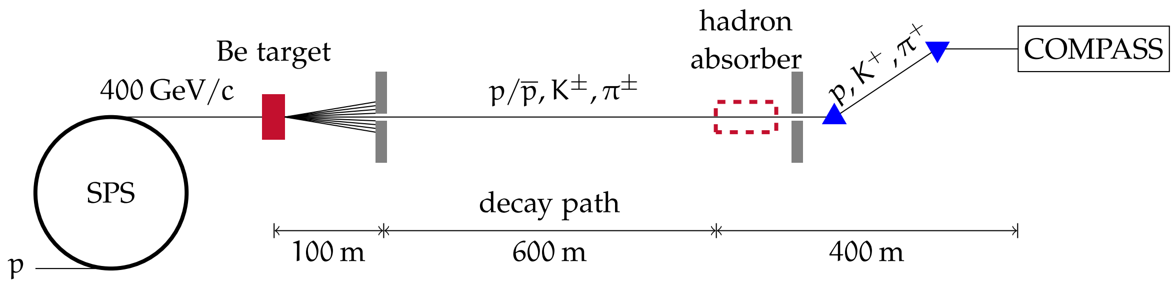

Figure 2.2: Schematic view of the M2 beam line [46] for positive hadron beam.

of 40, 100 or 500 mm long beryllium blocks. By the interaction with this target, charged hadrons ($p/\overline{p}, K^{\pm}, \pi^{\pm}$) are produced. In the so-called M2 beam line, which is schematically depicted in figure 2.2, the hadrons are transported, collimated and momentum selected over a total length of 1132 m. For the hadron beam measurements at an intensity of $5 \times 10^6\,s^{-1}$ and 190 GeV/c, 9×10^{12} protons per 10 s cycle are needed on the 500 mm target. In addition, the beam line contains a $\approx$ 600 m long decay path where hadrons decay to muons. After this decay path the remaining hadrons can be absorbed which allows also for data taking with a naturally polarised muon beam.

The beam line can deliver negative as well as positive hadron beams. While negative beams consist mainly of pions, the positive beams contain a large proton component. The composition of both beams at 190 GeV/c is shown in table 2.1. For the purpose of beam particle identification, two CEDAR (ChErenkov Differential Counter with Achromatic Ring focus) detectors are installed 30 m upstream of the COMPASS target. These detectors are described in detail in chapter 3.

negative beam		positive beam	
π^-	96.8%	π^+	24.0%
K^-	2.4%	K^+	1.4%
$\overline{p}$	0.8%	p	74.6%

Table 2.1: The composition of the 190 GeV/c hadron beams at the COMPASS target calculated from measurements [47]. The relative errors are 1% for pions ($\pi^{\pm}$) and protons and $2-3\%$ for kaons ($K^{\pm}$) and antiprotons.

2.2 THE TARGET REGION

In addition to the target itself, the target region, which is depicted in figure 2.3, contains a recoil proton detector (RPD), a beam telescope, a vertex detector and parts of the veto system. For hadron-proton scattering a liquid-hydrogen target is used. The target cell is a 400 mm long cylinder corresponding to 0.045 radiation length (X_0) and 0.055 nuclear interaction length λ_I. The diameter of 3.5 mm is chosen as four times the size of the beam spot ($\sigma \approx$ 8 mm). The hydrogen is contained in a Mylar cylinder with a thickness of 125 µm which is placed inside an evacuated aluminium cryostat. Due to the 1.8 mm thick wall of the cryostat, only protons with a momentum above 100 MeV/c can be measured in the RPD. The cryostat is connected to a cooling system and a vacuum system. The complete target can be removed from the area and substituted by a structure which can hold several different nuclear targets (Ni, Pb, W).

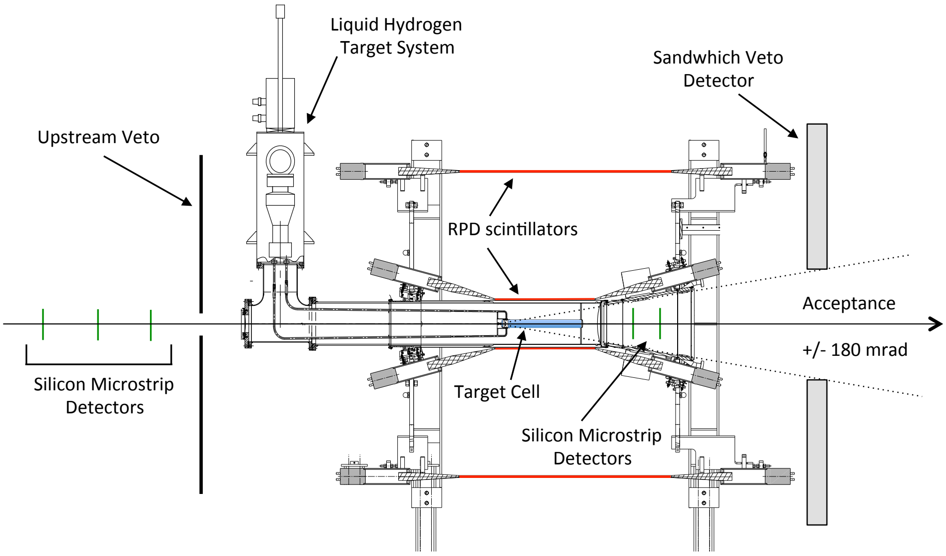

Figure 2.3: Schematic picture of the COMPASS target region. The target cell (blue) is surrounded by the two scintillator layers of the recoil proton detector (red). The silicon microstrip detectors for the beam telescope and the vertex detector are shown in green. In addition, parts of the veto system (compare section 2.6) are shown. The figure is taken from [48].

The target is surrounded by the RPD, which measures the energy loss and velocity of the hit protons which are pushed out of the target. It consists of two concentric cylindrical layers ("rings") of plastic scintillators, where the inner ring is made of 12 segments of $50 \times 6.6 \times 0.5\,\mathrm{cm}^3$ and the outer ring of 24 segments of $173 \times 20 \times 1\,\mathrm{cm}^3$. The RPD is also used in the trigger as described in section 2.6. A detailed description of the RPD can be found in [48]. Upstream of the target, three stations of silicon microstrip detectors are used as a beam telescope. Two additional stations downstream of the target are used for vertex reconstruction. To reduce noise induced by radiation damage as well as to improve spatial and time resolution, the stations are cooled with liquid nitrogen. The veto system is explained in section 2.6.

2.3 THE TRACKING SYSTEM

The COMPASS tracking system for charged particles is based on several tracking stations along the experiment. Different detector technologies are used. Far away from the beam, large area tracking systems use multi-wire proportional chambers (MWPC), drift chambers (DC) and straw tube chambers. Closer to the beam, where the rates are higher, Micromegas and gas electron multipliers (GEM) are used. In the beam region scintillating fibre detectors (SciFi) and GEMs with pixel readout are used. The tracking in the target region is done with silicon microstrip detectors.

The measurements of the tracking detectors are used to reconstruct particle tracks. The magnetic fields of the spectrometer magnets are used to determine the track momentum and the material distribution in the spectrometer to determine the number of passed radiation lengths. The algorithm for track reconstruction is divided into two steps. First, straight track segments are searched for in regions without magnetic field or much material. In the second step those segments are combined to tracks over the magnets and absorbers. An iterative algorithm is used to account for deviations from straight lines caused e. g. by multiple scattering inside the detector material.

2.4 THE RICH

For the identification of secondary particles in the LAS, a ring imaging Cherenkov detector (RICH) [49] is used. It covers the horizontal and vertical acceptance downstream of the first magnet (250 mrad × 180 mrad) and uses C_4F_{10} as radiator gas [50]. The Cherenkov light is reflected by an array of UV mirrors [51] onto the photon detectors. In the peripheral regions the detection is done using MWPCs with CsI photo cathodes, in the central region multi-anode photomultiplier tubes (MAPMT) [52] are used. In figure 2.4 the measured Cherenkov angle is shown as a function of the particle momentum. The Cherenkov thresholds are 2.5, 9 and 17 GeV/c for pions, kaons and protons, respectively. The particle identification is based on an extended maximum likelihood method. For each particle, the likelihoods for different particles hypotheses are compared. The method is trained with pions, kaons and protons from the decays of K^0_S, ϕ and Λ, respectively. Up to 30 GeV/c the efficiency for particle separation is above 90%, a separation is possible up to 50 GeV/c.

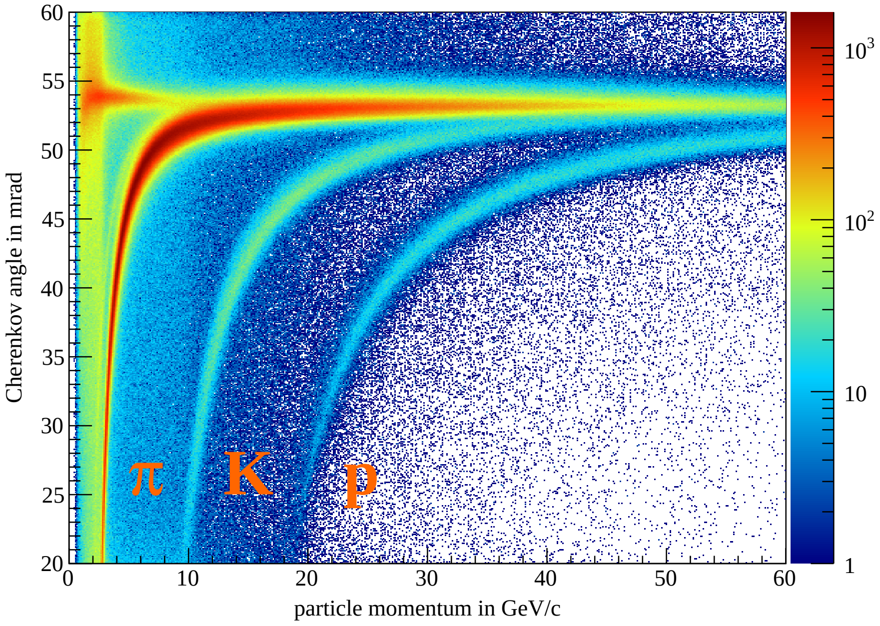

Figure 2.4: Cherenkov angles measured in the RICH as a function of the particle momentum. Clear bands are seen for pions, kaons and protons. The background mainly stems from electrons. The different particle species can be separated up to 50 GeV/c. This picture is based on run 77723 from the 2009 data taking.

2.5 THE ELECTROMAGNETIC CALORIMETERS

In both spectrometer stages, electromagnetic calorimeters are used to detect photons. Details on the set-up of the two calorimeters and the calibration procedure are given in the following.

2.5.1 ECAL1

The electromagnetic calorimeter of the LAS, ECAL1, consist of 1500 lead glass modules of different dimensions. These are the GAMS ($3.83 \times 3.83\,\text{cm}^2$) [53], Mainz ($7.5 \times 7.5\,\text{cm}^2$) [54] and OLGA ($14.1 \times 14.1\,\text{cm}^2$) [55] modules, respectively. The configuration of the modules is shown in figure 2.5, details on the modules can be found in table 4 in [45]. The Cherenkov light from the electromagnetic showers is detected with PMTs and sampled through sampling analogue-to-digital converters (SADC). The angular coverage for photons from the target centre is 37 mrad to 136 mrad in horizontal and 21 mrad to 98 mrad in vertical direction. For offline calibration, a 15 GeV electron beam is used in an automatic calibration procedure, which is typically run twice per data taking period. In addition, a laser monitoring system is installed to control the light collection efficiency and photomultiplier gains of all 1500 modules during the data taking.

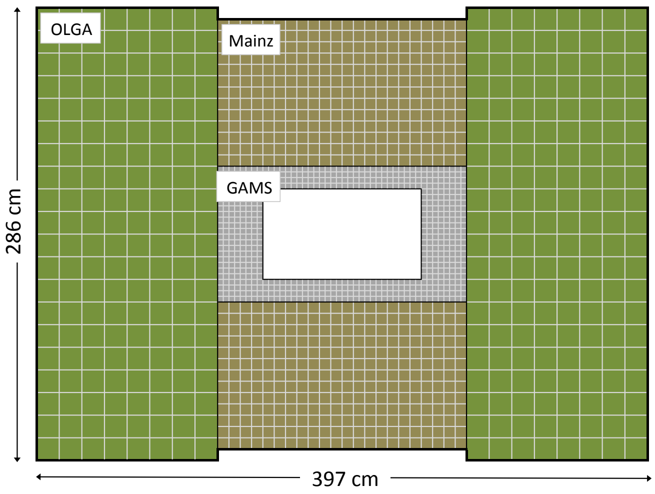

Figure 2.5: The configuration of ECAL1.

2.5.2 ECAL2

The SAS electromagnetic calorimeter, ECAL2, has its modules arranged in a 64×48 matrix stretching over $244 \times 183\,\text{cm}^2$. The configuration is shown in figure 2.6. The 1332 outer modules are identical to the ECAL1 GAMS modules, the 848 modules in the intermediate part (GAMS-R) are radiation hardened. In the inner part, there are 888 modules of the Shashlik type, which are composed of 154 double layers of 0.8 mm of lead and 1.55 mm of scintillator. The photomultiplier signals are again sampled by SADCs. The angular coverage of 1.3 mrad to 39 mrad in horizontal and 1.3 mrad to 29 mrad has an overlap with the acceptance of ECAL1. The according rows and columns of ECAL2 are therefore not used for photon reconstruction as the photons can be detected by ECAL1. Offline calibration is done similar to ECAL1, but using a 40 GeV electron beam. Time stability of the ECAL2 modules is ensured by a LED-based monitoring system.

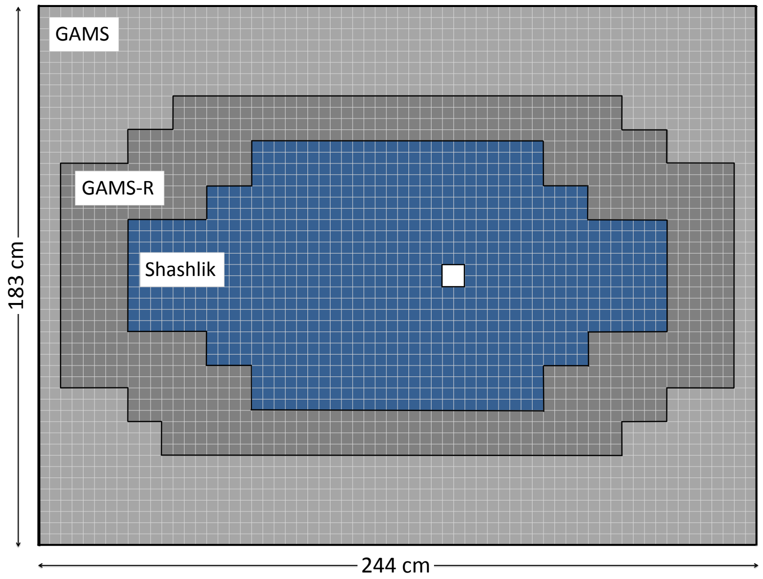

Figure 2.6: The configuration of ECAL2.

2.5.3 ECAL calibration with $\pi^0 \to \gamma\gamma$

Before physics analyses a calibration of the ECALs is performed which uses the decay $\pi^0 \to \gamma\gamma$. Events with up to five electromagnetic showers are used and the two-photon invariant mass $M_{\gamma\gamma}$ is calculated for each pair of showers. Pairs with $M_{\gamma\gamma}$ within $50\,\mathrm{MeV}/c^2$ of the π^0 mass are taken into account and assigned to the module with the highest energy deposit (central module). For each module the photon energies against $(M_{\gamma\gamma} - M_{\pi^0})$ are filled into a two-dimensional histogram. From these histograms the mass-difference spectrum is fitted in slices of $2\,\mathrm{GeV}/c^2$ with a Gaussian peak and a first-order polynomial background. The fits are used to calculate a correction factor for each energy slice in each module

$$\alpha = \frac{1}{\left(1 + \frac{\Delta m}{M_{\pi^0}}\right)^2}, \tag{2.1}$$

where M_{π^0} is the nominal π^0 mass and Δm the fitted mass offset. With this procedure the mass resolution for the π^0 in ECAL2 is $4.6\,\mathrm{MeV}/c^2$.

2.6 HADRON TRIGGERS

The processes investigated in hadron data analyses mainly stem from diffractive dissociation (see 1.3.3) and thus have a common signature:

An incoming beam particle interacts in the liquid-hydrogen target and produces a recoil proton. In this interaction the beam particle is either deflected or destroyed while additional particles are produced.

The idea behind the principle hadron trigger (diffractive trigger DT-0) is to use this signature and to trigger on

1. an incoming beam particle,
2. a recoiling target proton and

3. no non-interacting beam.

The DT-0 trigger does not account for any outgoing particles and thus introduces only a minimum bias. The different components used for this trigger condition are explained in the following.

2.6.1 Beam Trigger

The beam trigger (BT) consists of a coincidence of SciFi1 (located 7 m upstream of the target) and a beam counter. Its purpose is the selection of incoming beam particles and the setting of the reference time for a single event. The beam counter is a scintillator disc with a diameter of 3.2 cm located 50 cm downstream of SciFi1. Its geometry fits the geometric acceptance of the target.

2.6.2 Proton Trigger

The proton trigger (PT) uses the RPD information (see 2.2) for target pointing and the discrimination of protons from pions and delta electrons. Target pointing is implemented through a coincidence of an element in the inner ring with three corresponding elements in the outer ring as depicted in figure 2.7). The discrimination of protons from other particles is achieved by thresholds on the energy loss in the two rings.

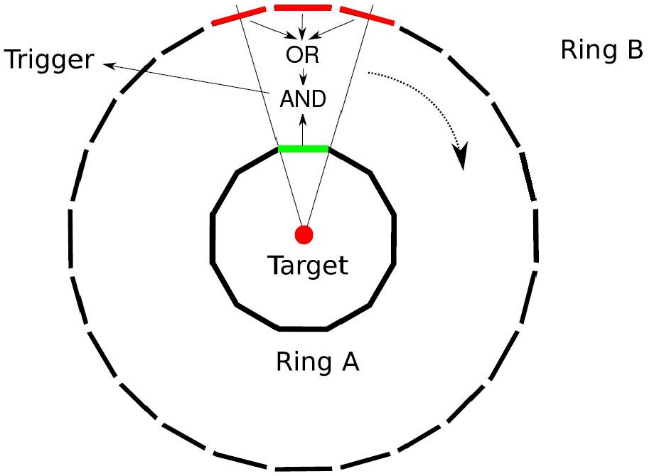

Figure 2.7: Allowed combinations for target pointing in the RPD.

2.6.3 Veto System

The veto system consists of different parts and serves the following purposes:

1. A veto on non-interacting beam particles is achieved using two scintillators at $z = +15\,\text{m}$ and $z = +33\,\text{m}$.

2. The Sandwich veto detector [56] covers most of the acceptance gap between the RPD and the LAS to veto on events with photons or charged particles inside this gap.

3. A hodoscope veto system [44, 57] located at $z = -20\,\text{m}$, $z = -7.5\,\text{m}$ and $z = -1.5\,\text{m}$ removes events with high multiplicities in the RPD.

2.6.4 Physics Triggers

The trigger condition of the DT-0 trigger can now be written as

$$\mathrm{BT} \wedge \mathrm{PT} \,\overline{\wedge}\, \mathrm{veto}\,,$$

which fulfils the requirement listed above. A kaon trigger,

$$\mathrm{BT} \wedge \mathrm{CEDAR} \,\overline{\wedge}\, \mathrm{veto}\,,$$

uses the particle identification of both CEDAR detectors, requiring a multiplicity of 6 (see section 3.1). It is used for luminosity monitoring with free kaon decays ($K^{\pm} \rightarrow \pi^{\pm}\pi^{+}\pi^{-}$) and systematic studies. For data takings with special requirements such as the measurement of Primakoff reactions [58] further triggers are available. Those are described in [45].

I

BEAM PARTICLE IDENTIFICATION WITH STATISTICAL METHODS

3

THE CEDAR DETECTORS

The hadron beam used in the COMPASS experiment contains different particle species, the beam composition was given in table 2.1. For physics analyses, it is crucial to separate the particle species. To identify beam particles, two Cherenkov detectors of the CEDAR (ChErenkov Differential Counter with Achromatic Ring focus) type are used. They are located $\approx$ 30 m upstream of the COMPASS target. The location of the CEDARs is shown in figure 3.1, which shows the last 100 m of the M2 beam line. Detailed information on the CEDAR detectors and their operation can be found in [59] and [60], the main features will be presented in the following.

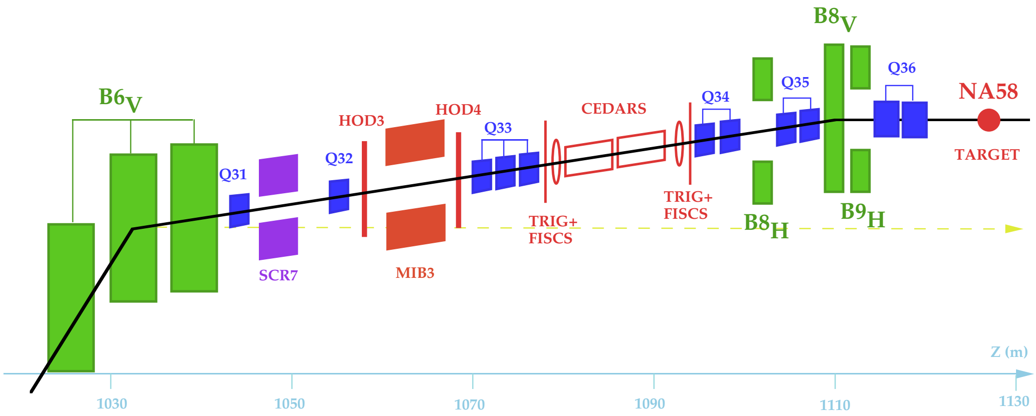

Figure 3.1: Side view of the last 100 m of the M2 beam line [61]. Dipole magnets are shown in green, quadrupole magnets in blue, steering and monitoring systems (including the CEDAR detectors) in red and purple.

3.1 FUNCTIONAL PRINCIPLE OF A CEDAR

At COMPASS, the CEDAR detectors are used to distinguish pions from kaons (when taking data with negative hadron beams) or protons from pions and kaons (when taking data with positive hadron beam). To achieve this distinction, the Cherenkov effect is used. Charged particles in a medium, which move faster than the speed of light in that medium, emit light at an angle θ with respect to the direction of flight. The angle depends on the velocity $\beta = \frac{v}{c}$ of the particle and the refractive index n of the medium according to

$$\cos(\theta) = \frac{1}{n\beta}\,. \tag{3.1}$$

Particles with the same momentum but differing masses, which are components of the M2 hadron beam, produce Cherenkov light at different angles. If the light for all particle species has to travel through the same optics, as depicted in figure 3.2, the difference in the angles translates to a difference in the radius of the light rings of

$$\Delta R = \frac{f}{\theta}\frac{\Delta M^2}{2p^2} \tag{3.2}$$

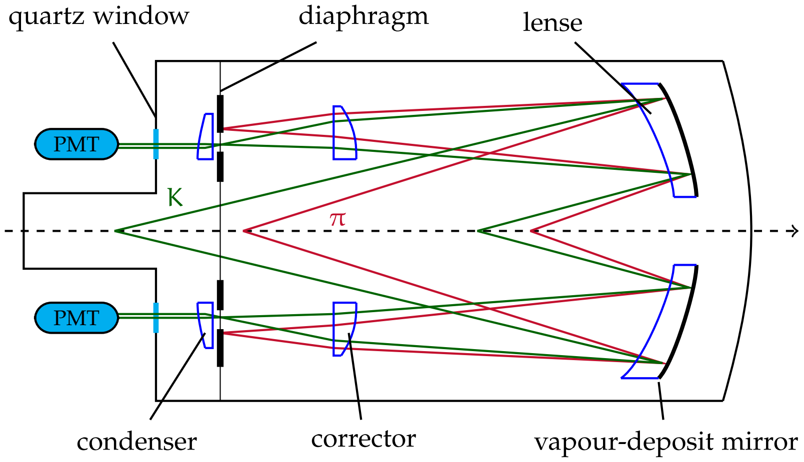

Figure 3.2: Functional principle of a CEDAR detector. The pions and kaons emit Cherenkov light at different angles. Via a mirror and several lenses the light rings emitted at different positions in the detector are focused to a common point in the focal plane. There one of the rings can be selected by a diaphragm with an adjustable opening. The radius of the rings is controlled via the pressure of the helium gas.

with the focal length $f = 3.88\,\mathrm{m}$, the squared mass difference ΔM^2 and the momentum p of the particles. In the CEDAR detectors a diaphragm with a small opening of typically 0.5 mm is used to select a certain radius of the light ring and thus only one particle species. The light is then collected with 8 photomultiplier tubes (PMT).

To ensure the correct ring is selected, the refractive index of the helium filling has to be adjusted. This is done by changing the pressure of the gas. The approximate form of the Lorenz-Lorentz equation [62, 63] is

$$n \approx \sqrt{1 + \frac{3A}{R}\frac{p}{T}}, \tag{3.3}$$

where $R = 8.3144621(75)\,\mathrm{J/mol\,K}$ is the gas constant and

$$A = \frac{4\pi}{3} N_A \alpha \tag{3.4}$$

the molar refractivity with the Avogadro number N_A and the polarisability α of the gas molecules. The refractive index does not depend only on the pressure but on the ratio of pressure and temperature $\frac{p}{T}$. Thus, the temperature has to be controlled during the running of the detectors. For thermal conduction and insulation, the vessel of the CEDARs is covered with copper filaments and 10 cm of polyethylene foam, which also ensures that the temperature gradient inside the vessel is as small as possible. The PMT voltage dividers are placed outside of the detector to reduce heat emission into the gas. The correct value for $\frac{p}{T}$ is obtained by a so-called pressure scan. During this scan the pressure is changed in small steps over the range of interest and the count rates in the PMTs are measured and normalised to the number of total beam particles crossing the detector, which is obtained from two scintillator discs (FISCs in figure 3.1). A typical output of such a scan is shown in figure 3.3. The different colours correspond to multiplicities (i. e. the number of photomultipliers with a signal) of $\geqslant 6$ (red), $\geqslant 7$ (green) and 8 (blue). The larger peak at lower pressure is produced by pions, the smaller peak at higher pressure by kaons. The separation of the peaks is better for a higher multiplicity, on the other hand a higher multiplicity reduces the total number of measured particles and thus the efficiency of the particle identification. A detailed description of the performance of the CEDAR detectors and more information on pressure scans can be found in [64].

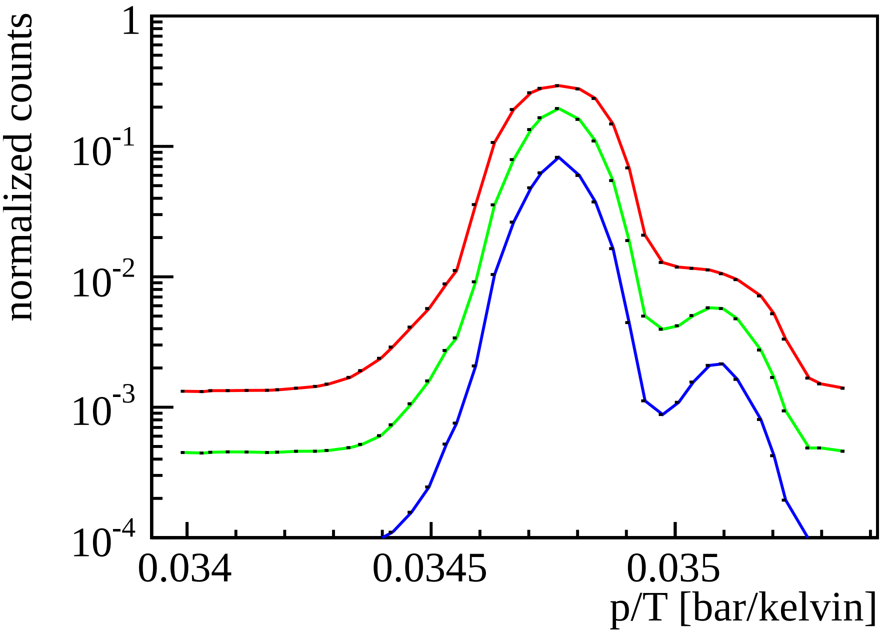

Figure 3.3: Outcome of a typical pressure scan. The different colours correspond to multiplicities of 6 (red), 7 (green) and 8 (blue). The larger peak at lower pressure is produced by pions, the smaller peak at higher pressure by kaons. The scan was done at CEDAR 1 on May 30, 2012 during the preparation of the data taking.

3.2 CEDAR DETECTORS IN ANALYSES

No CEDAR information is used in the principle hadron trigger (DT-0 trigger, see section 2.6). Therefore, the selection of single beam particle species is done during the physics analyses. Up to now, a multiplicity method was used in analyses to distinguish the beam particles: $\frac{p}{T}$ is chosen to allow the light ring of one particle species (e. g. kaons) to pass the diaphragm. A particle which produces Cherenkov light is then assumed to be a kaon if at least a certain number of PMTs have seen a signal. The actual number is chosen by means of efficiency and purity needed for the performed analysis. The larger the number of required PMT hits the cleaner the selected sample but on the other hand more particles are missed and the selection efficiency drops, which can be seen in figure 3.3. For most analyses a multiplicity setting of 6 of 8, which results in a good balance between efficiency and purity, is used. This setting will also be used for a comparison with the new method in chapter 5. Details on the performance of the multiplicity method can be found in [64].

3.3 LIMITATIONS FOR PARTICLE IDENTIFICATION

The multiplicity method explained above will only work correctly if the emitted light rings are perfectly shaped when they pass the focal plane with the diaphragm. But, there are many effects which influence the shape and width of the light ring, such as

- optical aberration
- chromatic dispersion
- multiple scattering
- inhomogeneity of the refractive index

The influence of these effects could be reduced to a certain point during the development of the detectors [59]. In addition, the position of the light ring is mainly affected by two effects, namely misalignment of the detectors with respect to the beam axis and the (intrinsic) beam divergence.

MISALIGNMENT: The influence of misalignment is reduced by a correct alignment of the optical axis of the cedar with the direction of the beam. This alignment is done with a step motor and thus is only possible up to a small remaining deviation which is small compared to the beam divergence and can thus be neglected.

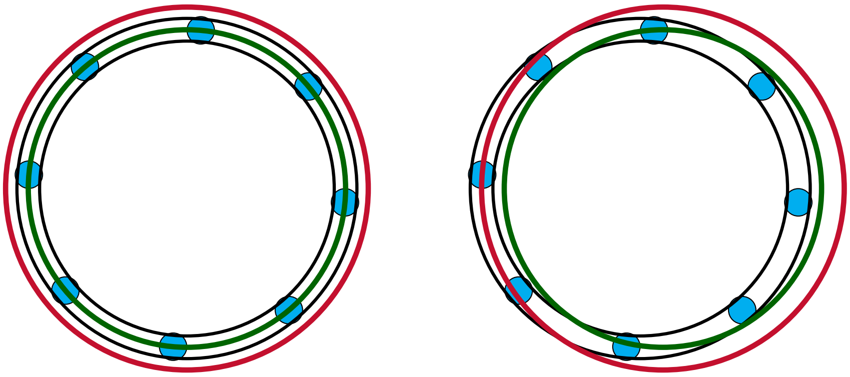

Figure 3.4: Influence of beam divergence: If a beam particle traverses the CEDAR parallel to the beam axis (left) the rings for kaons (green) and pions (red) are correctly focused for the kaon ring to pass the diaphragm (indicated in black) and hits the photomultiplier tubes (blue). If the beam has a certain divergence (right) the rings are shifted and the pion ring enters the acceptance of the diaphragm.

BEAM DIVERGENCE: The M2 beam is focused to the hole of HCAL2 which is located 30 m downstream of the target. Thus, the focal point of the beam is ≈ 60 m away from the CEDAR region. Still, the beam is not completely parallel when it passes the CEDAR region. This can only partially be corrected for by quadrupoles in front of and behind the CEDARs (Q33 and Q34 in figure 3.1). Thus, the light rings are shifted to a different direction for each single particle, which is depicted in figure 3.4. This can lead to a misidentification of beam particles.

To reduce the influence of the beam divergence on the identification of beam particles a new method has been developed. This method will be explained in detail and discussed in the following chapters.

4

THE STATISTICAL APPROACH

Due to the large influence of beam divergence on the identification of beam particles a new method based on a purely statistical approach was developed. The key idea of this method is to use calibration samples to determine the hit patterns of the CEDAR photomultiplier tubes as a function of the beam divergence. These hit patterns are used to calculate the probabilities for any beam particle to be a kaon or a pion, respectively. To identify beam particles five steps have to be made:

1. The divergence of the single beam particles has to be determined.
2. Samples, which contain only pions and only kaons, respectively, have to be produced to determine the hit patterns for kaons and pions.
3. The hit patterns are used to calculate the probabilities of a beam particle to be a pion or a kaon. This is done for each photomultiplier tube separately.
4. The probabilities of the single photomultipliers are combined to likelihoods.
5. The likelihoods are used to identify beam particles.

These single steps are described in the following sections. So far, the method is only valid for separating kaons from pions in the 2008 negative hadron beam data. The adaption to further data sets will be discussed in section 4.6.

4.1 DETERMINATION OF BEAM DIVERGENCE

The beam divergence is calculated from the position of the beam upstream and downstream of the CEDARs. No direct measurement of the beam position is possible in the CEDAR region, therefore, the position and direction measured in the beam telescope (see section 2.2) are propagated backwards to positions upstream of CEDAR 1 and downstream of CEDAR 2. The beam divergence is then calculated by

$$\theta_x = \arctan\left(\frac{\Delta x}{\Delta z}\right) \approx \frac{\Delta x}{\Delta z} \tag{4.1a}$$

$$\theta_y = \arctan\left(\frac{\Delta y}{\Delta z}\right) \approx \frac{\Delta y}{\Delta z}\,, \tag{4.1b}$$

where $\Delta z = 1283.4\,\mathrm{cm}$ is the distance between the two calculated positions.

As the propagation through the beam line magnets is not fully implemented in the analysis software, the calculated divergence is not centred around zero. To correct for this offset, the divergence distribution of particles, which produce a signal in all eight PMTs of a given CEDAR, is used. These particles are assumed to pass the CEDAR parallel to the beam axis and thus without any divergence. The divergence calculated for that type of particles is shown in figure 4.1 and the values for offset and width of the divergence distribution obtained from a Gaussian fit are given in table 4.1.

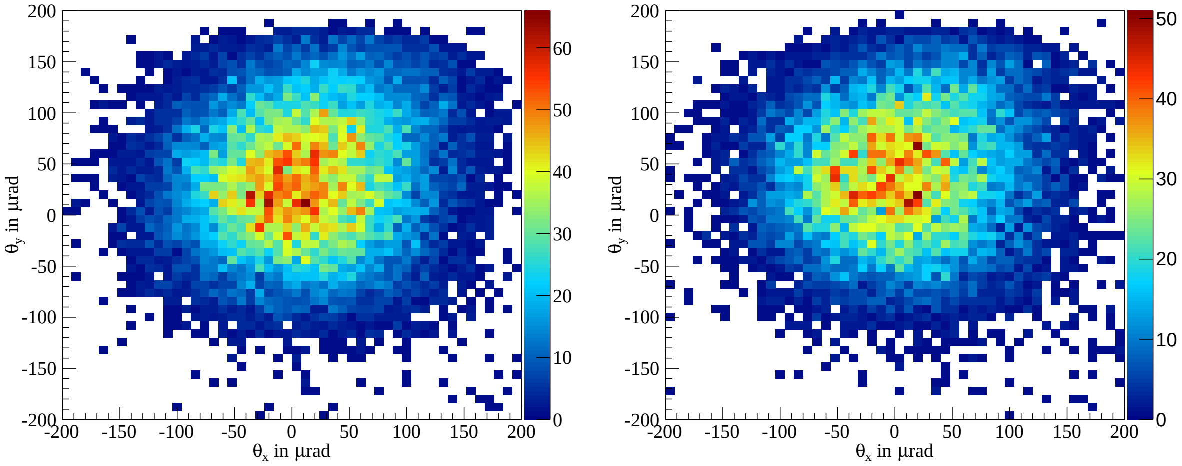

(a) Divergence at CEDAR 1 (b) Divergence at CEDAR 2

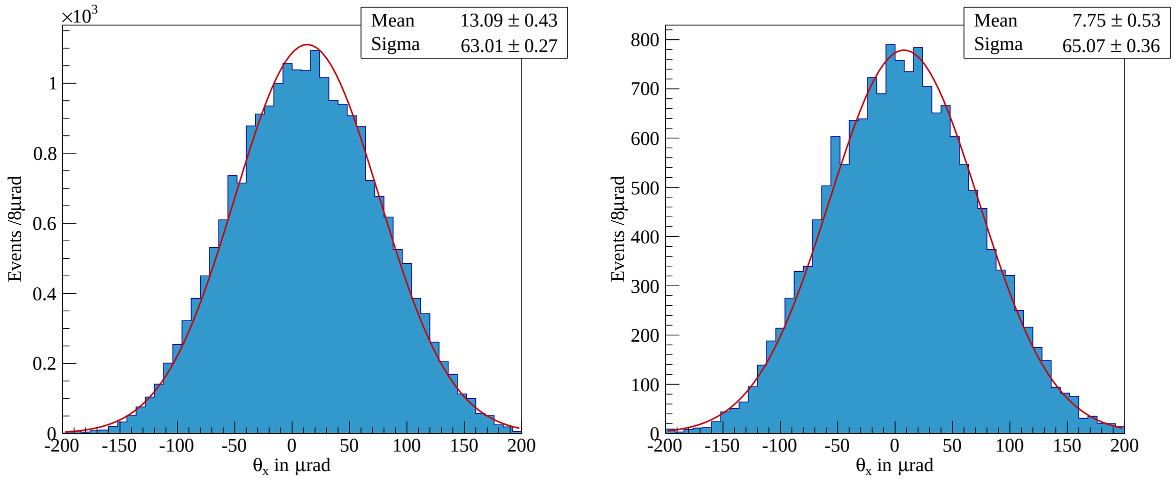

(c) x-Divergence at CEDAR 1 (d) x-Divergence at CEDAR 2

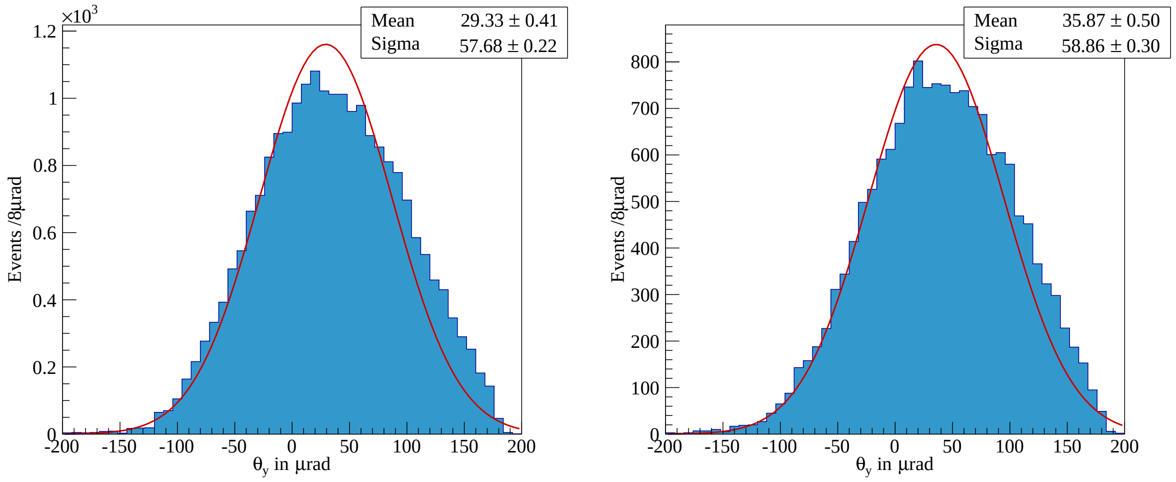

(e) y-Divergence at CEDAR 1 (f) y-Divergence at CEDAR 2

Figure 4.1: Determination of the offset of the beam divergence at the CEDARs using events with signals in all eight photomultipliers.The upper panel shows the two-dimensional distribution of divergence for CEDAR 1 (left) and CEDAR 2 (right). The two lower lines show the divergences θ_x and θ_y, respectively. The given fit values are obtained from a Gaussian fit although the beam profile is not fully Gaussian in y.

CEDAR 1

θ_{x_0}	13.09 ± 0.43	σ_x	63.01 ± 0.27
θ_{y_0}	29.33 ± 0.41	σ_y	57.68 ± 0.22

CEDAR 2

θ_{x_0}	7.75 ± 0.53	σ_x	65.07 ± 0.36
θ_{y_0}	35.87 ± 0.05	σ_y	58.86 ± 0.30

Table 4.1: Offset (θ_{x_0}, θ_{y_0}) and width (σ_x, σ_y) of the beam divergence distributions in the two CEDARs (in µrad).

Several conclusions can be drawn from those numbers:

- The two CEDARs are not fully aligned with respect to each other, the values for the divergence offset differ by $\approx 5.3\,\mu$rad for x and $\approx 6.5\,\mu$rad for y, respectively. This is due to the step motor which was already mentioned before. In the following sections all given values for θ_x and θ_y are already corrected for the offset.
- The divergence distribution is slightly broader in x than in y. Also both in x and y the divergence is smaller than in the target region, where $\theta_x = 80\,\mu$rad and $\theta_y = 200\,\mu$rad [45].
- The width of the divergence distribution is around $60\,\mu$rad both in x and y. Given the focal length of 3.88 m the displacement of the light ring for a particle with a 1σ deviation from the optical axis is already 0.23 mm, which is about half of the typical opening of the diaphragm. This shows, that a method taking divergent beams into account is crucial for a correct treatment of beam particles.

4.2 CREATION OF CALIBRATION SAMPLES

No dedicated data has been taken to produce calibration samples for this method. Therefore, the calibration samples have to be extracted from the full data set. The samples have to be as clean as possible to reduce contamination that would lead to problems with particle identification.

4.2.1 Kaon Sample

A kaon sample is prepared from the decay $K^- \rightarrow \pi^-\pi^+\pi^-$ of kaons outside of the target. This channel provides a clean signal with an easily reconstructible final state. To obtain this sample the following cuts have been applied:

- The decay of free kaons is a rare process. Thus, the kaon trigger had to be used to enrich the sample. This leads to a small bias in the angular distributions of this sample as the CEDARs are already used. In further data takings the use of the kaon trigger can be avoided by performing dedicated calibration runs with only beam trigger, which does not induce a bias on particle species in the CEDAR region.
- The primary vertex of the event is required to be located outside of the target, which corresponds to $z_{\text{vertex}} < -70$ cm. Therefore, the outgoing particles should not originate from a diffractive reaction.
- The number of outgoing charged particles has to be equal to 3 with a total charge of -1. These particles are assumed to be pions.

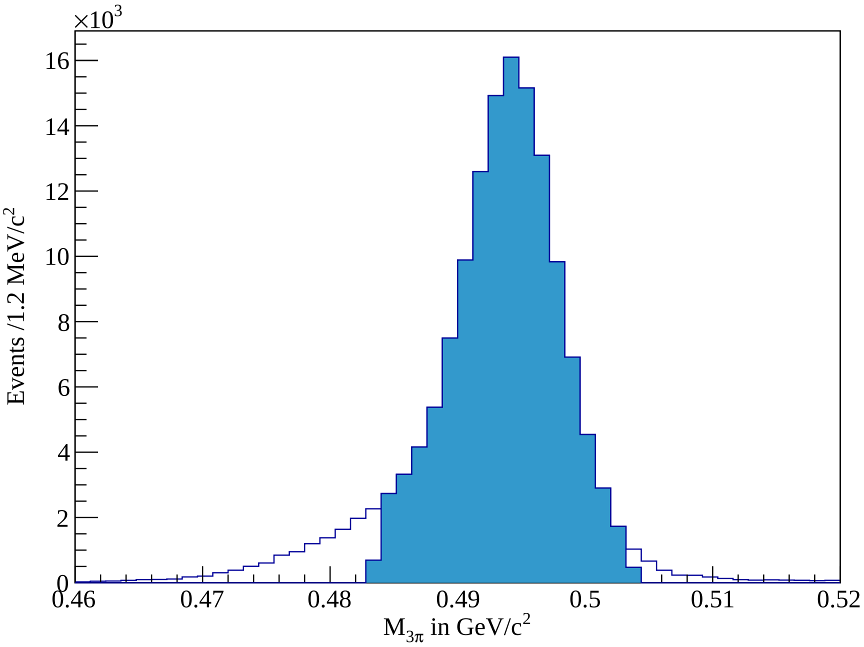

Figure 4.2: Invariant mass of $\pi^-\pi^+\pi^-$ in the kaon mass region after selection of free kaon decays. The coloured area shows the events accepted by the cut on the kaon mass.

- Exclusive events[1] are selected by a cut of $|190\,\text{GeV} - p_{3\pi}c| < 4\,\text{GeV}$ for the momentum $p_{3\pi}$ of the three pion system.
- As a last step kaon events are selected if the mass of the three pion system is within $50\,\text{MeV}/c^2$ around the physical kaon mass [1] of $M_K = 493.677\,\text{MeV}/c^2$. The mass of the three pion system in the region of the kaon mass is shown in figure 4.2.

With the full 2008 hadron beam data, the final sample after all cuts contains 124470 events.

4.2.2 Pion Sample

To obtain a clean pion beam sample is more challenging. There is no final state which can only be produced by an incoming pion and can be easily reconstructed. The idea is to use diffractively produced three pion events. If all outgoing particles are pions, the incoming particle must also be a pion. Therefore, events with three outgoing charged particles with a small angle with respect to each other and similar momenta are selected. These particles are most likely of the same species as a heavier particle would introduce some transverse momentum and have a larger angle with respect to the others. The following cuts are applied:

- Only events with DT-0 trigger are used to ensure a reaction with a target proton which produces a recoil particle.
- The primary vertex of the event has to be reconstructed within the target region, i. e. $-70\,\text{cm} < z_{\text{vertex}} < -30\,\text{cm}$.
- The number of outgoing charged particles has to be equal to 3 with a total charge of -1. These particles are then assumed to be pions.

---

[1] More information on the selection of exclusive events can be found in chapter 6.3.2

- Exclusive events are selected by a cut of $|190\,\text{GeV} - p_{3\pi}c| < 4\,\text{GeV}$ for the momentum $p_{3\pi}$ of the three pion system.
- To get rid of kaon contamination the angle α of the single pions with respect to each other has to fulfil $\alpha < 0.2\,\text{rad}$ and the momentum difference between each pair of particles has to be smaller than $10\,\text{GeV}/c$.

The final sample contains 107334 events. The invariant mass distribution shown in figure 4.3 does not show any resonant structures. This shows that the required small angles enhance non-resonant production of pions. In addition, the inlay in figure 4.3 shows the kaon mass region where no peak is observed as expected.

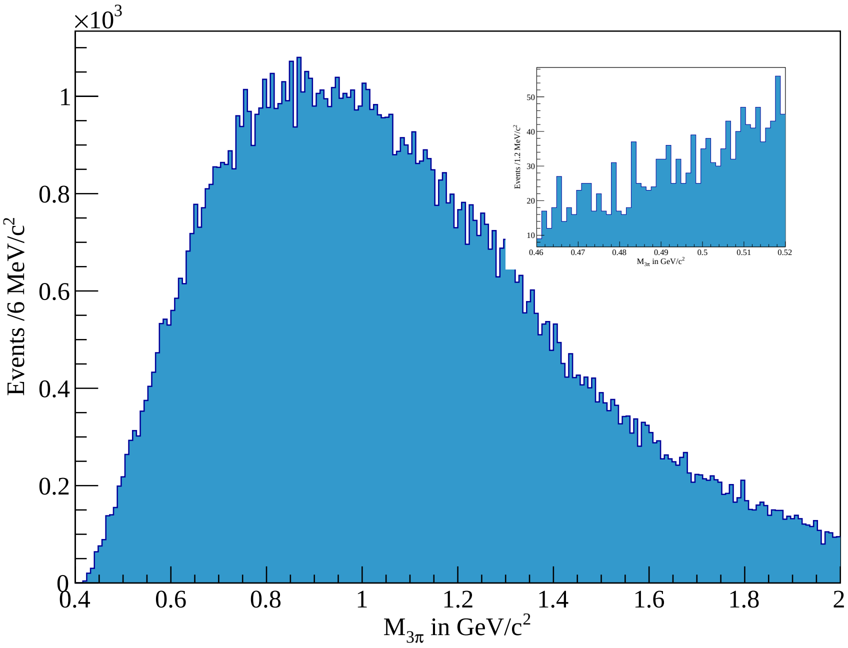

Figure 4.3: Invariant mass of $\pi^-\pi^+\pi^-$ after selection of free diffractive pion events. As expected no resonant structures are visible. The inlay shows the kaon mass region (same x-axis as in figure 4.2) where no kaon mass peak is observed.

4.2.3 Beam Sample

The method could in principle be tested with the full 2008 data set which would take unnecessarily much computing time. Therefore, a sub-sample of the full data set, which contains about 3.7 million beam trigger events, is used. Beam trigger events have an incoming beam particle which reaches the target. No further requirements were put on this data set.

4.3 OBTAINING PROBABILITIES

In the next step, the probability for a particle to be a kaon or pion has to be determined. The only available information is the hit pattern in the PMTs and the divergence. This calculation is a bit complicated and thus a simplified example will be given before the full formalism is built up.

EXAMPLE: Assume, a beam particle traverses the CEDAR with a certain divergence $\Theta = (\theta_x, \theta_y)$ and a signal in a given photomultiplier is observed. Assume further, that we want to know if this particle was a kaon. Thus, the probability $P_\Theta(\text{kaon}|\text{signal})$, that this observed signal was produced by a kaon, has to be calculated. Bayes' theorem[2] [65]

$$P_\Theta(\text{kaon}|\text{signal}) = \frac{P_\Theta(\text{signal}|\text{kaon}) \cdot P_\Theta(\text{kaon})}{P_\Theta(\text{signal})} . \tag{4.2}$$

connects this probability with its 'inverse', namely the probability $P_\Theta(\text{signal}|\text{kaon})$ that a kaon with divergence Θ produces a signal. This probability can be obtained from the kaon sample of section 4.2 and is simply the number of events in the bin with divergence Θ that have a signal in our given PMT divided by the full number of events in this bin. All events either have a signal in a PMT or not and thus the relation

$$P_\Theta(\text{signal}|\text{kaon}) + P_\Theta(\overline{\text{signal}}|\text{kaon}) = 1 \tag{4.3}$$

holds for each single bin and each PMT.
Two additional probabilities are needed to use Bayes' theorem:

1. The probability $P_\Theta(\text{kaon})$ that a kaon traverses the CEDAR region with a given divergence Θ can also be obtained from the kaon sample. It is simply the number of events in the corresponding Θ bin divided by the number of events in the full kaon sample.

2. $P_\Theta(\text{signal})$ is the probability that any particle with a divergence Θ produces a signal in the given PMT. This probability is obtained from the beam sample and is given as the number of events in the given Θ bin divided by the full number of events.

Therefore, the calculation of the desired probability $P_\Theta(\text{kaon}|\text{signal})$ that the observed signal was produced by a kaon is possible by correctly combining information from the calibration samples.

GENERAL CASE: The formula from the example can now be generalised and the probability $P^i_{(\theta_x,\theta_y)}(\text{particle}|\text{PMT response})$ that a given response (either signal or no signal) in PMT i was produced by a given particle (either kaon or pion) can be calculated as:

$$P^i_{(\theta_x,\theta_y)}(\text{particle}|\text{PMT response}) = \frac{P^i_{(\theta_x,\theta_y)}(\text{PMT response}|\text{particle}) \cdot P_{(\theta_x,\theta_y)}(\text{particle})}{P^i_{(\theta_x,\theta_y)}(\text{PMT response})} . \tag{4.4}$$

Every particle species in the beam is assumed to have the same behaviour in means of divergence. This assumption might not fully be true but with the available data it is not possible to check for it. It is assumed that the difference between pions and kaons is small compared to the total divergence and therefore, the relation

$$P_{(\theta_x,\theta_y)}(\text{kaon}) = P_{(\theta_x,\theta_y)}(\text{pion}) \equiv P_{(\theta_x,\theta_y)}(\text{beam}) \tag{4.5}$$

is used. This factor $P_{(\theta_x,\theta_y)}(\text{beam})$ is common for all calculated probabilities and thus can be dropped out. In addition, $P^i_{(\theta_x,\theta_y)}(\text{PMT response})$ is another common factor for all probabilities of a given response in PMT i. In total only two values are needed to calculate the four desired probabilities:

$$P^i_{(\theta_x,\theta_y)}(\text{kaon}|\text{signal}) \propto P^i_{(\theta_x,\theta_y)}(\text{signal}|\text{kaon}) \tag{4.6a}$$

$$P^i_{(\theta_x,\theta_y)}(\text{kaon}|\overline{\text{signal}}) \propto \left(1 - P^i_{(\theta_x,\theta_y)}(\text{signal}|\text{kaon})\right) \tag{4.6b}$$

$$P^i_{(\theta_x,\theta_y)}(\text{pion}|\text{signal}) \propto P^i_{(\theta_x,\theta_y)}(\text{signal}|\text{pion}) \tag{4.6c}$$

$$P^i_{(\theta_x,\theta_y)}(\text{pion}|\overline{\text{signal}}) \propto \left(1 - P^i_{(\theta_x,\theta_y)}(\text{signal}|\text{pion})\right) \tag{4.6d}$$

---

[2] A short remark: Although Bayes' theorem is used for the calculations in this chapter, nevertheless a frequentist interpretation of probabilities is used throughout the whole method.

As an example the probability $P^{i=2}_{(\theta_x,\theta_y)}(\text{signal}|\text{pion})$ for a pion to produce a signal in PMT 2 of CEDAR 1 is shown in figure 4.4. The distributions for all PMTs are collected in appendix B.1.

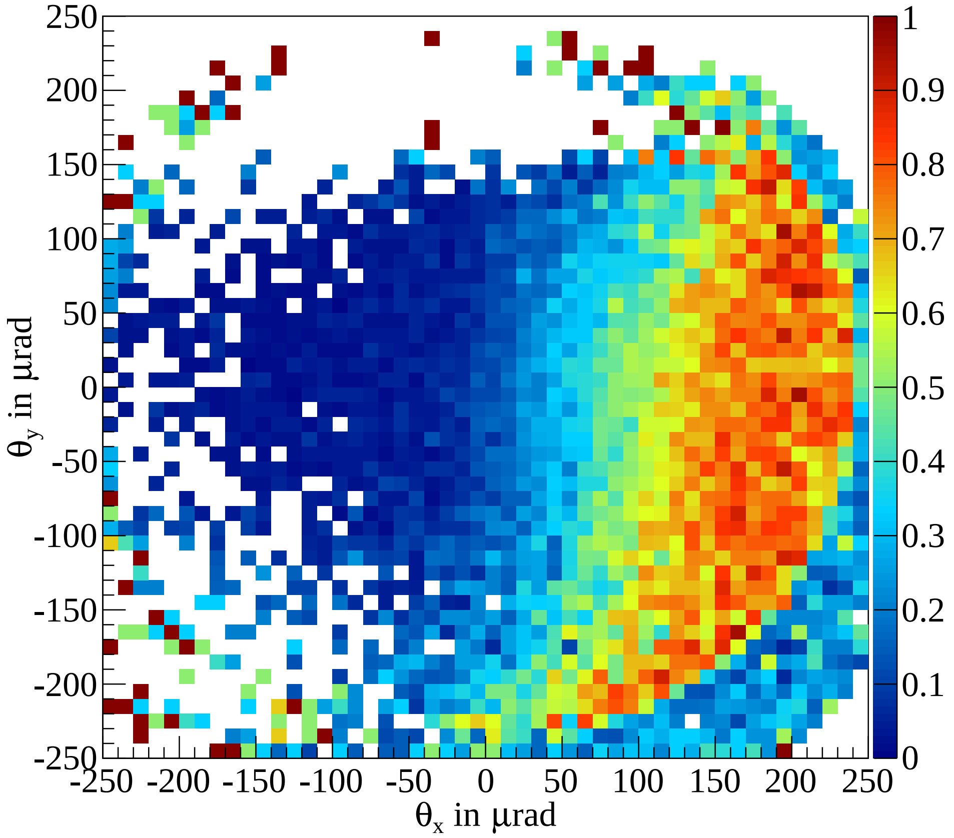

Figure 4.4: Probability distribution $P^{i=2}_{(\theta_x,\theta_y)}(\text{signal}|\text{pion})$ for pions in PMT 2 of CEDAR 1. The colour scale denotes the percentage of particles in the given bin that produce a signal in the photomultiplier.

Several observations can be made on this distribution:

- For small divergences only few signals are seen which is expected as only the light ring produced by kaons should be able to pass the diaphragm.
- For a certain direction of the beam divergence the number of received signals grows rapidly as the pion light ring enters the acceptance. For divergences in the opposite direction the number of signals nearly drops to zero.
- For large divergences ($\theta_{x,y} > 200\,\mu\text{rad}$) many empty bins as well as bins with a probability of exactly 100% can be observed due to low statistics in this region. This leads to problems in the following calculation of likelihoods. To avoid these problems two strategies were tested:

  METHOD 1: Impose an additional cut of $\sqrt{\theta_x^2 + \theta_y^2} < 200\,\mu\text{rad}$ to get rid of the low statistics region. This method will be referred to as `cut200` in the following.

  METHOD 2: Do not use any events which have an entry of exactly 1 or exactly 0 in any of the probability distributions, which will be denoted as `cut01` in the following.

These two methods will be compared to each other by means of efficiency and purity in chapter 5.

4.4 CALCULATING LIKELIHOODS

With the probabilities determined in section 4.3, likelihoods for any particle to be a kaon or pion can be calculated. The likelihood is given as the product of the according probabilities for the eight single photomultipliers. It is more convenient to calculate the logarithm of the likelihood as a sum of the logarithms of the probabilities for the single PMTs. The log-likelihood for kaons is given by

$$\begin{aligned}\ln L(\text{kaon}) = \sum_{i=1}^{8} \eta_i \log\left(P^i_{(\theta_x,\theta_y)}(\text{kaon}|\text{signal})\right) \\ + \sum_{i=1}^{8} (1-\eta_i) \log\left(P^i_{(\theta_x,\theta_y)}(\text{kaon}|\overline{\text{signal}})\right) \, ,\end{aligned} \tag{4.7}$$

where

$$\eta_i = \begin{cases} 1 & \text{signal in PMT } i \\ 0 & \text{no signal in PMT } i \end{cases} \tag{4.8}$$

makes sure that the correct probabilities are taken into account. The likelihood for pions is calculated accordingly. The resulting likelihood distributions (for CEDAR 2) for the three different samples are shown in figure 4.5. Particles above the red line are more likely kaons and particles below the red line are more likely pions, respectively. Most particles in the kaon sample have a larger likelihood to be kaons rather than pions. The likelihood distribution for the pion sample and the beam sample look similar as the beam mainly contains pions.

4.5 IDENTIFYING BEAM PARTICLES

The likelihoods calculated in 4.4 can be used to identify any beam particle, i. e. this method is able to identify not only kaons (like the multiplicity method) but also pions. For the distinction between pions and kaons likelihood ratios are used. A particle is identified as a kaon if the likelihoods fulfil

$$\frac{L(\text{kaon})}{L(\text{pion})} > \alpha \tag{4.9a}$$

with $\alpha > 1$. This can be directly translated into a condition for the log-likelihoods

$$\ln L(\text{kaon}) > \ln L(\text{pion}) + A \, , \tag{4.9b}$$

with $A = \ln(\alpha) > 0$. To identify a given particle as a pion the relations

$$\frac{L(\text{pion})}{L(\text{kaon})} > \beta \tag{4.10a}$$

$$\ln L(\text{pion}) > \ln L(\text{kaon}) + B \, , \tag{4.10b}$$

with $\beta > 1, \; B = \ln(\beta) > 0$, have to be fulfilled. For particles that do not fulfil any of these conditions no ID is set. α and β or accordingly A and B can in principle be chosen freely but have an influence on the efficiency and the purity of the method. This influence will be discussed in detail in chapter 5.

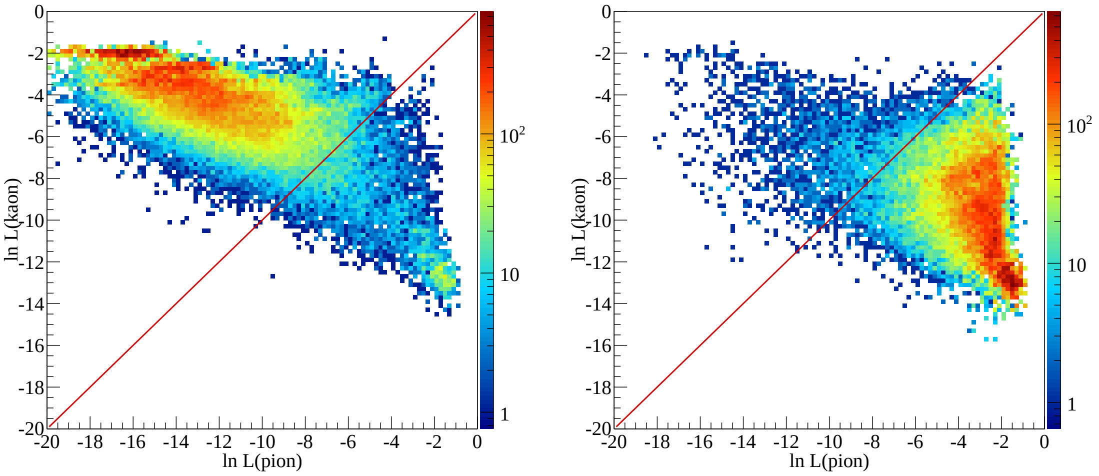

(a) kaon sample

(b) pion sample

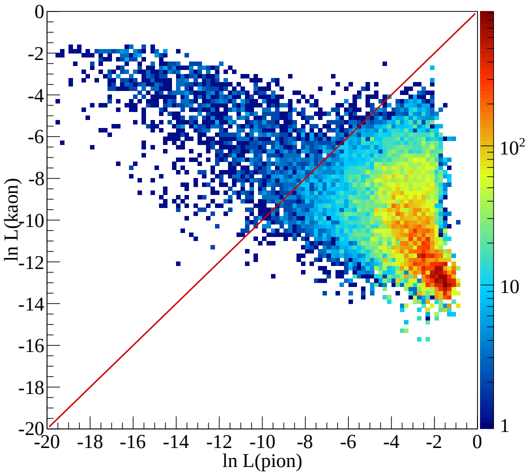

(c) beam sample

Figure 4.5: Likelihoods at CEDAR 2 for the different samples. Particles above the red line are more likely kaons and particles below the red line are more likely pions, respectively.

Combining the Two CEDARs

To finally identify a given particle as a pion or a kaon the information of the two CEDAR detectors has to be combined. Every particle has one of the three tags `kaon`, `pion`, `no ID` from each of the two CEDARs. To combine these two single IDs to a final ID there are three different possibilities:

OR COMBINATION: In this case a particle is identified as a kaon if the particle is identified as a kaon (conditions (4.9a) and (4.9b) are fulfilled) in one of the two CEDARs and not identified as a pion in the other one. In this case, the final ID is set to `kaon`. The same is done for the identification of pions. Particles that pick up `no ID` from both CEDARs or `kaon` from one CEDAR and `pion` from the other one obtain the final flag `no ID`. All possible combinations and resulting final IDs are given in table 4.2.

AND COMBINATION: In this case a particle is identified as a kaon if and only if a `kaon` ID is received from both CEDARs. The identification for pions is done the same way as for the OR combination as the kaon contamination is not expected to be large. The number of kaons in the beam is only 2.4% and thus a contamination of identified pions with misidentified kaons is not that important compared to a contamination of identified kaons with misidentified pions, which amount to 97% of the total beam. Further investigations on these issues will be done in chapter 5. Also for this case the full list of combinations and final IDs is given in table 4.2.

COMBINED LIKELIHOOD: A last possibility is to treat the two CEDARs as one detector with 16 photomultiplier tubes. In this case the likelihood in equation (4.7) is not calculated separately for both CEDARs but as a sum over all 16 photomultipliers in both detectors. Then, only one single ID is received which is then used as the final ID.

A comparison of these different methods will be given in chapter 5.4.

OR		CEDAR 2		
		kaon	pion	no ID
CEDAR 1	kaon	kaon	no ID	kaon
	pion	no ID	pion	pion
	no ID	kaon	pion	no ID

AND		CEDAR 2		
		kaon	pion	no ID
CEDAR 1	kaon	kaon	no ID	no ID
	pion	no ID	pion	pion
	no ID	no ID	pion	no ID

Table 4.2: Resulting PIDs for the AND and OR combination of the two CEDARs

4.6 APPLICATION TO FURTHER DATA TAKINGS

The method presented here has been developed for 2008 negative hadron beam data. The adaption to further data takings will be discussed in the following.

4.6.1 2009 Negative Hadron Beam

The most convenient data to adapt the method to is the 2009 negative hadron beam data as most of the settings for this data taking were similar to the 2008 data. The only crucial difference is the beam divergence. On the one hand the beam is tuned differently for every data taking, on the other hand the CEDAR detectors were taken out of the beam line in between and thus had to be newly aligned for the 2009 data taking. Thus new calibration samples and new hit patterns have to be produced. For the production of these hit patterns a phast user event is provided in the CEDAR part of the COMPASS hadron tools (see appendix G).

4.6.2 Primakoff Data Taking

For the adaption to Primakoff data taking (2009 and 2012) the trigger time shift has also to be taken into account. The new timings have already been implemented in the CEDAR helper class of the hadron tools. Hence, also in this case only new calibration samples and hit patterns have to be produced with the provided software.

4.6.3 Positive Hadron Beam

For positive hadron beam data normally only an identification of protons is desired. The pressure scan in figure 4.6 shows the clear separation of the proton peak and the meson (pion, kaon) peak. Therefore, in this case the multiplicity method works sufficiently well.

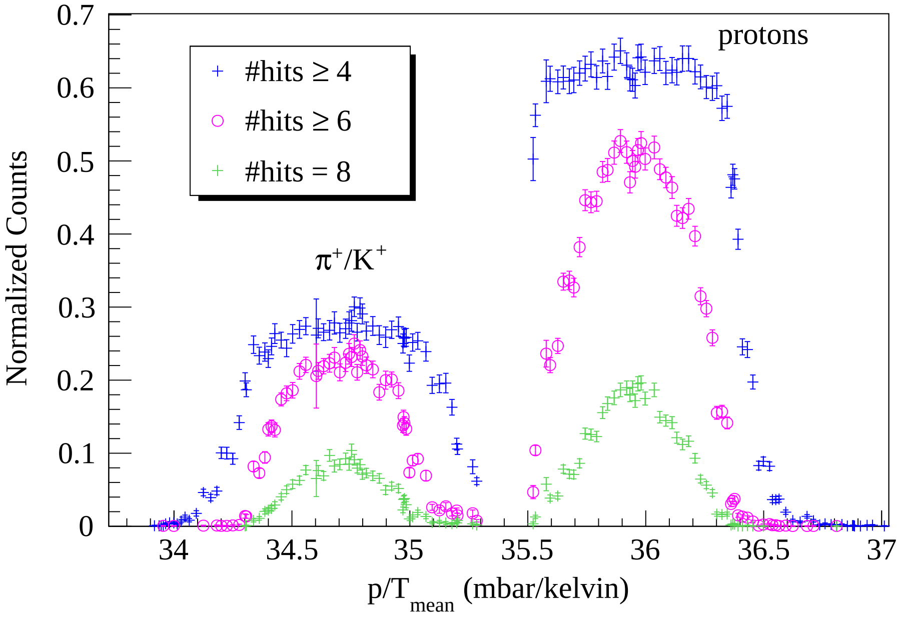

Figure 4.6: Pressure scan for positive hadron beam for different multiplicities [45]. The proton peak is well separated from the peak which contains the pions and kaons.

5

PERFORMANCE OF THE NEW METHOD

In this chapter, the performance of the new likelihood method will be investigated and compared to the multiplicity method. First, the performance of the single photomultipliers is studied. Afterwards, techniques to calculate the efficiency and the purity of the method will be presented and values for the likelihood differences A and B will be determined. All calculations will be done for the OR combination of the two CEDARs. In a final step, the different possible combinations of the two CEDARs will be compared.

5.1 PERFORMANCE OF THE SINGLE PHOTOMULTIPLIERS

In a first step, the correlation among the photomultipliers in CEDAR 1 and CEDAR 2 is examined. In figure 5.1 the correlation matrix between CEDAR 1 and CEDAR 2 is shown. To obtain this matrix, the hits in the single photomultipliers are counted for the beam sample. Afterwards the numbers are normalised to the full number of beam particles in the sample. If the beam was perfectly parallel and all photomultipliers were 100% efficient, a uniform distribution of hits would be expected in the matrix with a value of 2.44%, which corresponds

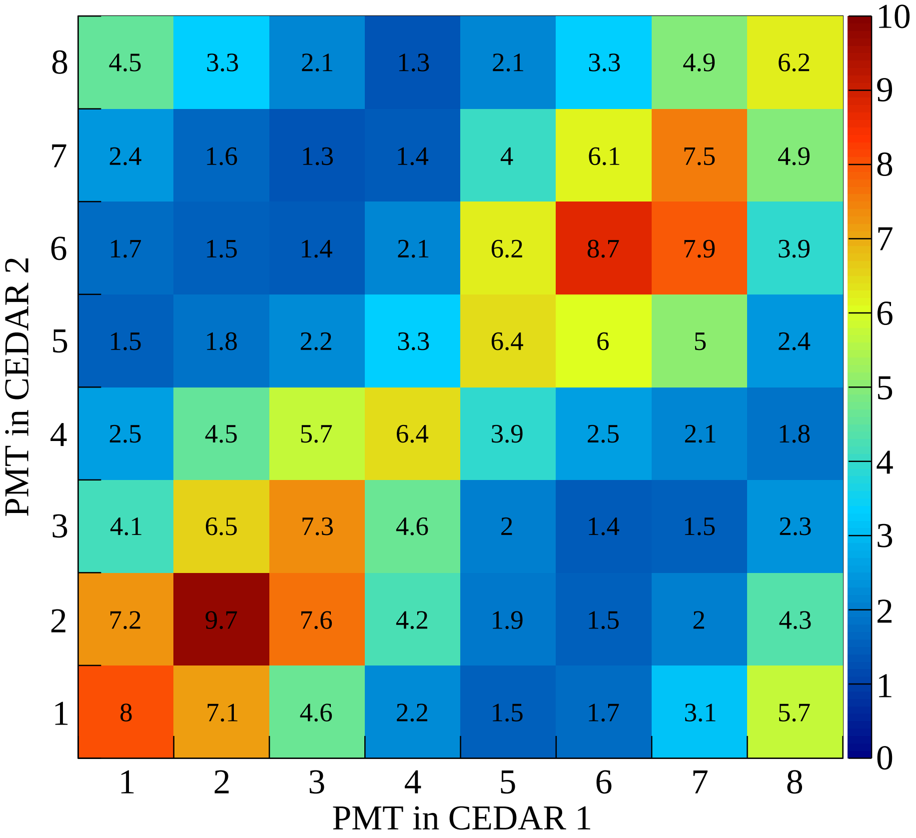

PMT in CEDAR 2	1	2	3	4	5	6	7	8
8	4.5	3.3	2.1	1.3	2.1	3.3	4.9	6.2
7	2.4	1.6	1.3	1.4	4	6.1	7.5	4.9
6	1.7	1.5	1.4	2.1	6.2	8.7	7.9	3.9
5	1.5	1.8	2.2	3.3	6.4	6	5	2.4
4	2.5	4.5	5.7	6.4	3.9	2.5	2.1	1.8
3	4.1	6.5	7.3	4.6	2	1.4	1.5	2.3
2	7.2	9.7	7.6	4.2	1.9	1.5	2	4.3
1	8	7.1	4.6	2.2	1.5	1.7	3.1	5.7

Figure 5.1: Correlation Matrix of PMT hits for the beam sample in percent of all particles. A clear correlation between the two CEDARs is visible.

to the number of kaons in the beam. In fact, a strong correlation between photomultipliers with the same number is observed. These have the same orientation relative to the beam axis. Thus, for a divergent beam the pion ring hits the same photomultipliers in both CEDARs. The correlation is not uniform due to different efficiencies of the single PMTs.
To investigate the efficiencies of the photomultipliers the kaon sample is used. In addition, the divergence is chosen to be small ($\theta_x, \theta_y < 30\,\mu\text{rad}$) to ensure the kaon light ring passes the diaphragm. The correlation matrix for these events is shown in figure 5.2. If all photomultipliers would be equally efficient, again uniform distribution is expected. Instead of that, clear band structures can be observed which point to lower efficiencies for single photomultipliers. The number of hits in the single photomultipliers compared to the number of beam particles with small divergence in the sample can be used as an estimate for the efficiencies of the photomultipliers. The resulting numbers are given in table 5.1. Most of the photomultipliers have an efficiency of more than 80%, where PMTs 3,7 and 8 in CEDAR 2 have much lower efficiencies. This can also be seen in figure 5.2 where these photomultipliers produce horizontal bands. Corrections to these efficiencies may stem from remaining pion background, which would not produce any signal. Additionally, also for the chosen small divergences, the Cherenkov photons from the kaon ring might not reach every PMT.

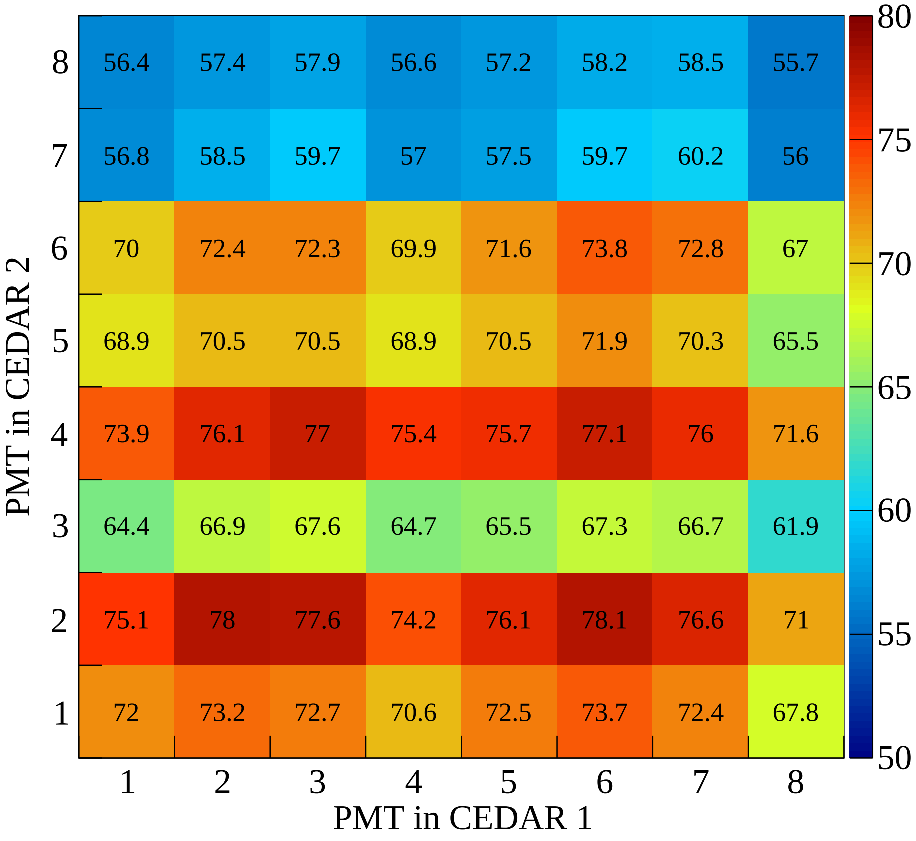

PMT in CEDAR 2	1	2	3	4	5	6	7	8
8	56.4	57.4	57.9	56.6	57.2	58.2	58.5	55.7
7	56.8	58.5	59.7	57	57.5	59.7	60.2	56
6	70	72.4	72.3	69.9	71.6	73.8	72.8	67
5	68.9	70.5	70.5	68.9	70.5	71.9	70.3	65.5
4	73.9	76.1	77	75.4	75.7	77.1	76	71.6
3	64.4	66.9	67.6	64.7	65.5	67.3	66.7	61.9
2	75.1	78	77.6	74.2	76.1	78.1	76.6	71
1	72	73.2	72.7	70.6	72.5	73.7	72.4	67.8

Figure 5.2: Correlation matrix of low-divergence PMT hits for the kaon sample to determine the efficiency of the single photomultipliers.

PMT	Efficiency in %	
	CEDAR 1	CEDAR 2
1	83.5	82.5
2	85.3	87.0
3	85.2	74.6
4	83.1	86.4
5	84.8	79.7
6	86.7	81.5
7	85.9	66.5
8	80.0	66.5

Table 5.1: Estimated efficiencies (in %) of the single photomultipliers in CEDAR 1 and CEDAR 2.

5.2 EFFICIENCY CALCULATION

One method to determine the efficiency are pressure scans as explained in [64]. Due to the low number and low quality of available pressure scans this method will not be used in the following. Instead of that, the efficiency is determined through a comparison of the number of identified particles with the expected number. The beam composition at the CEDAR detectors is (see chapter 2.1)

$$\begin{aligned} \pi^- &: (96.77 \pm 0.98)\% \\ K^- &: (2.44 \pm 0.07)\% \\ \bar{p} &: (0.79 \pm 0.02)\% \,. \end{aligned}$$

The number of identified kaons and pions in the beam sample for different log likelihood differences is compared to the numbers given above to obtain the efficiency. Basically, any data sample could be used here. For stable beam conditions over the full data taking, the results obtained here should not change on a different sample.

5.2.1 Kaon Efficiency

Figure 5.3 shows the calculated kaon identification efficiency as a function of the log likelihood difference A as defined in equation (4.9b). For A a logarithmic binning is used to cover a larger range of values from 0.1 to 20. The left plot shows the results for `cut200`, the right one for `cut01`, respectively. The blue dotted line denotes the value obtained from the multiplicity method (48.4%).

Two observations can be made:

1. The number of identified kaons is much higher for `cut200` than for `cut01`. This is due to the strict handling of low statistic bins for `cut01`: If any of the 8 PMTs of a CEDAR has a low statistic bin, the particle picks up a `no ID` flag. This case occurs in a sizeable number of bins with large divergence. Nevertheless, we will still keep this cut to investigate the purity.

2. The number of identified kaons drops – as expected – with increasing A, where the drop between $A = 0.1$ and $A = 1$ is small.

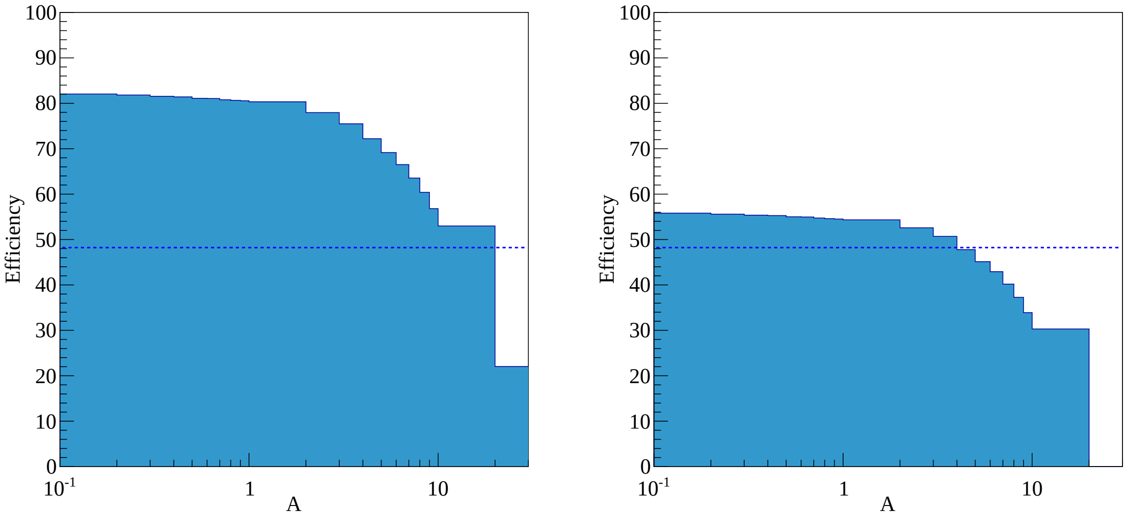

Figure 5.3: Kaon identification efficiency for `cut200` (left) and `cut01` (right) as a function of the log likelihood difference A. Displayed are the results for an OR combination of the two CEDARs. The blue dotted line shows the result for the multiplicity method.

5.2.2 Pion Efficiency

For the pion case the procedure is the same as for the kaon case. Figure 5.4 shows the resulting efficiencies for the OR combination of the CEDARs as a function of the log likelihood difference B.

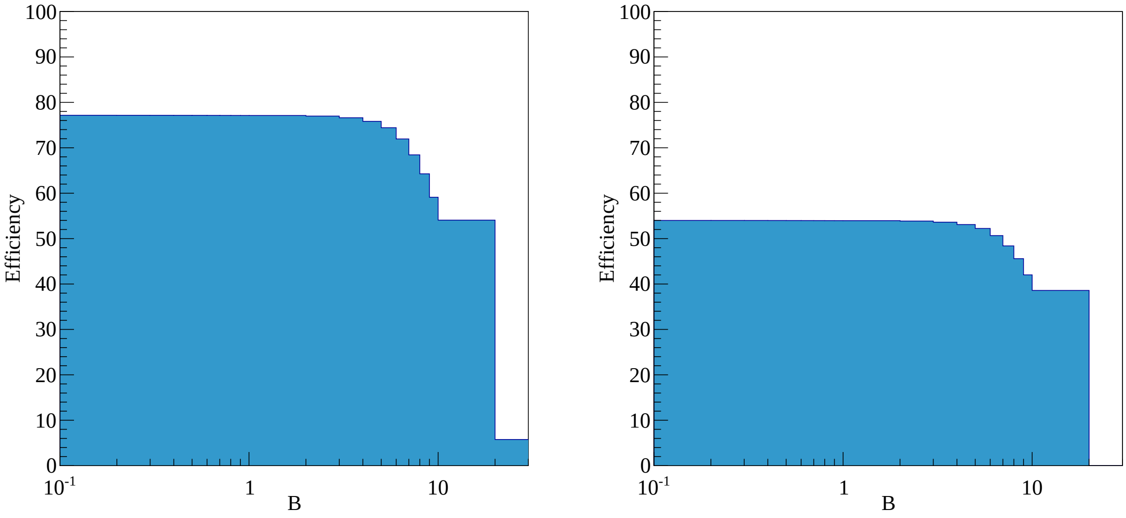

Figure 5.4: Pion identification efficiency for `cut200` (left) and `cut01` (right) as a function of the log likelihood difference B. Displayed are the results for an OR combination of the two CEDARs.

The obtained efficiencies are in the same order of magnitude (for `cut200` as well as `cut01`) as in the kaon case. This is expected as the method used here is a purely statistical approach and thus does not distinguish between kaon and pion identification. Therefore, the efficiency for kaon and pion identification should be of the same order of magnitude.

In figure 5.4 no value for the multiplicity method is given. The reason is simple: The multiplicity method only identifies kaons, while every particle not identified as a kaon is tagged as a pion (there is simply no `no ID` decision foreseen). Hence, it is not sensible to define a pion efficiency for that method.

5.3 PURITY CALCULATION

For the calculation of the CEDAR purity the beam particle has to be identified without the CEDARs themselves. No direct method is available at COMPASS and thus, a reaction has to be used in which the beam particle is determined via the final state particles. One possible pair of reactions [66] is the production of single neutral kaons

$$\begin{aligned} &\pi^- p \to K^- K^0_S p \\ &K^- p \to \pi^- K^0_S p\,. \end{aligned} \tag{5.1}$$

In this reactions, the final charged meson (K^- or π^-) is linked to the beam particle (π^- or K^-) due to conservation of strangeness in the strong interaction: If the beam particle is a pion, a K^0 in the final state can only be produced together with a charged kaon ($S = 0 \to S = 0$). If otherwise the beam particle itself is a kaon, the K^0 in the final state can only occur together with a pion ($S = -1 \to S = -1$).
Therefore, it is sufficient to identify the outgoing charged hadron to determine the type of beam particle. This identification of the outgoing hadron is achieved by the RICH. The purity of the RICH selection itself causes a systematic error which is considered to be small and thus neglected.

5.3.1 Kaon Purity

To determine the kaon purity, final states with a reconstructed K^0 and a negatively charged hadron are selected from the full 2008 data set with negative hadron beam. Only events with CEDAR identified beam kaons are used, the number of available events depends on the likelihood cut and ranges from 6967 ($A = 10$ and `cut01`) to 20710 ($A = 1$ and `cut200`). The RICH probabilities for the outgoing hadron to be a pion or kaon, respectively, are used. In figure 5.5 the base 2 logarithm of the ratio of kaon probability over pion probability $\log_2(p(K)/p(\pi))$ for the outgoing charged hadron is shown as a function of the momentum. Entries above zero correspond to RICH identified kaons, entries below zero to RICH identified pions, respectively. If the CEDAR kaon selection was perfect, only RICH identified pions would be visible. The appearance of RICH identified kaons shows the impurity of the CEDAR selection. For the calculation of purity the RICH identified pions are counted and compared to the total number of RICH identified particles. Before this calculation, two additional cuts are applied:

1. Only particles with a momentum between 12 GeV/c and 50 GeV/c are taken into account. This is the momentum range where the separation of kaons and pions in the RICH is sufficient.

2. RICH identified kaons are required to fulfil $\log_2(p(K)/p(\pi)) > 0.4$, which corresponds to a ratio of $p(K)/p(\pi) > 1.32$. Similarly, pions have to fulfil $\log_2(p(K)/p(\pi)) < -0.1$ or $p(\pi)/p(K) > 1.07$. This ensures a clean selection of particles in the RICH.

Figure 5.6 shows the results for the purity obtained for different values of the log likelihood difference A for both `cut200` (red) and `cut01` (blue). The black line corresponds to the value obtained by the same event counting with the multiplicity method. The error bars and error band are $\sqrt{n}$ Poisson counting errors. The obtained purity is nearly constant as a function of

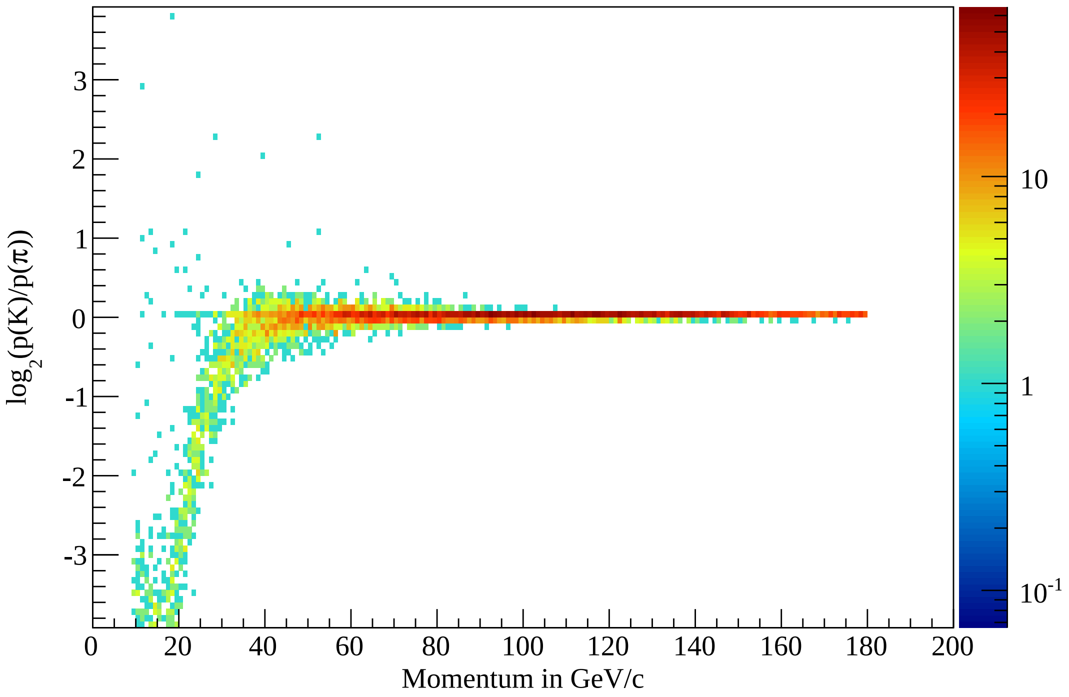

Figure 5.5: RICH probabilities $\log_2(p(K)/p(\pi))$ for CEDAR identified kaons as a function of the momentum of the outgoing charged hadron.

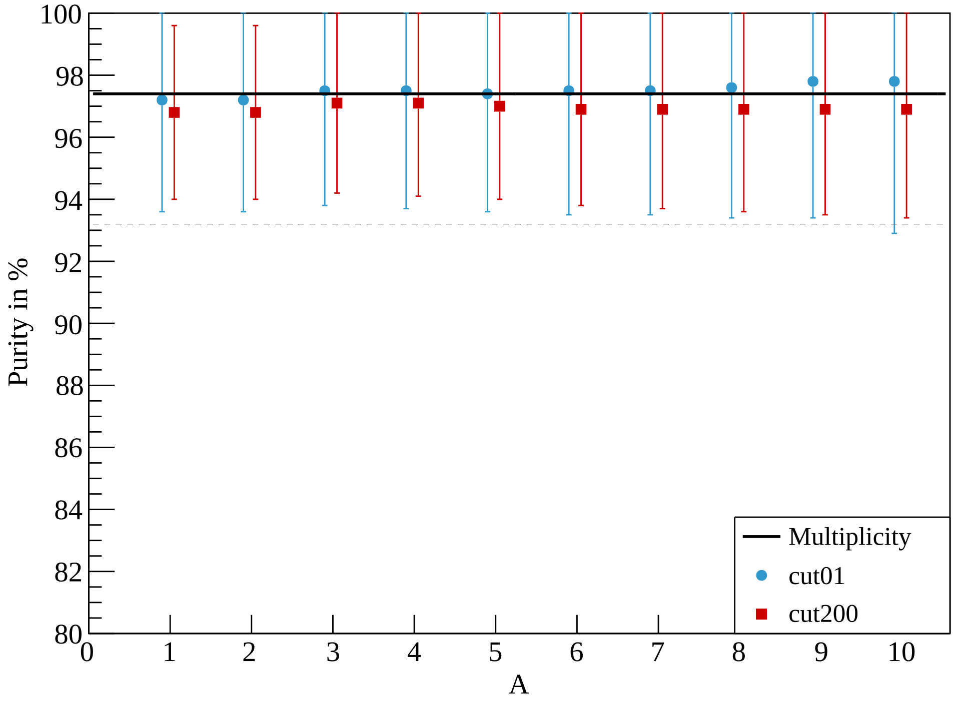

Figure 5.6: Kaon purity as a function of the log likelihood difference A for `cut200` (red) and `cut01` (blue). The black line corresponds to the multiplicity method.

the likelihood difference A. For `cut200` the purity is slightly smaller compared to the multiplicity method, but the errors are large due to the small available statistics in this channel. For both of the cuts, the values are compatible with the multiplicity method. Due to the small change of purity as a function of the likelihood difference A, this difference can be tuned purely for efficiency.

5.3.2 Pion Purity

The purity of the pion selection is determined in the same way as for the kaon selection by switching the CEDAR and RICH conditions. The RICH probabilities of CEDAR identified pions are shown in figure 5.7. Each RICH identified pion (corresponding to a value below zero) contributes to the impurity of the CEDAR selection. The same cuts as before are used, the obtained purities are shown in figure 5.8 as a function of the log likelihood difference B. Here, the value given for the multiplicity method needs some further clarification. The multiplicity is only valid to positively identify kaons. Hence, each kaon which is not identified by the multiplicity method is counted as a pion in this calculation. The low kaon identification efficiency then accounts for the lower purity of the multiplicity method compared with the likelihood method. The purity obtained from the likelihood method slightly rises up to $B = 6$ and drops again for higher values of B. The observed variations are smaller than the statistical errors. Similar to the kaon case, the purity does not strongly depend on the likelihood difference B, which can be tuned for efficiency.

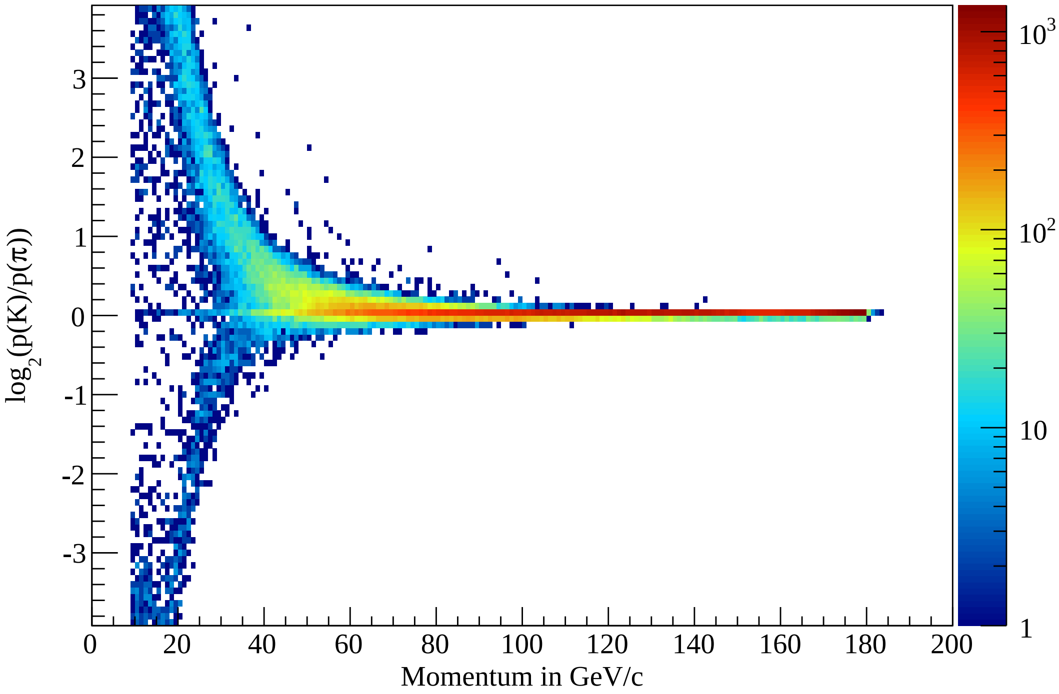

Figure 5.7: RICH probabilities $\log_2(p(K)/p(\pi))$ for CEDAR identified pions as a function of the momentum of the outgoing charged hadron.

5.4 DIFFERENT COMBINATIONS OF THE CEDAR DETECTORS

The beam sample is used for the comparison of the different possible combinations of the two CEDARs. Table 5.2 shows the obtained PIDs for the different combinations and for the multiplicity method as well as the kaon and pion identification efficiency, which is calculated

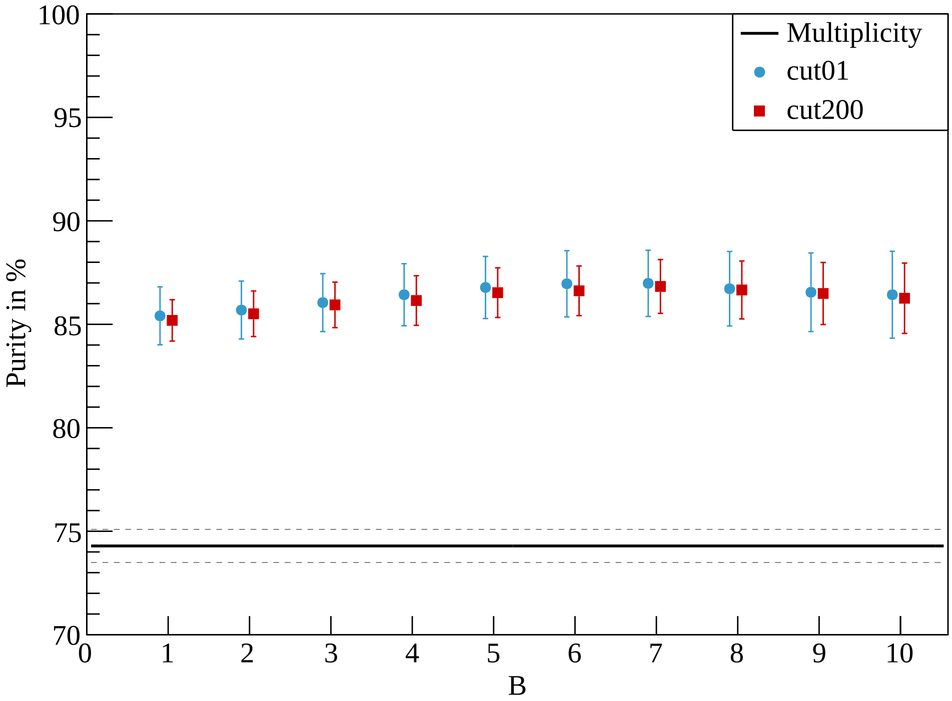

Figure 5.8: Pion purity as a function of the log likelihood difference B for `cut200` (red) and `cut01` (blue). The black line corresponds to the multiplicity method.

as explained above. For all methods `cut200` and likelihood differences $A = B = 1$ are used. As the pion identification efficiency is of the same size for all the different combinations, the

method	`kaon`	`pion`	`no ID`	K eff.	π eff.
CEDAR 1	2.35%	75.0%	22.6%	96.3%	77.4%
CEDAR 2	2.66%	74.3%	23.1%	109.0%	76.8%
AND	1.62%	74.6%	23.8%	66.4%	77.0%
OR	1.96%	74.6%	23.4%	80.3%	77.1%
16 PMT	2.66%	75.2%	22.2%	109.0%	77.7%
Multiplicity	1.18%	98.8%		48.4%	
Beam	2.44%	96.8%			

Table 5.2: PIDs obtained from the beam sample for CEDAR 1 and 2 separately, for different combinations of both and for the multiplicity method (in percent of the full sample). The last line shows the nominal beam composition. The two rightmost columns give the kaon and pion identification efficiency.

kaon identification efficiency is the main criterion for the selection of the method. The OR combination results in the best value of 80%, where the AND combination only yields 66%. The calculated efficiency for the direct combination of all 16 photomultipliers is even above 100%, which leads to a low purity as at least 9% of the identified kaons simply cannot be kaons.

SUMMARY – BEAM PARTICLE IDENTIFICATION WITH STATISTICAL METHODS

A new method for the identification of beam particles in the CEDAR detectors has been developed. The method is based on statistical methods and likelihoods are used to distinguish the different particle species. As shown in section 5.3 the purity of the likelihood method does not depend strongly on the log likelihood differences A and B. Therefore, the method can be tuned purely by means of efficiency. The efficiency drops with increasing values of A and B (see section 5.2). The efficiency for `cut01` is much smaller compared with `cut200`, while the purity does not differ between those two. Thus, a good starting point for analyses would be the choice of $A = B = 1$ with `cut200`, which results in the efficiencies and purities given in table 5.3.

	Likelihood	Multiplicity
Kaon Efficiency	$(80.3 \pm 0.4)\%$	$(48.4 \pm 0.2)\%$
Kaon Purity	$(96.8 \pm 2.8)\%$	$(97.4^{+2.6}_{-4.2})\%$
Pion Efficiency	$(77.1 \pm 0.3)\%$	X
Pion Purity	$(85.2 \pm 0.1)\%$	$(78.0 \pm 0.3)\%$

Table 5.3: Efficiencies and purities for the likelihood method ($A = B = 1$, `cut200`) in comparison with the multiplicity method.

The efficiency for the identification of kaons is $\approx 80\%$ which is a gain of $\approx 65\%$ compared to the multiplicity method. The pion efficiency is in the same order of magnitude. The purity for kaon identification is compatible with the value obtained from the multiplicity method; the pion purity is $\approx 85\%$, which is an improvement compared to the multiplicity method. For the multiplicity method no value for the pion efficiency can be given (see section 5.2.2) and the value for the purity is not reliable as explained in section 5.3.2.

The presented likelihood method is a big improvement – concerning the kaon identification efficiency – compared to the multiplicity method. In addition a positive identification of pions (and not only a kaon rejection) is possible. Last but not least, the new method works well up to total divergences of $\sqrt{\theta_x^2 + \theta_y^2} < 200\,\mu\text{rad}$, whereas the multiplicity method only works sufficiently for small divergences.

II

PRODUCTION OF SINGLE MESONS IN *pp* REACTIONS

6

EVENT SELECTION FOR DIFFERENT CHANNELS

In the following, the production of a single meson M in the reaction $pp \to p_{\text{recoil}} M p_{\text{fast}}$ will be investigated. The goal is the determination of cross section ratios. This reaction is schematically shown in figure 6.1. The meson M decays into the final state X. A fast outgoing proton and a recoil proton can are measured together with X. There are several different final states X, in which a single meson M can be found:

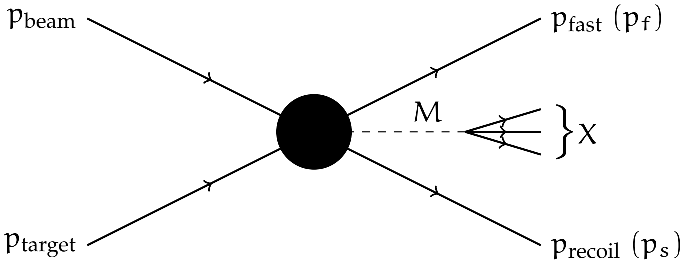

Figure 6.1: Schematic picture of the production of a single meson M in proton-proton reactions. The meson M decays into the final state X. A fast outgoing proton and a recoil proton can are measured together with X.

In the final state $p_{\text{recoil}}\gamma\gamma p_{\text{fast}}$, the two photons can originate from decays of the pseudoscalar mesons π^0 and η. There is also a small fraction of $\eta' \to \gamma\gamma$, which will not be considered here.

The ω dominantly decays into $\pi^+\pi^-\pi^0$ and thus will be selected in the $p_{\text{recoil}}\pi^+\pi^-\gamma\gamma p_{\text{fast}}$ final state. In this channel also the decay $\eta \to \pi^+\pi^-\pi^0$ and $\eta' \to \pi^+\pi^-\eta$ could be investigated.

In the $p_{\text{recoil}}K^+K^-p_{\text{fast}}$ final state, there is a significant contribution of ϕ mesons, which dominantly decay into K^+K^-.

Finally, the event selection for $p_{\text{recoil}}\pi^+\pi^-p_{\text{fast}}$ is essentially the same as for kaon pair production. This channel contains a contribution of $\rho \to \pi^+\pi^-$ which cannot be easily used for analyses due to the large decay width of that meson. Nevertheless, the kinematic distributions in this channel are very similar to $p_{\text{recoil}}K^+K^-p_{\text{fast}}$ but with a much higher statistics and therefore, this channel is also considered in the following.

Thus, the following reactions will be investigated:

$$
\begin{aligned}
pp \to & p_{\text{recoil}}\pi^0 p_{\text{fast}} \\
& \text{with } \pi^0 \to \gamma\gamma \\
pp \to & p_{\text{recoil}}\eta p_{\text{fast}} \\
& \text{with } \eta \to \gamma\gamma \\
pp \to & p_{\text{recoil}}\omega p_{\text{fast}} \\
& \text{with } \omega \to \pi^+\pi^-\pi^0 \\
pp \to & p_{\text{recoil}}\phi p_{\text{fast}} \\
& \text{with } \omega \to K^+K^- \\
\Big(pp \to & p_{\text{recoil}}\pi^+\pi^- p_{\text{fast}}\Big)
\end{aligned}
$$

In the following, a common basic selection for the different final states will be presented. Afterwards, the selection for the two-particle ($\pi^0 p_{\text{fast}}$ and ηp_{fast}), three-particle ($K^+K^- p_{\text{fast}}$ and $\pi^+\pi^- p_{\text{fast}}$) and the ωp_{fast} final states will be discussed.

6.1 THE 2009 DATA TAKING WITH PROTON BEAM

The 2009 data taking with a positive hadron beam took place during six weeks between July 16, 2009 and August 26, 2009. In three periods more than 11 billion data events were recorded. The available statistics with all triggers for the single periods and the full data taking is given in table 6.1. For the analyses shown here the full data set was used. Basically, this data could be supplemented with the 2008 data set, which contains another 1.2 billion events. However, the combination of the two data sets is not easy, due to some differences in the set-up of the spectrometer. Given the high statistics obtained for the single channels using 2009 data, the 2008 data are not included here.

Period	Time	#Runs	#Spills	#Events	%
W29	July 16 – July 29	190	93,554	4,110,218,046	36.3
W31	July 29 – August 9	208	77,357	3,791,891,038	33.5
W33	August 13 – August 26	200	64,625	3,418,950,503	30.2
total	July 16 – August 26	598	235,536	11,321,059,587	

Table 6.1: Available statistics with all triggers for the 2009 data taken with proton beam. 96% of these events were recorded with the DT-0 trigger (see 6.3.1).

6.2 EVENT RECONSTRUCTION AND DATA ANALYSIS

Before the reconstruction of events, the recorded raw detector information is calibrated and corrected with methods specific for each single detector. After these calibrations, the event reconstruction is performed by the CORAL (COMPASS Reconstruction ALgorithms [67]) software package. In this step the hits in the detectors are used to construct physics events. The following steps are performed by CORAL:

- Hits in tracking detectors are formed into track segments.
- The track segments are combined into tracks taking magnetic fields and detector material into account. In this step also the track momentum is determined.
- Vertices are reconstructed from charged tracks.
- Calorimeter showers are reconstructed from hits in the calorimeter modules.
- Likelihoods for particle identification in the RICH detector are calculated.

CORAL provides the information on reconstructed events (vertex positions, particle momenta and charge, particle ID information,...) in the form of ROOT trees, which are in this context referred to as mini Data Summary Trees (mDST).

For the analysis of the data stored in the mDST, the PHAST (PHysics Analysis Software Tools [68]) package is used. It provides ready-to-use classes to easily access the available information, e. g. for the construction of Lorentz vectors for the different outgoing particles. The up-to-date list of available classes and the manual can be found at [69]. For data taking with hadron beams, the detector information of the CEDARs and the RPD is not processed by CORAL, but contained in the mDST as raw information. To process these information, an additional package ("HadronTools" [70]) is provided.

6.3 DATA SELECTION

In this section some of the cuts which are used in the selection of different channels are explained in detail. In addition, the common selection criteria for the investigated reactions are given.

6.3.1 Trigger

The main trigger for hadron data taking is the so-called DT-0 trigger (see section 2.6). It is a minimum bias trigger requiring three conditions to be fulfilled:

1. An incoming beam particle has to be detected.
2. A recoil proton has to be measured in the RPD.
3. No particle is found in the veto system.

For data analyses, only events which fulfil the DT-0 trigger conditions are used. These are 96% of the recorded events.

6.3.2 Exclusivity and Coplanarity

In this thesis only exclusive measurements, i. e. only fully reconstructed events, are used for analyses. Therefore, the energy of the full final state has to match with the energy of the incoming beam. The energy of the hadron beam is not measured at COMPASS. Thus, exclusive events are selected in two steps:

1. The beam energy is calculated from the final state particles. There are two possible methods: For the $\pi^+\pi^-$ and K^+K^- channel the beam energy is calculated as the energy sum of the outgoing particles (including the recoil proton). For all other final states (π^0, η, ω) a kinematic calculation of the beam energy based on [71] is done. In both cases the reconstructed energy has a peak at the nominal beam energy of 191 GeV. Events outside a certain range (normally 1σ) around the peak position are rejected. The distribution and the effect of the cut for the π^0 case is shown in figure 6.2a.
2. To further improve the selection of exclusive events a check on the conservation of transverse momentum is performed. The azimuthal angle of the outgoing system ($p_{\text{fast}} + X$) and of the recoiling proton should differ by exactly 180 degrees. Only events that fulfil this condition within a certain range (normally ±0.26 rad, which is the resolution of the RPD) are taken into account for further analyses. Figure 6.2b shows the distribution for the π^0 case as well as the influence of the cut and the correlation with the energy cut.

6.3.3 CEDAR and RICH particle ID

For positive hadron beams both CEDARs are set to select the proton light ring. As shown in figure 4.6 the proton peak in the pressure scan is well separated from the pion peak, thus it is sufficient if one of the CEDARs identifies the beam particle as a protons as long as the

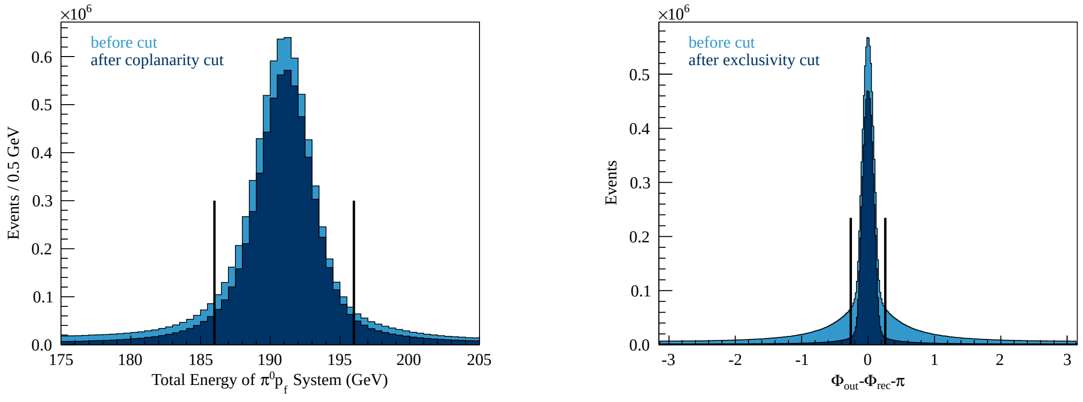

(a) Exclusivity

(b) Coplanarity

Figure 6.2: This figure shows the influence of the exclusivity (left) and coplanarity (right) cut for $pp \to p_{recoil}\pi^0 p_{fast}$. The light blue area corresponds to the distribution before both cuts, the dark blue area to the distribution after the other cut. The lines denote the cut on the value itself.

other CEDAR does not identify it as a pion. In this way 71.6% of the events pass this cut (see table 6.2) where 75% of the events should contain an incoming proton.

For the channels containing charged pions or kaons there are two positively charged particles in the final state, namely π^+ and proton or K^+ and proton. To fully reconstruct the final state the charged meson has to be identified by the RICH. The identification is done using ratios of RICH likelihoods. For the identification of a pion the likelihood for a pion should be larger than for the other hypothesis, namely

$$\frac{L(\pi)}{L(K)} > 1.0, \qquad \frac{L(\pi)}{L(p)} > 1.0 \text{ and } \qquad \frac{L(\pi)}{L(bkg)} > 1.0\,. \tag{6.1}$$

As the number of kaon events is much smaller it is crucial to get rid of as much pion background as possible. Therefore, the required likelihood ratio of kaons compared to pions is chosen to be larger than 1.3. This leads to the following ratios:

$$\frac{L(K)}{L(\pi)} > 1.3, \qquad \frac{L(K)}{L(p)} > 1.0 \text{ and } \qquad \frac{L(K)}{L(bkg)} > 1.0 \tag{6.2}$$

In both cases, only tracks with a momentum between 12 GeV/c and 50 GeV/c are used to ensure a good separation efficiency (compare figure 2.4).

6.3.4 Common selection criteria for the investigated reactions

A number of basic cuts are common for all analysis channels. These are:

1. Events are required to be recorded by the DT-0 trigger.
2. Only events with exactly one primary vertex inside the liquid hydrogen target, i. e. $-74\,\text{cm} < z_{vertex} < -24\,\text{cm}$, are used.
3. The beam particle is identified as a proton.
4. Events should contain exactly one reconstructed recoil proton in the RPD.

These cuts are passed by 35% of all available events. The numbers of events after each cut are given in table 6.2.

Cut	Events
no cuts	11,321,059,587
1. DT-0 trigger	10,825,412,397
2. 1 primary vertex in target	7,925,572,030
3. incoming proton in CEDAR	5,674,142,337
4. recoil proton in RPD	3,967,769,836

Table 6.2: Cut flow for the cuts that are common to all analyses.

6.4 EVENT SELECTION FOR TWO-PARTICLE FINAL STATES

After the common cuts given in 6.3.4, the two-particle final states $\pi^0 p_{\text{fast}}$ and ηp_{fast} can be selected with another set of cuts, which is discussed in the following.

There should be only a single charged track attached to the primary vertex. This track is assigned to be the outgoing proton. Basically, this track could also be a pion if the incoming particle was misidentified in the CEDAR. However, there is no way to check whether the charged track belongs to a proton as the RICH can only identify particles up to a momentum of 50 GeV/c where the momentum of the fast particle, which is shown in figure 6.3, reaches 190 GeV/c.

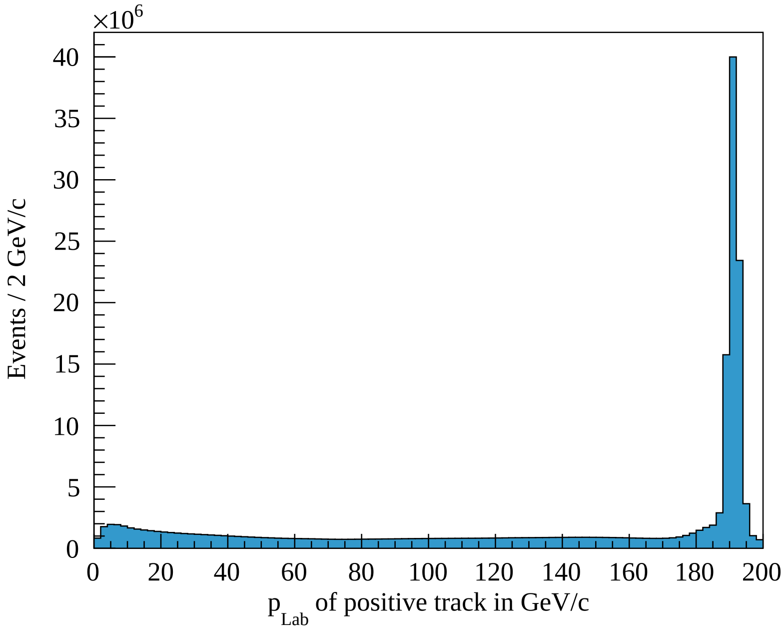

Figure 6.3: Momentum of the charged particle attached to the primary vertex which is most likely a proton.

The incoming beam particles are positively charged. Therefore, due to charge conservation, the outgoing track is required to have a measured positive charge.

To reconstruct a π^0 or η the event should contain exactly two clusters without an associated charged track in the ECAL with an energy of at least 1 GeV in ECAL1 and 2 GeV in ECAL2, respectively. The energy of the clusters is corrected using the LED/Laser calibration. Due to missing corrections, three runs (77594, 77595 and 77598) with in total 1.4 million events (0.8% of all events) are not used for the analysis.

The invariant mass of the two neutral clusters is fitted for different combinations of the two ECALs. The fits, which are shown in figure 6.5, are performed in the region of the PDG masses ($60 - 200$ MeV for π^0 and $370 - 730$ MeV for η) using a Gaussian signal and a polynomial background. Only events within 2σ around the central peak value are used for the analysis. The widths obtained from the fit are given in table 6.3. For these events the energy of the ECAL clusters is rescaled[1] such, that the invariant mass of the reconstructed particle fits the nominal mass of the π^0 or η.

ECAL	π^0	η
1 only	9.79	26.0
2 only	4.68	14.1
mixed	8.87	25.8

Table 6.3: Widths in MeVc^2 of the $\gamma\gamma$ peaks obtained from the fits given in figure 6.5.

The beam energy calculated from the formulas given in [71] is required to be in the range of ±5 GeV around the peak value of 191 GeV. In addition, the difference of the azimuthal angles between the two-particle final state and the recoiling proton has to be within ±0.26 rad around the expected value of π. The connection between those two cuts for $pp\pi^0$ was already demonstrated in figure 6.2, where the two distributions are shown each without (light blue) and with (dark blue) the cut on the other variable. Black lines denote the cut on the variable itself. Figure 6.4 shows the same distributions for $pp\eta$.

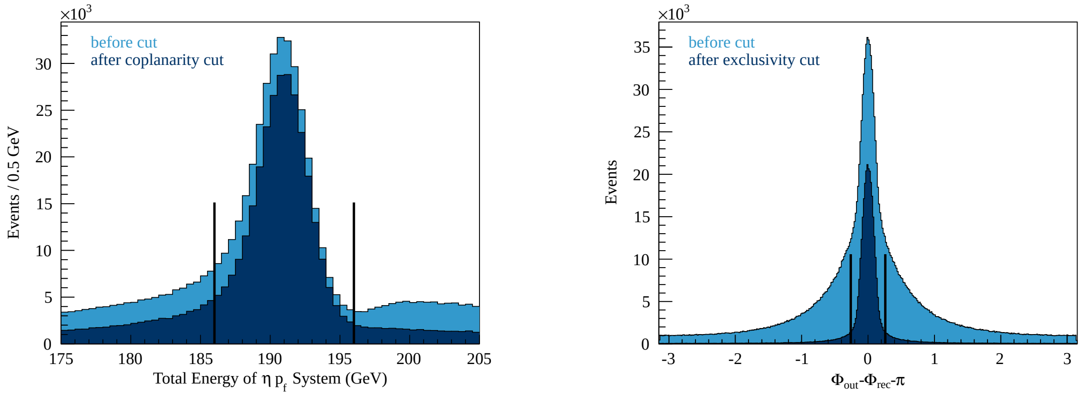

(a) Exclusivity

(b) Coplanarity

Figure 6.4: This figure shows the influence of the exclusivity (left) and coplanarity (right) cut for $pp \to p_{recoil}\pi^0 p_{fast}$. The light blue area corresponds to the distribution before both cuts, the dark blue area to the distribution after the other cut. The lines denote the cut on the value itself.

The momentum transfer t is defined as $t = (p_{beam} - p_X)^2$ with the four momenta p_{beam} of the beam and p_X of the outgoing $p\pi^0$ or $p\eta$ system. For diffractive reactions, it is useful to subtract the minimal t necessary to produce the outgoing system with mass m_X and define

$$t' = |t| - |t_{min}| \geqslant 0\,. \tag{6.3}$$

---

[1] The energy is rescaled by $\frac{M_{nominal}}{M_{measured}}$.

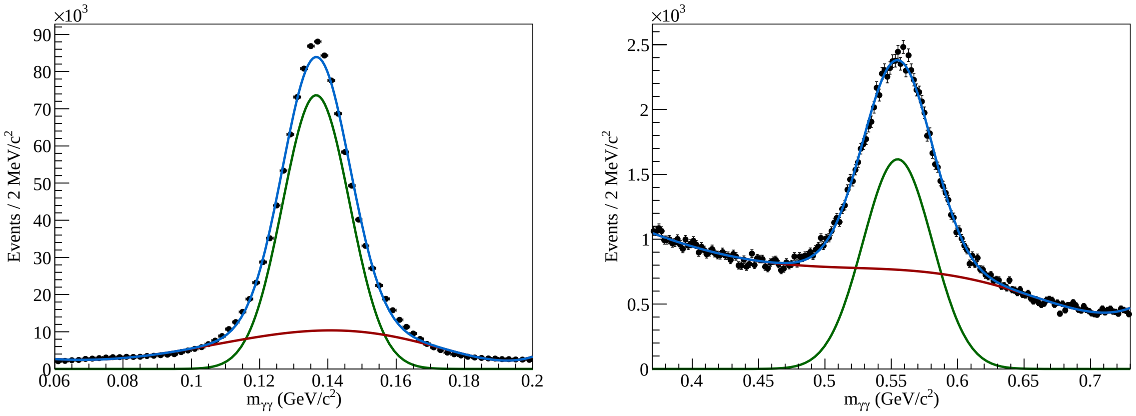

(a) π^0 – both photons in ECAL1
$\sigma = 9.79\,\mathrm{MeV/c^2}$

(b) η – both photons in ECAL1
$\sigma = 26.0\,\mathrm{MeVc^2}$

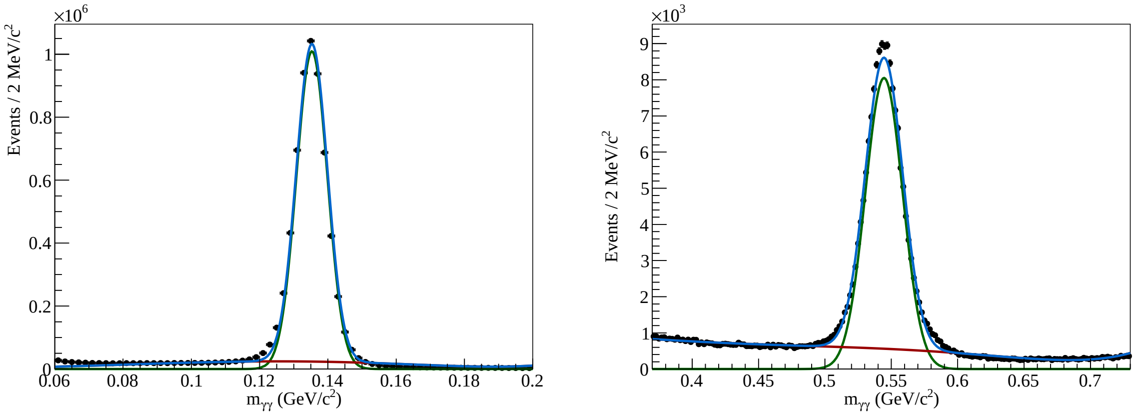

(c) π^0 – both photons in ECAL2
$\sigma = 4.68\,\mathrm{MeVc^2}$

(d) η – both photons in ECAL2
$\sigma = 14.1\,\mathrm{MeVc^2}$

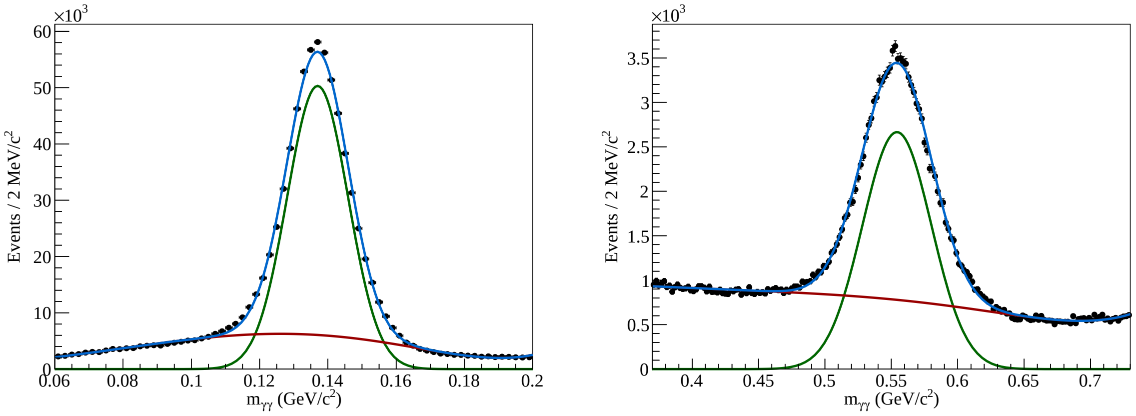

(e) π^0 – one photon in each ECAL
$\sigma = 8.87\,\mathrm{MeVc^2}$

(f) η – one photon in each ECAL
$\sigma = 25.8\,\mathrm{MeVc^2}$

Figure 6.5: Invariant $\gamma\gamma$ mass in the π^0 region (left column) and the η region (right column) for the different ECAL combinations. The fits (blue) are done using a Gaussian signal (green) together with a polynomial background (red).

For high beam energies, the minimal momentum transfer can be approximately calculated as [71]

$$|t_{\text{min}}| \approx \frac{(m_X^2 - m_{\text{beam}}^2)^2}{4\,|\vec{p}_{\text{beam}}|_{\text{lab}}^2} \,. \tag{6.4}$$

A cut on the momentum transfer t' of $0.1\,(\text{GeV}/c)^2 < t' < 1.0\,(\text{GeV}/c)^2$ is performed. Above $1.0\,(\text{GeV}/c)^2$ non-diffractive events may contribute too much, the lower cut is due to the threshold of the RPD of $0.07\,(\text{GeV}/c)^2$. Figure 6.6 shows the t' distribution for t' for $pp \to p_{\text{recoil}}\pi^0 p_{\text{fast}}$ before the cuts on exclusivity and coplanarity. The RPD threshold around $0.1\,(\text{GeV}/c)^2$ is clearly visible.

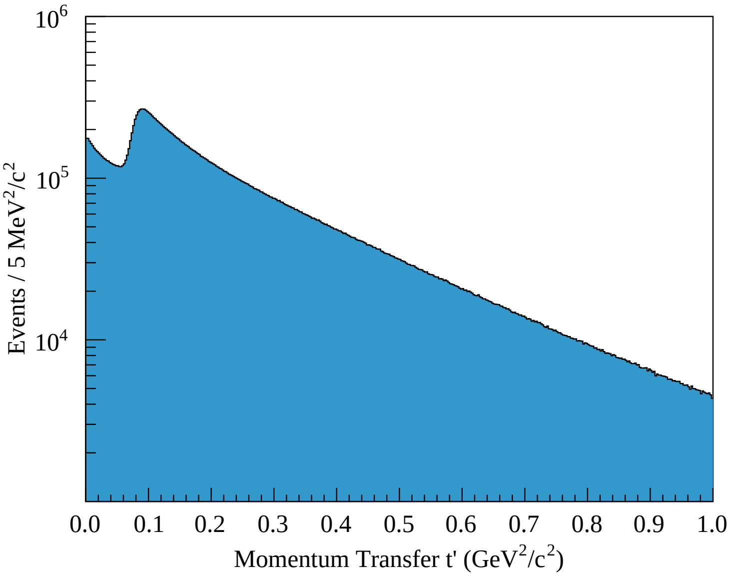

Figure 6.6: Momentum transfer t' for $pp \to p_{\text{recoil}}\pi^0 p_{\text{fast}}$ before the exclusivity cuts.

Table 6.4 shows the cut flow for the selection of the two final states $\pi^0 p_{\text{fast}}$ and ηp_{fast}.

	π^0	η
after common selection	3,967,769,836	
1 charged track	2,538,252,264	
$Q = +1$	2,509,970,011	
2 ECAL clusters	181,914,889	
without skipped runs	180,531,815	
π^0/η identified	25,026,750	2,955,537
exclusivity and coplanarity	10,844,146	526,620
t'	8,835,835	442,236

Table 6.4: Cut flow for final selection of events for $pp \to p_{\text{recoil}}\pi^0 p_{\text{fast}}$ and $pp \to p_{\text{recoil}}\eta p_{\text{fast}}$

6.5 EVENT SELECTION FOR THREE-PARTICLE FINAL STATES

The selection cuts for three-particle final states $\pi^+\pi^- p_{\text{fast}}$ and $K^+K^- p_{\text{fast}}$ are very similar to the ones for two-particle final states. However, the presence of two equally charged particles has to be taken into account according to 6.3.3. The selection is done as follows:

1. Three charged tracks have to be assigned to the primary vertex.

2. The charge sum of these tracks has to be +1 matching the charge of the incoming beam particle.
3. The positive meson (π^+ or K^+) has to be identified by the RICH following the criteria given in section 6.3.3.

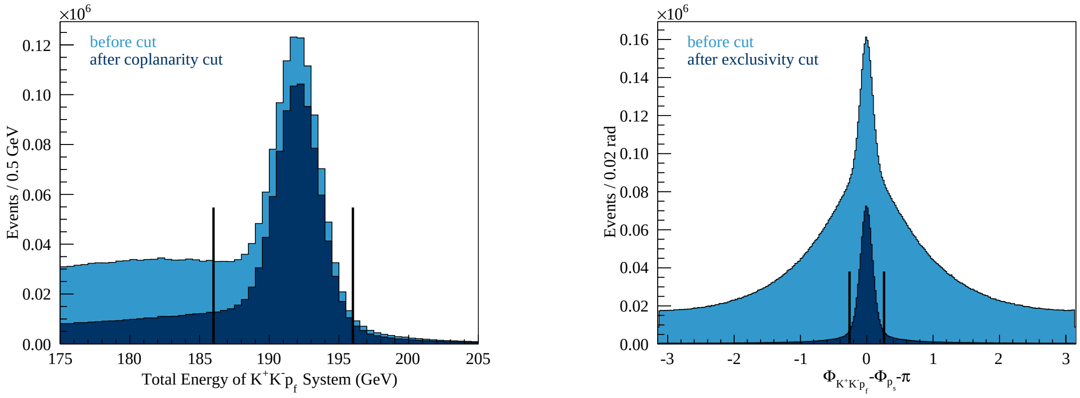

(a) Exclusivity

(b) Coplanarity

Figure 6.7: This figure shows the influence of the exclusivity (left) and coplanarity (right) cut for $pp \rightarrow p_{\text{recoil}}K^+K^-p_{\text{fast}}$. The light blue area corresponds to the distribution before both cuts, the dark blue area to the distribution after the other cut. The lines denote the cut on the value itself.

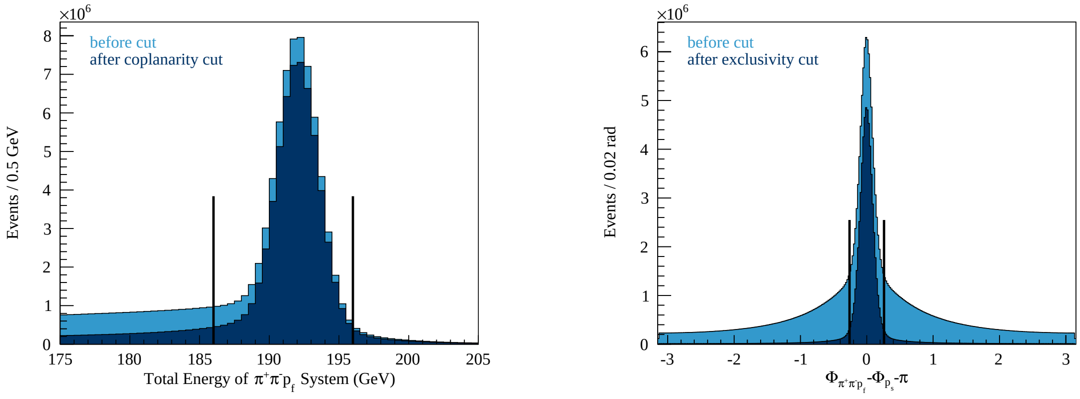

(a) Exclusivity

(b) Coplanarity

Figure 6.8: This figure shows the influence of the exclusivity (left) and coplanarity (right) cut for $pp \rightarrow p_{\text{recoil}}\pi^+\pi^-p_{\text{fast}}$. The light blue area corresponds to the distribution before both cuts, the dark blue area to the distribution after the other cut. The lines denote the cut on the value itself.

4. The energy of the outgoing $\pi^+\pi^-p$ (K^+K^-p) system has to be within ± 5 GeV around the peak value of 191 GeV. Additionally, the difference of the azimuthal angles between the three-particle final state and the recoiling proton has to be within ± 0.26 rad around the expected value of π. The cuts are demonstrated in figure 6.7 for the case of $pp \rightarrow p_{\text{recoil}}K^+K^-p_{\text{fast}}$. In this channel, the non-exclusive background is much larger compared to $pp \rightarrow p_{\text{recoil}}\pi^+\pi^-p_{\text{fast}}$, which is shown in figure 6.8 for comparison. However, the background contribution is reduced very well by the two cuts.

5. A cut on the momentum transfer $0.1\,(\mathrm{GeV}/c)^2 < t' < 1.0\,(\mathrm{GeV}/c)^2$ is performed.

The cut flow for the two final states $p_{\mathrm{recoil}}K^+K^-p_{\mathrm{fast}}$ and $p_{\mathrm{recoil}}\pi^+\pi^-p_{\mathrm{fast}}$ is shown in table 6.5.

<table>
<tr><th></th><th>$\pi^+\pi^-$</th><th>K^+K^-</th></tr>
<tr><td>after common selection</td><td colspan="2">3,967,769,836</td></tr>
<tr><td>1. 3 charged tracks</td><td colspan="2">463,920,924</td></tr>
<tr><td>2. $\sum Q = +1$</td><td colspan="2">413,080,610</td></tr>
<tr><td>3. RICH cut</td><td>228,904,119</td><td>13,043,511</td></tr>
<tr><td>4. exclusivity and coplanarity</td><td>58,219,871</td><td>900,671</td></tr>
<tr><td>5. t'</td><td>46,470,396</td><td>733,704</td></tr>
</table>

Table 6.5: Cut flow for final selection of events for $p_{\mathrm{recoil}}\pi^+\pi^-p_{\mathrm{fast}}$ and $p_{\mathrm{recoil}}K^+K^-p_{\mathrm{fast}}$

6.5.1 The reaction $pp \to p_{\mathrm{recoil}}\phi p_{\mathrm{fast}}$

In the K^+K^- mass spectrum shown in figure 6.9, the ϕ peak is clearly visible directly above the K^+K^- threshold. The peak is narrow (the ϕ meson has a width of $4.266(31)\,\mathrm{MeV}/c^2$) and asymmetric. Therefore, a relativistic Breit-Wigner [72], which includes the spin of the resonance and a mass dependent width, is used to fit the peak. To take the experimental resolution into account, this relativistic Breit-Wigner is convoluted with a Gaussian. For the background a functional form is chosen to describe the threshold behaviour and the following decrease, namely

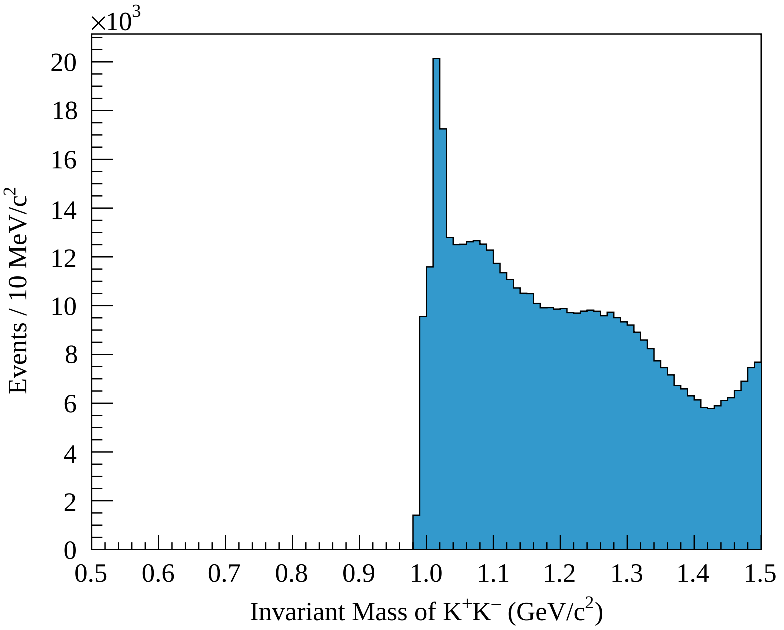

Figure 6.9: Invariant mass of K^+K^-. The ϕ peak is clearly visible above threshold.

$$bg(m_{KK}) = (m_{KK} - m_{\mathrm{thr}})^n \exp\left[-a(m_{KK} - m_{\mathrm{thr}})\right]. \tag{6.5}$$

An extended likelihood fit is performed to ensure that the number of signal and background events from the fit sum up to the total number of events. Figure 6.10 shows the invariant mass spectrum of K^+K^- in the ϕ region together with the full fit in red and the ϕ contribution in blue. The fit yields a total number of

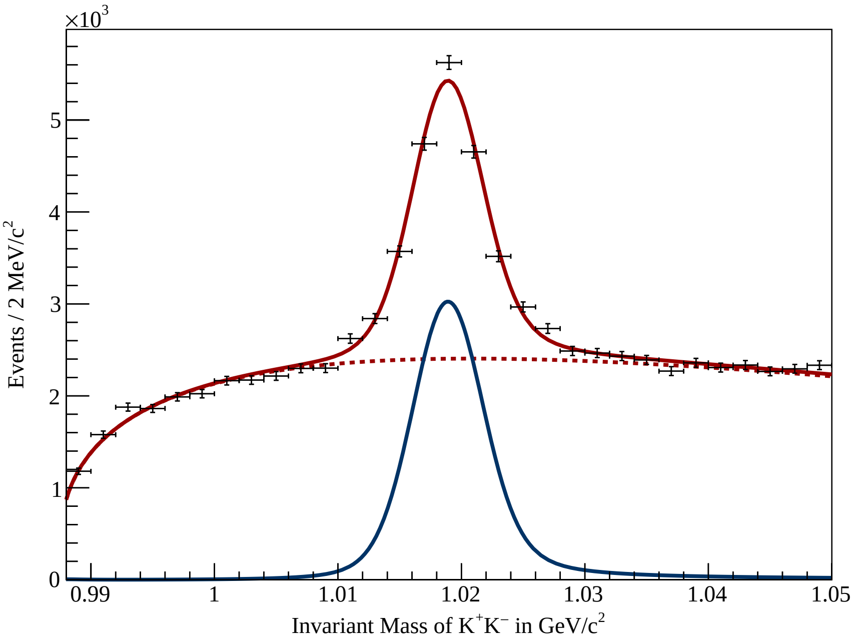

Figure 6.10: Fit of ϕ mass together with the background. The full fit is shown as a red line, the background as a dashed red line. The pure ϕ contribution is shown in blue.

$$N_\phi = 12228 \pm 303\,,$$

which corresponds to roughly 1.7% of all K^+K^- events.

6.6 EVENT SELECTION FOR $pp \rightarrow p_{\text{RECOIL}}\omega p_{\text{FAST}}$

In the presented analysis, the decay $\omega \rightarrow \pi^+\pi^-\pi^0$ is used. Thus, the event selection for this channel is a combination of both selections described in 6.4 and 6.5. The following cuts are performed after the preselection:

1. Events must contain three outgoing charged tracks with one RICH identified pion, where the conditions from 6.5 have to be fulfilled. In addition, two ECAL clusters as described in 6.4 are required.

2. The ECAL clusters must form a π^0 within 2σ for the single ECAL combinations.

3. Cuts on the beam energy, the coplanarity angle and the momentum transfer t' are performed in the same way as for the π^0/η selection.

The cut flow is given in table 6.6. The invariant mass of the $\pi^+\pi^-\pi^0$ system after these cuts is shown in figure 6.11. Besides the large ω peak also a small contribution from $\eta \rightarrow \pi^+\pi^-\pi^0$ is visible.

The number of ω mesons in this spectrum is determined by a fit. As the background is moderate, the peak is fitted together with a third degree polynomial background. For the peak itself a convolution of a Breit-Wigner function and a Gaussian is used. An extended likelihood fit is performed to ensure that the number of signal and background events from the fit sum up to the total number of events. In figure 6.12 the data is shown together with

	$\pi^+\pi^-\pi^0$
1. tracks and ECAL clusters	38,764,390
2. identified π^0	10,354,227
3. exclusivity, coplanarity, t'	4,455,400

Table 6.6: Cut flow for final selection of events for $pp \to p_f \pi^+\pi^-\pi^0 p_s$

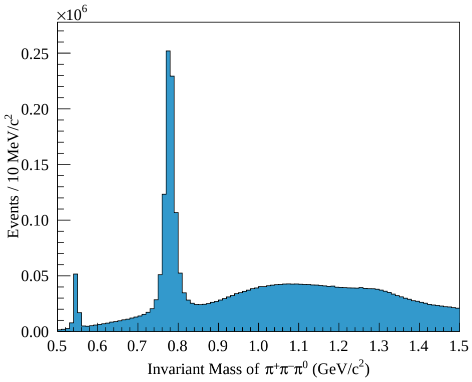

Figure 6.11: Mass of the $\pi^+\pi^-\pi^0$ system after all cuts. The large peak stems from ω decays, whereas the smaller peak is due to $\eta \to \pi^+\pi^-\pi^0$.

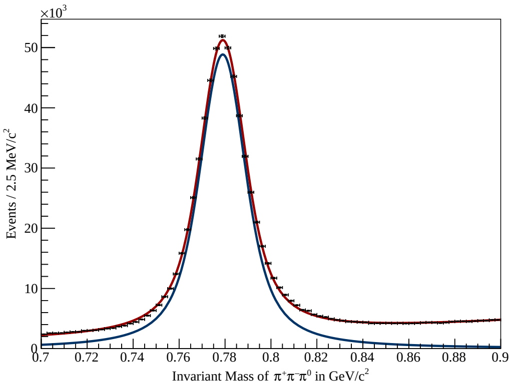

Figure 6.12: Fit of ω mass together with a polynomial background.

the fit where the peak is shown in blue and the full fit is shown in red. The number of ω events obtained from the fit is

$$N_\omega = 613479 \pm 1607\,,$$

which corresponds to roughly 14% of all $\pi^+\pi^-\pi^0$ events.

7

DETERMINATION OF EXPERIMENTAL ACCEPTANCE

A proper knowledge of the experimental acceptance (which is composed of geometric acceptance as well as detector efficiencies) is crucial for the correct determination of physical quantities such as cross sections. A Monte-Carlo simulation is used to obtain the acceptance. The simulated events are processed and reconstructed in the same way as the real data events. The comparison of reconstructed events and the generated events allows to determine the loss of events as a function of kinematic variables. Only reactions with a single meson in the final state, namely

$$
\begin{aligned}
pp &\rightarrow p_{\text{recoil}}\pi^0 p_{\text{fast}}\\
pp &\rightarrow p_{\text{recoil}}\eta p_{\text{fast}}\\
pp &\rightarrow p_{\text{recoil}}\omega p_{\text{fast}}\\
pp &\rightarrow p_{\text{recoil}}\phi p_{\text{fast}}
\end{aligned}
$$

are considered. These two-particle final states can be described by three independent kinematic variables and therefore, a three-dimensional acceptance correction in these variables is performed. For this analysis, the choice of variables corresponds to the variables, which will be used for the partial wave analysis in part III. These variables are

- the invariant mass of the proton-meson system M_{pM} and
- the angles $\cos(\theta)$ and φ of the meson in the Gottfried-Jackson frame, which is defined as shown in figure 7.1.

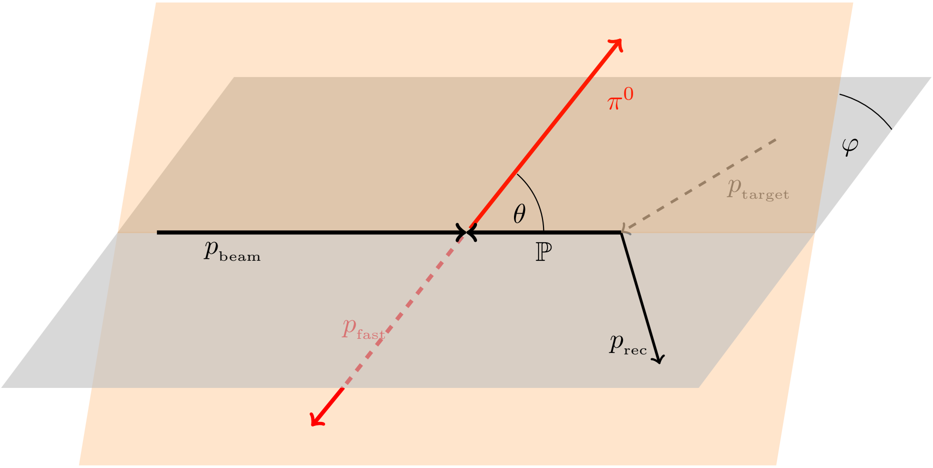

Figure 7.1: The Gottfried-Jackson frame is defined as the rest frame of the resonance X, where the z-axis points in the direction of the beam, the x-axis is the original direction of the resonance and $y = z \times x$. Then, the angle θ is the angle between the beam direction and one of the outgoing particles (in this case the meson) and the angle φ is the angle between the production plane (beam + recoiling proton, grey) and decay plane (beam + outgoing particles, red).

7.1 THE MONTE-CARLO SET-UP

The acceptance calculation with a Monte-Carlo simulation is done in three steps:

1. Monte-Carlo events are generated.
2. The generated events are processed through a detector simulation and the same event reconstruction as real data events.
3. The acceptance is calculated by comparing the reconstructed Monte-Carlo events with the information from the Monte-Carlo generator.

These three steps are described in the following.

7.1.1 Generator

Monte-Carlo events are generated using the genpw generator from the rootpwa package [73]. The generator produces events that are "flat in phase space" which simply means, that no resonant processes etc. are taken into account. The only inputs for the generator, which simulates the diffractive production of mesons, are the measured slope of the momentum transfer t' from the target proton to the beam proton and information on the beam profile, which is taken from real data events. The generated events contain four-vectors of the initial and final state particles as well as an interaction vertex in the target region. The distributions (for $pp \to pp\pi^0$) of generated events in the three variables are shown in figure 7.2.

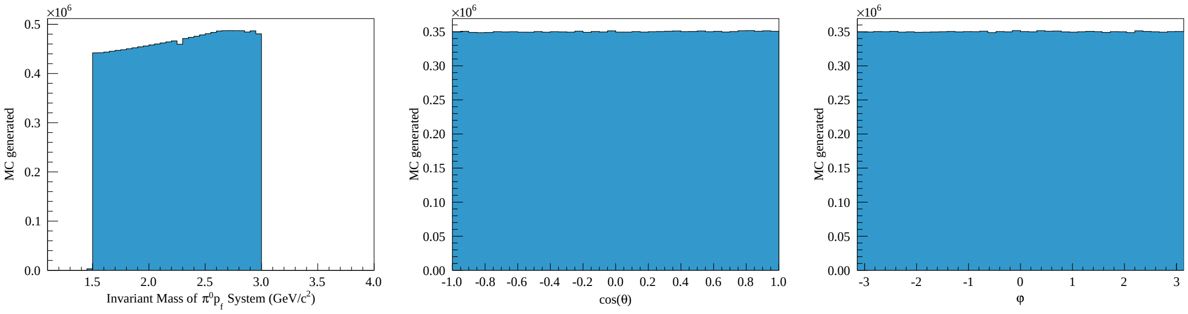

Figure 7.2: Kinematic distributions of generated Monte-Carlo events for $M_{p\pi^0}$, $\cos(\theta)$ and φ (from left to right).

7.1.2 Detector Simulation and Event Reconstruction

The generated events are directly used in the detector simulation done by COMGEANT which is based on GEANT3 [74]. The full material description and active detector volumes are included in the description. In COMGEANT particles from the generator are traversed through the detector material, where the interaction of the particles with the material are simulated. This includes positron annihilation, bremsstrahlung, Compton scattering, decay in flight, delta-electron production, hadron interactions, energy loss, multiple scattering, muon-nucleus interactions, pair production and photoelectric effect. Some details can be found in [75]. Hits and deposed energy in the single detectors are stored to be used in the event reconstruction. The event reconstruction itself is done with CORAL (compare section 6.2). Here, the same CORAL version, that was used in the reconstruction of the real data events, has to be used to ensure a consistent handling of the detector information in real data and Monte-Carlo.

7.1.3 Calculation of Acceptance

The calculation of the acceptance is done in PHAST. The same cuts as for the data (see chapter 6) are performed on reconstructed Monte-Carlo events. The acceptance and its error is then calculated with the help of the ROOT TEfficiency class [76], which calculates the acceptance from the generated Monte-Carlo events and the information whether they passed all cuts or not. The result is a three-dimensional acceptance matrix (in M_{pM}, $\cos(\theta)$ and φ) which contains the fractions of the generated events (= acceptance) that passed the full reconstruction and analysis. For the error a 95% confidence Clopper-Pearson [77] interval, which is based on binomial statistics, is used. The acceptance correction of kinematic distributions is then done on an event by event basis. For each event, the corresponding acceptance is taken from the three-dimensional matrix and the event is weighted with 1/acceptance.

7.1.4 Available Monte-Carlo Statistics

In table 7.1 the available Monte-Carlo statistics N_{MC} for the individual reactions together with the number of accepted events N_{acc} and the available data statistics N_{data} are shown.

channel	N_{MC}	N_{acc}	N_{data}
$pp \to pp\pi^0$	17,493,052	2,229,354	8,835,835
$pp \to pp\eta$	14,005,248	2,144,556	442,241
$pp \to pp\omega$	13,884,149	1,124,837	613,479
$pp \to pp\phi$	15,160,323	2,224,502	12,228

Table 7.1: Available statistics of generated Monte-Carlo events (N_{MC}), reconstructed Monte-Carlo events (N_{acc}) and data events (N_{data}) for different channels.

For a sufficiently smooth calculation of the acceptance the number of accepted events should at least be as large as the number of data events. Then, the error on the acceptance is in the same order as the statistical error on the data. Especially for the π^0 channel, more Monte-Carlo statistics would be desirable but is presently not available.

7.2 ACCEPTANCE FOR PION PRODUCTION

In figure 7.3, the one-dimensional projections of the three-dimensional acceptance matrix for $pp \to pp\pi^0$ are shown as a function of the three variables $M_{p\pi^0}$, $\cos(\theta)$ and φ. The acceptance in the invariant mass is flat, the acceptance in $\cos(\theta)$ shows a dip around 0.7 which can be attributed to photons absorbed in the RICH beam pipe. The sinusoidal variation of the acceptance in φ is most likely connected to the rectangular shape of the geometric acceptance of the single detectors. To prove this assumption, further studies are needed in the future.

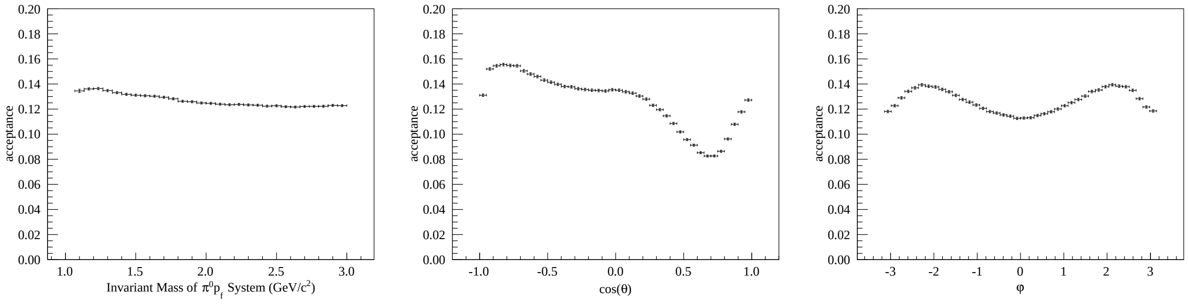

Figure 7.3: One-dimensional projections of the acceptance for $M_{p\pi^0}$, $\cos(\theta)$ and φ (from left to right) for $pp \to pp\pi^0$.

7.3 ACCEPTANCE FOR ETA PRODUCTION

The following figures show the same distributions for $pp \to pp\eta$ which were shown in the pion case before. For η production the acceptance in the invariant mass is also flat. The effect of the RICH pipe is smaller due to larger angles of the decay photons in $\eta \to \gamma\gamma$ compared to $\pi^0 \to \gamma\gamma$.

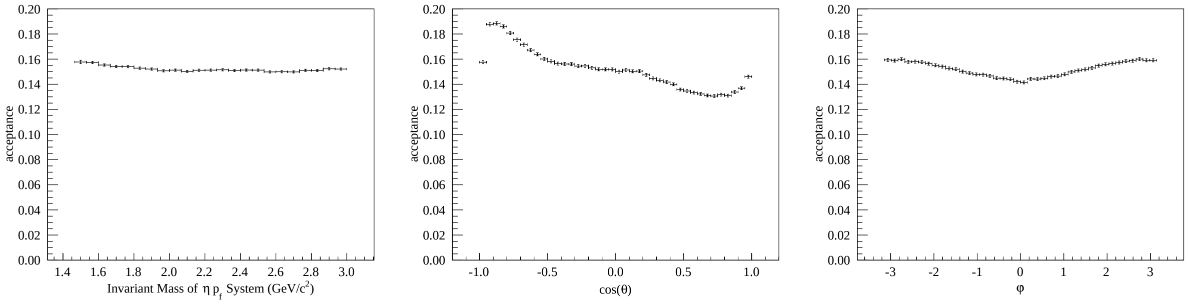

Figure 7.4: One-dimensional projections of the acceptance for $M_{p\eta}$, $\cos(\theta)$ and φ (from left to right) for $pp \to pp\eta$.

7.4 ACCEPTANCE FOR PHI PRODUCTION

The one-dimensional projections of the acceptance for ϕ production in the same variables as before is shown in figure 7.5. The acceptance in the invariant mass and in the azimuthal angle φ looks similar as for π^0 and η production. In contrast, the acceptance in the polar angle drops to zero for $\cos(\theta) \gtrsim 0.4$. This behaviour can be attributed to the momentum cut on the K^+, which is needed for the kaon identification in the RICH detector (see section 6.3.3). Previous analyses showed, that this affects also the acceptance as a function of Feynman x_F of the fast proton [48]. In the following, a cut of $0.5 < x_F(p) < 0.9$ will be applied on the $pp \to pp\phi$ data to account for the effects of the RICH momentum cut.

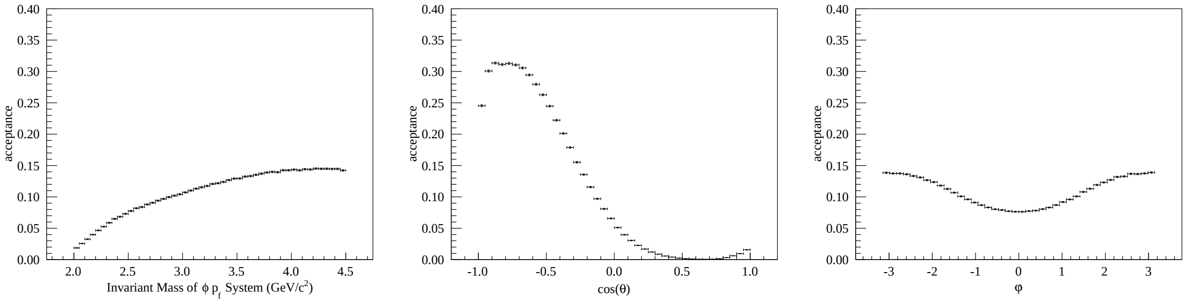

Figure 7.5: One-dimensional projections of the acceptance for $M_{p\phi}$, $\cos(\theta)$ and φ (from left to right) for $pp \rightarrow pp\phi$.

7.5 ACCEPTANCE FOR OMEGA PRODUCTION

In figure 7.6 the one-dimensional projections of the acceptance for $pp \rightarrow pp\omega$ are shown in the three variables. Also here, the acceptance drops for large $\cos(\theta)$, but this is mainly due to the ECAL acceptance as in the $pp \rightarrow pp\pi^0$ case and not an effect induced by the RICH. However, in order to compare ω and ϕ production, the same cut on x_F of the fast proton is applied on the ω data.

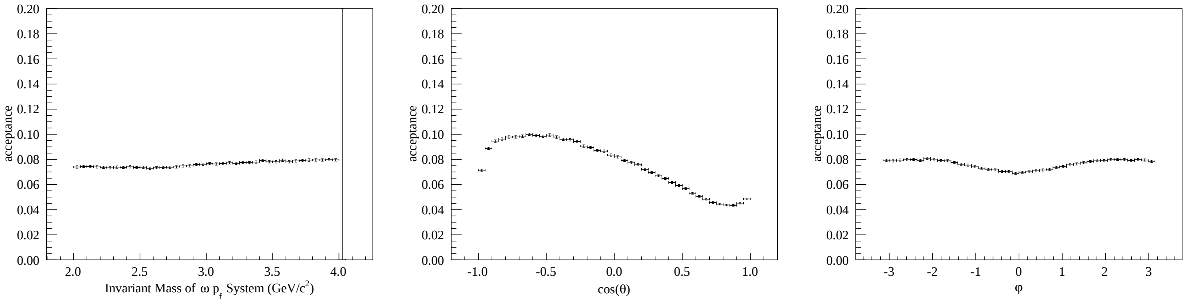

Figure 7.6: One-dimensional projections of the acceptance for $M_{p\phi}$, $\cos(\theta)$ and φ (from left to right) for $pp \rightarrow pp\omega$.

8

KINEMATIC DISTRIBUTIONS

In this chapter kinematic distributions, namely invariant masses and angular distributions, for the different channels will be shown and possible contributions from different reaction mechanisms and resonances will be discussed. In addition, the effects of the acceptance correction will be examined. The investigated channels are $pp \to pp\pi^0$, $pp \to pp\eta$, $pp \to ppK^+K^-$ (which includes $\phi \to K^+K^-$) and $pp \to pp\pi^+\pi^-\pi^0$ (which includes $\omega \to \pi^+\pi^-\pi^0$). The reaction $pp \to pp\pi^+\pi^-$ is additionally discussed in appendix C.

8.1 PION PRODUCTION

8.1.1 Invariant Mass of $p\pi^0$

In the left panel of figure 8.1 the invariant mass of the outgoing $p\pi^0$ system is shown with acceptance correction applied. The distribution shows some eye-catching features:

- There are two peaks at roughly 1500 MeV/c^2 and a bit below 1700 MeV/c^2. Candidate resonances for the first peak are the $N(1520)3/2^-$ and the $N(1535)1/2^-$ as well as the Roper resonance $N(1440)1/2^+$. For the second peak there are at least two candidates, namely the $N(1675)5/2^-$ and $N(1680)5/2^+$, but there are further resonances close to this mass region. A compilation of known resonances will be given in chapter 10.
- Beyond the second peak the mass spectrum drops exponentially without any clear further resonance contributions. This can be explained by the weak coupling of the higher resonances into the $N\pi$ channel [78]. The exponential decrease of non-resonant processes is predicted by theory and will be discussed in chapter 13.

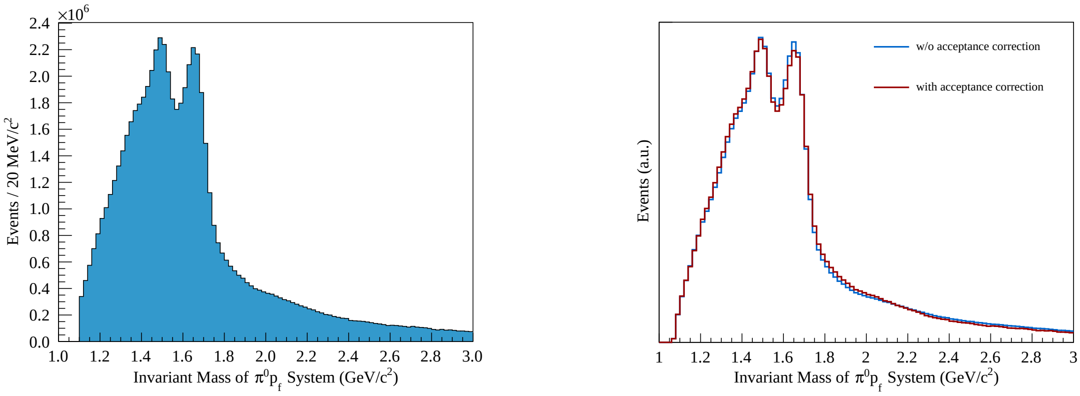

Figure 8.1: Invariant Mass of $p\pi^0$. The left plot shows the acceptance corrected distribution, the right plot shows a comparison of uncorrected and corrected data normalised to each other.

Another observation is the absence of the $\Delta(1232)$. This shows the dominance of diffractive dissociation (see section 1.3.3) in the reaction: The exchanged Pomeron does not transfer any isospin between the target and beam protons. As the recoiling proton is detected, the final state must have isospin $I = \frac{1}{2}$. Without transfer of isospin, only N^* resonances (and non-resonant background) are expected in the final state. This simplifies the analysis procedure.

The influence of the acceptance correction can be seen in the right panel of figure 8.1, where the distributions with and without acceptance correction applied are shown normalised to each other. The influence of the acceptance correction is small, the only visible effect is a slight change in the ratio of the two peak heights as well as a small change in the exponential drop, which is less steep with applied acceptance correction.
In chapter 13 the background contributions will be investigated in comparison with theory, in chapters 12 and 14 the possibility to disentangle resonant contributions with a partial wave analysis will be discussed.

8.1.2 Angular Distributions

The angular distributions are given in the Gottfried-Jackson frame as defined in figure 7.1. The angle θ is defined as the angle between the outgoing π^0 and the beam direction, and φ is the angle between the production plane (containing the beam and the recoiling proton) and the decay plane (containing the beam and the outgoing π^0) in the $p\pi^0$ rest frame.

The φ distribution, which is shown in the left panel of figure 8.2 is symmetric around $\varphi = 0$, which is expected if there is no dominant phase correlation in the final state. The influence of the acceptance correction can be seen in the right panel of figure 8.2. The distribution is a bit narrower around $\varphi = 0$ and gets enhanced around $\varphi = \pi$.

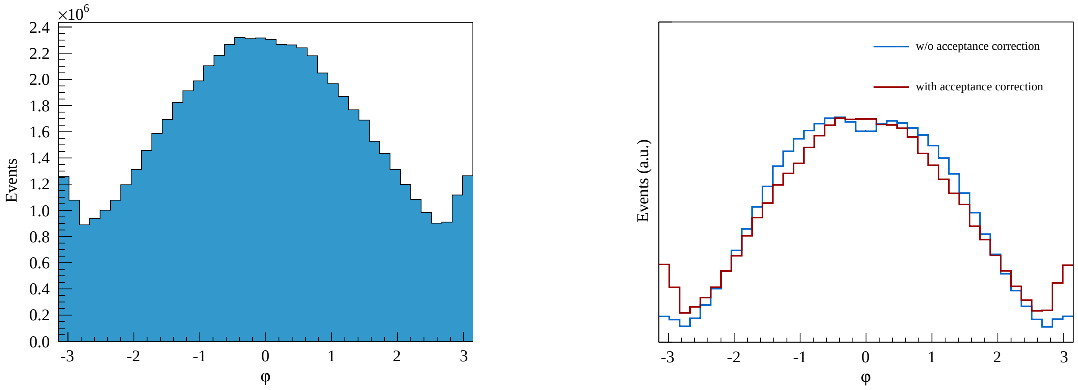

Figure 8.2: Gottfried-Jackson angle φ for $p\pi^0$. The left plot shows the distribution with applied acceptance correction, the right plot shows the comparison of corrected and uncorrected data normalised to each other.

The $\cos(\theta)$ distribution in the left panel of figure 8.3 shows a clear backward peak ($\cos(\theta) \approx -1$). This is a clear hint for pions which are not produced in resonance decays but in exchange processes, which will be discussed in chapter 13. Due to acceptance correction the height of the peak is reduced[1]. This can be seen in the right panel of figure 8.3. The contribution of the backward peak changes with the invariant mass; this can be seen in figure 8.4, where $\cos(\theta)$ is plotted against the invariant mass with a linear scale (left panel) and a logarithmic scale (right panel). While in the region with the two peaks significant contributions are observed for $\cos(\theta) \approx 1$, the backward peak dominates the distribution for masses above 1800 MeV/c^2. This behaviour is better visible in the plot with a logarithmic scale: Some structure in $\cos(\theta)$ is observed in the peak region, but is no longer visible in the higher mass region, which is dominated by the backward peak.

---

[1] Actually the distribution is enhanced for positive values of $\cos(\theta)$ due to the smaller acceptance there (compare middle panel of figure 7.3). This leads to a smaller peak compared to the rest of the distribution.

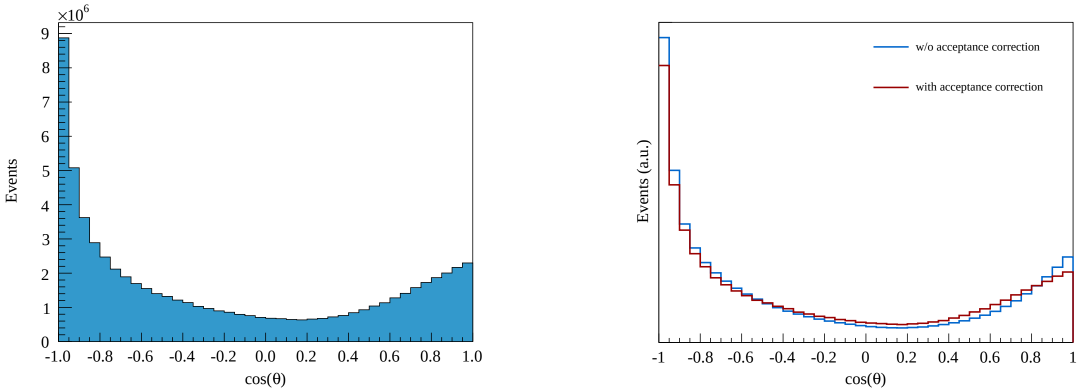

Figure 8.3: Gottfried-Jackson angle cos(θ) for $p\pi^0$. The left plot shows the distribution with applied acceptance correction, the right plot shows the comparison of corrected and uncorrected data normalised to each other.

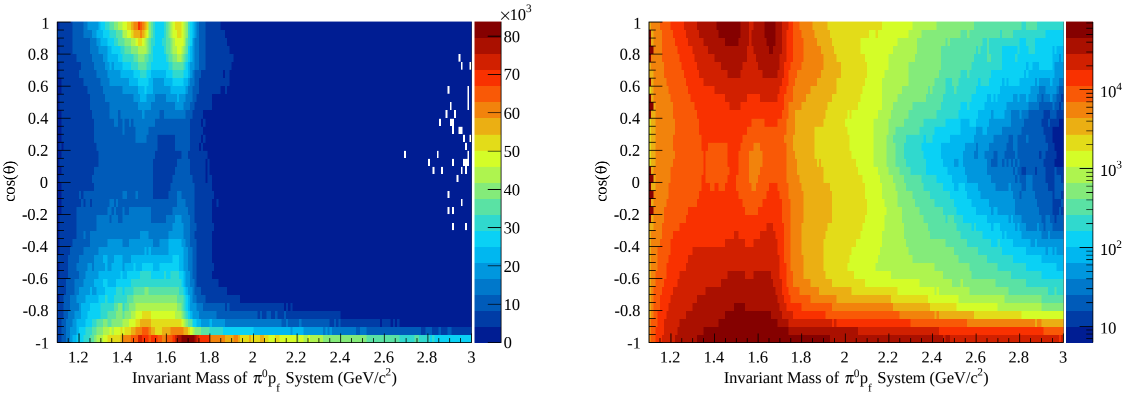

(a) linear scale

(b) logarithmic scale

Figure 8.4: Gottfried-Jackson angle cos(θ) for $p\pi^0$ plotted against the invariant mass $M_{p\pi^0}$ with acceptance correction applied.

8.2 ETA PRODUCTION

8.2.1 Invariant Mass of $p\eta$

The invariant mass spectrum of $p\eta$ is shown in the left panel of figure 8.5. It also shows an exponential decrease for higher masses, which is less steep than in the case of $p\pi^0$. In this spectrum there are some weak structures around 1700 MeV/c^2 and 1900 MeV/c^2, which might be due to resonances. The structure directly at threshold could originate from the decay of N(1535)1/2^-, which has a large branching ratio (42 ± 10%) into $p\eta$ and is located directly above the $p\eta$ threshold (1485.8 MeV/c^2). The acceptance correction enhances the structures; this can be seen in the right panel of figure 8.5.

8.2.2 Angular Distributions

In figure 8.6 cos(θ) is shown as a function of the invariant mass of $p\eta$ with a linear scale (left panel) and a logarithmic scale (right panel). Similar to the $p\pi^0$ case, the region above the possibly resonant structures is dominated by a backward peak. In the $p\eta$ case, the backward

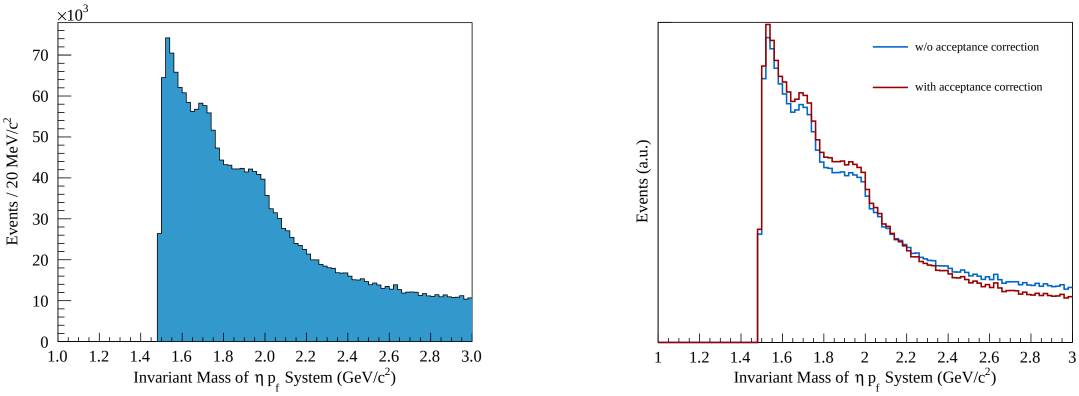

Figure 8.5: Invariant Mass of $p\eta$. The left plot shows the distribution with applied acceptance correction, the right plot shows the comparison of corrected and uncorrected data normalised to each other.

peak is broader compared with $p\pi^0$. The $\cos(\theta)$ and φ distributions for this channel are shown and discussed in appendix C.

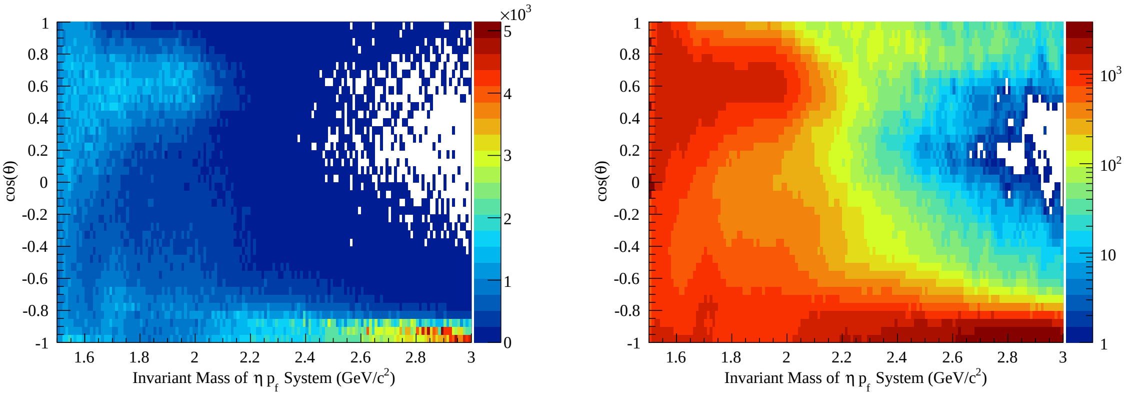

(a) linear scale

(b) logarithmic scale

Figure 8.6: Gottfried-Jackson angle $\cos(\theta)$ for $p\eta$ plotted against the invariant mass $M_{p\eta}$ with acceptance correction applied.

8.3 KAON PAIR PRODUCTION

For the channel $\bar{p}p \rightarrow \bar{p}pK^+K^-$, Monte-Carlo data is only available for the sub-channel, where the two kaons stem from the decay of a ϕ meson. Therefore, no acceptance correction is applied to the distributions which are shown in the following. The production of ϕ mesons will be investigated in chapter 9.3.

In figure 8.7 the invariant mass spectra of pK^+K^- and the three possible sub-systems are shown. In the three-particle invariant mass (top left) there are no visible structures. This is in agreement with the PDG listings, where no baryons are known which decay into pK^+K^- (or $p\phi$). In the K^+K^- spectrum (top right) the most striking contribution stems from the decay $\phi \rightarrow K^+K^-$, which produces a narrow peak just above the two-kaon threshold. The prominent peak around 1500 MeV/c^2 could come from $f'_2(1525)$ decays, which have a branching fraction of nearly 90% into K^+K^-. The pK^- spectrum (bottom left) exhibits a large $\Lambda(1520)$ contribution, which could serve as a starting point for future analyses of the interesting chan-

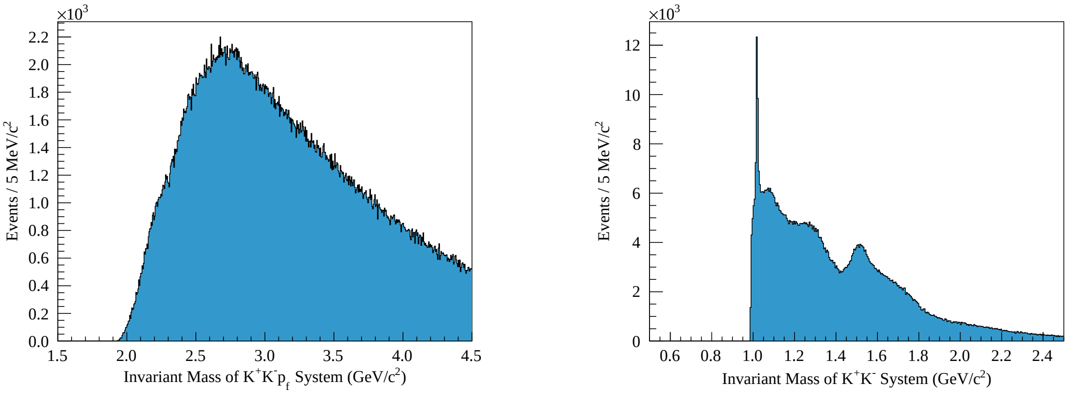

(a) pK^+K^- (b) K^+K^-

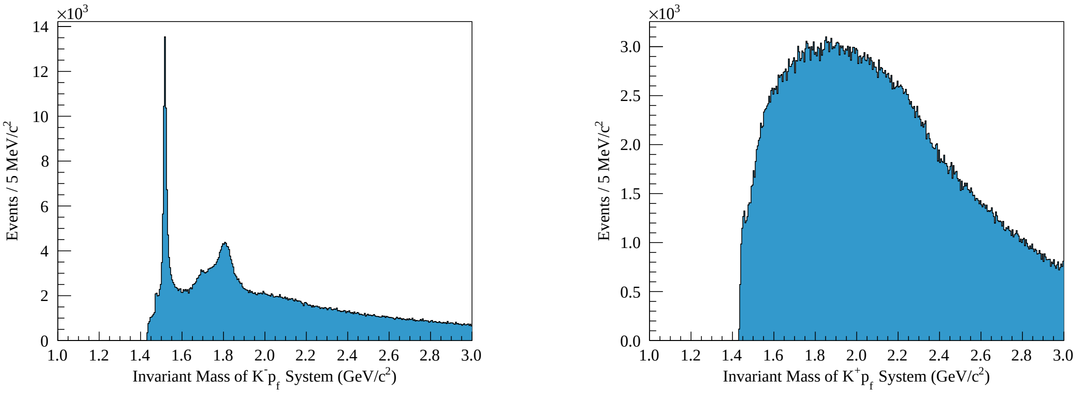

(c) pK^- (d) pK^+

Figure 8.7: Invariant mass spectra of pK^+K^- and the different two-particle sub-systems for $pp \rightarrow ppK^+K^-$.

nel $pp \rightarrow pK^+\Lambda$. The second peak in this spectrum is probably some mixture of $\Lambda(1800)$, $\Lambda(1810)$, $\Lambda(1820)$ and $\Lambda(1830)$. Finally, no resonant structures are observed in pK^+ (bottom right). Those would result from strange baryons with a charge of +2, which do not exist in the quark model and are thus not expected. Any structure in the pK^+ invariant mass distribution would be a hint for exotic states.

8.4 THREE-PION PRODUCTION

The channel $pp \to pp\pi^+\pi^-\pi^0$ has a four-particle final state and is thus complicated to handle. Similar to the kaon pair production, Monte-Carlo data is only available for the $pp \to pp\omega$ sub-channel and thus, no acceptance corrections are applied to the spectra shown in this section.

The three-body $\pi^+\pi^-\pi^0$ invariant mass spectrum, which is given in figure 8.8, shows a large contribution of $\omega(782)$. In addition, there are some $\eta \to \pi^+\pi^-\pi^0$ events, which could be used to enhance the statistics of the $\eta \to \gamma\gamma$ final state. However, the gain in statistics is not high enough to justify the additional work in the framework of this thesis. In figure 8.9 the invariant mass of $p\pi^+\pi^-\pi^0$ is shown without any cuts on the three-body mass. The bump around 1700 MeV/c^2 possibly stems from the known decay of N(1710) into $p\omega$ (BR= $(8 \pm 5)\%$) and $p\eta$ (BR= $10 - 30\%$).

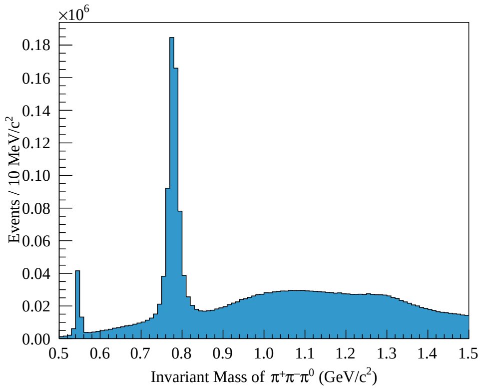

Figure 8.8: Invariant mass of $\pi^+\pi^-\pi^0$.

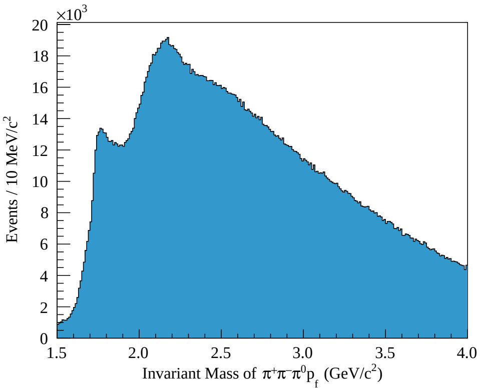

Figure 8.9: Invariant mass of $p\pi^+\pi^-\pi^0$.

9

RESULTS FOR SINGLE MESON PRODUCTION

In this chapter, the production cross sections for pseudoscalar mesons (π^0, η) and vector mesons (ω, ϕ) will be compared. For the case of pseudoscalar mesons, this comparison was done in several experiments, but in a very limited kinematic range. The production of vector mesons has been investigated before at COMPASS in view of a study of the OZI rule [79].

9.1 CALCULATION OF CROSS SECTION RATIOS

For the calculation of cross section ratios, the acceptance corrected data sets described in the previous chapters are used. The different reactions are extracted from the same measurement and thus, the luminosity drops out and the cross section ratio is simply given as the ratio of the (acceptance corrected) number of events, e. g.

$$\frac{\sigma(pp \to pp\eta)}{\sigma(pp \to pp\pi^0)} = \frac{N(pp \to pp\eta)}{N(pp \to pp\pi^0)} \,. \tag{9.1}$$

As only one decay channel of the meson is used in the analysis, the event numbers have to be corrected by the according branching fraction, i. e.

$$\frac{\sigma(pp \to pp\eta)}{\sigma(pp \to pp\pi^0)} = \frac{N(pp \to pp\eta \to pp\gamma\gamma)/BR(\eta \to \gamma\gamma)}{N(pp \to pp\pi^0 \to pp\gamma\gamma)/BR(\pi^0 \to \gamma\gamma)} \,. \tag{9.2}$$

The branching ratios for the decays used in this analysis are given as [1]

$$\begin{aligned} \pi^0 &\to \gamma\gamma & BR &= 98.823(34)\% \\ \eta &\to \gamma\gamma & BR &= 39.41(20)\% \\ \omega &\to \pi^+\pi^-\pi^0 & BR &= 89.2(7)\% \\ \phi &\to K^+K^- & BR &= 48.9(5)\% \,. \end{aligned}$$

In the case of ω and ϕ production, the number of events is taken from the fit, that was introduced in 6.6 and 6.5.1, respectively. The cross section ratios will be calculated in bins of the Feynman scaling variable x_F [80] of the meson M. It measures the longitudinal momentum fraction of a particle in the centre-of-mass-frame and can be approximately calculated as

$$x_F = \frac{2p_L(M)}{\sqrt{s}} \approx \left(\frac{p_z(M)}{p_z(\text{beam})}\right)_{\text{CMS}} \,, \tag{9.3}$$

where the momenta have to be calculated in the pp centre-of-mass frame (CMS). The variable x_F can take values between -1 and 1, where negative values of the meson x_F are outside of the acceptance of the COMPASS spectrometer. It can – to some extend – be used to characterize the reaction: Mesons produced with small x_F are less likely produced in a decay of a pM bound state, but more likely in a meson exchange process. In the case of π^0 and η, which are available in the full x_F range, a comparison is performed not only in bins of x_F but also in bins of t', which was defined in equation (6.3). Additionally, due to the large statistics of the data set, a two-dimensional binning in x_F and t' is possible.

9.2 RESULTS FOR PSEUDOSCALAR MESONS

In the following, the results for the cross section ratio $\frac{\sigma(pp\to pp\eta)}{\sigma(pp\to pp\pi^0)}$ will be shown in bins of x_F, in bins of t' and in a two-dimensional x_F-t' binning.

9.2.1 Cross Section Ratio as a Function of x_F

In figure 9.1, the cross section ratio of η and π^0 production is shown as a function of x_F. the corresponding values are given in the table within the figure. The ratio varies roughly between 6.5% and 12.5% with a dip around $x_F = 0.2$. This dip is correlated with the different shapes of the x_F distributions, which are shown in figure 9.2. The bump on the falling x_F distributions can be mainly attributed to resonance production, which is enhanced for pion production. The dotted line in figure 9.1 denotes the average cross section ratio over the full data set of

$$\frac{\sigma(pp \to pp\eta)}{\sigma(pp \to pp\pi^0)} = 9.245 \pm 0.004\% \tag{9.4}$$

The statistical uncertainties ($\sqrt{N}$ Poisson errors) are small due to the large available data set. As discussed in 9.4, the systematic uncertainties cancel to a large part in the ratios as the observed final state is identical for both π^0 and η.

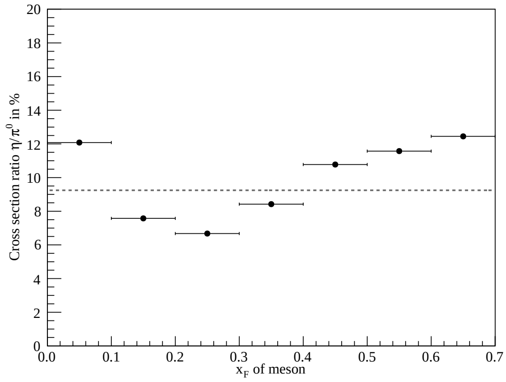

x_F	Cross section ratio absolute	Cross section ratio in %
0.0 – 0.1	1722676/14259389	12.08 ± 0.02
0.1 – 0.2	1031969/13621049	7.58 ± 0.01
0.2 – 0.3	1015047/15206953	6.68 ± 0.01
0.3 – 0.4	1117607/13269721	8.42 ± 0.01
0.4 – 0.5	1009381/9367214	10.78 ± 0.02
0.5 – 0.6	596959/5158200	11.57 ± 0.02
0.6 – 0.7	231332/1858381	12.45 ± 0.04

Figure 9.1: Cross section ratio η/π^0 as a function of x_F. The statistical uncertainties are smaller than the size of the symbols. The dotted line denotes the average ratio over the full x_F range.

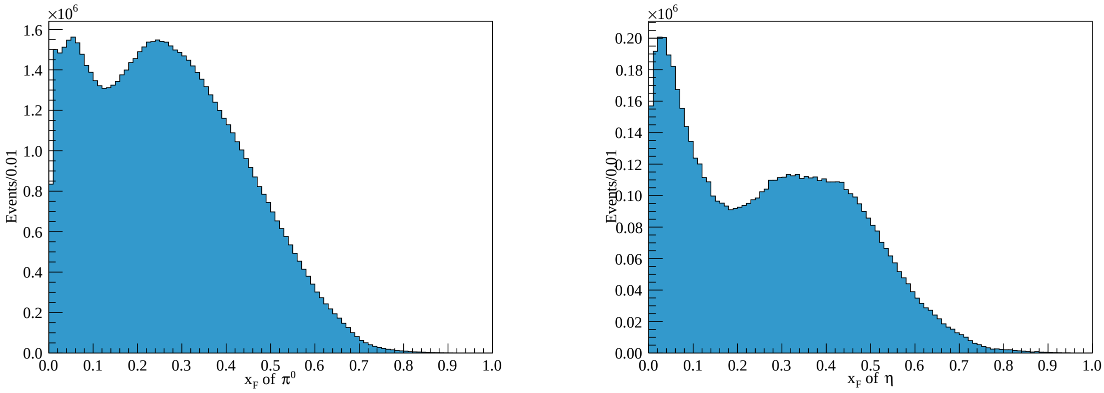

Figure 9.2: The Feynman x_F distributions of π^0 (left) and η (right) produced in $pp \to p(\pi^0/\eta)p$.

The cross section ratio of η and π^0 production was already measured in several experiments in different regions of x_F:
The WA102 experiment measured the cross section ratio in 450 MeV/c pp reactions on a fixed target. They report a cross section ratio of

$$\sigma(\pi^0) : \sigma(\eta) = 1 : 0.073 \pm 0.005 \tag{9.5}$$

for $0.0 \leqslant x_F \leqslant 0.1$ [81]. This result is in tension to the result of this analysis of

$$\sigma(\pi^0) : \sigma(\eta) = 1 : 0.1208 \pm 0.0002 \tag{9.6}$$

in the same x_F range. However, the cuts used in the WA102 analysis are not given in detail in [81]. The x_F distributions of π^0 and η given in their paper fall off quite steeply. The bump, which is observed in figure 9.2, is missing and no data is available for $x_F > 0.4$. The only cut, which is given in [81], is a cut on the invariant proton-π^0 mass of $M(p\pi^0) > 2.0\,\text{GeV}/c^2$ "to remove proton excitations". Applying this cut in my analysis yields an even larger cross section ratio of $1 : 0.2016 \pm 0.0002$. Thus, there seem to be additional cuts in the WA102 analysis.
The NA12/2 experiment [82] measured the same cross section ratios at 300 GeV/c fixed-target $\pi^- N$ reactions. They report a value of

$$\sigma(\pi^0) : \sigma(\eta) = 1 : 0.083 \pm 0.014 \tag{9.7}$$

for $0.05 \leqslant x_F \leqslant 0.20$. For the same range, I obtain a result of

$$\sigma(\pi^0) : \sigma(\eta) = 1 : 0.0866 \pm 0.0002\,, \tag{9.8}$$

which is in reasonable agreement (2.6σ) with the published result.
The Axial Field Spectrometer collaboration [83] measured cross section ratios at $\sqrt{s} = 53\,\text{GeV}$ pp and $p\overline{p}$ collisions for large transverse momenta $2\,\text{GeV}/c \leqslant p_T \leqslant 6\,\text{GeV}/c$ of the meson. In this totally different kinematic regime a value of

$$\sigma(\pi^0) : \sigma(\eta) = 1 : 0.55 \pm 0.04 \tag{9.9}$$

is reported but cannot be compared to the COMPASS result.

9.2.2 Cross Section Ratio as a Function of t'

The cross section ratio $\frac{\sigma(pp\to pp\eta)}{\sigma(pp\to pp\pi^0)}$ is now calculated in nine bins of t' between $0.1\,(\text{GeV}/c)^2$ and $1.0\,(\text{GeV}/c)^2$. The results is shown in figure 9.3, the corresponding values are given in the table in the figure. The dotted line denotes the value for the full data set of $9.245 \pm 0.004\%$. This value is dominated by the first bin, which has the largest statistics (the t' distribution falls exponentially, compare figure 6.6), and thus, most of the data points are above the average value. The cross section ratio rises slowly from $\approx 8\%$ to $\approx 14\%$ over the investigated range. A possible explanation of this behaviour is the enhanced production of the heavier η meson when more energy is transferred from the target to the final state.
Finally, a two-dimensional comparison in x_F and t' is possible. Figure 9.4 shows the cross section ratio $\frac{\sigma(pp\to pp\eta)}{\sigma(pp\to pp\pi^0)}$ as a function of x_F in bins of t'. The t' bins are denoted by different colours, the single distributions come with an offset c_i, which is given in the figure. The dip in the cross section ratio as a function of x_F which can be seen in figure 9.1 is even more pronounced in the region above $t' = 0.3\,(\text{GeV}/c)^2$.
In figure 9.5, the cross section ratio $\frac{\sigma(pp\to pp\eta)}{\sigma(pp\to pp\pi^0)}$ is shown as a function of t' in bins of x_F. The rise of the cross section ratio as a function of t' can be observed in all x_F bins, but is weaker

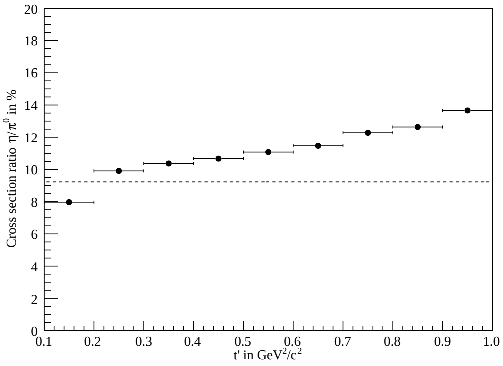

t' in $(\mathrm{GeV}/c)^2$	Cross section ratio in %
$0.1 - 0.2$	7.98 ± 0.01
$0.2 - 0.3$	9.91 ± 0.01
$0.3 - 0.4$	10.37 ± 0.01
$0.4 - 0.5$	10.67 ± 0.01
$0.5 - 0.6$	11.08 ± 0.02
$0.6 - 0.7$	11.47 ± 0.02
$0.7 - 0.8$	12.28 ± 0.03
$0.8 - 0.9$	12.63 ± 0.04
$0.9 - 1.0$	13.66 ± 0.05

Figure 9.3: Cross section ratio η/π^0 as a function of t'. The error bars are not visible due to the large statistics. The dotted line denotes the average ratio over the full t' range.

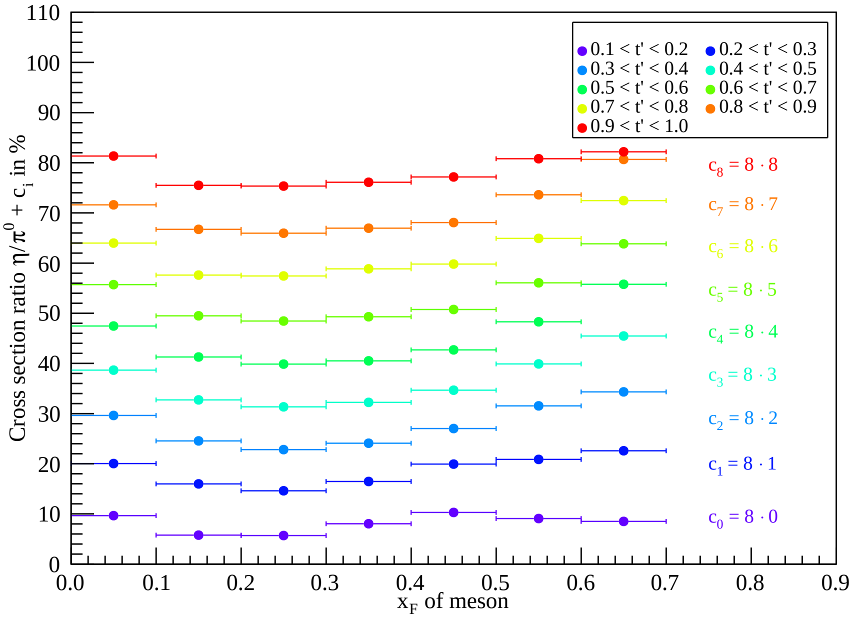

Figure 9.4: Cross section ratio η/π^0 as a function of x_F in bins of t'. The bins are denoted by different colours, the single distributions come with an offset c_i given in the figure.

in the medium x_F range between 0.3 and 0.5, where the bump in the x_F distribution of the η meson is located (compare right panel of figure 9.2). The largest effect can be observed in the highest x_F bin, where the cross section ratio rises rapidly in the low t' bins.

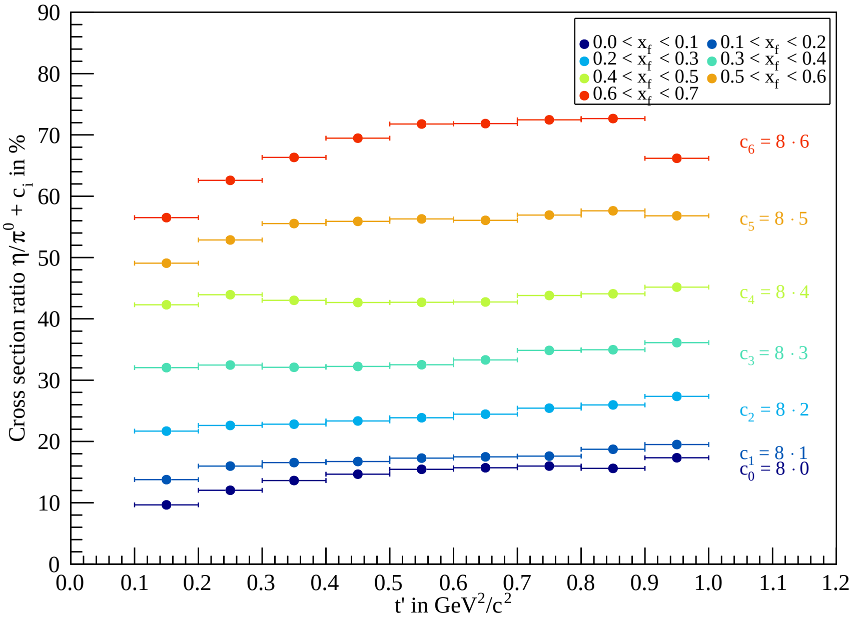

Figure 9.5: Cross section ratio η/π^0 as a function of x_F in bins of t'. The bins are denoted by different colours, the single distributions come with an offset c_i given in the figure.

9.3 RESULTS FOR VECTOR MESONS

The production of vector mesons has already been investigated at COMPASS as a function of x_F of the fast proton [48, 79]. In addition, the analysis was performed on the combined 2008 and 2009 data set, and therefore, the results cannot be directly compared to the ones obtained for the pseudoscalar mesons. However, it is possible to compare the ratio of ϕ and ω production, which is independent of the data set, when the same cuts are applied.

As shown in section 7.4 the acceptance for ϕ mesons is nearly zero in certain ranges of the proton x_F. Therefore, a cut of $0.5 < x_F(p) < 0.9$ is performed on ϕ as well on ω data and the selection is done in the remaining 4 bins of the meson x_F between 0.1 and 0.5. The invariant mass spectra, corrected for acceptance and branching fractions, for $\pi^+\pi^-\pi^0$ and K^+K^- in the full x_F range are shown in figures 9.6 and 9.7 together with the fits of the ω and ϕ peak, respectively. The full fit is shown in red, the contribution from ω and ϕ in blue.

With acceptance correction and branching fraction the fit yields a total number of $N_\phi = 139067 \pm 1648$ ϕ mesons and $N_\omega = 8704642 \pm 1029$ ω mesons, which corresponds to a ratio of

$$\frac{N_\phi}{N_\omega} = 1.60(2)\%\,.$$

This result is in perfect agreement with the value of 1.60(3)%, which was obtained before at COMPASS.

In figure 9.8 the absolute numbers, corrected for acceptance and branching fractions, of produced mesons (π^0, η, ω, ϕ) are shown as a function of the meson x_F. Dividing these numbers by the integrated luminosity would yield the cross section. In the case of π^0 and η the open symbols denote the values without the cut on x_F, the filled symbols the values with the cut on x_F of the fast proton. The statistical errors are too small to be visible in the plot. In the upper part of table 9.1 the event numbers used in figure 9.8 are given for the case of the

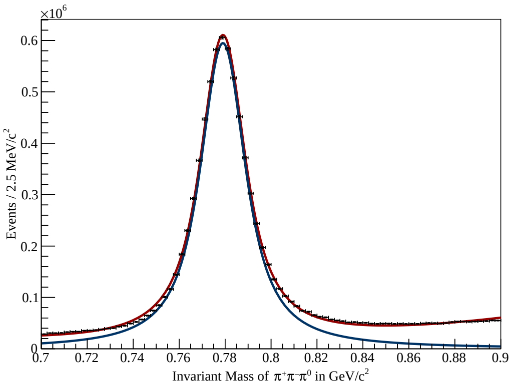

Figure 9.6: Fit of ω mass together with a polynomial background on acceptance corrected data. The full fit is shown in red, the ω contribution in blue.

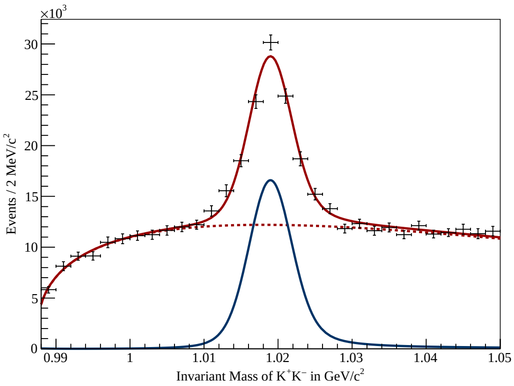

Figure 9.7: Fit of ϕ mass together with background on acceptance corrected data. The full fit is shown in red, the ϕ contribution in blue.

cut on x_F of the fast proton[1]. In addition, the cross section ratios for η, ω and ϕ relative to the production of π^0 mesons are given in the lower part of table 9.1. The cross section for ω meson production is roughly twice as high as for η meson production. The cross section ratio $\frac{\sigma(\omega)}{\sigma(\pi^0)}$ behaves very similar to $\frac{\sigma(\eta)}{\sigma(\pi^0)}$ in the considered x_F range. The cross section for ϕ production is quite small, which is expected due to the OZI suppression of ϕ production [84–87]. The change of the cross section ratio $\frac{\sigma(\phi)}{\sigma(\omega)}$ as a function of the meson x_F is in agreement with the previous COMPASS result [79].

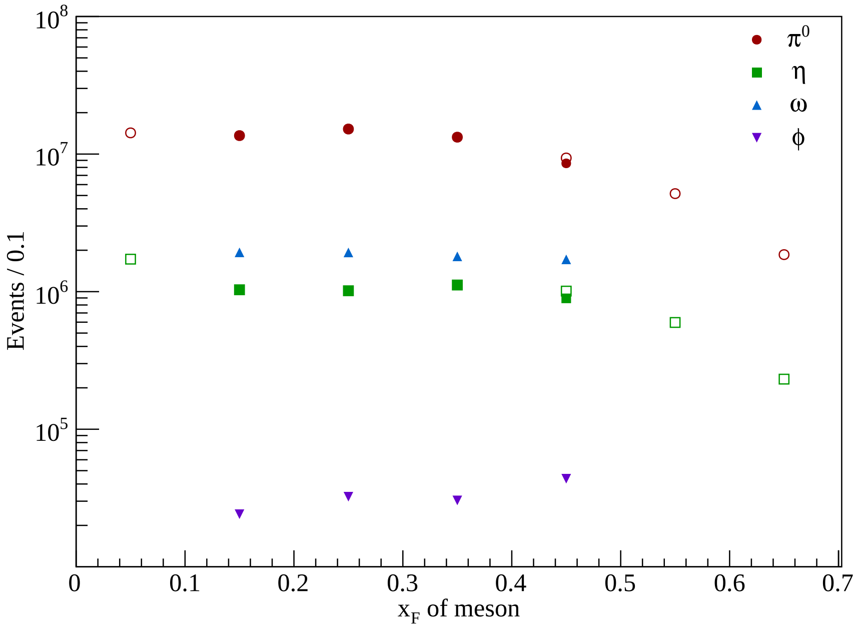

Figure 9.8: Number of produced mesons (π^0, η, ω, ϕ) as a function of their x_F. In the case of π^0 and η the open symbols denote the values without the cut on x_F, the filled symbols the values with the cut on x_F of the fast proton as it is done for ω and ϕ.

---

[1] The numbers for π^0 and η without the cut are already given in the table in figure 9.1.

	Number of events			
x_F	π^0	η	ω	ϕ
$0.1 - 0.2$	13602595 ± 5959	1031969 ± 5335	1930117 ± 15450	24134 ± 723
$0.2 - 0.3$	15206953 ± 6525	1015047 ± 5249	1927425 ± 15392	32339 ± 679
$0.3 - 0.4$	13269721 ± 5841	1117607 ± 5769	1804984 ± 14715	30388 ± 515
$0.4 - 0.5$	8562599 ± 4152	893812 ± 4633	1716769 ± 13672	43694 ± 770

	Cross section ratio relative to π^0 in %		
x_F	η	ω	ϕ
$0.1 - 0.2$	7.59 ± 0.04	14.19 ± 0.11	0.177 ± 0.005
$0.2 - 0.3$	6.67 ± 0.03	12.69 ± 0.10	0.229 ± 0.004
$0.3 - 0.4$	8.42 ± 0.04	13.60 ± 0.11	0.229 ± 0.004
$0.4 - 0.5$	10.44 ± 0.05	20.05 ± 0.16	0.510 ± 0.009

Table 9.1: Absolute number of events for the production of π^0, η, ω and ϕ mesons in $pp \to ppM$ (upper table) and cross section ratios for the production of η, ω and ϕ mesons relative to the production of π^0 mesons (lower table).

9.4 DISCUSSION OF SYSTEMATIC UNCERTAINTIES

In the calculation of cross section ratios, most of the detector effects (CEDAR, RPD, tracking) cancel due to the same selection criteria for all investigated reactions. Since the acceptance correction is done in three dimensions, the systematic effects from the Monte-Carlo generator are small. Remaining systematic effects stem from the identification of charged particles in the RICH, photon reconstruction in the electromagnetic calorimeters and from the fits that are used to determine the number of ω and ϕ events. These systematic uncertainties were already studied during the previous analysis [48]. The uncertainty from the RICH is estimated to 5%, the photon reconstruction efficiency to 10%. The systematic uncertainty on the ω and ϕ fits was confirmed to be 5% in this analysis by applying different parametrisations for the background descriptions. In the different cross section ratios, some of these effects also cancel to a large part:

$\frac{\sigma(\eta)}{\sigma(\pi^0)}$ The selection of π^0 and η uses the same final state ($pp\gamma\gamma$). Thus, this ratio is (nearly) free of systematic uncertainties.

$\frac{\sigma(\omega)}{\sigma(\pi^0)}$ In this case, the ECAL uncertainties cancel to a large part as both states have two photon clusters in the final state. The quadratic sum of the RICH and fit uncertainties yields a total systematic uncertainty of 7% for this cross section ratio.

$\frac{\sigma(\phi)}{\sigma(\pi^0)}$ In the cross section ratio of ϕ and π^0 all sources of systematic uncertainties have to be taken into account. The total uncertainty is 12% in this case.

SUMMARY – PRODUCTION OF SINGLE MESONS IN pp REACTIONS

In the previous chapters, the determination of cross sections for single meson production was presented. This is the first measurement of four different mesons (π^0, η, ω and ϕ) over a large range of the Feynman variable x_F of the meson. The final results for the cross section ratios relative to π^0 production are given in table 9.2. The results include the systematic uncertainties, which were discussed in section 9.4. The cross section ratio of η and π^0 as a function of x_F shows a resonant enhancement of π^0 production in the medium x_F range. The obtained cross section ratio of ϕ and ω production is in agreement with the previous COMPASS analysis [79]. In addition, the cross section ratio of η and π^0 production was analysed as a function of the momentum transfer t' and in a two-dimensional binning of x_F and t'. The results were shown in figures 9.4 and 9.5.

	Cross section ratio relative to π^0 in %		
x_F	η	ω	ϕ
$0.1 - 0.2$	7.59 ± 0.04	$14.19 \pm 0.11 \pm 0.99$	$0.177 \pm 0.005 \pm 0.021$
$0.2 - 0.3$	6.67 ± 0.03	$12.69 \pm 0.10 \pm 0.89$	$0.213 \pm 0.004 \pm 0.026$
$0.3 - 0.4$	8.42 ± 0.04	$13.60 \pm 0.11 \pm 0.95$	$0.229 \pm 0.004 \pm 0.027$
$0.4 - 0.5$	10.44 ± 0.05	$20.05 \pm 0.16 \pm 1.40$	$0.510 \pm 0.009 \pm 0.061$

Table 9.2: Cross section ratios for the production of η, ω and ϕ mesons relative to the production of π^0 mesons with statistical and systematic uncertainties as discussed in section 9.4.

For the future, an inclusion of the two additional neutral mesons, namely η' and ρ would be desirable. Both are available in the data set used in this analysis. However, the extraction of event numbers is more complicated for those. The production cross section for η' mesons is quite small, therefore several decay channels have to be combined to achieve enough statistics. The ρ meson is available from $pp\pi^+\pi^-$ final states, but the ρ resonance has a large width and is located in a mass region with large background[2]. Thus, a precise determination of the number of ρ mesons is challenging.

---

[2] The $\pi^+\pi^-$ mass spectrum can be found in the upper right panel of figure C.3 in the appendix.

III

PARTIAL WAVE ANALYSIS OF $p\pi^0$ FINAL STATES

10

LIGHT BARYONS IN EXPERIMENT AND THEORY

In this chapter an overview on experimental results in baryon spectroscopy, that were obtained in the past decades and with experiments that are still ongoing, will be given. Only light baryon resonances, containing u and d (and some s) quarks, which are important in this work, are covered. A more detailed review, which also includes heavy baryons, can be found in [88]. An up-to-date analysis of all available data on light baryons may be found in [89], recent results in $N\eta$ final states are given in [90]. In addition, a short overview over theoretical baryon models will be given, those are reviewed in [91], oscillator models are covered in more detailed in [92]. A recent report on experimental techniques as well as theoretical approaches appeared in [93].

10.1 NAMING AND NOTATION CONVENTIONS FOR BARYONS

The naming convention for light baryons is based on the number of strange quarks:

- Baryons without strange quarks (only u and d) are called N ($I = \frac{1}{2}$) or Δ ($I = \frac{3}{2}$).
- Baryons with one strange quark are called Λ ($I = 0$) or Σ ($I = 1$).
- Baryons with two strange quarks are called Ξ ($I = \frac{1}{2}$).
- Baryons with three strange quarks are called Ω ($I = 0$).

Strongly decaying baryons have their mass in MeV/c^2 as a part of their name, e. g. $\Delta(1232)$, $N(1440)$,... For baryons containing heavy quarks (c,b) the heavy quark, that substitutes one of the strange quarks, is given as an index, e. g. $\Lambda_c^- = (udc)$.
Exited baryons (with u and d quarks) are either characterised with $J^{\mathcal{P}}$, i. e. spin J and parity $\mathcal{P}$, or in a spectroscopic notation $L_{2I,2J}$, with total spin J, isospin I and angular momentum L, denoted in spectroscopic notation $(S, P, D, \ldots)$. A relation between the two notations for N resonances is given in table

$J^{\mathcal{P}}$	$\frac{1}{2}^+$	$\frac{1}{2}^-$	$\frac{3}{2}^+$	$\frac{3}{2}^-$	$\frac{5}{2}^+$	$\frac{5}{2}^-$	$\frac{7}{2}^+$	$\frac{7}{2}^-$	$\frac{9}{2}^+$	$\frac{9}{2}^-$
$L_{2I,2J}$	P_{11}	S_{11}	P_{13}	D_{13}	F_{15}	D_{15}	F_{17}	G_{17}	H_{19}	G_{19}

Table 10.1: Different notation conventions for N baryon resonances.

10.2 BARYONS IN EXPERIMENTS

Baryon resonances are accessible in different types of experiments, namely

- meson-nucleon (or nucleon-nucleon) scattering
- decay of charmonium states
- photoproduction.

Results from those will be discussed in the following.

10.2.1 Scattering Experiments

The first large analyses in the field of baryon spectroscopy were based on pion-nucleon scattering data. The cross sections for the scattering of $\pi^\pm$ off protons as shown in figure 10.1 exhibit several structures. The dominant contribution arises from the $\Delta(1232)$ resonance. The original analyses were performed in the late 70s [94–96], later reanalyses [97, 98] mainly confirmed the original results for strong resonances but yielded different results for several weaker resonances. The results from these (re)analyses are the main ingredients for the listings and the rating of resonances by the PDG.

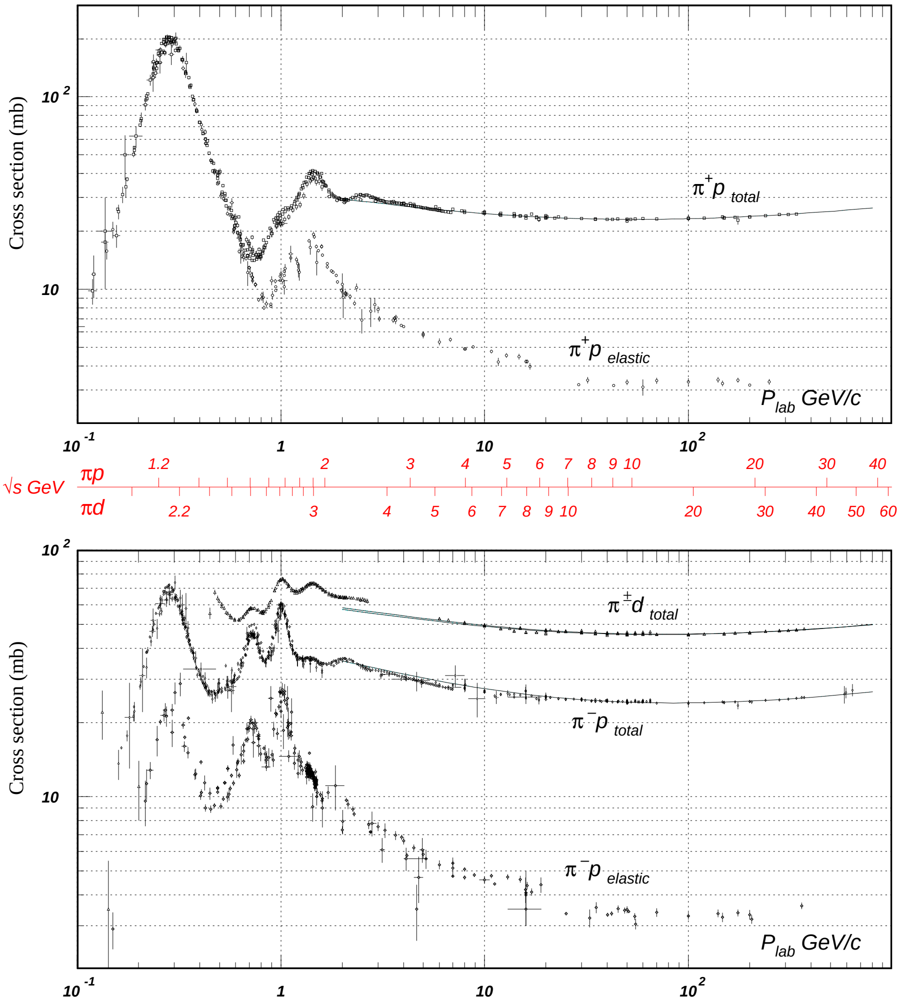

Figure 10.1: Total and elastic cross sections for $\pi^\pm$ scattering off protons and deuterons taken from the PDG at `http://pdg.lbl.gov/current/xsect` (called August 30, 2015, courtesy of the COMPAS group, IHEP, Protvino).

Inelastic reactions of pions and kaons (e. g. $\pi^- p \rightarrow n\pi^+\pi^-$) were investigated at the Large Aperture Superconducting Solenoid (LASS) spectrometer at SLAC [99] in the 80s. The focus of the analyses was on meson spectroscopy, nevertheless the data also contain information on strange baryons, but only few results were actually published [100, 101]. Prior to that analyses, those inelastic channels were investigated in bubble chamber experiments. A review on these is given in [102].

In the late 90s, the Crystal Ball Collaboration at BNL measured different reactions with negative pions and kaons impinging on protons. Cross sections and angular distributions were measured in the reaction $\pi^- p \to n\eta$ starting from threshold [103, 104] and resonance parameters were extracted using the SAID partial wave analysis program [105, 106]. In $\pi^- p \to n\pi^0$ the effect of the η threshold [107] and the $\Delta(1232)$ region [108] were investigated.

10.2.2 Charmonium Decays

Baryon resonances can be observed in decays of charmonium states such as $J/\psi \to p\bar{p}\pi^0$ or $J/\psi \to p\bar{p}\eta$, where resonances appear both in the $p\pi^0(\eta)$ and the $\bar{p}\pi^0(\eta)$ system. Such decays are studied at the BESIII experiment [109] at the BEPCII e^+e^- collider. Reviews on baryon spectroscopy results can be found in [110, 111].

10.2.3 Photoproduction

Alternatively, baryon resonances can be produced in the reaction of high energy photons with protons ($\gamma p \to X$). The total photoabsorption cross section is shown in figure 10.2. It shows a large peak for the $\Delta(1232)$ but also further structures at higher masses. The necessity of photoproduction experiments is based on open questions arising from πN-scattering results:

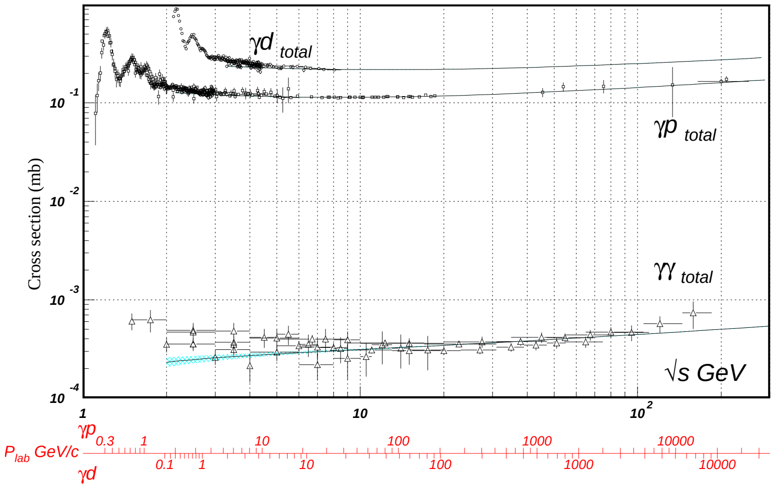

Figure 10.2: Total photoabsorption cross sections for protons and deuterons taken from the PDG at `http://pdg.lbl.gov/current/xsect` (called August 30, 2015, courtesy of the COMPAS group, IHEP, Protvino).

- The reanalysis [98] of the original πN-scattering data [95, 96] points to some open questions about the existence of several states, which should be clarified by independent measurements.

- The number of baryon resonances found above 1.8 GeV/c^2 is smaller than expected in any model. A reason might be that these high mass states decouple from the πN channel [78]. Some of these resonances should be accessible in photoproduction experiments.

- Photoproduction allows to access additional properties of baryon resonances such as form factors, polarisabilities and helicity amplitudes. A review on these low Q^2 properties can be found in [112].

First photoproduction experiments were carried out in the 60s and 70s on bubble chambers, e. g. at DESY [113] or SLAC [114, 115], and at the electron synchrotron NINA (see [116, 117] and references therein).

Today, photoproduction experiments are done in a large range of photon energies. The MAMI electron accelerator facility in Mainz [118] consists of three racetrack microtrons and a harmonic double-sided microtron, reaching an electron energy up to 1.5 GeV. Baryon spectroscopy and other photoproduction experiments are carried out with the Crystal Ball detector and a forward calorimeter (TAPS) [119]. The CBELSA experiment at the electron stretcher ring ELSA in Bonn uses the 4π detector Crystal Barrel [120] together with a a forward calorimeter (TAPS). The electron beam has an energy of up to 3.5 GeV. At JLab Hall B the CLAS spectrometer [121] is used for baryon spectroscopy using a primary 6 GeV electron beam.

10.3 PARTIAL WAVE ANALYSIS FOR BARYON SPECTROSCOPY

To disentangle the contributions of different resonances a partial wave analysis (PWA) is used. Different resonances have different spin and parity $J^{\mathcal{P}}$ which results in different angular distributions of the decay particles. These angular distributions can be calculated from models and then be fitted to the data. From the fit, the contributions of the single resonances as well as resonance parameters – namely the mass and the width – can be extracted. For the partial wave analysis of baryon resonances several programs have been developed which use different descriptions of the amplitudes. The most commonly used models are MAID [122, 123], SAID [124], the Bonn-Gatchina [125, 126] and the Giessen [127, 128] model. These models use different theoretical approaches to the production of resonances. In the following, the MAID model for photoproduction of single pions will be discussed as an example[1].

The production of single pions in photoproduction is shown in figure 10.3. The four-momentum of the photon $q = (\omega, \mathbf{q})$ is fixed by the incoming and scattered electron. The momentum transfer is denoted by $Q^2 = -q^2$. The scattered electron is measured in coincidence with the recoiling nucleon $P_f = (E_f, \mathbf{P}_f)$ and the produced pion $k = (\omega_\pi, \mathbf{k})$. The target nucleon is described by the four-momentum $P_i = (E_i, \mathbf{P}_i)$. As all particles (except for the photon) are on-shell, the system has three independent kinematic variables which are chosen to be the momentum transfer Q^2 and two of the Mandelstam variables

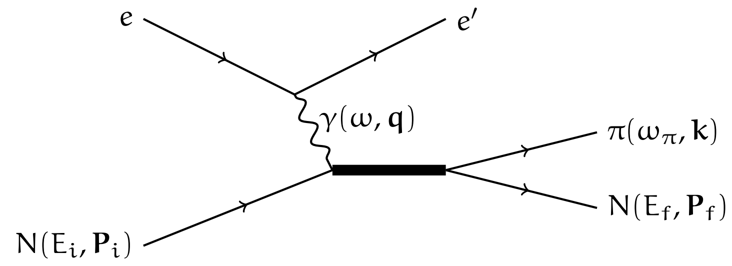

Figure 10.3: Photoproduction of single pions.

$$
\begin{aligned}
s &= W^2 = (P_i + q)^2 \\
t &= (q - k)^2 \\
u &= (P_i - k)^2 ,
\end{aligned}
\tag{10.1}
$$

---

[1] Natural units $\hbar = c = 1$ will be used.

where the centre-of-mass energy $\sqrt{s}$ is equal to the invariant mass W of the produced resonance. The transition current $J^{\mu} = (\rho, \mathbf{J})$ between initial and final states can be written in terms of CGLN[2] amplitudes, which are defined in [129], as

$$\begin{aligned}\mathbf{J} = \frac{4\pi W}{m}\Big(&i(\boldsymbol{\sigma} - (\boldsymbol{\sigma}\cdot\hat{\mathbf{q}})\hat{\mathbf{q}})F_1 + (\boldsymbol{\sigma}\cdot\hat{\mathbf{k}})(\boldsymbol{\sigma}\times\hat{\mathbf{q}})F_2 + i(\hat{\mathbf{k}} - (\hat{\mathbf{k}}\cdot\hat{\mathbf{q}})\hat{\mathbf{q}})(\boldsymbol{\sigma}\cdot\hat{\mathbf{q}})F_3 \\ &+ i(\hat{\mathbf{k}} - (\hat{\mathbf{k}}\cdot\hat{\mathbf{q}})\hat{\mathbf{q}})(\boldsymbol{\sigma}\cdot\hat{\mathbf{k}})F_4 + i\hat{\mathbf{q}}(\boldsymbol{\sigma}\cdot\hat{\mathbf{q}})F_5 + i\hat{\mathbf{q}}(\boldsymbol{\sigma}\cdot\hat{\mathbf{k}})F_6\Big) \qquad (10.2a)\end{aligned}$$

$$\rho = \frac{4\pi W}{m}\Big(i(\boldsymbol{\sigma}\cdot\hat{\mathbf{k}})F_7 + i(\boldsymbol{\sigma}\cdot\hat{\mathbf{q}})F_8\Big) = \frac{\mathbf{q}\cdot\mathbf{J}}{\omega}\,. \qquad (10.2b)$$

The structure functions F_i describe the transverse ($i = 1,2,3,4$) and longitudinal ($i = 5,6$) components of the current, respectively. They are complex-valued and therefore reactions can be described by six moduli and five relative phases. The structure functions can be decomposed into a series of electric ($E_{\ell\pm}$), magnetic ($M_{\ell\pm}$) and longitudinal ($L_{\ell\pm}$) multipoles [130] in terms of first and second order derivatives of the Legendre polynomials P_ℓ, where ℓ is the orbital angular momentum between pion and recoiling nucleon and the ± sign denotes whether the spin of the nucleon is parallel (+) or anti-parallel (−) to the orbital angular momentum.

$$\begin{aligned}
F_1 &= \sum_{\ell\geqslant 0}\Big[(\ell M_{\ell+} + E_{\ell+})P'_{\ell+1} + ((\ell+1)M_{\ell-} + E_{\ell-})P'_{\ell-1}\Big] \\
F_2 &= \sum_{\ell\geqslant 1}\big((\ell+1)M_{\ell+} + \ell M_{\ell-}\big)P'_{\ell} \\
F_3 &= \sum_{\ell\geqslant 1}\Big[(E_{\ell+} - M_{\ell+})P''_{\ell+1} + (E_{\ell-} + M_{\ell-})P''_{\ell-1}\Big] \\
F_4 &= \sum_{\ell\geqslant 2}(M_{\ell+} - E_{\ell+} - M_{\ell-} - E_{\ell-})P''_{\ell} \qquad (10.3) \\
F_5 &= \sum_{\ell\geqslant 0}\Big[(\ell+1)L_{\ell+}P'_{\ell+1} - \ell L_{\ell-}P'_{\ell-1}\Big] \\
F_6 &= \sum_{\ell\geqslant 1}\big(\ell L_{\ell-} - (\ell+1)L_{\ell+}\big)P'_{\ell}
\end{aligned}$$

The Legendre polynomials depend on the polar angle of the pion in the centre-of-mass frame, the multipoles depend on the centre-of-mass energy $W = \sqrt{s}$ and the momentum transfer Q^2.

Assuming isospin conservation, the electromagnetic current can be split into an isoscalar and an isovector part [131]. The amplitudes F_i (or equivalently the multipoles) can then be written in terms of three independent isospin amplitudes [132] for the isoscalar part ($A^{(0)}$) and for the isovector part ($A^{(1/2)}$ and $A^{(3/2)}$) for a total isospin of the πN system of $I = \frac{1}{2}$ and $I = \frac{3}{2}$, respectively[3]. These are used to construct the proton and neutron isospin-$\frac{1}{2}$ amplitudes as

$$\begin{aligned}
{}_pA^{(1/2)} &= A^{(0)} + \frac{1}{3}A^{(1/2)} \\
{}_nA^{(1/2)} &= A^{(0)} - \frac{1}{3}A^{(1/2)}\,. \qquad (10.4)
\end{aligned}$$

---

[2] They were introduced by Chew, Goldberger, Low and Nambu.

[3] The isoscalar part of the current can produce only N^* ($I = \frac{1}{2}$) resonances when coupling to the target proton. The isovector part can produce N^* ($I = \frac{1}{2}$) as well as Δ ($I = \frac{3}{2}$) resonances.

With these, the amplitudes of different physical processes can be expressed as follows:

$$\begin{aligned}
A(\gamma^* p \to n\pi^+) &= \sqrt{2}\Big[\,{}_pA^{(1/2)} - \frac{1}{3}A^{(3/2)}\Big]\\
A(\gamma^* p \to p\pi^0) &= {}_pA^{(1/2)} + \frac{2}{3}A^{(3/2)}\\
A(\gamma^* n \to p\pi^-) &= \sqrt{2}\Big[\,{}_nA^{(1/2)} + \frac{1}{3}A^{(3/2)}\Big]\\
A(\gamma^* n \to n\pi^0) &= -{}_nA^{(1/2)} + \frac{2}{3}A^{(3/2)}\,.
\end{aligned} \tag{10.5}$$

All observables in these processes can also be expressed in terms of the structure functions F_i. In pion photoproduction these are in general 16 different polarisation observables for different combinations of photon, target and recoil polarisation. Details can be found in [133].

In the MAID model, resonant contributions from real as well as from virtual photons are included. In the model "dressed" resonances are considered which contain not only the "bare" resonance parameters but also vertex corrections from interference with the background. For the resonance contributions of the multipoles Breit-Wigner forms

$$A_{\ell\pm} = \bar{\mathcal{A}}_{\ell\pm} f_{\gamma N}(W) \frac{\Gamma_{tot} W_R e^{i\phi}}{W_R^2 - W^2 - iW_R\Gamma_{tot}} f_{\pi N}(W) C_{\pi N}\,. \tag{10.6}$$

are used. The factor $C_{\pi N}$ is $\sqrt{\frac{3}{2}}$ for $I = \frac{1}{2}$ and $-\frac{1}{\sqrt{3}}$ for $I = \frac{3}{2}$, respectively. The decay of the resonance with spin j, which has a partial decay width $\Gamma_{\pi N}$ into πN and a total decay width Γ_{tot}, is described by the function $f_{\pi N}(W)$ with

$$f_{\pi N}(W) = \sqrt{\frac{1}{(2j+1)\pi} \frac{k_W}{|\mathbf{q}|} \frac{m_N}{W} \frac{\Gamma_{\pi N}}{\Gamma_{tot}^2}} \quad \text{with} \quad k_W = \frac{W^2 - m_N^2}{2W}\,. \tag{10.7}$$

The energy dependence of the partial width [134, 135] is given by

$$\Gamma_{\pi N} = \beta_\pi \Gamma_{tot} \left(\frac{|\mathbf{q}|}{q_R}\right)^{2\ell+1} \left(\frac{X^2 + q_R^2}{X^2 + \mathbf{q}^2}\right)^{\ell} \frac{W_R}{W} \tag{10.8}$$

with the πN branching fraction β_π and the pion momentum q_R in the centre-of-mass frame at the resonance mass ($W = W_R$). The damping parameter X is assumed to be 500 MeV for all resonances. Further contributions to the total decay width are assumed to be dominated by the two-pion channel and parametrised according to [136]. Only in the case of $N(1535)1/2^-$, which has a large branching fraction into into ηN, an additional ηN width similar to (10.8) is added. The energy dependence of the coupling of the photon with the target proton into the resonance is parametrised with a form factor

$$f_{\gamma N}(W) = \left(\frac{k_W}{k_R}\right)^n \left(\frac{X^2 + k_R^2}{X^2 + k_W^2}\right), \quad n \geqslant \ell_\gamma \tag{10.9}$$

with X as above and $k_R = k_W$ for $W = W_R$. The parameter $n \geqslant \ell_\gamma$ is introduced to reproduce the correct threshold behaviour induced by the Born terms, where ℓ_γ is the photon orbital angular momentum. The unitary phase ϕ in (10.6) adjusts the phase of the total multipole (with background) to the pion-nucleon scattering phase (Fermi-Watson theorem [131]: The amplitude is complex only due to pion-nucleon interaction.) or to the experimentally observed phase. The main challenge when including virtual photons is the determination of the Q^2 dependence of the amplitudes, which is described in [123]. The main sources of background are on the one hand Born and vector meson exchange terms and on the other hand non-resonant multipoles. Details on these backgrounds are given in [123]. More details on the fitting procedure are given in [137].

10.4 LIGHT BARYONS IN THE PDG

The PDG lists a total of 26 N resonances ($I = \frac{1}{2}$). Out of these 26 N resonances, 10 are rated as certain ($****$), 5 as very likely ($***$), 7 as fair ($**$) and 4 as poor ($*$). Figure 10.4 shows the spectrum of those states. The colour of the boxes denotes the rating, the size of the boxes shows the mass range that is given for the single resonances. In addition, 22 Δ resonances ($I = \frac{3}{2}$) are listed. Those are not the topic of this thesis and will not be considered here.

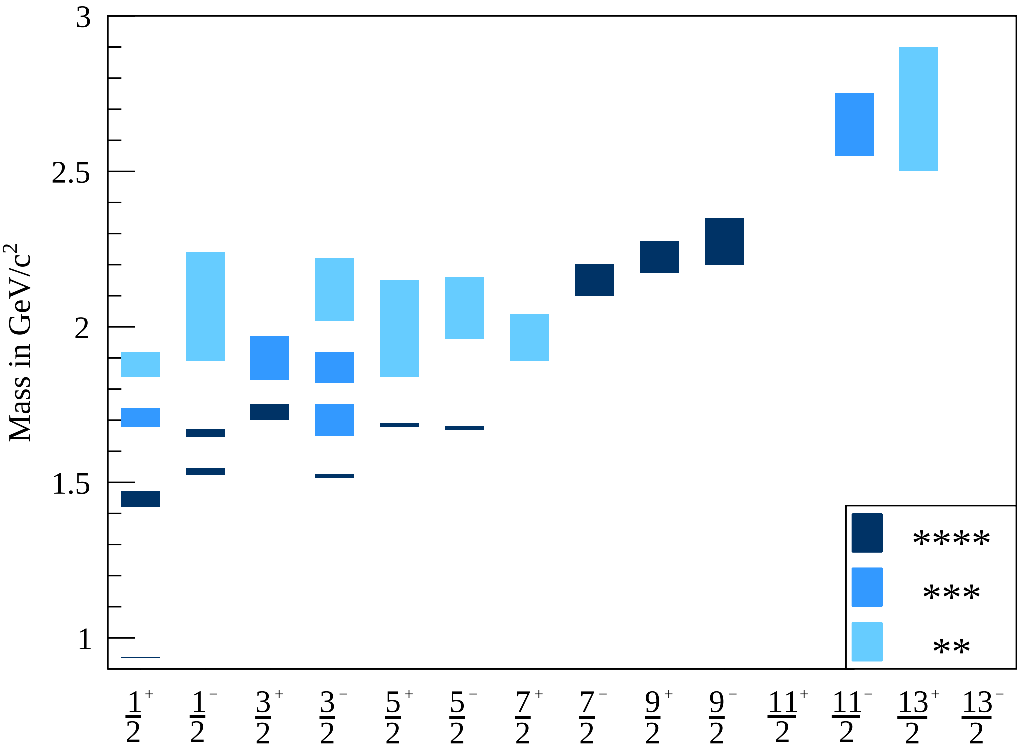

Figure 10.4: The spectrum of N ($I = \frac{1}{2}$) Baryons as listed by the PDG (2012 edition, see [138]). The colours correspond to the status of the resonances ($****$ certain, $***$ very likely, $**$ fair). Baryons with a $*$ rating (poor evidence) are omitted. The size of the boxes denotes the mass range for the resonances given in the listings.

10.5 BARYON MODELS

The excitation spectrum of baryons cannot be directly calculated from QCD. A perturbative treatment is also not possible due to the large coupling constant in the low energy regime. Therefore, models are needed to predict the spin and mass of resonances. Several models for the three-quark interaction inside a baryon are used. In the case of equal masses ($m_u = m_d \approx m_s$) Jacobi coordinates

$$\begin{aligned} R &= \frac{r_1 + r_2 + r_3}{3} \\ x &= r_2 - r_1 \\ y &= \frac{2r_3 - r_1 - r_2}{\sqrt{3}}, \end{aligned} \tag{10.10}$$

as depicted in figure 10.5, describe the three quarks inside a baryon. In the centre of mass

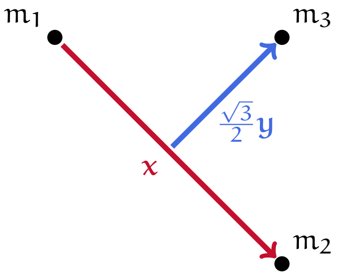

Figure 10.5: Jacobi coordinates for the three quarks inside a baryon. The coordinate $\mathbf{R}$ is the centre of mass of the three quarks.

frame the intrinsic Hamiltonian becomes

$$\mathcal{H} = \frac{\mathbf{p}_x^2}{m} + \frac{\mathbf{p}_y^2}{m} + V(\mathbf{x}, \mathbf{y})\,, \tag{10.11}$$

with an unknown potential $V(\mathbf{x}, \mathbf{y})$. A typical choice for this potential is a harmonic oscillator

$$V(\mathbf{r}_1, \mathbf{r}_2, \mathbf{r}_3) = \frac{2}{3}K(r_{12}^2 + r_{23}^2 + r_{13}^2)\,, \tag{10.12}$$

where $r_{ij} = |\mathbf{r}_{ij}| = |\mathbf{r}_j - \mathbf{r}_i|$. The transformation into Jacobi coordinates yields

$$\mathcal{H} = \frac{\mathbf{p}_x^2}{m} + \frac{\mathbf{p}_y^2}{m} + K(\mathbf{x}^2 + \mathbf{y}^2)\,. \tag{10.13}$$

This corresponds to the sum of two independent three-dimensional harmonic oscillators. The energies are given as

$$E = 2(N+3)\sqrt{\tfrac{K}{m}}\,, \tag{10.14}$$

where $N = 2n_x + \ell_x + 2n_y + \ell_y$ is the cumulated quantum number. For $N \geqslant 2$ different J^P states are degenerate. These states form $SU(6)$ supermultiplets $(d, \ell^P)^{(N)}$, where d is the spin-flavour dimensionality, ℓ the total angular momentum and P the total parity. The ground state supermultiplet $(56, 0^+)^{(0)}$ contains the spin-$\frac{1}{2}$ octet from figure 1.5 (2 spin projections each) and the spin-$\frac{3}{2}$ decuplet from figure 1.6 (4 spin projections each) giving a total of $2 \times 8 + 4 \times 10 = 56$ states.

More sophisticated calculations include e. g. perturbative expansions [139–141], variational methods [142, 143], Fadeev equations [144] or hyperspherical expansions [145, 146] of the harmonic oscillator.

Figure 10.6 shows the results of a quark model calculation [147] together with the states listed in the PDG review. Up to 2.4 GeV/c^2 about 45 N resonances are predicted, but only 19 are found, 7 of which are only $**$ or $*$. This has been known for a long time as the 'missing resonance' problem.

Baryons in Lattice QCD

Lattice QCD [148] allows for an *ab initio* treatment of QCD in the non-perturbative regime, where quarks are confined into hadrons. It introduces a four-dimensional Euclidean space-time lattice on which the properties of hadrons can be calculated numerically. In the limit of an infinite large lattice with an infinitesimal small spacing, continuum QCD is recovered. In the past years a lot of effort has been undertaken in lattice QCD to determine the hadron spectrum. A recent overview on methods and results can be found in [149]. A comparison between lattice results and experimental values is given in [150] and is shown in figure 10.7. The calculations (red circles) are in good agreement with the experiment (black lines).

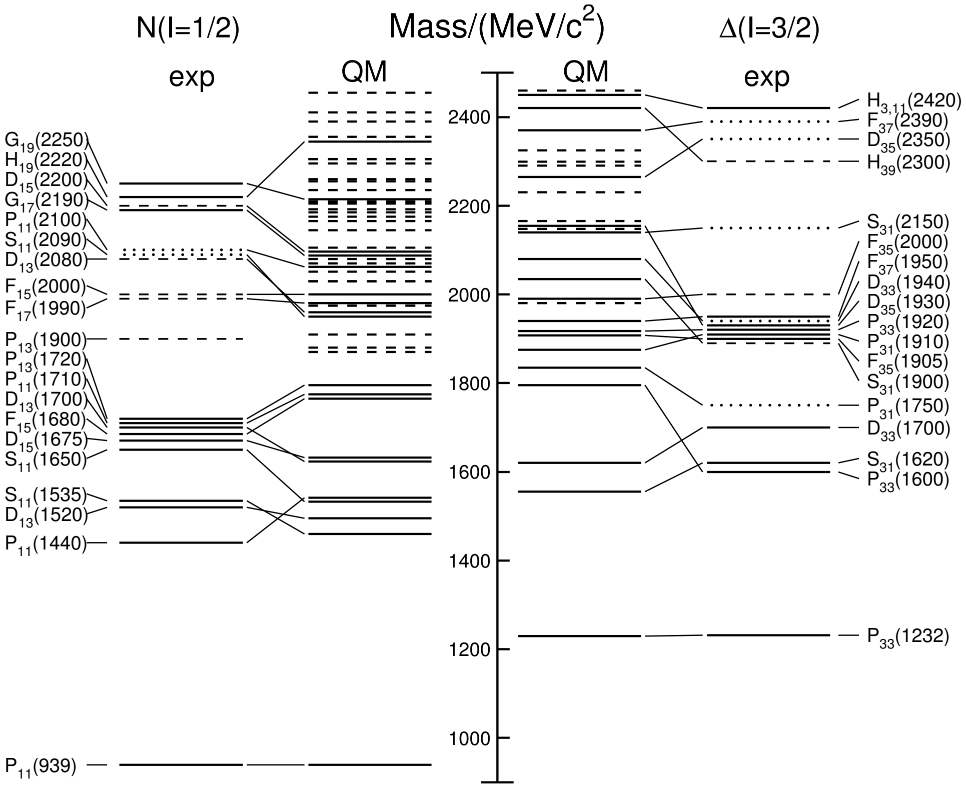

Figure 10.6: Excitation spectrum of the nucleon [1]. The states found in experiment (exp) are compared to a quark model calculation (QM) [147] for N baryons ($I = \frac{1}{2}$, left) and Δ baryons ($I = \frac{3}{2}$, right). Many states cannot be matched between experiment and theory.

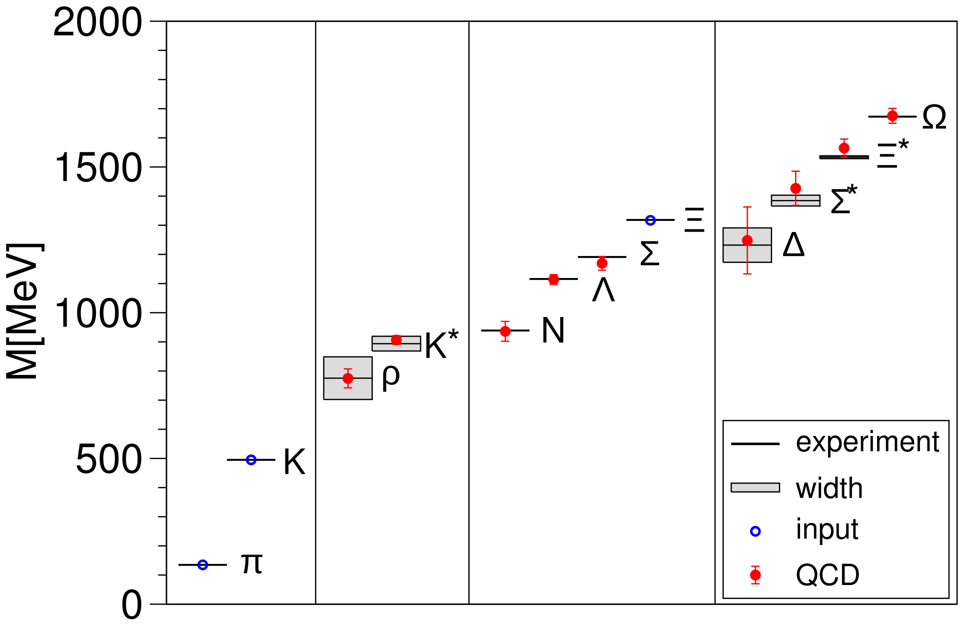

Figure 10.7: Comparison of Lattice QCD calculations [150] (red circles) with experimental values (black lines), the grey boxes denote the experimentally determined decay width. The masses of π, K and Ξ have been fixed in the Lattice calculation to fix the mass scale.

11

THE HELICITY FORMALISM

11.1 MOTIVATION

To describe the contribution of a single resonance to the total cross section, the angular distribution of a resonance with a given spin J and parity $\mathcal{P}$, the so-called partial-wave amplitude, has to be calculated. The coherent sum of those amplitudes yields the total cross section. To calculate the partial-wave amplitudes, the helicity formalism [151, 152] is used.
For a decay of a particle a with spin J (parity is ignored for now and will be added later) and spin projection M into two particles

$$a \to 1 + 2 \tag{11.1}$$

the amplitude is given by the transition matrix element between the initial state and the final state. In the centre-of-mass system of a, the outgoing particles have momenta $\mathbf{p}_1 = -\mathbf{p}_2 \equiv \mathbf{p}_f$ and helicities λ_1 and λ_2. The transition matrix element is given as[1]

$$A = \langle \mathbf{p}_f, \lambda_1; \mathbf{p}_f, \lambda_2 | \mathcal{U} | J, M \rangle \tag{11.2}$$

where $\mathcal{U}$ is the transition operator. In spherical coordinates the momentum $\mathbf{p}_f$ is replaced by the angles θ and φ,

$$A = \langle \theta, \varphi, \lambda_1, \lambda_2 | \mathcal{U} | J, M \rangle \,, \tag{11.3}$$

where $|A|^2$ describes the probability for a to decay with particle 1 emitted with angles θ and φ and thus describes the angular distribution. Therefore, the calculation of amplitudes will be sketched in the following.

11.2 ROTATIONS IN ANGULAR MOMENTUM SPACE

11.2.1 Euler Angles

A rotation of a coordinate system $(\hat{x}, \hat{y}, \hat{z})$ into a new system $(\hat{X}, \hat{Y}, \hat{Z})$ can be parametrised through the Euler angles [153], where one of the possible conventions is:

1. Rotation about $\hat{z}$ with angle α: $\hat{y} \to \hat{u}$
2. Rotation about $\hat{u}$ with angle β: $\hat{z} \to \hat{Z}$
3. Rotation about $\hat{Z}$ with angle γ: $\hat{u} \to \hat{Y}$

With the generators of the Lie algebra $so(3)$, which are the angular momentum operators J_i, the rotation operator can be written as

$$R(\alpha, \beta, \gamma) = \exp(-i\gamma J_Z) \exp(-i\beta J_u) \exp(-i\alpha J_z) \,. \tag{11.4}$$

This equation can be rewritten to use only rotations about the original coordinate system $(\hat{x}, \hat{y}, \hat{z})$ as

$$R(\alpha, \beta, \gamma) = \exp(-i\alpha J_z) \exp(-i\beta J_y) \exp(-i\gamma J_z) \,. \tag{11.5}$$

---

[1] Note: In this and the following chapters natural units $c = \hbar = 1$ will be used.

11.2.2 Wigner D-Matrices

Rotations commute with the angular momentum operator J^2

$$[R, J^2] = 0 \tag{11.6}$$

and therefore, the eigenfunctions $|jm\rangle$ transform in an irreducible representation of the group SO(3), i. e. states with different total angular momentum j do not mix. A rotation of an angular momentum state is given as

$$R(\alpha,\beta,\gamma)|jm\rangle = \sum_{m'=-j}^{j} D^j_{m'm}(\alpha,\beta,\gamma)|jm'\rangle\,, \tag{11.7}$$

with the elements of the Wigner D-matrices [154] $D^j_{m'm}(\alpha,\beta,\gamma)$. These are calculated with equation (11.5)

$$\begin{aligned} D^j_{m'm}(\alpha,\beta,\gamma) &= \langle jm'|\exp(-i\alpha J_z)\exp(-i\beta J_y)\exp(-i\gamma J_z)|jm\rangle \\ &= \exp(-i\alpha m')\langle jm'|\exp(-i\beta J_y)|jm\rangle\exp(-i\gamma m) \\ &= \exp(-i\alpha m')d^j_{m'm}(\beta)\exp(-i\gamma m)\,, \end{aligned} \tag{11.8}$$

with the elements of the Wigner d-matrices $d^j_{m'm}(\beta)$. The Wigner D-matrix elements are orthogonal and normalised as

$$\int_0^{2\pi} d\alpha \int_0^{2\pi} d\gamma \int_{-1}^{1} d(\cos\beta) D^j_{mn}(\alpha,\beta,\gamma)^* D^{j'}_{m'n'}(\alpha,\beta,\gamma) = \frac{8\pi^2}{2j+1}\delta_{jj'}\delta_{mm'}\delta_{nn'} \tag{11.9}$$

and are connected to spherical harmonics by

$$Y^m_l(\theta,\varphi) = \sqrt{\frac{2l+1}{4\pi}}d^l_{m0}(\theta)\exp(im\varphi) = \sqrt{\frac{2l+1}{4\pi}}D^l_{m0}(\varphi,\theta,\psi)\,. \tag{11.10}$$

An explicit form of the D-functions can for example be found in [155]. Some of the functions used in this work are listed in appendix A.2.

11.3 PLANE-WAVE HELICITY STATES

For the calculation of decay amplitudes $\langle\theta,\varphi,\lambda_1,\lambda_2|\mathcal{U}|J,M\rangle$, two particle states $|\theta,\varphi,\lambda_1,\lambda_2\rangle$ are needed. In the following, these two-particle states will be constructed from one-particle states.

11.3.1 One-Particle States

Starting point is a particle with spin s and spin projection λ along the $\hat{z}$ axis in its rest frame $|\mathbf{p}=0,s,\lambda\rangle$. In the rest frame, spin projection and helicity $\lambda = \mathbf{s}\cdot\mathbf{p}$ are equivalent, but only λ remains invariant under a rotation of the state. To obtain the state $|\mathbf{p},s,\lambda\rangle$ in the laboratory system, the state is rotated such, that the quantisation axis $\hat{Z}$ points along the particle momentum and then a Lorentz boost is performed

$$|\mathbf{p},s,\lambda\rangle = L(\mathbf{p})R(\alpha=\varphi,\beta=\theta,\gamma=0)|\mathbf{p}=0,s,\lambda\rangle \tag{11.11}$$

The choice $\gamma = 0$ is convention and has no influence on physics quantities [156]. The one-particle states are normalised in a Lorentz-invariant way as

$$\langle\mathbf{p}',s',\lambda'|\mathbf{p},s,\lambda\rangle = (2\pi)^3 2E\delta^3(\mathbf{p}'-\mathbf{p})\delta_{s's}\delta_{\lambda'\lambda}\,. \tag{11.12}$$

11.3.2 Two-Particle State

A two-particle state is the direct product of two one-particle states

$$|\mathbf{p}_1,\lambda_1;\mathbf{p}_2,\lambda_2\rangle = |\mathbf{p}_1,s_1,\lambda_1\rangle \otimes |\mathbf{p}_2,s_2,\lambda_2\rangle \tag{11.13}$$

and is also normalised in a Lorentz invariant way as

$$\begin{aligned}&\langle \mathbf{p}_1',\lambda_1';\mathbf{p}_2',\lambda_2'|\mathbf{p}_1,\lambda_1;\mathbf{p}_2,\lambda_2\rangle \\ &\quad = (2\pi)^6 4E_1E_2\delta^3(\mathbf{p}_1'-\mathbf{p}_1)\delta^3(\mathbf{p}_2'-\mathbf{p}_2)\delta_{\lambda_1'\lambda_1}\delta_{\lambda_2'\lambda_2}\,.\end{aligned} \tag{11.14}$$

In the centre-of-mass system, $\mathbf{p}_1 = -\mathbf{p}_2 = \mathbf{p}$, spherical coordinates (p,θ,φ) can be used, where $p = |\mathbf{p}_1| = |\mathbf{p}_2|$ is the centre-of-mass momentum and (θ,φ) denote the direction of $\mathbf{p}_1$. The state can then be written as $|p,\theta,\varphi,\lambda_1,\lambda_2\rangle$ with the normalisation

$$\begin{aligned}&\langle p',\theta',\varphi',\lambda_1',\lambda_2'|p,\theta,\varphi,\lambda_1,\lambda_2\rangle \\ &\quad = (2\pi)^6\frac{4\sqrt{s}}{p}\delta^4(P'^{\alpha}-P^{\alpha})\delta(\cos\theta'-\cos\theta)\delta(\varphi'-\varphi)\delta_{\lambda_1'\lambda_1}\delta_{\lambda_2'\lambda_2}\,.\end{aligned} \tag{11.15}$$

Here,

$$P^{\alpha} = P_1^{\alpha} + P_2^{\alpha} = (\sqrt{s},0,0,0)$$

is the total four-momentum with the centre-of-mass energy

$$\sqrt{s} = E_1 + E_2 = \sqrt{p^2+m_1^2} + \sqrt{p^2+m_2^2}\,. \tag{11.16}$$

For the calculation of angular distributions, the centre-of-mass momentum can be separated from the two-particle states

$$|p,\theta,\varphi,\lambda_1,\lambda_2\rangle = (2\pi)^3\sqrt{\frac{4\sqrt{s}}{p}}|\theta,\varphi,\lambda_1,\lambda_2\rangle|P^{\alpha}\rangle\,, \tag{11.17}$$

where the normalisation of the separated state $|\theta,\varphi,\lambda_1,\lambda_2\rangle$ is given as

$$\langle P'^{\alpha}|P^{\alpha}\rangle = \delta^4(P'^{\alpha}-P^{\alpha}) \tag{11.18a}$$

$$\langle \theta',\varphi',\lambda_1',\lambda_2'|\theta,\varphi,\lambda_1,\lambda_2\rangle = \delta(\cos\theta'-\cos\theta)\delta(\varphi'-\varphi)\delta_{\lambda_1'\lambda_1}\delta_{\lambda_2'\lambda_2}\,. \tag{11.18b}$$

For the construction of partial wave amplitudes the states can be expressed through the total spin J and the spin projection M. After the separation of the centre-of-mass momentum one obtains

$$|\theta,\varphi,\lambda_1,\lambda_2\rangle = \sum_{J,M}\sqrt{\frac{2J+1}{4\pi}}D^J_{M\lambda}(\varphi,\theta,0)|J,M,\lambda_1,\lambda_2\rangle\,. \tag{11.19}$$

The choice of the third angle in the Wigner function is arbitrary (the rotation is around the z-axis) and thus, again a value of 0 is chosen. This relation is inverted with the orthogonality relation (11.9) for the final result

$$|J,M,\lambda_1,\lambda_2\rangle = \sqrt{\frac{2J+1}{4\pi}}\int_0^{2\pi}d\varphi\int_{-1}^{1}d(\cos\theta)D^J_{M\lambda}(\varphi,\theta,0)^*|\theta,\varphi,\lambda_1,\lambda_2\rangle \tag{11.20}$$

and with this

$$\langle J,M,\lambda_1',\lambda_2'|\theta,\varphi,\lambda_1,\lambda_2\rangle = \delta_{\lambda_1'\lambda_1}\delta_{\lambda_2'\lambda_2}\sqrt{\frac{2J+1}{4\pi}}D^J_{M\lambda}(\varphi,\theta,0)\,. \tag{11.21}$$

11.4 CALCULATION OF THE ANGULAR DISTRIBUTION FOR $a \to 1+2$

The two-particle helicity state of the decay products is given as

$$|f\rangle = |p_f, \theta_f, \varphi_f, \lambda_1, \lambda_2\rangle = (2\pi)^3 \sqrt{\frac{4m_a}{p_f}} |\theta_f, \varphi_f, \lambda_1, \lambda_2\rangle |\mathcal{P}_f^\alpha\rangle \,, \tag{11.22}$$

where (θ_f, φ_f) are the angles of $\mathbf{p}_f$ in the rest frame of a. The decay amplitude is

$$A(a \to 1+2) = (2\pi)^3 \sqrt{\frac{4m_a}{p_f}} \langle \theta_f, \varphi_f, \lambda_1, \lambda_2 | U | J, M \rangle \,. \tag{11.23}$$

A complete set of two-particle states is introduced

$$\begin{aligned} A(a \to 1+2) &= \mathcal{C} \, \langle \theta_f, \varphi_f, \lambda_1, \lambda_2 | U | J, M \rangle \\ &= \mathcal{C} \sum_{J_f, M_f} \langle \theta_f, \varphi_f, \lambda_1, \lambda_2 | J_f, M_f, \lambda_1, \lambda_2 \rangle \langle J_f, M_f, \lambda_1, \lambda_2 | U | J, M \rangle \\ &\overset{(11.21)}{=} \mathcal{C} \sum_{J_f, M_f} \sqrt{\frac{2J_f+1}{4\pi}} D^{J_f}_{M_f \lambda}(\varphi_f, \theta_f, 0)^* \delta_{J_f J} \delta_{M_f M} \langle \lambda_1, \lambda_2 | U | J, M \rangle \,, \end{aligned} \tag{11.24}$$

where $\lambda = \lambda_1 - \lambda_2$, and $\mathcal{C} = (2\pi)^3 \sqrt{\frac{4m_a}{p_f}}$. The matrix element $\langle \lambda_1, \lambda_2 | U | J, M \rangle$ is rotationally invariant and thus cannot depend on M, i. e. $\langle \lambda_1, \lambda_2 | U | J, M \rangle = A_{\lambda_1, \lambda_2}$, and thus

$$A(a \to 1+2) = \mathcal{C} \sqrt{\frac{2J+1}{4\pi}} D^{J\,*}_{M\lambda}(\varphi_f, \theta_f, 0) A_{\lambda_1, \lambda_2} \,. \tag{11.25}$$

11.5 INCLUSION OF PARITY

In the decay $a \to 1+2$ the parity $\mathcal{P}(a)$ of the initial state is connected to the parities of the final states $\mathcal{P}(1,2)$ via

$$\mathcal{P}(a) = \mathcal{P}(1) \cdot \mathcal{P}(2) \cdot (-1)^L \,, \tag{11.26}$$

where L is the orbital angular momentum between the particles 1 and 2. Therefore, if parity is considered, the amplitude from (11.24) has to be modified to include an explicit dependence on the angular momentum L. Again, a complete set of two-particle states is introduced

$$\begin{aligned} A(a \to 1+2) &= \mathcal{C} \sqrt{\frac{2J+1}{4\pi}} D^{J\,*}_{M\lambda}(\varphi_f, \theta_f, 0) \langle \lambda_1, \lambda_2 | U | J, M \rangle \\ &= \mathcal{C} \sum_{L,S} \sqrt{\frac{2J+1}{4\pi}} D^{J\,*}_{M\lambda}(\varphi_f, \theta_f, 0) \langle \lambda_1, \lambda_2 | J, M, L, S \rangle \langle J, M, L, S | U | J, M \rangle \,. \end{aligned} \tag{11.27}$$

The product $\langle \lambda_1, \lambda_2 | J, M, L, S \rangle$ can be written in terms of Clebsch-Gordan coefficients as (see [151])

$$\langle \lambda_1, \lambda_2 | J, M, L, S \rangle = \big(L S 0 \lambda \big| J M \big) \big(s_1 s_2 \lambda_1 - \lambda_2 \big| S \lambda \big) \,. \tag{11.28}$$

With this, the final form of the decay amplitude is obtained

$$A(a \to 1+2) = \mathcal{C} \sum_{L,S} \sqrt{\frac{2L+1}{4\pi}} D^{J\,*}_{M\lambda}(\varphi_f, \theta_f, 0) \big(L S 0 \lambda \big| J M \big) \big(s_1 s_2 \lambda_1 - \lambda_2 \big| S \lambda \big) A^J_{LS} \,, \tag{11.29}$$

where the matrix element $A^J_{LS} = \langle J, M, L, S | U | J, M \rangle$ again does not depend on the spin projection M due to rotational invariance. The possible values of orbital angular momentum L and the total spin S of the decay products are determined by their spin and parity $J^{\mathcal{P}}$.

12

FIRST APPROACH FOR PARTIAL WAVE ANALYSIS

The resonant contributions observed in the $p\pi^0$ invariant mass spectrum (see figure 8.1) have to be entangled by a partial wave analysis. The first approach for this partial wave analysis is to parameterise only the decay of the baryon resonance into $p\pi^0$, neglecting the formation of the resonance. For this parametrisation, the helicity formalism from chapter 11 is used.

12.1 THE AMPLITUDES

Starting point for the construction of amplitudes is the decay amplitude from equation (11.29)

$$A(a \to 1+2) = \mathcal{C} \sum_{L,S} \sqrt{\frac{2L+1}{4\pi}} D^{J\,*}_{M\lambda}(\varphi,\theta,0)\big(LS0\lambda\big|JM\big)\big(s_1 s_2 \lambda_1 - \lambda_2\big|S\lambda\big) A^J_{LS}\,.$$

For the angles θ and φ the Gottfried-Jackson frame (see figure 12.1) is chosen. The Gottfried-Jackson frame is defined as the rest frame of the resonance X, where the z-axis points in the direction of the beam, the x-axis is the original direction of the resonance and $y = z \times x$. Then, the angle θ is the angle between the beam direction and one of the outgoing particles (in our case the meson) and the angle φ is the angle between the production plane (beam + recoiling proton, grey in figure 12.1) and decay plane (beam + outgoing particles, red in figure 12.1).

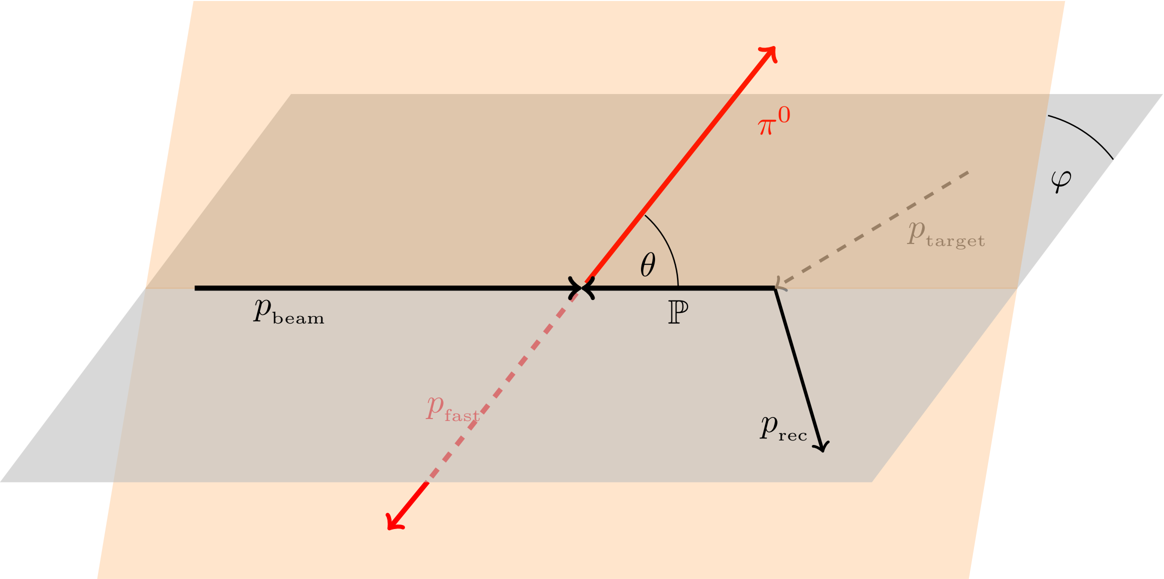

Figure 12.1: The Gottfried-Jackson frame.

For the case of $a \to p\pi^0$ the spins are given as $s_1 = 0$ and $s_2 = \frac{1}{2}$. Thus, the second Clebsch-Gordan coefficient $\big(s_1 s_2 \lambda_1 - \lambda_2\big|S\lambda\big)$ fixes S to $\frac{1}{2}$ and no summation over S is needed. Furthermore, all constant factors can be included into the partial wave amplitude $T^L_J = \frac{\mathcal{C}}{\sqrt{4\pi}} A^J_{LS}$ and thus, one obtains

$$A(a \to 1+2) = \sum_{L} \sqrt{2L+1} D^{J\,*}_{M\lambda}(\varphi,\theta,0)\big(LS0\lambda\big|JM\big) T^L_J\,. \tag{12.1}$$

To account for the angular momentum barrier in the decay of the resonance, the Blatt-Weisskopf barrier factors [157–159] $F_L(p_f)$ (see A.3) are introduced in the amplitude. When the parity of the resonance is considered, the angular momentum L is fixed by parity and the partial wave amplitude T^L_J can be written a as function of parity $T_{J^{\mathcal{P}}}$. In this work, the Wigner D-functions are taken in the reflectivity base [160]

$$D^{J,\epsilon}_{M\lambda}(\varphi,\theta,0) = \frac{1}{\sqrt{2}}\left[D^J_{M\lambda}(\varphi,\theta,0) - \epsilon\cdot\mathcal{P}\cdot(-1)^{J-M}D^J_{-M\lambda}(\varphi,\theta,0)\right], \tag{12.2}$$

where the reflectivity ϵ is given as $\epsilon = \pm i$ and only positive values of the spin projection M are taken into account. In this case, the partial wave amplitude additionally depends on the reflectivity, $T^{\epsilon}_{J^{\mathcal{P}}}$. The decay amplitude 12.1 can now be written as

$$A^{\epsilon,\lambda}_{J^{\mathcal{P}}}(\theta,\varphi;m_X) = \sqrt{2L+1}\left(L\tfrac{1}{2}0\lambda\middle|JM\right)D^{J,\epsilon\,*}_{M\lambda}(\varphi,\theta,0)F_L(p_f)T^{\epsilon}_{J^{\mathcal{P}}}\,. \tag{12.3}$$

The parity $\mathcal{P}$ of the resonance X is connected to the relative angular momentum L via

$$\mathcal{P}(X) = \mathcal{P}(p)\cdot\mathcal{P}(\pi^0/\eta)\cdot(-1)^L = (+1)\cdot(-1)\cdot(-1)^L = (-1)^{L+1}\,. \tag{12.4}$$

The Clebsch-Gordan coefficient $\left(L\frac{1}{2}0\lambda\middle|J\lambda\right)$ fixes the helicity[1] such, that only one amplitude remains for each $J^{\mathcal{P}}$ and ϵ. Thus, the intensity function, that will be fitted to the data, is given by

$$\mathcal{I}(m_X) = \sum_{\epsilon}\left|\sum_{J^{\mathcal{P}}} T^{\epsilon}_{J^{\mathcal{P}}}A^{\epsilon,\lambda}_{J^{\mathcal{P}}}(\theta,\varphi;m_X)\right|^2, \tag{12.5}$$

where the complex numbers $T^{\epsilon}_{J^{\mathcal{P}}}$ contain the strengths and phases of the individual resonances. The following amplitudes remain after the evaluation of the Clebsch-Gordan coefficients and calculation of all factors:

$$\begin{array}{lr}
\frac{1}{2}^+: & T^{\epsilon}_{\frac{1}{2}^+}\cdot\frac{1}{\sqrt{2}}\cdot\left(D^{\frac{1}{2}}_{\frac{1}{2}\frac{1}{2}} - \epsilon D^{\frac{1}{2}}_{-\frac{1}{2}\frac{1}{2}}\right)\cdot F_1(q)\\
\frac{1}{2}^-: & -T^{\epsilon}_{\frac{1}{2}^-}\cdot\frac{1}{\sqrt{2}}\cdot\left(D^{\frac{1}{2}}_{\frac{1}{2}\frac{1}{2}} + \epsilon D^{\frac{1}{2}}_{-\frac{1}{2}\frac{1}{2}}\right)\cdot F_0(q)\\
\\
\frac{3}{2}^+: & -T^{\epsilon}_{\frac{3}{2}^+}\cdot 1\cdot\left(D^{\frac{3}{2}}_{\frac{1}{2}\frac{1}{2}} + \epsilon D^{\frac{3}{2}}_{-\frac{1}{2}\frac{1}{2}}\right)\cdot F_1(q)\\
\frac{3}{2}^-: & T^{\epsilon}_{\frac{3}{2}^-}\cdot 1\cdot\left(D^{\frac{3}{2}}_{\frac{1}{2}\frac{1}{2}} - \epsilon D^{\frac{3}{2}}_{-\frac{1}{2}\frac{1}{2}}\right)\cdot F_2(q)\\
\\
\frac{5}{2}^+: & T^{\epsilon}_{\frac{5}{2}^+}\cdot\sqrt{\frac{3}{2}}\cdot\left(D^{\frac{5}{2}}_{\frac{1}{2}\frac{1}{2}} - \epsilon D^{\frac{5}{2}}_{-\frac{1}{2}\frac{1}{2}}\right)\cdot F_3(q)\\
\frac{5}{2}^-: & -T^{\epsilon}_{\frac{5}{2}^-}\cdot\sqrt{\frac{3}{2}}\cdot\left(D^{\frac{5}{2}}_{\frac{1}{2}\frac{1}{2}} + \epsilon D^{\frac{5}{2}}_{-\frac{1}{2}\frac{1}{2}}\right)\cdot F_2(q)\\
\\
\frac{7}{2}^+: & -T^{\epsilon}_{\frac{7}{2}^+}\cdot\sqrt{2}\cdot\left(D^{\frac{7}{2}}_{\frac{1}{2}\frac{1}{2}} + \epsilon D^{\frac{7}{2}}_{-\frac{1}{2}\frac{1}{2}}\right)\cdot F_3(q)\\
\frac{7}{2}^-: & T^{\epsilon}_{\frac{7}{2}^-}\cdot\sqrt{2}\cdot\left(D^{\frac{7}{2}}_{\frac{1}{2}\frac{1}{2}} - \epsilon D^{\frac{7}{2}}_{-\frac{1}{2}\frac{1}{2}}\right)\cdot F_4(q)\\
\\
\frac{9}{2}^+: & T^{\epsilon}_{\frac{9}{2}^+}\cdot\sqrt{\frac{5}{2}}\cdot\left(D^{\frac{9}{2}}_{\frac{1}{2}\frac{1}{2}} - \epsilon D^{\frac{9}{2}}_{-\frac{1}{2}\frac{1}{2}}\right)\cdot F_5(q)\\
\frac{9}{2}^-: & -T^{\epsilon}_{\frac{9}{2}^-}\cdot\sqrt{\frac{5}{2}}\cdot\left(D^{\frac{9}{2}}_{\frac{1}{2}\frac{1}{2}} + \epsilon D^{\frac{9}{2}}_{-\frac{1}{2}\frac{1}{2}}\right)\cdot F_4(q)\,.
\end{array}$$

In addition, the reflectivity is coupled directly to the parity (see appendix A.4) and thus only $\epsilon = +i$ is used in the following.

---

[1] The coupling of $(L,0)$ and $(\frac{1}{2},\lambda)$ to (J,M) leads to $M = \lambda$ only. In the reflectivity base, M is only positive and thus fixed to $\frac{1}{2}$.

12.2 FITTING PROCEDURE

The fit of resonances in this simple model is done in two steps:
In a first step the intensity given in equation (12.5) are fitted to the angular distributions in bins of the invariant mass to obtain the strengths and phases of the single $J^{\mathcal{P}}$ contributions. The outcome of these fits are expected to already produce visible resonance-like structures. In a second step, the outcome of the fits for the single $J^{\mathcal{P}}$ combinations can be fitted by resonance descriptions which include the phase shifts between the resonances (e. g. complex Breit-Wigner functions). From this fit, the resonance parameters (position and width) can be obtained. In the following sections, the first step will be performed on pseudo data first and on real data afterwards.

12.3 FITS ON PSEUDO DATA AND FIT PERFORMANCE

I developed a program that mimics the fits on real data in order to test the performance of the fitting algorithm. The program features are the following:

- The program is able to sample angular distributions for the 14 three-star and four-star resonances of the PDG up to $J = \frac{9}{2}$:
  $N(1440)\frac{1}{2}^+$, $N(1520)\frac{3}{2}^-$, $N(1535)\frac{1}{2}^-$, $N(1650)\frac{1}{2}^-$, $N(1675)\frac{5}{2}^-$, $N(1680)\frac{5}{2}^+$, $N(1700)\frac{3}{2}^-$, $N(1710)\frac{1}{2}^+$, $N(1720)\frac{3}{2}^+$, $N(1875)\frac{3}{2}^-$, $N(1900)\frac{3}{2}^+$, $N(2190)\frac{7}{2}^-$, $N(2220)\frac{9}{2}^+$ and $N(2250)\frac{9}{2}^-$.
- The resonance shapes in the invariant mass m_X are implemented as relativistic Breit-Wigner distributions [161]

$$f(m_X) = \frac{k}{(m_X^2 - M^2)^2 + M^2\Gamma^2} \tag{12.6}$$

$$\tag{12.7}$$

with

$$k = \frac{2\sqrt{2}M\Gamma\gamma}{\pi\sqrt{M^2+\gamma^2}}, \qquad \gamma = \sqrt{M^2(M^2+\Gamma^2)},$$

where M and Γ are the resonance mass and width, respectively. The values used are given in table 12.1.

Resonance	Mass	Width	Resonance	Mass	Width
$N(1440)\frac{1}{2}^+$	1440	300	$N(1710)\frac{1}{2}^+$	1710	100
$N(1520)\frac{3}{2}^-$	1520	115	$N(1720)\frac{3}{2}^+$	1720	250
$N(1535)\frac{1}{2}^-$	1535	150	$N(1875)\frac{3}{2}^-$	1875	220
$N(1650)\frac{1}{2}^-$	1655	150	$N(1900)\frac{3}{2}^+$	1900	250
$N(1675)\frac{5}{2}^-$	1675	150	$N(2190)\frac{7}{2}^-$	2190	500
$N(1680)\frac{5}{2}^+$	1685	130	$N(2220)\frac{9}{2}^+$	2250	400
$N(1700)\frac{3}{2}^-$	1700	150	$N(2250)\frac{9}{2}^-$	2275	500

Table 12.1: Mass and width (in MeV/c^2) of the resonances used in the model. The values are the given averages or the centre of the given ranges listed by the PDG (2012 edition [1]).

- The phase of the resonances is taken to be a smooth curve, changing from $-\frac{\pi}{2}$ to $\frac{\pi}{2}$ over the resonance (i. e. between $M - \frac{\Gamma}{2}$ and $M + \frac{\Gamma}{2}$). A centrally symmetric polynomial of degree five,

$$\varphi(m_X) = \frac{6\pi}{\Gamma^5}(m_X - M)^5 - \frac{5\pi}{\Gamma^3}(m_X - M)^3 + \frac{15\pi}{8\Gamma}(m_X - M)\,, \tag{12.8}$$

  is chosen. The calculation of this polynomial and the comparison to a degree-three polynomial are shown in appendix A.5.

- The data is sampled in 76 bins of m_X between 1.1 GeV/c^2 and 3.0 GeV/c^2 and 40 bins each in $\cos(\theta)$ and φ, i. e. the same binning as in the real data case is used. After the sampling, the histograms are smeared by setting the content N_i of each of the $76 \times 40 \times 40$ to a random Gaussian number with $\mu = N$ and $\sigma = \sqrt{N}$, i. e. 68% of the bin contents are now within 1σ of the nominal value obtained from the model.

- A binned minimum-χ^2 fit in 40 bins each of $\cos(\theta)$ and φ is performed in each of the 76 mass bins. The fits are done using Minuit2 [162] in the numerical minimisation package [163] `ROOT::Math::Minimizer` of ROOT. Each fit is done up to 20 times until Minuit reaches a valid minimum.

- To collect possible background (or $J^{\mathcal{P}}$ combinations which are not included in the fit) a simple constant parameter C is added to the fit function, thus the actual fit function is given as

$$\mathcal{I}(m_X) = \left| \sum_{J^{\mathcal{P}}} T^{\epsilon}_{J^{\mathcal{P}}} A^{\epsilon,\lambda}_{J^{\mathcal{P}}}(\theta, \varphi; m_X) \right|^2 + C\,. \tag{12.9}$$

- To be independent of the model input during the fit, the starting values for each single parameter are chosen randomly. To get rid of the freedom to choose an overall phase, the phase for the $\frac{1}{2}^+$ wave is fixed to zero in the fit.

- Fits on real data can be performed using the same program. The sampled pseudo-data histograms are simply substituted by real data histograms in this case.

12.3.1 Fits to the Model

In this section, results of fits to the model described above for different number of included waves are presented. Starting point are the $\frac{1}{2}^\pm$ waves, the number of waves is increased to the full model up to $\frac{9}{2}^\pm$. The fits for the single waves, which are not shown in this chapter, can be found in appendix E.

Resonances with $J^{\mathcal{P}} = \frac{1}{2}^\pm$

In a first step the two resonances N1440($\frac{1}{2}^+$) and N1535($\frac{1}{2}^-$) are used. In each mass bin ten fits are performed yielding a total number of 380 fits[2]. The fit with the best value of χ^2/ndf is kept as the final result. The model input as a function of the invariant mass and the result of the fit are shown in figures 12.2 and 12.3, respectively. Besides the moduli of the single waves, also the relative phases have to be fitted correctly. The phase between the two waves

---

[2] All fits are performed on the CERN LXBATCH system (`http://information-technology.web.cern.ch/services/batch`).

$\frac{1}{2}^+$ and $\frac{1}{2}^-$ is shown in figure 12.4. The two phase motions for the two resonances are clearly visible. Due to the overlapping resonance, the phase does not shift by 180 degrees (compare equation (12.8)). Outside of the resonance region, the relative phase is ambiguous ($\pm 180\,°$) and therefore, the fits end up in one of the possibilities. Due to this ambiguity, the errors are quite large and thus, the phase in figure 12.4 is shown without error bars. In the following, always the same relative phase is shown and can be compared to figure 12.4.

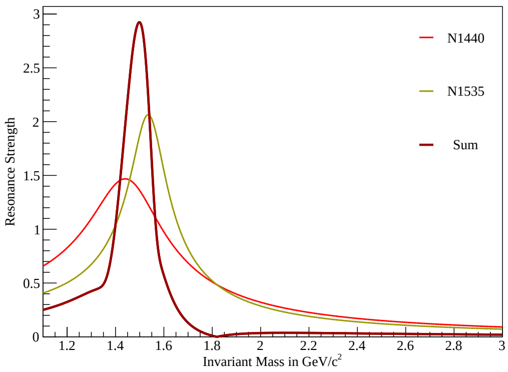

Figure 12.2: The model input for the two resonances N(1440) and N(1535) and their coherent sum.

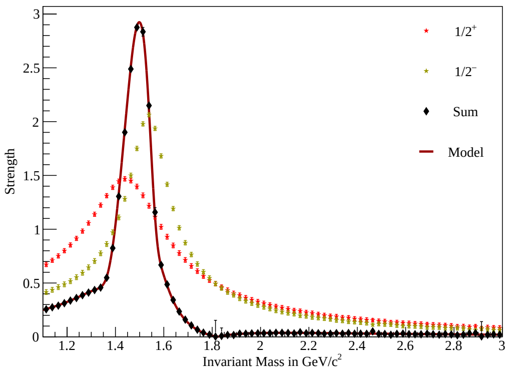

Figure 12.3: The results of the best fits for the single waves and the coherent sum together with the model input for N1440($\frac{1}{2}^+$) and N(1535)($\frac{1}{2}^-$).

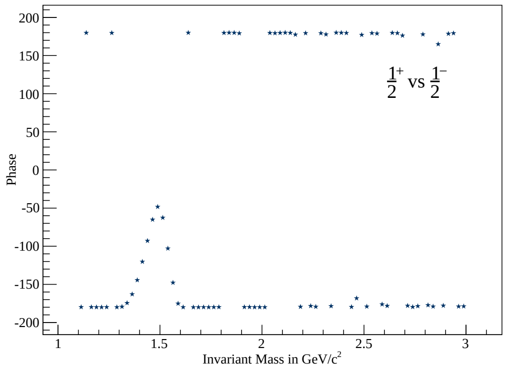

Figure 12.4: Relative phase between $\frac{1}{2}^+$ and $\frac{1}{2}^-$ in degrees. The phase shift due to the two resonances is clearly visible. No error bars are shown due to large errors outside of the resonance region.

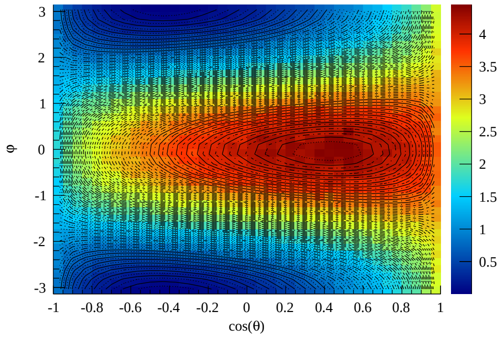

Figure 12.5: Fit output (black lines) together with the model data for the best fit in bin 15. All structures are reproduced correctly by the fit.

In this simple model the fit works fine and the resulting errors are low. An example for a fit together with the model input for bin 15 (1450 MeV/c^2) is shown in figure 12.5. The shape of the model is simple and all structures are reproduced by the fit.

Resonances with $J^{\mathcal{P}} = \frac{1}{2}^{\pm}$ *and* $\frac{3}{2}^{\pm}$

In addition to the resonances used before, the $J = \frac{3}{2}$ resonances N1720($\frac{3}{2}^+$) and N1520($\frac{3}{2}^-$) are added to the model. The model input is shown in figure 12.6. In each mass bin ten fits are performed, the result for the best-χ^2 fit is shown in figure 12.7. In most bins 10 fits were

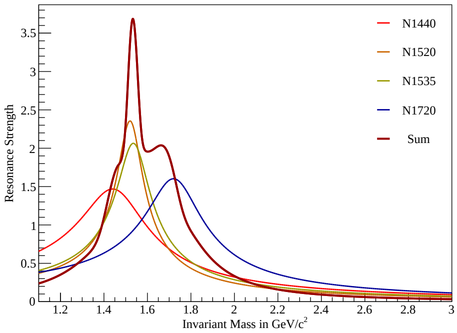

Figure 12.6: The model input for the four resonances $N1440(\frac{1}{2}^{+})$, $N(1535)(\frac{1}{2}^{-})$, $N1720(\frac{3}{2}^{+})$ and $N1520(\frac{3}{2}^{-})$ together with their coherent sum.

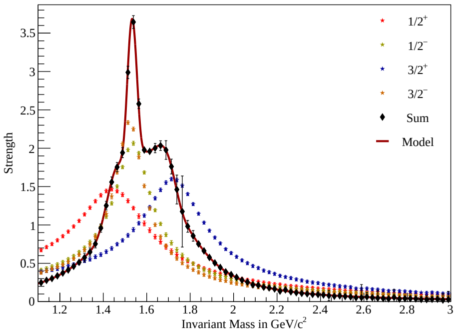

Figure 12.7: The results of the best fits for the single waves and the coherent sum together with the model input for $N1440(\frac{1}{2}^{+})$, $N(1535)(\frac{1}{2}^{-})$, $N1720(\frac{3}{2}^{+})$ and $N1520(\frac{3}{2}^{-})$.

sufficient to get a good description of the model. In figure 12.8, the phase shift between $\frac{1}{2}^{+}$ and $\frac{1}{2}^{-}$ is shown. No differences are visible compared to the fit of two resonances.

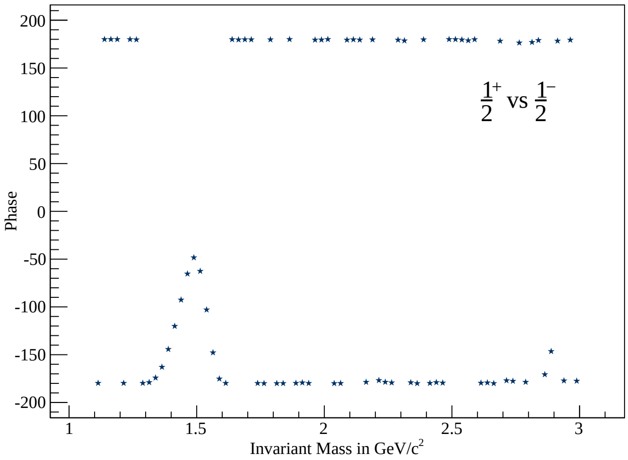

Figure 12.8: Relative phase between $\frac{1}{2}^{+}$ and $\frac{1}{2}^{-}$ in degrees. The phase shift due to the two resonances is clearly visible. No error bars are shown due to large errors outside of the resonance region.

In bin 27 at 1750 MeV/c^2 the fit output for the coherent sum is correct, nevertheless the error is large. As the errors on the single strengths are small, the error comes from a badly determined phase. The output of the best fit (black lines) together with the modelled data in this bin is shown in figure 12.9. The structures are in principle reproduced correctly but are a bit shifted from the position given by the model. This can be attributed to a badly fitted phase of at least one of the waves, as the phases control the "rotation" of the fit function in the $\cos(\theta) - \varphi$ plane. For comparison, the best fit in the neighbouring bin 28 (1775 MeV/c^2) is shown in figure 12.10, where all structures in a very similar angular distribution are reproduced in the correct place. Thus, increasing the number of fit attempts should lead to a proper fit of the badly fitted points.

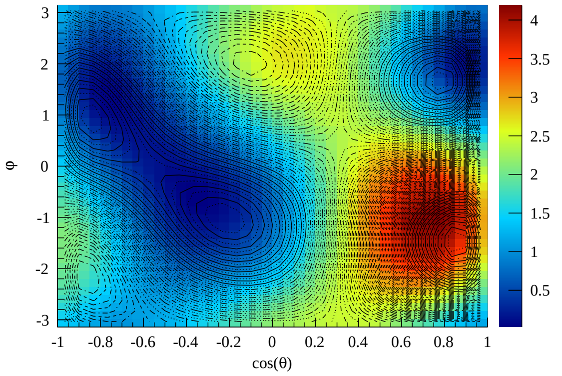

Figure 12.9: Fit output (black lines) together with the model data for the best fit in bin 27. The structures in the fit are off a bit from the structures in the model due to a bad fit of the phases.

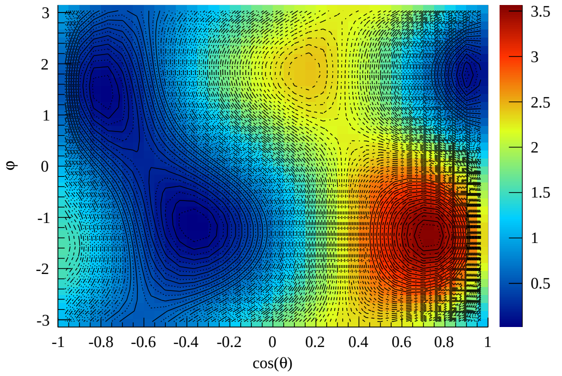

Figure 12.10: Fit output (black lines) together with the model data for the best fit in bin 28. All structures are reproduced correctly by the fit.

Full set of waves

For this test, all possible $J^{\mathcal{P}}$ combinations up to $\frac{9}{2}^{-}$ are included, where $\frac{7}{2}^{+}$ is excluded, because there is no known resonance with this quantum numbers. For waves with more than one known resonance, only the one with the lowest mass is used, which results in the following list of used resonances: $N(1440)\frac{1}{2}^{+}$, $N(1535)\frac{1}{2}^{-}$, $N(1720)\frac{3}{2}^{+}$, $N(1520)\frac{3}{2}^{-}$, $N(1680)\frac{5}{2}^{+}$, $N(1675)\frac{5}{2}^{-}$, $N(2190)\frac{7}{2}^{-}$, $N(2220)\frac{9}{2}^{+}$, $N(2250)\frac{9}{2}^{-}$. The model output is shown in figure 12.11.

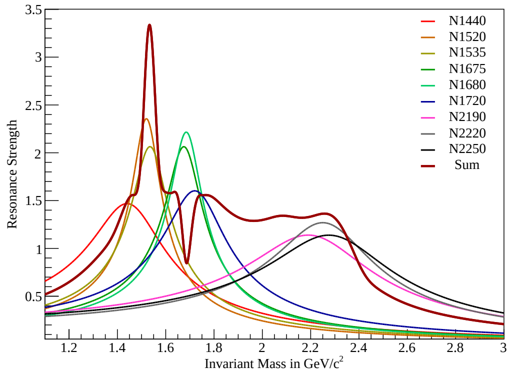

Figure 12.11: The model input for a complete list of resonances up to $\frac{9}{2}^{\pm}$ together with their coherent sum.

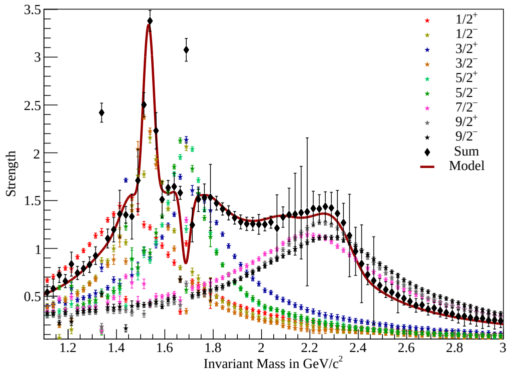

Figure 12.12: The results of the best fits out of 20 attempts for the single waves and the coherent sum together with the model input for the full list of waves up to $\frac{9}{2}^{\pm}$.

In figure 12.12, the best fit after 20 attempts is shown for this model. The result already looks quite reasonable in most regions of the spectrum, especially at low and high masses, but also in the region around $1.9\,\mathrm{GeV}/c^2$ between the two regions with resonances.

To improve the results also in the regions with many overlapping resonances, 50 fit attempts per mass bin are done. The result of the best fit of those 50 attempts is shown in figure 12.13. The improvement is reasonable, but there are still some points which do not fit to the model. However, when looking into the single waves, which are shown in figure 12.15, it is clearly visible, that they fit well to the model despite single points, which would not too much affect a fit of the single resonances. In figure 12.14, again the relative phase (after 50 fit attempts) between $\frac{1}{2}^+$ and $\frac{1}{2}^-$ is shown. Except for a single point outside of the resonance region, the phase behaviour is described correctly.

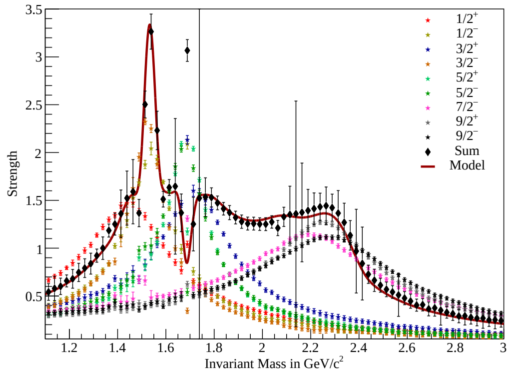

Figure 12.13: The results of the best fits out of 50 attempts for the single waves and the coherent sum together with the model input for the full list of waves up to $\frac{9}{2}^\pm$.

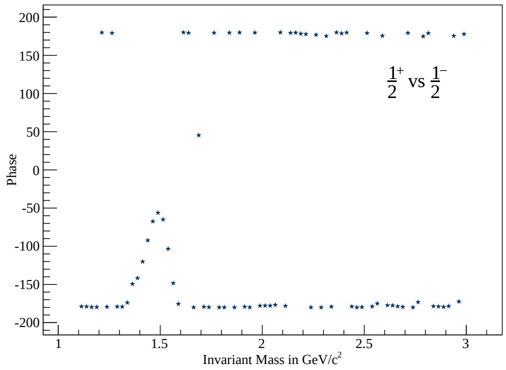

Figure 12.14: Relative phase between $\frac{1}{2}^+$ and $\frac{1}{2}^-$ in degrees. The phase shift due to the two resonances is clearly visible. No error bars are shown due to large errors outside of the resonance region.

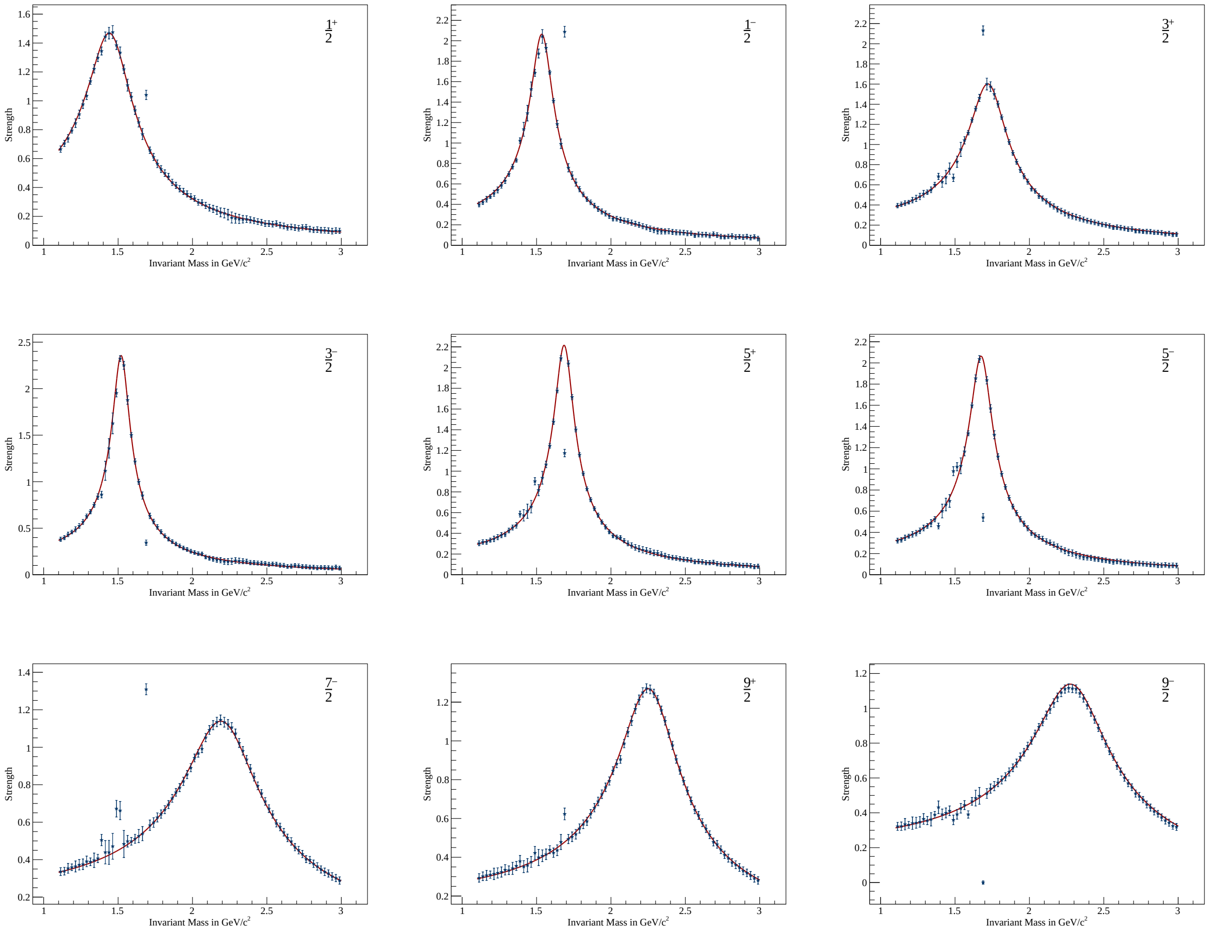

Figure 12.15: The fit results (blue points) together with the model (red line) for the single waves in the model. Except for single points the model is reproduced well by the fit.

12.3.2 Further Tests of the Fit

To further test the fit, more complicated fit scenarios, such as fits with too many or too few parameters, are considered. The starting point for these tests is a four resonance fit of N1440($\frac{1}{2}^+$), N(1535)($\frac{1}{2}^-$), N1720($\frac{3}{2}^+$) and N1520($\frac{3}{2}^-$) which will be modified accordingly. For each mass bin 20 fits are performed. Single bins, which are off after that or have large errors, can be improved by additional fits as shown above. The following three tests will be performed:

- A fit to a model with two resonances in a single wave.
- A fit of four waves to a model with resonances in only three waves.
- A fit of only three waves to a model with resonances in four waves.

In a first test an additional resonance is included into one of the waves, namely N1700($\frac{3}{2}^-$), i. e. in the $\frac{3}{2}^-$ wave, there are now two resonances. The fit shown in figure 12.16 perfectly describes the model also with this configuration. In figure 12.17, the phase shift between $\frac{1}{2}^+$ and $\frac{3}{2}^-$, which includes two resonances, is shown. Three phase motions due to N1440($\frac{1}{2}^+$) (up), N1520($\frac{3}{2}^-$) (down) and N1700($\frac{3}{2}^-$) (down) are clearly visible. The direction of the phase motion (up or down) and the sudden jump between N1520($\frac{3}{2}^-$) and N1700($\frac{3}{2}^-$) are due to the chosen model of phase shifts.

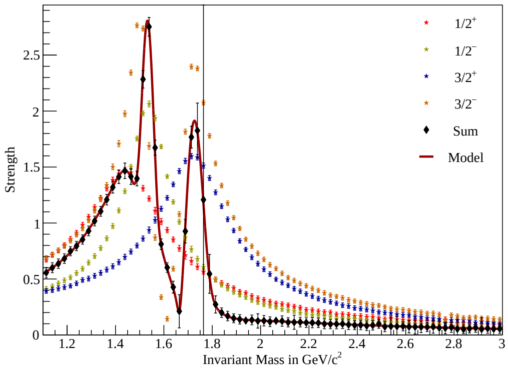

Figure 12.16: Fit results for the single waves and the coherent sum for the model with two resonances in one wave.

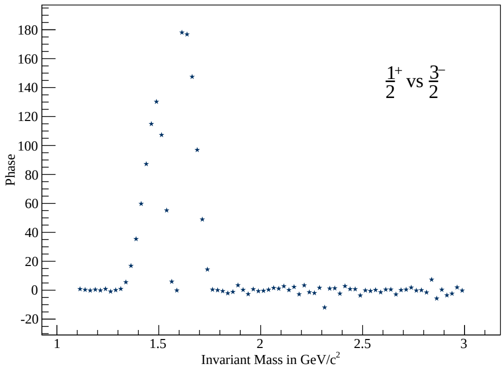

Figure 12.17: Relative phase between $\frac{1}{2}^+$ and $\frac{3}{2}^-$ in degrees for two resonances in the $\frac{3}{2}^-$ wave. The phase shift due to the three resonances is clearly visible. No error bars are shown due to large errors outside of the resonance region.

For the next test, the N1520($\frac{3}{2}^-$) resonance is excluded from the model sampling but, nevertheless, the $\frac{3}{2}^-$ wave is kept in the fit. Thus, the fit has two additional parameters, namely the strength and phase of this wave. The result for the fit is shown in figure 12.18. The model is fitted well, the $\frac{3}{2}^-$ is correctly set to zero by the fit. However, with a strength of zero, the phase of the resonance is completely arbitrary and thus it cannot be determined by the fit which then leads to larger errors on this phase and therefore also on the coherent sum. In figure 12.19, the relative phase between $\frac{1}{2}^+$ and $\frac{1}{2}^-$ is shown. Also in this scenario, the phase is fitted correctly.

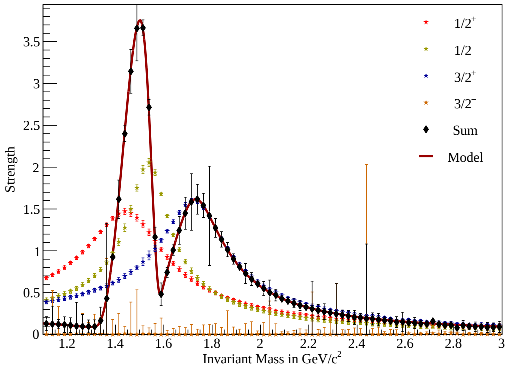

Figure 12.18: Fit result for the single waves and their coherent sum for a model without the $\frac{3}{2}^-$ wave (orange).

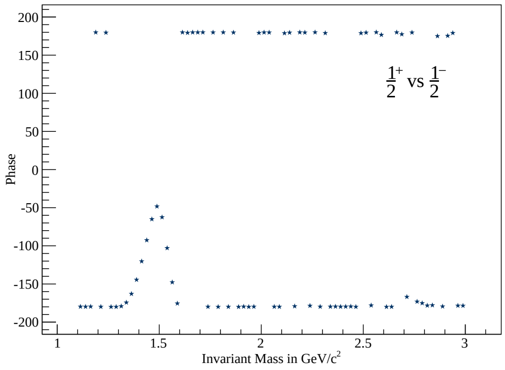

Figure 12.19: Relative phase between $\frac{1}{2}^+$ and $\frac{1}{2}^-$ in degrees. The phase shift due to the two resonances is clearly visible. No error bars are shown due to large errors outside of the resonance region.

Now, the opposite is done and N1520($\frac{3}{2}^-$) is kept in the sampling but the $\frac{3}{2}^-$ wave is removed from the fit. Thus, the fit is missing two parameters to fully describe the spectrum. The result shown in figure 12.20 does not follow the coherent sum any more but, nevertheless, describes the other resonances in a reasonable manner. This is even better visible when looking at the single fitted waves in figure 12.22. There, the peaks are disturbed by additional structures but they still are visible and remain more or less at the correct position. The relative phase between $\frac{1}{2}^+$ and $\frac{1}{2}^-$ shown in figure 12.21 does not have the same form as before, yet there are still phase shifts visible for the two resonances in these waves.

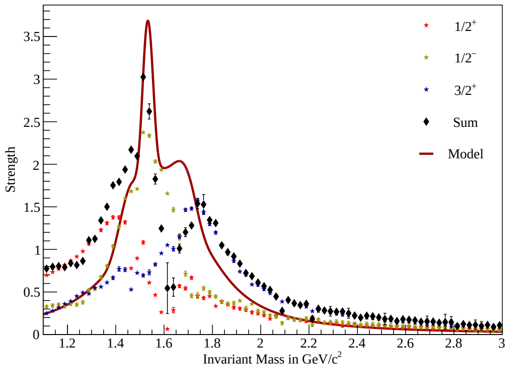

Figure 12.20: Fit result for the single waves and their coherent sum for a model with one resonance more than resonances in the fit.

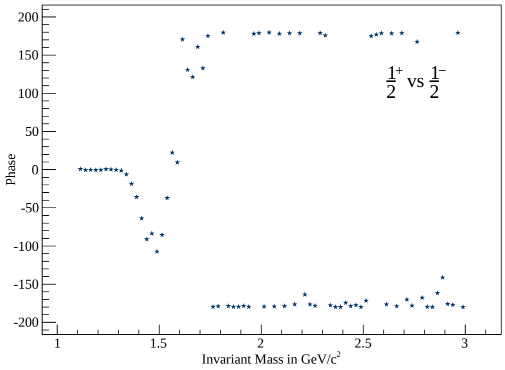

Figure 12.21: Relative phase between $\frac{1}{2}^+$ and $\frac{1}{2}^-$ in degrees for a fit with too few waves. The phase shift due to the two resonances is still visible. No error bars are shown due to large errors outside of the resonance region.

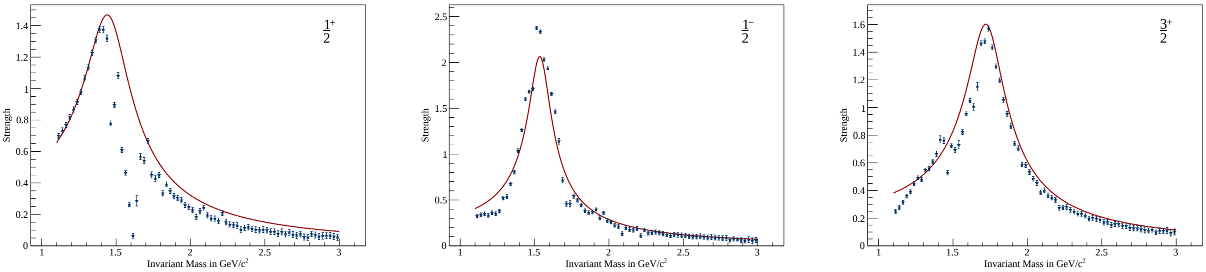

Figure 12.22: The fit results (blue points) together with the model (red line) for the single waves in the model. The model is still fitted reasonably although one resonance is missing in the fit.

From the several test fits shown above, I can conclude that the developed fit program is able to find resonances in a large number of waves (at least up to nine). The program is capable of finding more than one resonance in a single wave and also able to handle empty waves in a good way. The results obtained in fits with too few waves are still reasonable. Therefore – if the resonance decay is described appropriately by this model – it should be possible to also find resonances in the data with this fit program.

12.4 FITS ON REAL DATA

The model, which was developed and tested as described above, will now be applied to the $pp \to pp\pi^0$ data, which was already discussed in part II. Here, always the best-χ^2 fit out of 20 fits will be shown. The fits for the single waves, which are not shown here, can be found in appendix E.

12.4.1 Starting Point

As a first step, the data are analysed with the full model including all waves (except $\frac{7}{2}^+$, compare 12.3.1). Figure 12.23 shows the results for the strengths[3] of the single waves and their coherent sum. The strengths of the single waves are shown in different colours, their coherent sum is shown in black. The error bars of the coherent sum are again calculated using the formula given in appendix A.6. The coherent sum of all waves reproduces the overall invariant mass distribution well. This shows that the fit converged properly. In the single waves one would expect to observe resonance like peaks with a width of typically 150 MeV/c^2 equivalent to around six bins. Three single waves are shown in figure 12.25, the other ones can be found in the appendix. In this figure the blue stars show the outcome of the fit in the single bins. As the points jump around they are connected with a line to better guide the eye. The red lines denote the positions of known resonances (as listed in table 12.1). No resonant structures are observed at these positions (nor are any resonant structures observed anywhere else). In figure 12.24 the relative phase between $\frac{1}{2}^+$ and $\frac{1}{2}^-$ is shown. In the region of the resonances strong phase motions are expected. Instead of that, the observed phase only varies slowly over the full mass range, the two “bands” observed in figure 12.24 are separated by 360 degrees and are actual ambiguous outcomes of one solution.

---

[3] All real data fits shown here are not normalised to the total number of events. This could be done by a factor which includes essentially the bin area in the angular distributions and the total number of events. It does not change the physical meaning when this factor is omitted.

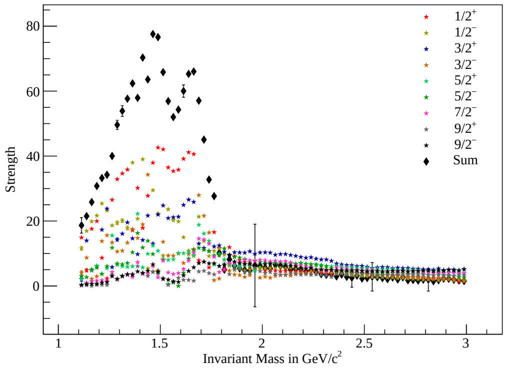

Figure 12.23: Fit result for the single waves and the coherent sum for the full model without any additional cuts.

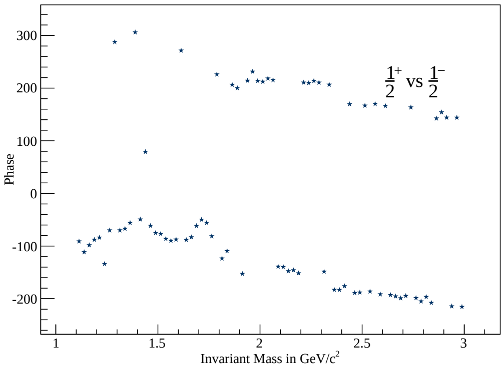

Figure 12.24: Relative phase between $\frac{1}{2}^+$ and $\frac{1}{2}^-$ in degrees for a fit to the data using the full model. No error bars are shown due to large errors of the single phases.

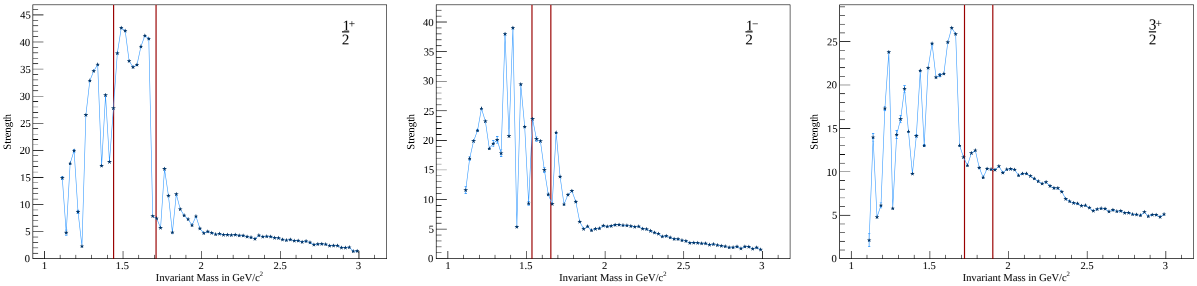

Figure 12.25: The fit results (blue points) connected by a line to better guide the eye for some of the single waves in the model. The red lines denote the nominal position of resonances as listed in table 12.1. The full set of fits can be found in appendix E.2.1.

Most of the intensity ends up in the $J = \frac{1}{2}$ waves. This can also be seen in the results for the fits in the single mass bins; an example for the mass bin $1700 - 1725\,\mathrm{MeV/c^2}$, which belongs to the second resonance like region in the $p\pi^0$ invariant mass distribution, is shown in figure 12.26. In this figure the angular distribution is shown as a two-dimensional histogram in colour scale together with the fit output as a contour plot. The fit converged to a valid minimum but does not fit the distribution. This is true for most of the mass bins. As the $J = \frac{1}{2}$ are not suppressed by Blatt-Weisskopf factors, they dominate the fits.

The structures in the angular distribution are obviously not clearly correlated to specific waves and thus, the fit has difficulties to disentangle the single waves. Therefore, in the following on the one hand the model will be simplified, on the other hand several cuts will be applied to the data set to reduce the background contributions from non-resonant processes and to enhance the structures produced by resonance decays.

12.4.2 Simplifying the Model

In a first step, the number of free parameters in the fit is reduced by omitting the waves with $J > \frac{5}{2}$. These waves couple only weakly into $p\pi^0$ and thus could be absorbed by the constant background term. The number of free parameters in the fit is reduced from 18 to 12. The result for the single waves and their coherent sum is shown in figure 12.27. Like the full

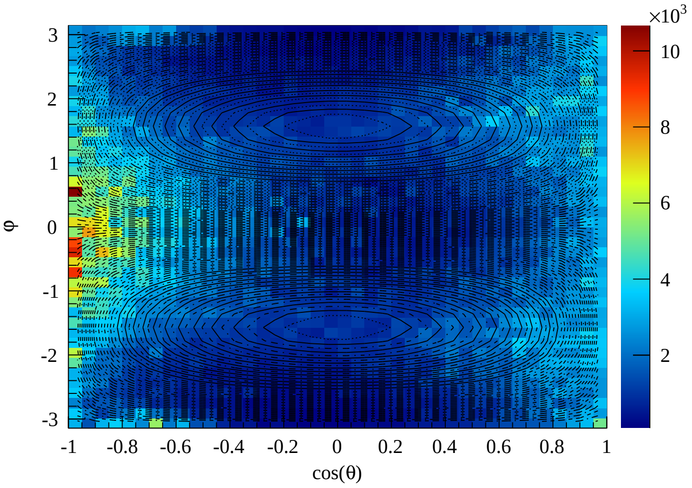

Figure 12.26: Fit result in bin 17 ($1700 - 1725\,\mathrm{MeV/c^2}$). The result is dominated by the $J = \frac{1}{2}$ waves.

model, this reduced model does not show any resonant structures in the single waves. Also in the relative phase between $\frac{1}{2}^+$ and $\frac{1}{2}^-$, which is shown in figure 12.28, no improvement is visible compared to the fit with the full data set. Therefore, this approach will not be followed any further

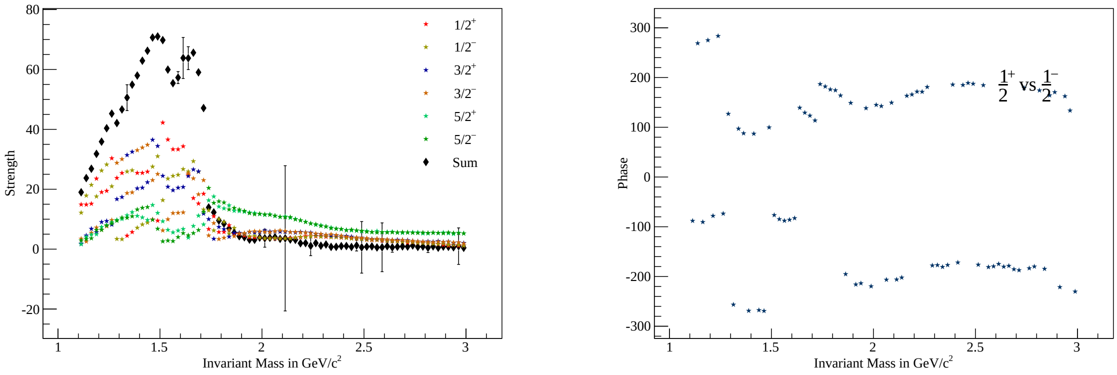

Figure 12.27: Fit result for the single waves and the coherent sum for the reduced model without any additional cuts.

Figure 12.28: Relative phase between $\frac{1}{2}^+$ and $\frac{1}{2}^-$ in degrees for a fit to the data using the reduced model. No error bars are shown due to large errors of the single phases.

As shown above, the structures due to resonances are not very pronounced in the angular distributions. To enhance the structures it is possible to enlarge the statistics in the angular distributions. Therefore, the number of mass bins is reduced by a factor of two, i. e. the fit is done in 38 mass bins of $50\,\mathrm{MeV/c^2}$ each. The result for the full model is shown in figure 12.29, the relative phase between $\frac{1}{2}^+$ and $\frac{1}{2}^-$ in figure 12.30. The result does not look promising for further analyses. In addition, the typical width of a baryon resonance would now only be three to four bins and thus not easy to fit in a second step. Therefore, this approach will not be followed any longer.

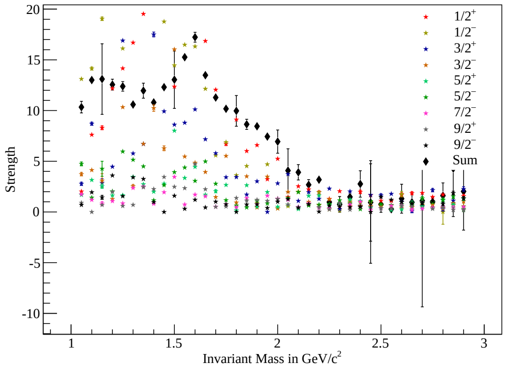

Figure 12.29: Fit result for the single waves and the coherent sum for the full model without any additional cuts in 38 mass bins.

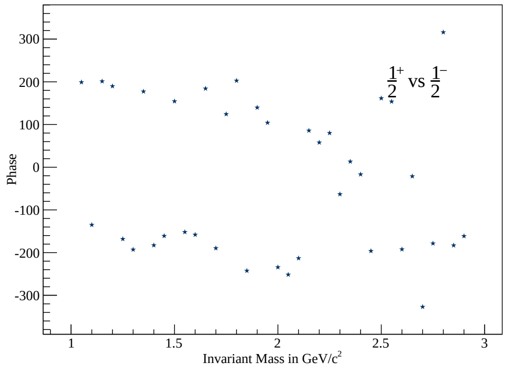

Figure 12.30: Relative phase between $\frac{1}{2}^+$ and $\frac{1}{2}^-$ in degrees for a fit to the data using the full model in 38 mass bins. No error bars are shown due to large errors of the single phases.

12.4.3 Reducing the Background

In this section, different approaches to reduce the amount of background in the data set are discussed. Two cuts will be tested, namely a cut on the proton momentum and a cut on the $\cos(\theta)$ distribution, both are done to reduce the amount of centrally produced pions in the data set. Finally, both cuts will be combined. Details are given in the following.

In the COMPASS central production analysis [164] a cut on the momentum of the fast proton of $p(p_f) > 140\,\text{GeV}/c$ is performed to enhance centrally produced $\pi^+\pi^-$ and K^+K^- events. In this analysis the contribution of central production should be reduced and thus, the cut is inverted and a momentum of $p(p_f) < 140\,\text{GeV}/c$ is required. With this cut, the number of events used in the analysis is reduced by more than a factor of two, 4,283,925 events survive the cut. The effect of the cut can be seen in figure 12.31. After the cut, the high mass tail of the invariant mass distribution is reduced and the ratio of the peak height to the background is enlarged.

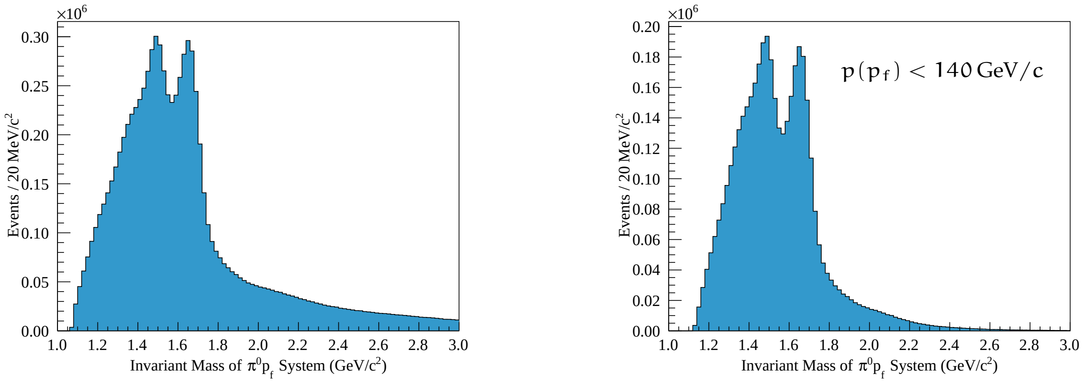

Figure 12.31: Invariant mass of $p\pi^0$ before (left) and after (right) the cut on the proton momentum.

In figure 12.32 the outcome of the fit for the full model is shown, figure 12.33 shows the relative phase between $\frac{1}{2}^+$ and $\frac{1}{2}^-$. The coherent sum does not resemble the invariant mass distribution properly. In addition, the phase correlation, which was observed for the full data set, is nearly lost. For higher invariant masses the errors on the waves and the coherent sum are larger, which is due to the reduced statistics in this region.

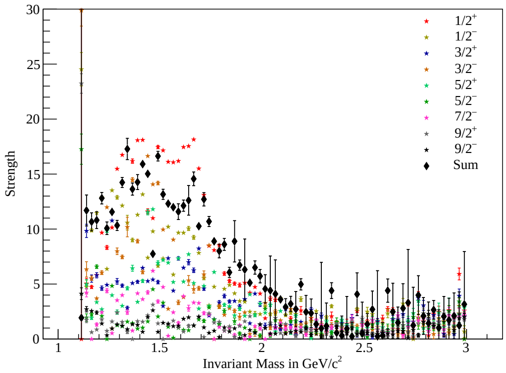

Figure 12.32: Fit result for the single waves and the coherent sum for the full model with cut on proton momentum.

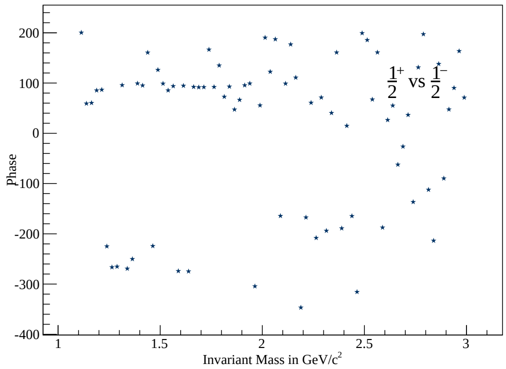

Figure 12.33: Relative phase between $\frac{1}{2}^+$ and $\frac{1}{2}^-$ in degrees for a fit to the data using the full model with a cut on the proton momentum. No error bars are shown due to large errors of the single phases.

Most of the intensity is again found in the $\frac{1}{2}^{\pm}$ waves. Especially the high-J waves only carry a small intensity. This was expected to some extend as the cut reduces the amount of central production events, which tend to have higher orbital angular momentum between the outgoing proton and the pion produced in $\pi^{0*}\mathbb{P}$ scattering.

Pions which are produced in a pion exchange process tend to go backwards in the Gottfried-Jackson frame. This produces a large peak at -1 in the angular distributions (see figure 8.4). Therefore, in a next step the first four bins ($-1 < \cos(\theta) < -0.8$) are excluded from the fit to be more sensitive on structures due to directly produced resonances. The outcome of the fit with the full model is shown in figure 12.34, the relative phase between $\frac{1}{2}^+$ and $\frac{1}{2}^-$ in figure 12.35. The invariant mass distribution is resembled by the fit, which shows that this fit describes the data better than the fit with a cut on the proton momentum. However, again no resonant structures can be observed in the single waves and the phase correlation between $\frac{1}{2}^+$ and $\frac{1}{2}^-$ is completely lost.

In the next step the two cuts discussed above are combined and the fit is performed on the data set with the momentum cut where we in addition exclude the first four bins in $\cos(\theta)$. The single waves and their coherent sum are shown in figure 12.36, the relative phase between $\frac{1}{2}^+$ and $\frac{1}{2}^-$ in figure 12.37. Again, the invariant mass distribution is not described by the fit and no phase correlation is observed.

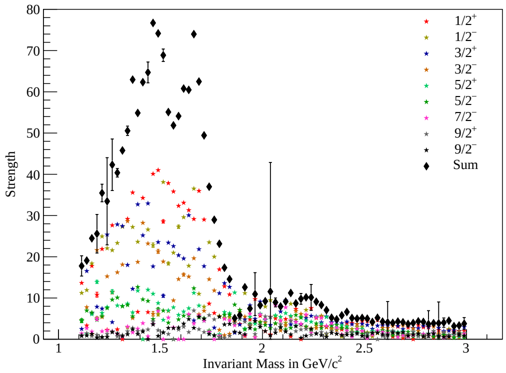

Figure 12.34: Fit result for the single waves and the coherent sum for the full model with excluded backward peak.

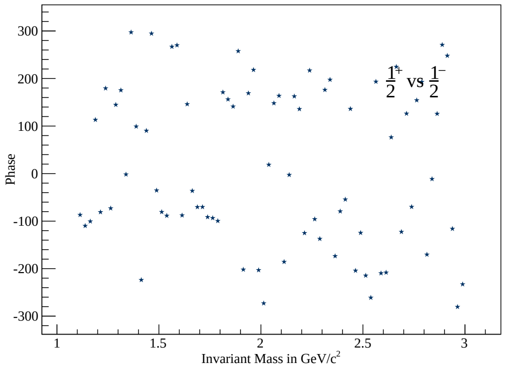

Figure 12.35: Relative phase between $\frac{1}{2}^+$ and $\frac{1}{2}^-$ in degrees for a fit to the data using the full model with a cut on the $\cos(\theta)$ distribution. No error bars are shown due to large errors of the single phases.

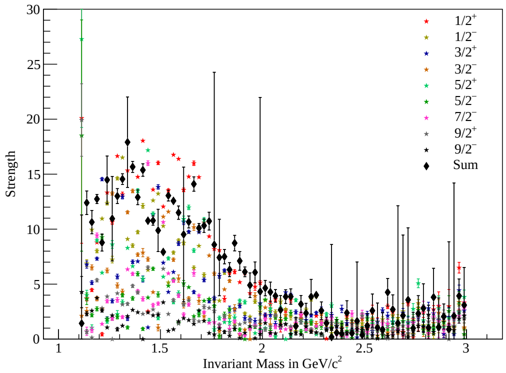

Figure 12.36: Fit result for the single waves and the coherent sum for the full model with momentum cut and excluded backward peak.

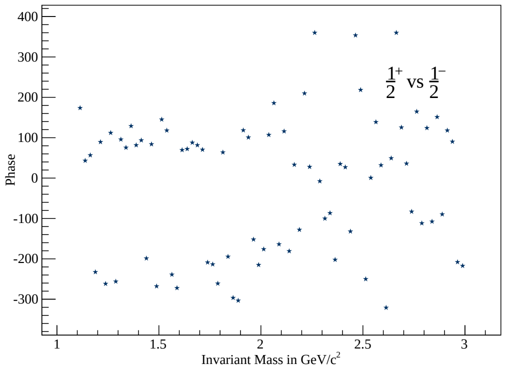

Figure 12.37: Relative phase between $\frac{1}{2}^+$ and $\frac{1}{2}^-$ in degrees for a fit to the data using the full model with a cut on the $\cos(\theta)$ distribution and the proton momentum. No error bars are shown due to large errors of the single phases.

12.5 CONCLUSION

In section 12.3 I have shown that the developed fit program is capable of fitting partial waves to distributions that were sampled using the model constructed using equation (12.5). However, the very same fit program cannot disentangle the partial waves in the real data distributions in a proper way. The fits shown in section 12.4 do not show any resonant structures at the expected positions (and also not at other positions) which could be fitted in a second step of the analysis. The relative phases between the single waves do not show the expected rapid phase motions due to resonances. Neither cuts on the data nor variations of the model lead to real improvements in the fit results.
The reasons may lie in the following shortcomings of the model:

1. The background in the model is described by a single constant parameter (see equation 12.9). Contrary to this simple approach, the background observed in data has an

angular dependence (see figure 8.4), which cannot be described by a single parameter. Therefore, intensity from the background is distributed among the single partial waves.

2. The model used in this analysis only describes the decay of the resonance. This simple ansatz seems to be not sufficient to describe the complete process. The azimuthal angle φ in the Gottfried-Jackson frame, which is used in the Wigner functions, is the angle between the production plane of the resonance and the decay plane of the resonance (see figure 12.1), i. e. the angle is correlated to the formation of the resonance which is not included in the model.

In the following chapter the non-resonant processes in $pp \to pp\pi^0$ will be discussed to get an estimate for the background contribution in the partial wave analysis. Afterwards, an alternative approach for a partial wave analysis of $pp \to pp\pi^0$ will be presented.

13

SINGLE PION PRODUCTION IN PROTON-PROTON REACTIONS

The simple partial wave analysis approach, which was presented in the previous chapter, did not yield any sensible results on the data. This is most likely due to the large contribution from non-resonant backgrounds, which have an angular distribution by themselves. The non-resonant production of single π^0 in $pp \to pp\pi^0$ is calculated in [165] for RHIC ($\sqrt{s} = 500\,\mathrm{GeV}$) and LHC ($\sqrt{s} = 14\,\mathrm{TeV}$) energies. In this chapter the main ideas of the calculation will be presented and compared with COMPASS data. The goal is to understand the contribution of background as well as resonances to the invariant mass spectrum, which is shown again in figure 13.1. The most striking features of the spectrum are the two peaks, which may stem from different resonances (compare section 8.1), and the rapid decline after the second peak.

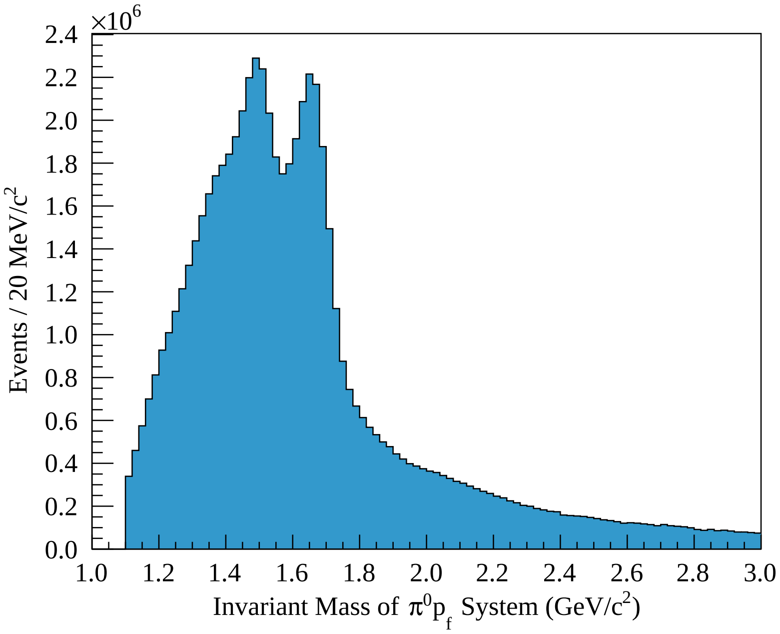

Figure 13.1: Invariant Mass of $p\pi^0$. The spectrum shows two peaks followed by a rapid decline.

13.1 PRODUCTION MECHANISMS

For the production of single π^0 in $pp \to pp\pi^0$ several mechanisms are possible, namely diffractive dissociation (compare section 1.3.3), photon-photon and omega-photon fusion processes, and photon-odderon fusion, where the odderon $\mathbb{O}$ is the $C = -1$ partner of the pomeron [166]. At COMPASS energies ($\sqrt{s} \approx 19.5\,\mathrm{GeV}$), diffractive dissociation (also called diffractive bremsstrahlung in this context) is the dominant contribution to the total cross section and will be discussed in the following.

The dominant mechanism for diffractive bremsstrahlung is the Drell-Hiida-Deck mechanism [167, 168]. At large $\sqrt{s}$ diffractive processes are dominated by pomeron exchange, the possible contributions are shown in figure 13.2. Here, only reactions on the beam proton are taken into account, as reactions on the target proton are not part of the data set used in this thesis.

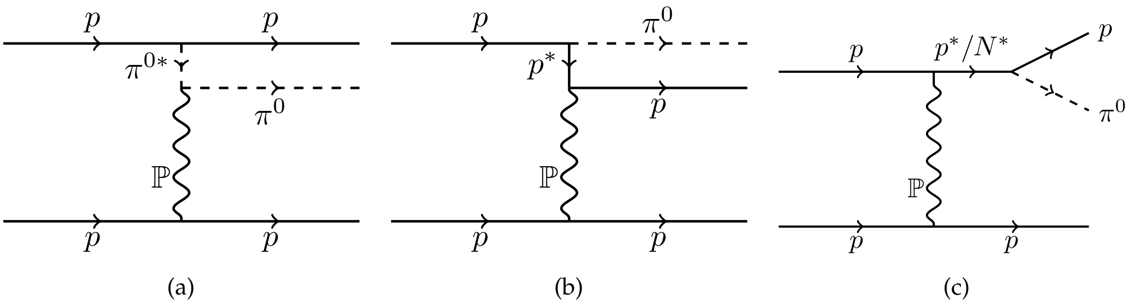

Figure 13.2: The diffractive bremsstrahlung processes: (a) pion exchange, (b) proton exchange, (c) direct production.

In addition, these are suppressed in fixed-target experiments. However, in a collider the role of the protons is interchangeable. Reactions 13.2a and 13.2b are exchange reactions of virtual particles which are put on-shell by the pomeron. Processes of type (a) are sometimes referred to as central production. In the direct production channel 13.2c non-resonant off-shell protons (p^*) as well as resonances (N^*) can be produced.
In [165] the cross sections for the three processes in figure 13.2 are calculated as a function of different kinematic variables for RHIC ($\sqrt{s} = 500\,\text{GeV}$) and LHC ($\sqrt{s} = 14\,\text{TeV}$) energies. In the direct production channel 13.2c only non-resonant contributions are taken into account and no resonances are included in the calculations.

13.2 RESULTS AND COMPARISON TO DATA

Figure 13.3 shows the result of the calculation in [165] of the differential cross section for the different production mechanisms as a function of the rapidity y_π (see equation (1.53)) of the π^0. The solid black line shows the contribution from bremsstrahlung, the dashed purple and dotted blue line the contributions from $\gamma\omega$ and $\gamma\gamma$ exchange, respectively. The different line widths correspond to $\sqrt{s} = 45\,\text{GeV}$ (ISR), $\sqrt{s} = 500\,\text{GeV}$ (RHIC) and $\sqrt{s} = 14\,\text{TeV}$ (LHC) from thin to thick. For lower centre-of-mass energies, the diffractive processes are the dominant contribution to the cross section. This rapidity distribution can now be compared with the

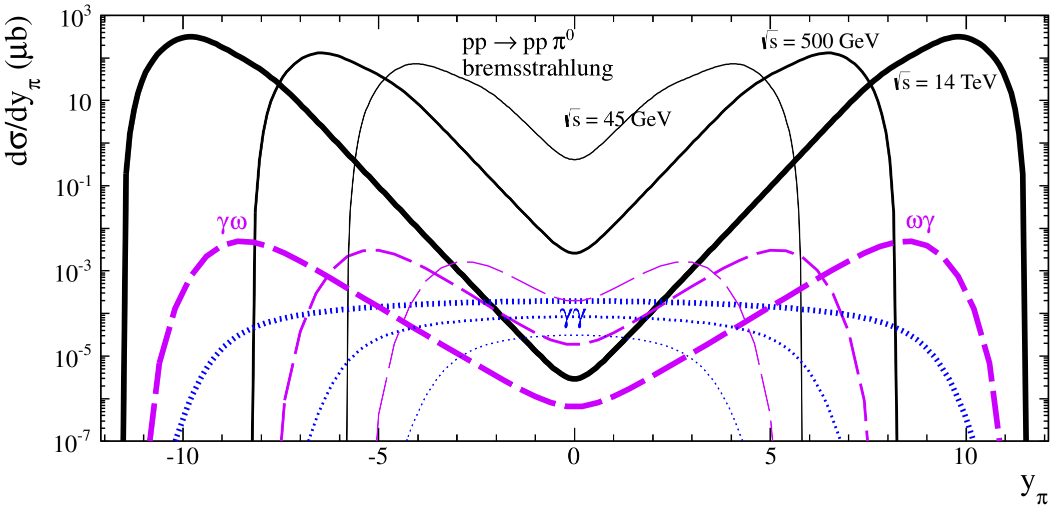

Figure 13.3: Rapidity of the π^0 in $pp \to pp\pi^0$ for different production mechanisms (denoted by different colours) and different centre-of-mass energies (denoted by different line widths). The figure is taken from [165].

one measured at COMPASS, which is shown in figure 13.4:

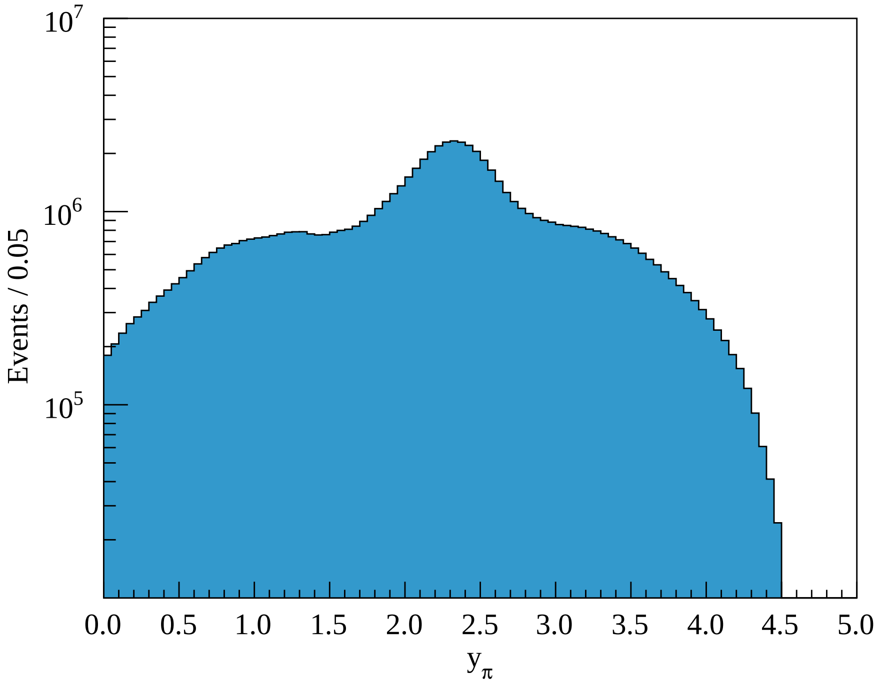

Figure 13.4: Rapidity of the π^0 in $pp \to pp\pi^0$ measured at COMPASS.

- Due to the fixed target geometry, only positive rapidity values are inside of the acceptance of the COMPASS spectrometer.
- Comparing to the theory calculations in figure 13.3, the shape of the distribution is similar, the maximum value is $y_\pi \approx 4.5$, which is smaller than for the experiments with higher centre-of-mass energies.
- The measured rapidity distribution has a peak around 2.4. This peak is a hint for the production of resonances, which seem to be dominantly produced in this kinematic region.

13.2.1 Background Contribution in the Invariant Mass Distribution

The best comparison between theory results and data can be done in the invariant mass distribution of $p_f\pi^0$. In figure 13.5 the calculated invariant mass distribution for diffractive bremsstrahlung from [165] is shown on the left in comparison to COMPASS data in the same scale on the right.

The form of the invariant mass spectrum can be understood as non-resonant diffractive π^0 production with additional resonance production in the low mass region. The exponential decay of the measured spectrum is very similar to the calculation although the slope is smaller. This can be a hint on further resonant contributions at higher masses. Now, that the shape of the non-resonant contributions is known, it can be used to estimate the amount of background in the mass spectrum. The functional form of the bremsstrahlung processes as a function of mass is not given in [165] (they only give the matrix elements, from which the

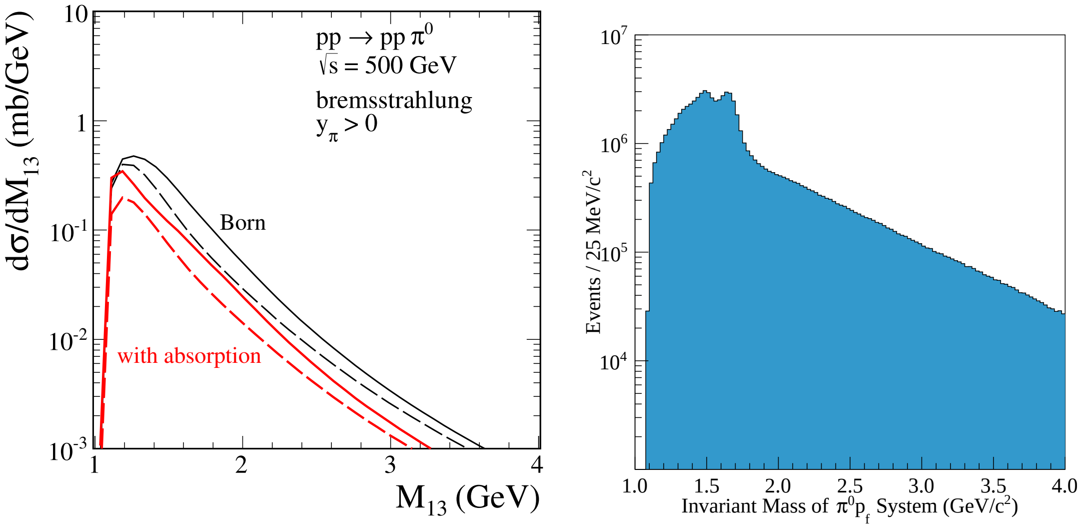

Figure 13.5: The theory calculation for the invariant mass of $p_f\pi^0$ (left, only bremsstrahlung) together with COMPASS data (right). The dashed lines correspond to a different choice of free QCD parameters, the red lines include one photon exchange diagrams. For details see [165].

mass dependence can be derived). Therefore, the non-resonant pion production as a function of the invariant $p\pi^0$ mass is parametrised as

$$\mathcal{F}(m_{p\pi}) = (m_{p\pi} - m_{thr})^n \exp\left[-a(m_{p\pi} - m_{thr})\right], \tag{13.1}$$

where $m_{thr} = 1073.249\,\text{MeV}/c^2$ is the $p\pi^0$ threshold. This function is fitted to the high mass tail of the $p\pi^0$ mass spectrum and extrapolated to the resonance region. The fits are performed in bins of the momentum transfer t'. In figure 13.6 two examples[1] are shown for $0.1 \leqslant t\prime < 0.2\,\text{GeV}^2/c^2$ (left) and $0.6 \leqslant t\prime < 0.7\,\text{GeV}^2/c^2$ (right). The different colours denote different ranges in which the fit is performed. The dashed lines show the extrapolation of the single fits into the resonance region. For the higher t' regions (right panel of 13.6) the choice of the fit range has no large influence on the extrapolation, in the lower t' region (left panel of 13.6) the influence is clearly visible. For lower limits of the fitting range of $2.2\,\text{GeV}/c^2$ and below, the shape of the background function changes compared to higher limits, where the shape does not change much. By eye, the blue curve (lower limit of $2.2\text{GeV}/c^2$) seems to describe the background shape reasonably for all t' bins.

To estimate the non-resonant contribution beneath the resonances, the extrapolated fit curves are compared to the mass distribution in the region between threshold and $3\,\text{GeV}/c^2$. The background contribution is given as the ratio of the integral of the extrapolated function and the total number of events in that mass region. The ratios in bins of t' for the different fit regions are shown in figure 13.7. For all fits, the background contribution is at least 15% in all bins of the momentum transfer. If again the blue curve is assumed to be the most suited one, the background contribution is larger than 20%.

---

[1] The fits in the full set of t' bins is given in appendix F.

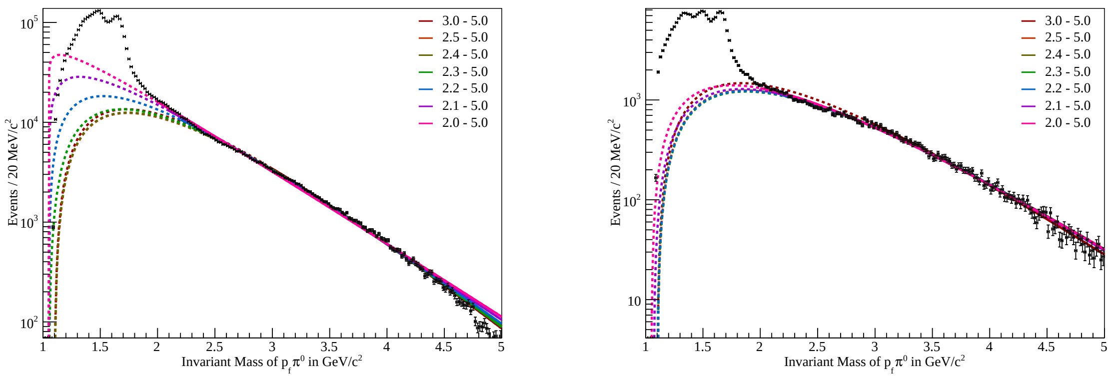

(a) $0.1 \leqslant t\prime < 0.2\,\mathrm{GeV}^2/c^2$ (b) $0.6 \leqslant t\prime < 0.7\,\mathrm{GeV}^2/c^2$

Figure 13.6: Fits of the non-resonant background contribution to the invariant mass spectrum of $p\pi^0$ in bins of the momentum transfer t'. Different colours denote different fit ranges in the invariant mass.

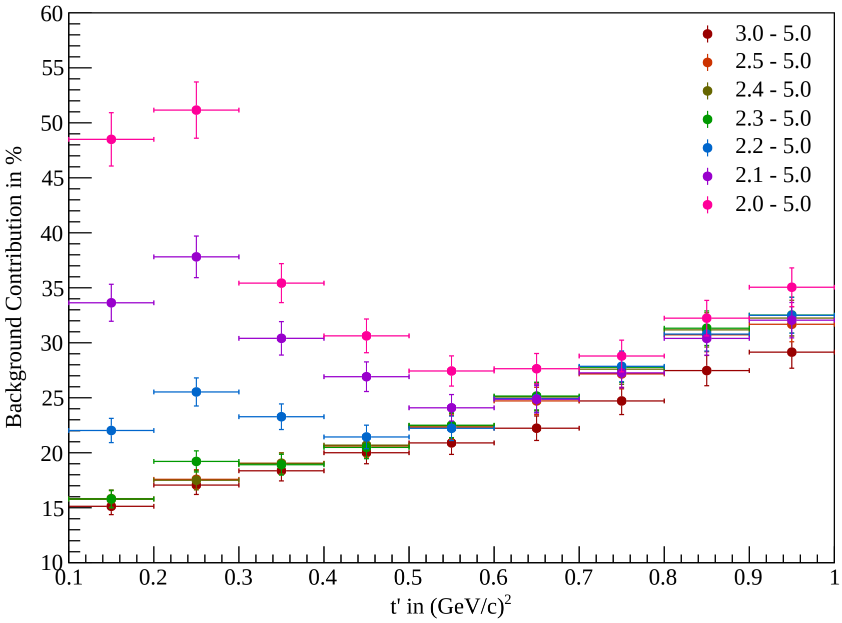

Figure 13.7: Contribution from non-resonant bremsstrahlung processes in % as a function of t'. The different colours denote different fit regions in the invariant mass of $p\pi^0$.

13.3 INCLUSION OF RESONANCES IN THE THEORY

The inclusion of resonances in the theoretical description of this channel is not an easy task. Nevertheless, there exists an approach which includes single and double Reggeon (Pomeron) exchange for LHC data [169, 170]. In the calculation, only the resonances of the Regge-trajectory of the proton, namely N(1680), N(2220) and N(2700) as well as the N(1440) are included. A theory prediction for the differential cross section as a function of the squared pion-proton mass is shown in figure 13.8 (left panel) together with COMPASS data (right panel). Although the calculation is done for $\sqrt{s} = 1.8\,\mathrm{TeV}$ the main features are quite similar in calculation and measured data.

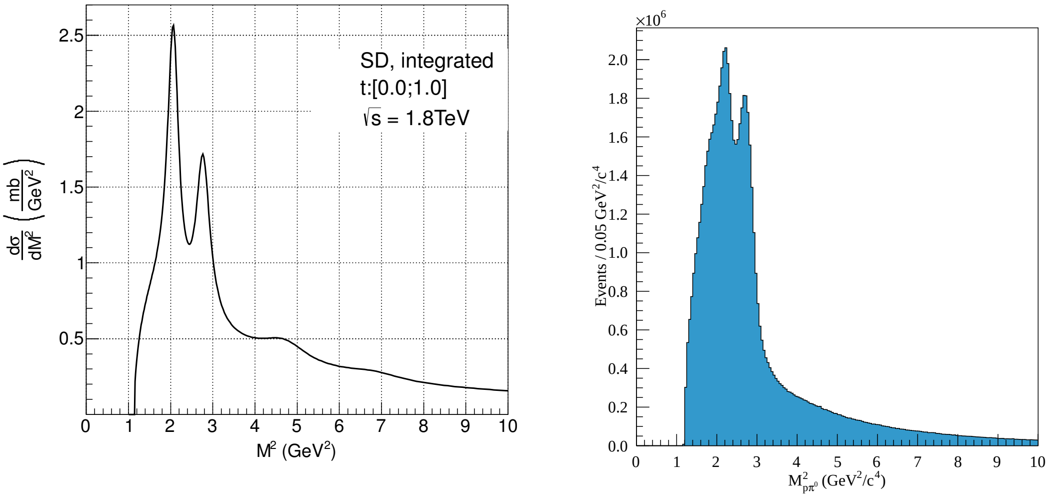

Figure 13.8: The theory calculation for the square of the invariant mass of $p_f\pi^0$ (left, only single Reggeon exchange) together with COMPASS data (right).

13.4 CONCLUSION

The form of the $p\pi^0$ invariant mass spectrum (see figure 13.1) from $pp \rightarrow pp\pi^0$ can be understood as non-resonant diffractive pion production together with resonances in the low mass region (below $2\,\text{GeV}/c^2$). The calculations done in [165] could also be done for COMPASS energies but have not been performed so far. However, the matrix elements for the different processes are known and can be used for a proper description of the non-resonant background in a partial wave analysis. For such an inclusion, a description of the resonances is needed that includes the full process (formation and decay of the resonance). A possible approach, which is loosely based on the MAID model (compare section 10.3), will be presented in the following chapter.

14

ALTERNATIVE APPROACH FOR PARTIAL WAVE ANALYSIS

A simple approach for a partial wave analysis of $pp \to pp\pi^0$, which only models the decay of the resonance to $p\pi^0$, was presented and tested in chapter 12. This approach did not yield sensible results due to the large non-resonant background, which was estimated to be of the order of 20% in chapter 13. To account for this background contribution, a model for a partial wave analysis is needed, which takes the full process (production and decay of the resonance) into account. In such a model, a proper inclusion of background amplitudes is possible.

14.1 THE PARTIAL WAVE AMPLITUDE

After a discussion with baryon experts in Mainz, a new model was proposed by A. Fiks [171], which is partly inspired by the model used in the MAID analysis (see section 10.3). In this model the complete reaction, i. e. the formation of the resonance in single-Pomeron exchange and the decay of the resonance to $p\pi^0$, is described. The resonant production of N^* in the diffractive scattering of protons

$$p(E,\vec{p}) + p(E,-\vec{p}) \to p(E_1',\vec{p}_1') + p(E_2',\vec{p}_2') + \pi^0(\omega_\pi,\vec{q}_\pi) \qquad (14.1)$$

in the pp centre-of-mass frame is shown in figure 14.1, where $\vec{p}$ is the momentum of the incident proton, $\vec{p}_1'$ and $\vec{p}_2'$ are the momenta of the fast proton and the recoiling proton, respectively and $q = (\omega_\pi, \vec{q}_\pi)$ is the four-momentum of the π^0. The spin projections m_i, m_f, m, m' of the protons are $\pm\frac{1}{2}$. In this reaction there are five independent kinematic variables, which will be chosen as follows:

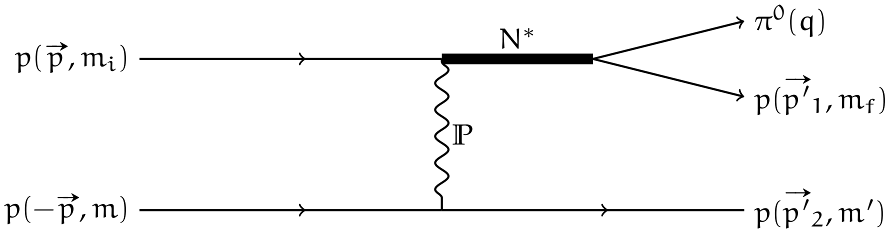

Figure 14.1: Diffractive production of N^* resonances in proton diffraction.

- The invariant mass $\mathcal{M}_{\pi p}$ of pion and fast proton p_1'.
- The direction of the π-p_1'-system (or equivalently the direction of the recoil proton p_2'), in the following denoted by the two angles $\Omega = (\theta, \varphi)$.
- The direction of the outgoing pion in the Gottfried-Jackson frame, again denoted by two angles $\Omega_\pi^* = (\theta_\pi^*, \varphi_\pi^*)$.

Additional kinematic variables appearing in the following (e. g. Mandelstam variables) are not independent and can be expressed by those five variables. The fivefold differential cross section for this reaction is then given as

$$\frac{d\sigma}{d\mathcal{M}_{\pi p}\, d\Omega\, d\Omega_\pi^*} = \frac{1}{(2\pi)^5} \frac{2M_N^4 p_2' q}{E^2 p} \sum_{S_i, M_i, S_f, M_f} |T_{S_i,M_i,S_f,M_f}|^2 \,, \qquad (14.2)$$

where the total spins of the initial and final state are given by $S_{i,f} = 0, 1$ with $M_{i,f} = -S_{i,f}, \ldots, S_{i,f}$. The amplitude $T_{S_i,M_i,S_f,M_f}(\mathcal{M}_{\pi p}, \Omega, \Omega^*_\pi)$ is given as a sum over the different N^* resonances with spin-parity $J^\mathcal{P}$

$$T_{S_i,M_i,S_f,M_f}(\mathcal{M}_{\pi p}, \Omega, \Omega^*_\pi) = \sum_{N^*(J^\mathcal{P})} \sum_{m_i,m_f,m,m',m_\pi,m_\mathbb{P},M_J}$$

$$\left(\frac{1}{2}m_i, \frac{1}{2}m\middle|S_i M_i\right)\left(\frac{1}{2}m_f, \frac{1}{2}m'\middle|S_f M_f\right)\left(\frac{1}{2}m_i, L_\mathbb{P} m_\mathbb{P}\middle|J M_J\right)\left(\frac{1}{2}m_f, L_\pi m_\pi\middle|J M_J\right) \tag{14.3}$$

$$\frac{f_{\mathbb{P}NN^*} f_{\mathbb{P}NN}}{M_\pi^{L_\pi + L_\mathbb{P}}} \times F(\mathcal{M}_{\pi p}) f_{\pi N N^*} G_{N^*}(\mathcal{M}_{\pi p}) \times G_\mathbb{P}(t) \times (-1)^{m_\mathbb{P}} q^{[L_\pi]}_{m_\pi} p^{[L_\mathbb{P}]}_{-m_\mathbb{P}} .$$

The different contributions to this amplitude will be described in the following: The second sum in (14.3) runs over the spin projections of the four protons (m_i, m_f, m, m', compare figure 14.1), the spin projection of the resonance M_J and the projections m_π and $m_\mathbb{P}$ of the orbital angular momenta of the pion and the pomeron with respect to the proton. Those orbital angular momenta, L_π and $L_\mathbb{P}$, are fixed for a given $J^\mathcal{P}$ as shown in table 14.1.

$N^*(J^\mathcal{P})$	$S_{11}(\frac{1}{2}^-)$	$P_{11}(\frac{1}{2}^+)$	$P_{13}(\frac{3}{2}^+)$	$D_{13}(\frac{3}{2}^-)$	$D_{15}(\frac{5}{2}^-)$	$F_{15}(\frac{5}{2}^+)$
L_π	0	1	1	2	2	3
$L_\mathbb{P}$	1	0	2	1	3	2

Table 14.1: The orbital angular momenta of pion and pomeron for the lowest values of $J^\mathcal{P}$.

The four Clebsch-Gordan coefficients (in the given order) describe the couplings of

1. the beam proton and the target proton to the total spin S_i of the initial state,
2. the outgoing fast proton and the recoil proton to the total spin S_f of the final state,
3. the spin of the beam proton and the orbital angular momentum of the pomeron to the resonance with spin-parity $J^\mathcal{P}$ (formation of the resonance) and
4. the spin of the outgoing fast proton and the orbital angular momentum of the pion to the resonance (decay of the resonance).

The couplings $f_{\mathbb{P}NN^*}$ of the pomeron to the proton and the resonance and $f_{\mathbb{P}NN}$ of the pomeron to two protons are unknown (and thus arbitrary) constants. M_π is the mass of the π^0.

$F(\mathcal{M}_{\pi p})$ is a vertex form factor

$$F(\mathcal{M}_{\pi p}) = \frac{\Lambda^4}{\Lambda^4 - (\mathcal{M}^2_{\pi p} - M^2_{N^*})^2} , \tag{14.4}$$

with $\Lambda = 1.3\,\text{GeV}$ and the mass of the resonance M_{N^*}.

The coupling of the resonance to pion and proton $f_{\pi N N^*}$ is related to the $N^* \to \pi^0 N$ partial decay width as

$$\Gamma_{N^*}(\mathcal{M}_{\pi p}) = \frac{f^2_{\pi N N^*}}{4\pi} \frac{F^2(\mathcal{M}_{\pi p})}{\mathcal{M}_{\pi p}} \frac{2M_N}{M_\pi^{2L_\pi}} \frac{L_\pi!}{(2L_\pi + 1)!!} q^{2L_\pi + 1} , \tag{14.5}$$

where q is the momentum of the pion in the centre-of-mass frame as introduced above and $F(\mathcal{M}_{\pi p})$ is again the vertex form factor from eq. (14.4).

$G_{N^*}(\mathcal{M}_{\pi p})$ is the propagator of the resonance. Here a non-relativistic Breit-Wigner ansatz is chosen with

$$G_{N^*}(\mathcal{M}_{\pi p}) = \frac{1}{\mathcal{M}_{\pi p} - M_{N^*} + \frac{i}{2}\Gamma_{N^*}(\mathcal{M}_{\pi p})} \,. \tag{14.6}$$

The pomeron propagator is assumed to have the reggeized form (see chapter 1.3)

$$G_{\mathbb{P}}(t) = \left(\frac{s}{s_0}\right)^{\alpha(t)-1} \frac{\pi\alpha'}{\sin\left(\pi\alpha(t)\right)} \frac{e^{-i\pi\alpha(t)}}{\Gamma\left(\alpha(t)\right)} \,, \tag{14.7}$$

with $s_0 = 1\,\mathrm{GeV}^2$ and the Mandelstam variables

$$\begin{aligned} s &= 2\sqrt{\vec{p}'^2_1 + M_N^2} \\ t &= (E(N^*) - E)^2 - (\overrightarrow{N^*} - \vec{p})^2 \,. \end{aligned} \tag{14.8}$$

The parameters of the Regge trajectory are given as

$$\begin{aligned} \alpha(t) &= \alpha_0 + \alpha' t \\ \alpha_0 &= 1.08 \\ \alpha' &= 0.25\,\mathrm{GeV}^{-2} \,. \end{aligned} \tag{14.9}$$

The last two terms appearing in (14.3) are momenta $Q^{[L]}_M$ of rank L, which are determined as

$$Q^{[L]}_M = \sqrt{\frac{4\pi L!}{(2L+1)!!}} Q^L Y_{LM}(\theta_Q, \varphi_Q) \,, \tag{14.10}$$

where Y_{LM} are the spherical harmonics. The momenta are the centre-of-mass momentum $\vec{q}$ of the π^0 and the relative momentum $\vec{P}$ of the Pomeron and the beam proton that is calculated as

$$\vec{P} = \frac{\vec{p}_{\mathbb{P}} E - \vec{p} E_{\mathbb{P}}}{E + E_{\mathbb{P}}} \tag{14.11}$$

with he momentum and energy of the Pomeron

$$\vec{p}_{\mathbb{P}} = \overrightarrow{N^*} - \vec{p} \,, \quad E_{\mathbb{P}} = E(N^*) - E \,. \tag{14.12}$$

The model has two free parameters for each resonance, namely the mass M_{N^*} and the coupling constant $f_{\pi N N^*}$, which is related to the partial decay width (see equation (14.5)). Unfortunately, these parameters appear in the amplitude (14.3) in a complicated way and are thus not easy to extract. In addition, there are many kinematic variables (like momenta or Mandelstam variables) which are of course not independent but depend on the five chosen variables. Therefore, this model can only be fitted to data with a likelihood formalism. The inclusion of the experimental acceptance can then be achieved with an extended likelihood formalism, which will be described in the following.

14.2 THE EXTENDED LIKELIHOOD FORMALISM

In short-hand notation the cross section from (14.2) and (14.3) is given as

$$\Sigma(\tau) \equiv \frac{d\sigma}{d\tau} = \sum_{\alpha} \Big| \sum_{\beta} \tilde{T}_{\alpha\beta}(\tau) \Big|^2 , \tag{14.13}$$

where $\tau = (\mathcal{M}_{\pi p}, \Omega, \Omega^*_\pi)$ denotes the kinematic variables, $\alpha = (S_i, M_i, S_f, M_f)$ the incoherent summation variables and $\beta = (N^*(J^{\mathcal{P}}); m_i, m_f, m, m', m_\pi, m_{\mathbb{P}}, M_J)$ the coherent summation variables. $\tilde{T}$ in addition contains the kinematic factor $\frac{1}{(2\pi)^5} \frac{2M_N^4 p_2' q}{E^2 p}$.
The probability to observe an event with kinematic variables τ_i is given as

$$p_i = \frac{\Sigma(\tau_i)}{\int \Sigma(\tau)\mathcal{A}(\tau) d\tau} , \tag{14.14}$$

where the integral runs over the full phase space. The acceptance $\mathcal{A}(\tau)$ is the probability for an event with a given kinematics to be observed in the detector (see chapter 7). The simple likelihood function would then be the product of the probabilities for the single events

$$\mathcal{L}_0 = \prod_{i}^{N} p_i . \tag{14.15}$$

The number N of observed events in the experiment follows a Poisson distribution. This is taken into account by the extended likelihood formalism which includes the Poisson distribution in the calculation of the likelihood

$$\mathcal{L} = \frac{e^{-N_0} N_0^N}{N!} \mathcal{L}_0 = \frac{e^{-N_0} N_0^N}{N!} \prod_{i}^{N} p_i , \tag{14.16}$$

where the number N_0 of expected events is equal to the phase-space integral from equation (14.14)

$$N_0 = \int \Sigma(\tau)\mathcal{A}(\tau) d\tau . \tag{14.17}$$

The Poisson distribution has its maximum for $N = N_0$ and fixes the normalisation of the likelihood function. Details on this formalism can be for example be found in [172]. With the probabilities p_i from equation (14.14) the likelihood function simplifies as

$$\mathcal{L} = \frac{e^{N_0}}{N!} \prod_{i}^{N} \Sigma(\tau_i) , \tag{14.18}$$

which yields the more convenient logarithmic likelihood

$$\log \mathcal{L} = -\log N! - N_0 + \sum_{i}^{N} \log \Sigma(\tau_i) . \tag{14.19}$$

The number of observed events N does not depend on the cross section but only on the used data set. Thus, the term $-\log N!$ can be omitted in the likelihood calculation. The final extended log-likelihood function is then given as

$$\log \mathcal{L} = -\int \Sigma(\tau)\mathcal{A}(\tau) d\tau + \sum_{i}^{N} \log \Sigma(\tau_i) . \tag{14.20}$$

The acceptance $\mathcal{A}(\tau)$ only enters in the first term, the experimental data only in the second term. Therefore, the first term can be evaluated from Monte Carlo events. A large number N_{MC} of Monte Carlo events with kinematic variables $\tau_{i,MC}$ with a flat distribution in phase space are produced and reconstructed (see chapter 7). The phase space integral can then be sampled numerically with the Monte Carlo events as

$$\int \Sigma(\tau)\mathcal{A}(\tau)d\tau \approx \frac{\int d\tau}{N_{MC}} \sum_{i}^{N_{MC}} \Sigma(\tau_{i,MC})\mathcal{A}(\tau_{i,MC}), \tag{14.21}$$

where the normalisation factor contains the phase space volume $\int d\tau$ [173].
Unfortunately, in this approach the free parameters M_{N^*} and $f_{\pi NN^*}$ are contained in the cross section $\Sigma(\tau)$ in a complicated way and thus, the phase space integral (14.21) has to be calculated in every single step of the likelihood calculation[1]. Therefore, the minimisation of the log-likelihood becomes expensive in computing time as it scales – in addition to the number of events in data – with the number of Monte Carlo events.

14.3 A FIRST FIT ATTEMPT

A Likelihood fit with more than eight million events is not possible in a reasonable time without a proper parallelisation of the likelihood calculation. Thus, I tried the same method as in the previous analysis, namely to do a fit in mass bins. For that, the mass dependent part

$$F(\mathcal{M}_{\pi p})f_{\pi NN^*}G_{N^*}(\mathcal{M}_{\pi p}) \tag{14.22}$$

was taken out of the amplitude (14.3) and substituted by a complex parameter. The modulus and phase of this parameter (one for each combination of $J^{\mathcal{P}}$) are then fitted with a simple likelihood fit in 25 MeV/c^2 mass bins of the invariant $p\pi^0$ mass $\mathcal{M}_{\pi p}$. From the result of those fits it should then be possible to extract the resonance parameters with a sophisticated fit. For a first test ten fit attempts were performed in each bin. Unfortunately, the fits did not give any promising results. In figure 14.2 as an example the result for $J^{\mathcal{P}} = \frac{3}{2}^-$ is shown. The dark blue line shows the result of the best fit, the light blue band gives the range of all ten fits. Errors are omitted as they are quite large. The red lines denote the nominal position of resonances for this $J^{\mathcal{P}}$. It is clearly visible, that the best fit does not show any sensible result, although the range of fits includes fits, which follow the distribution of the full invariant mass spectrum.

---

[1] In many analyses – for example in [173] – the free parameters can be factored out and the phase space integral becomes a constant for each event.

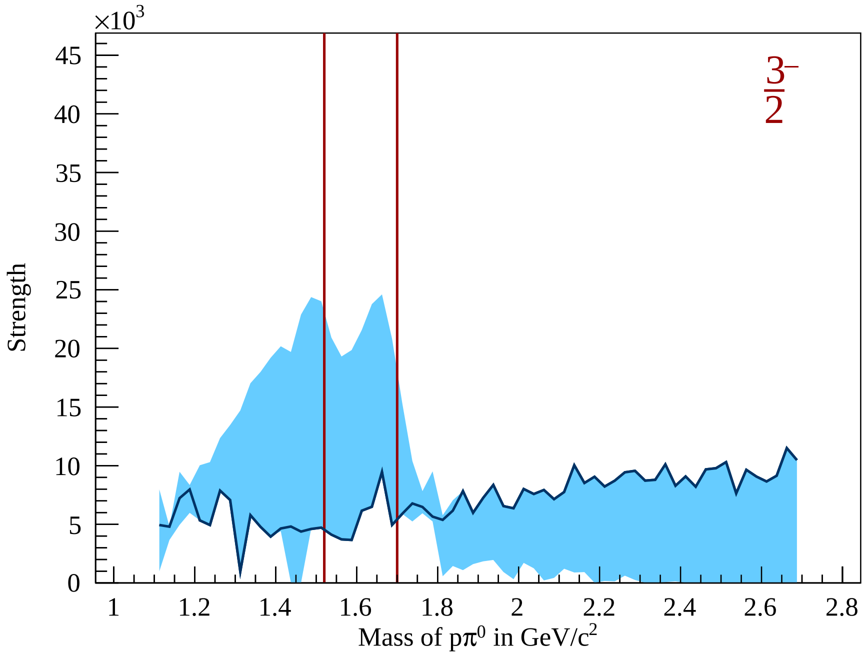

Figure 14.2: Fit result for the $J^{\mathcal{P}} = \frac{3}{2}^-$ channel. The dark blue line is the best fit, the light blue band gives the range of results for all fits. The red lines denote expected resonances.

14.4 CONCLUSION ON THIS APPROACH

Although the first fit attempt did not yield a promising result, this approach should be considered further. However, there are still some things which have do be done:

- The cross section (14.2) only includes the resonance amplitude (14.3). The background contributions discussed in chapter 13 are not included, but, in this approach an inclusion should be possible.
- For a proper extended likelihood fit, the Monte-Carlo statistics has to be improved. The number of used Monte Carlo events should be optimised in this case. A sufficient statistics is needed to ensure a smooth acceptance correction, but the computation time for the phase space integrals depends on the number of Monte Carlo events.
- The fit has to be done on the full number of events including the full description of the resonances. As stated above, the calculation of likelihoods for more than eight million events needs an appropriate handling of computer resources such as parallelisation of the calculation, which also should help in the calculation of the phase space integrals.

In summary, this approach is surely promising and has a potential to yield physics results, especially if the background description is fully included. Unfortunately, this project exceeds the time scale of this thesis.

SUMMARY – PARTIAL WAVE ANALYSIS OF $p\pi^0$ FINAL STATES

In chapter 12 a simple approach for the partial wave analysis of $pp \rightarrow pp\pi^0$ was presented. The helicity formalism was used to parametrise only the decay of a resonance in a $p\pi^0$ final state. A program was developed and several tests were performed on simulated angular distributions. The developed program proved to be capable to fit a large number of $J^{\mathcal{P}}$ states together. However, the simple approach failed to describe the measured angular distributions. This can be attributed to the large non-resonant background, which was estimated to be of the order of 20% by comparing the measured invariant mass distribution to a theory calculation (see chapter 13). Several cuts were tested to reduce the background contribution in the angular distributions, but non of those led to a sensible result in the partial wave fits. Therefore, the simple approach will not be considered any further. In chapter 14 an alternative approach for a partial wave analysis was shown. This time, the full process $pp \rightarrow pp\pi^0$ including the Pomeron exchange, the formation and the decay of the resonance was parametrised. The parametrisation contains a large number of kinematic variables (of which only five are independent) and thus a simple fit of angular distributions is no longer possible. The fits in this case have to be done with an extended likelihood formalism, which also takes the acceptance calculation into account. The advantage of this approach is the possible inclusion of correctly parametrised non-resonant contributions, which could be done in the future. However, with some effort and sufficient computing resources this approach seems very promising.

CONCLUSION AND OUTLOOK

Nihil tam difficile est, quin quaerendo investigari possit – I worked on several topics, some of them turned out to be more complicated than expected. Nevertheless, I obtained good results in some parts and deeper insights in others. Still, there are many possibilities to continue the work I have begun here.

I BEAM PARTICLE IDENTIFICATION WITH STATISTICAL METHODS

The newly developed likelihood method for the beam particle identification in the CEDAR detectors is clearly an improvement compared to the previously used multiplicity method. With the new method, the kaon identification efficiency is improved by ≈ 65% without losing purity. In addition, the method allows to identify pions with a good efficiency and purity. This method can be applied for future data takings; all tools that are needed are provided within the COMPASS software.

II PRODUCTION OF SINGLE MESONS IN pp REACTIONS

With the large available data set the determination of the cross section ratio $\sigma(\eta)/\sigma(\pi^0)$ was possible over a wide kinematic range. Results from previous experiments obtained in limited ranges could be improved due to a much better accuracy. The cross section ratio shows a resonant enhancement of π^0 production in the medium x_F range. The cross section ratio $\sigma(\phi)/\sigma(\omega)$ for vector mesons obtained in this thesis is compatible with a previous COMPASS analysis. The extracted cross section ratios can be used in the future for model building due to their small uncertainties. The presented analysis can be extended to η' and ρ mesons, which are more complicated to extract from the data. The data used in this work would also allow to study strangeness exchange reactions, such as $pp \to pK\Lambda$ or $pp \to pK\Sigma$.

III PARTIAL WAVE ANALYSIS OF $p\pi^0$ FINAL STATES

The $pp \to pp\pi^0$ data can also be used to study the production of baryon resonances. Although everything seemed to be easy in the beginning, it soon turned out that the channel $pp \to pp\pi^0$ is everything but simple. The simple approach for a partial wave analysis to only model the decay of the resonances proofed to be too naïve to describe the data. One reason for that is the non-resonant background, which turned out to be of the order of 20% and has an angular dependence. This angular dependence is not parametrised in the simple model. A comparison with theory calculations allowed to understand the invariant mass distribution qualitatively as a non-resonant background with resonances on top. An alternative model for partial wave analysis was developed, which describes the full reaction mechanism and therefore also allows to include a proper description of the background processes. However, applying this model to the available data still needs a larger amount of work, mainly due to the huge amount of data, which has to be treated properly during the fitting process to reduce the time consumption of the program. If the alternative method turns out to describe the data and yield results, an extension to the $p\eta$ final state should be possible without problems.

APPENDIX

A

SOME MATHEMATICS

A.1 THE GROUP SU(3)

The special unitary group of complex-valued 3×3 matrices with determinant $+1$ is a Lie group of dimension 8. The eight generators T_a of the corresponding Lie algebra $su(3)$ are for example given by the Gell-Mann matrices [13] λ_a via

$$T_a = \frac{\lambda_a}{2}\,. \tag{A.1}$$

The Gell-Mann matrices are traceless matrices and explicitly given as

$$\begin{aligned}
&\lambda_1 = \begin{pmatrix} 0 & 1 & 0 \\ 1 & 0 & 0 \\ 0 & 0 & 0 \end{pmatrix} \quad \lambda_2 = \begin{pmatrix} 0 & -i & 0 \\ i & 0 & 0 \\ 0 & 0 & 0 \end{pmatrix} \quad \lambda_3 = \begin{pmatrix} 1 & 0 & 0 \\ 0 & -1 & 0 \\ 0 & 0 & 0 \end{pmatrix} \\
&\lambda_4 = \begin{pmatrix} 0 & 0 & 1 \\ 0 & 0 & 0 \\ 1 & 0 & 0 \end{pmatrix} \quad \lambda_5 = \begin{pmatrix} 0 & 0 & -i \\ 0 & 0 & 0 \\ i & 0 & 0 \end{pmatrix} \quad \lambda_6 = \begin{pmatrix} 0 & 0 & 0 \\ 0 & 0 & 1 \\ 0 & 1 & 0 \end{pmatrix} \\
&\lambda_6 = \begin{pmatrix} 0 & 0 & 0 \\ 0 & 0 & 1 \\ 0 & 1 & 0 \end{pmatrix} \quad \lambda_8 = \frac{1}{\sqrt{3}} \begin{pmatrix} 1 & 0 & 0 \\ 0 & 1 & 0 \\ 0 & 0 & -2 \end{pmatrix}
\end{aligned} \tag{A.2}$$

The generators obey the following (anti-) commutator relations:

$$\begin{aligned}
&[T_a, T_b] = i f_{abc} T_c \\
&\{T_a, T_b\} = \frac{1}{3}\delta_{ab} + d_{abc} T_c
\end{aligned} \tag{A.3}$$

The structure constants f_{abc} are antisymmetric in all three indices and given as

$$\begin{aligned}
&f_{123} = 1 \\
&f_{147} = -f_{156} = f_{246} = f_{257} = f_{345} = -f_{367} = \frac{1}{2} \\
&f_{458} = f_{678} = \frac{\sqrt{3}}{2}\,,
\end{aligned} \tag{A.4}$$

where all combinations of abc which are not permutations of the ones given above lead to $f_{abc} = 0$. Similarly, the d_{abc} are symmetric in all three indices and the non-zero values are

$$\begin{aligned}
&d_{118} = d_{228} = d_{338} = -d_{888} = \frac{1}{\sqrt{3}} \\
&d_{448} = d_{558} = d_{668} = d_{778} = -\frac{1}{2\sqrt{3}} \\
&d_{146} = d_{157} = -d_{247} = d_{256} = d_{344} = d_{355} = -d_{366} = -d_{377} = \frac{1}{2}\,.
\end{aligned} \tag{A.5}$$

A.2 EXPLICIT FORM OF WIGNER D-FUNCTIONS

In the following tables, explicit forms of the Wigner (small) d-functions $d^J_{MM'}(\theta)$ are given for half-integer values of J. Only functions for certain combinations of M and M′ are listed, further functions can be calculated via

$$d^J_{MM'}(\theta) = (-1)^{M-M'} d^J_{M'M}(\theta) = -d^J_{-M'-M}(\theta) \tag{A.6}$$

All functions are taken from [174]. The $J = \frac{9}{2}$ functions are omitted as they are even more complicated.

$M \backslash M'$	$\frac{1}{2}$
$+\frac{1}{2}$	$\cos\left(\frac{\theta}{2}\right)$
$-\frac{1}{2}$	$\sin\left(\frac{\theta}{2}\right)$

Table A.1: $J = \frac{1}{2}$

$M \backslash M'$	$\frac{3}{2}$	$\frac{1}{2}$
$+\frac{3}{2}$	$\cos^3\left(\frac{\theta}{2}\right)$	$-\sqrt{3}\sin\left(\frac{\theta}{2}\right)\cos^2\left(\frac{\theta}{2}\right)$
$+\frac{1}{2}$	$\sqrt{3}\sin\left(\frac{\theta}{2}\right)\cos^2\left(\frac{\theta}{2}\right)$	$\cos\left(\frac{\theta}{2}\right)\left(3\cos^2\left(\frac{\theta}{2}\right)-2\right)$
$-\frac{1}{2}$	$\sqrt{3}\sin^2\left(\frac{\theta}{2}\right)\cos\left(\frac{\theta}{2}\right)$	$-\sin\left(\frac{\theta}{2}\right)\left(3\sin^2\left(\frac{\theta}{2}\right)-2\right)$
$-\frac{3}{2}$	$\sin^3\left(\frac{\theta}{2}\right)$	$\sqrt{3}\sin^2\left(\frac{\theta}{2}\right)\cos\left(\frac{\theta}{2}\right)$

Table A.2: $J = \frac{3}{2}$

M'	$M = \frac{5}{2}$	M'	$M = \frac{3}{2}$
$+\frac{5}{2}$	$\cos^5\left(\frac{\theta}{2}\right)$	$+\frac{3}{2}$	$\cos^3\left(\frac{\theta}{2}\right)\left(1-5\sin^2\left(\frac{\theta}{2}\right)\right)$
$+\frac{3}{2}$	$-\sqrt{5}\sin\left(\frac{\theta}{2}\right)\cos^4\left(\frac{\theta}{2}\right)$	$+\frac{1}{2}$	$-\sqrt{2}\sin\left(\frac{\theta}{2}\right)\cos^2\left(\frac{\theta}{2}\right)\left(2-5\sin^2\left(\frac{\theta}{2}\right)\right)$
$+\frac{1}{2}$	$\sqrt{10}\sin^2\left(\frac{\theta}{2}\right)\cos^3\left(\frac{\theta}{2}\right)$	$-\frac{1}{2}$	$-\sqrt{2}\sin^2\left(\frac{\theta}{2}\right)\cos\left(\frac{\theta}{2}\right)\left(2-5\cos^2\left(\frac{\theta}{2}\right)\right)$
$-\frac{1}{2}$	$-\sqrt{10}\sin^3\left(\frac{\theta}{2}\right)\cos^2\left(\frac{\theta}{2}\right)$	$-\frac{3}{2}$	$-\sqrt{2}\sin^2\left(\frac{\theta}{2}\right)\cos\left(\frac{\theta}{2}\right)\left(2-5\cos^2\left(\frac{\theta}{2}\right)\right)$
$-\frac{3}{2}$	$\sqrt{5}\sin^4\left(\frac{\theta}{2}\right)\cos\left(\frac{\theta}{2}\right)$	M'	$M = \frac{1}{2}$
$-\frac{5}{2}$	$-\sin^5\left(\frac{\theta}{2}\right)$	$\frac{1}{2}$	$\cos\left(\frac{\theta}{2}\right)\left(3-12\cos^2\left(\frac{\theta}{2}\right)+10\cos^4\left(\frac{\theta}{2}\right)\right)$
		$-\frac{1}{2}$	$-\sin\left(\frac{\theta}{2}\right)\left(3-12\sin^2\left(\frac{\theta}{2}\right)+10\sin^4\left(\frac{\theta}{2}\right)\right)$

Table A.3: $J = \frac{5}{2}$

M'	$M = \frac{7}{2}$
$+\frac{7}{2}$	$\cos^7\left(\frac{\theta}{2}\right)$
$+\frac{5}{2}$	$-\sqrt{7}\cos^6\left(\frac{\theta}{2}\right)\sin\left(\frac{\theta}{2}\right)$
$+\frac{3}{2}$	$\sqrt{21}\cos^5\left(\frac{\theta}{2}\right)\sin^2\left(\frac{\theta}{2}\right)$
$+\frac{1}{2}$	$-\sqrt{35}\cos^4\left(\frac{\theta}{2}\right)\sin^3\left(\frac{\theta}{2}\right)$
$-\frac{1}{2}$	$\sqrt{35}\cos^3\left(\frac{\theta}{2}\right)\sin^4\left(\frac{\theta}{2}\right)$
$-\frac{3}{2}$	$-\sqrt{21}\cos^2\left(\frac{\theta}{2}\right)\sin^5\left(\frac{\theta}{2}\right)$
$-\frac{5}{2}$	$\sqrt{7}\cos\left(\frac{\theta}{2}\right)\sin^6\left(\frac{\theta}{2}\right)$
$-\frac{7}{2}$	$-\sin^7\left(\frac{\theta}{2}\right)$
M'	$M = \frac{5}{2}$
$+\frac{5}{2}$	$\cos^5\left(\frac{\theta}{2}\right)\left(1-7\sin^2\left(\frac{\theta}{2}\right)\right)$
$+\frac{3}{2}$	$-\sqrt{3}\cos^4\left(\frac{\theta}{2}\right)\sin\left(\frac{\theta}{2}\right)\left(2-7\sin^2\left(\frac{\theta}{2}\right)\right)$
$+\frac{1}{2}$	$\sqrt{5}\cos^3\left(\frac{\theta}{2}\right)\sin^2\left(\frac{\theta}{2}\right)\left(3-7\sin^2\left(\frac{\theta}{2}\right)\right)$
$-\frac{1}{2}$	$\sqrt{5}\cos^2\left(\frac{\theta}{2}\right)\sin^3\left(\frac{\theta}{2}\right)\left(3-7\cos^2\left(\frac{\theta}{2}\right)\right)$
$-\frac{3}{2}$	$-\sqrt{3}\cos\left(\frac{\theta}{2}\right)\sin^4\left(\frac{\theta}{2}\right)\left(2-7\cos^2\left(\frac{\theta}{2}\right)\right)$
$-\frac{5}{2}$	$\sin^5\left(\frac{\theta}{2}\right)\left(1-7\cos^2\left(\frac{\theta}{2}\right)\right)$
M'	$M = \frac{3}{2}$
$+\frac{3}{2}$	$\cos^3\left(\frac{\theta}{2}\right)\left(10-30\cos^2\left(\frac{\theta}{2}\right)+21\cos^4\left(\frac{\theta}{2}\right)\right)$
$+\frac{1}{2}$	$-\sqrt{15}\cos^2\left(\frac{\theta}{2}\right)\sin\left(\frac{\theta}{2}\right)\left(2-8\cos^2\left(\frac{\theta}{2}\right)+7\cos^4\left(\frac{\theta}{2}\right)\right)$
$-\frac{1}{2}$	$\sqrt{15}\cos\left(\frac{\theta}{2}\right)\sin^2\left(\frac{\theta}{2}\right)\left(2-8\sin^2\left(\frac{\theta}{2}\right)+7\sin^4\left(\frac{\theta}{2}\right)\right)$
$-\frac{3}{2}$	$-\sin^3\left(\frac{\theta}{2}\right)\left(10-30\sin^2\left(\frac{\theta}{2}\right)+21\sin^4\left(\frac{\theta}{2}\right)\right)$
M'	$M = \frac{1}{2}$
$+\frac{1}{2}$	$-\cos\left(\frac{\theta}{2}\right)\left(4-30\cos^2\left(\frac{\theta}{2}\right)+60\cos^4\left(\frac{\theta}{2}\right)-35\cos^6\left(\frac{\theta}{2}\right)\right)$
$-\frac{1}{2}$	$-\sin\left(\frac{\theta}{2}\right)\left(4-30\sin^2\left(\frac{\theta}{2}\right)+60\sin^4\left(\frac{\theta}{2}\right)-35\sin^6\left(\frac{\theta}{2}\right)\right)$

Table A.4: $J = \frac{7}{2}$

A.3 BLATT-WEISSKOPF BARRIER FACTORS

The Blatt-Weisskopf barrier factors [157] describe the centrifugal barrier in a particle decay. They have been parametrised by von Hippel and Quigg [158]. In this work, a slightly different parametrisation given in [159] is used. In this parametrisation, the Blatt-Weisskopf factors are defined as

$$F_\ell(p) = \sqrt{\frac{\left|h_\ell^{(1)}(1)\right|^2}{\left|x h_\ell^{(1)}(x)\right|^2}} \qquad x = \frac{p}{p_R}, \tag{A.7}$$

where $x = \frac{p}{p_R}$ with $p_R = 0.1973\,\mathrm{GeV}/c$. The spherical Hankel functions of the first kind are solutions to Bessel's differential equation

$$x^2 \frac{d^2 h_\ell^{(1)}(x)}{dx^2} + x \frac{d h_\ell^{(1)}(x)}{dx} + \left[x^2 - \left(\ell + \frac{1}{2}\right)\right] h_\ell^{(1)}(x) = 0\,. \tag{A.8}$$

They can be calculated via

$$h_\ell^{(1)}(x) = -i(-x)^\ell \left(\frac{1}{x}\frac{d}{dx}\right)^\ell \frac{e^{ix}}{x} \tag{A.9}$$

or, with a series expansion,

$$h_\ell^{(1)}(x) = \left(\frac{-ie^{ix}}{x^\ell}\right) \sum_{k=0}^{\ell} \left[\frac{(\ell+k)!}{2^k k!(\ell-k)!}(-ix)^{\ell-k}\right] . \tag{A.10}$$

The normalisation of the Blatt-Weisskopf factors is chosen, that $F_\ell(p_R) = 1$. The first six barrier factors (up to $\ell = 5$) are

$$\begin{aligned}
F_0(p) &= 1 \\
F_1(p) &= \sqrt{\frac{2z}{z+1}} \\
F_2(p) &= \sqrt{\frac{13z^2}{z^2+3z+9}} \\
F_3(p) &= \sqrt{\frac{277z^3}{z^3+6z^2+45z+225}} \\
F_4(p) &= \sqrt{\frac{12746z^4}{z^4+10z^3+135z^2+1575z+11025}} \\
F_5(p) &= \sqrt{\frac{998881z^5}{z^5+15z^4+315z^3+6300z^2+99225z+893025}} ,
\end{aligned}$$

where $z = \left(\frac{p}{p_R}\right)^2$. They are shown in figure A.1

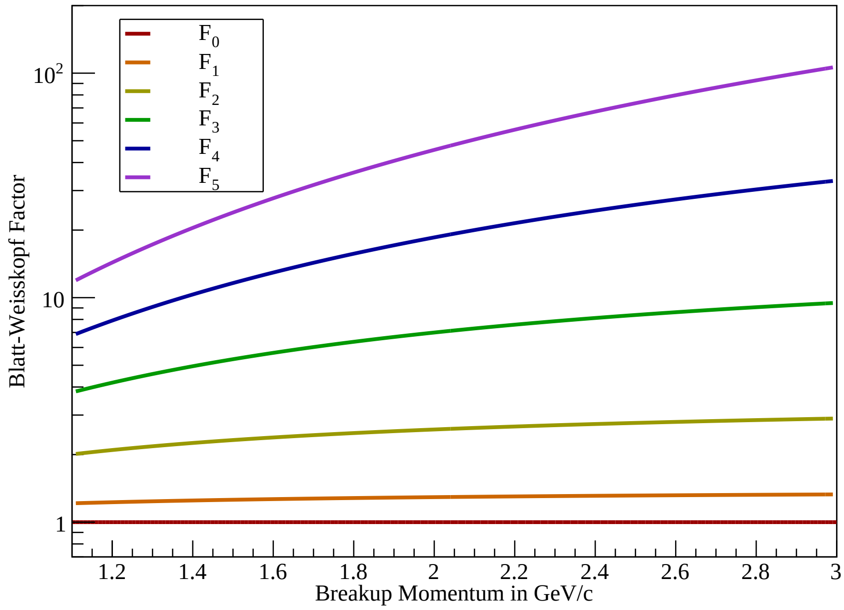

Figure A.1: The first six Blatt-Weisskopf barrier factors.

A.4 WHY THE REFLECTIVITY ϵ CAN BE FIXED

The Wigner D-functions in the reflectivity base are given as

$$D^{J,\epsilon}_{M\lambda}(\phi,\theta,0) = \frac{1}{\sqrt{2}}\left[D^J_{M\lambda}(\phi,\theta,0) - \epsilon\cdot\mathcal{P}\cdot(-1)^{J-M}D^J_{-M\lambda}(\phi,\theta,0)\right] . \tag{A.11}$$

The angular distributions are given by the square of the absolute value, which we will calculate here (omitting the factor $\frac{1}{\sqrt{2}}$ for convenience):

$$\begin{aligned}
|D^{J,\epsilon}_{M\lambda}|^2 &\propto |D^J_{M\lambda} - \epsilon\mathcal{P}(-1)^{J-M}D^J_{-M\lambda}|^2 \\
&= \left(D^J_{M\lambda} - \epsilon\mathcal{P}(-1)^{J-M}D^J_{-M\lambda}\right) \cdot \left(D^{J\,*}_{M\lambda} - \epsilon^*\mathcal{P}(-1)^{J-M}D^{J\,*}_{-M\lambda}\right) \\
&= |D^J_{M\lambda}|^2 - D^J_{M\lambda}D^{J\,*}_{-M\lambda}\epsilon^*\mathcal{P}(-1)^{J-M} \\
&\quad - D^{J\,*}_{M\lambda}D^J_{-M\lambda}\epsilon^*\mathcal{P}(-1)^{J-M} + \underbrace{\epsilon\epsilon^*\mathcal{P}^2(-1)^{2(J-M)}}_{=1}|D^J_{-M\lambda}|^2 \\
&= |D^J_{M\lambda}|^2 + |D^J_{-M\lambda}|^2 - \mathcal{P}(-1)^{J-M} \\
&\quad \times \left[\epsilon^* e^{-iM\phi}d^J_{M\lambda} \cdot e^{-iM\phi}d^J_{-M\lambda} + \epsilon e^{iM\phi}d^J_{M\lambda} \cdot e^{iM\phi}d^J_{-M\lambda}\right] .
\end{aligned}$$

From $\epsilon = \pm i$ follows $\epsilon^* = -\epsilon$. Substituting $\epsilon = \eta i$ with $\eta = \pm 1$ yields

$$= |D^J_{M\lambda}|^2 + |D^J_{-M\lambda}|^2 - \eta\mathcal{P}(-1)^{J-M}d^J_{M\lambda}d^J_{-M\lambda}i\left[-e^{-2iM\phi} + e^{2iM\phi}\right] .$$

With $2i\sin(x) = e^{ix} - e^{-ix}$ the final result is obtained as

$$\begin{aligned}
|D^{J,\epsilon}_{M\lambda}(\phi,\theta,0)|^2 \propto\, & |D^J_{M\lambda}(\phi,\theta,0)|^2 + |D^J_{-M\lambda}(\phi,\theta,0)|^2 \\
& + 2\cdot\eta\mathcal{P}\cdot(-1)^{J-M}d^J_{M\lambda}(\phi,\theta,0)d^J_{-M\lambda}(\phi,\theta,0)\sin(2M\phi) .
\end{aligned} \tag{A.12}$$

Thus, for given J and (in our case) $M = \frac{1}{2}$ the angular distributions depend only on $\eta\mathcal{P}$. Therefore, switching the sign of the reflectivity corresponds to a parity flip and

$$D^{J^+,i}_{M\lambda} = D^{J^-,-i}_{M\lambda} . \tag{A.13}$$

This effect can be seen in figure A.2. Changing both, parity and reflectivity, results in the same angular distributions.

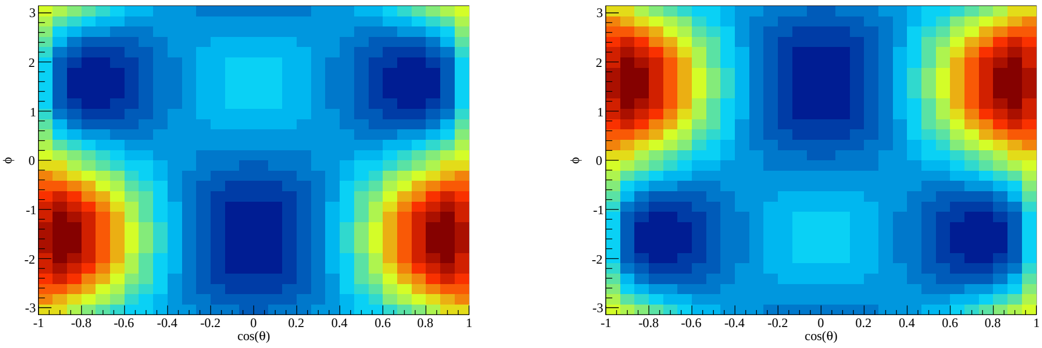

(a) $\epsilon = +i$, $\mathcal{P} = +$ (b) $\epsilon = -i$, $\mathcal{P} = +$

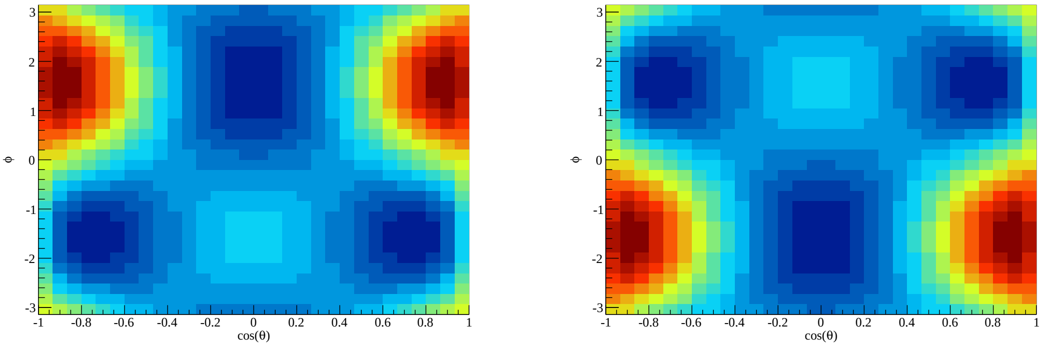

(c) $\epsilon = +i$, $\mathcal{P} = -$ (d) $\epsilon = -i$, $\mathcal{P} = -$

Figure A.2: Absolute value squared of $D^{\frac{3}{2}^{\mathcal{P}},\epsilon}_{\frac{1}{2}\frac{1}{2}}$ for different combinations of reflectivity ϵ and parity $\mathcal{P}$.

A.5 MODELLING A SMOOTH PHASE SHIFT

For a model of several baryon resonances a model for the phase shifts is needed. The actual $\arctan\left(\frac{M^2\Gamma^2}{x^2-M^2}\right)$ behaviour, where M and Γ are the resonance mass and width, has a too steep phase jump for $x = M$ and leads to jumps in the modelled invariant mass distributions. A model is needed, that provides a smooth phase shift from $-\frac{\pi}{2}$ to $\frac{\pi}{2}$ over the resonance. Thus, the phase $p(x)$ has to fulfil the following properties:

$$\begin{aligned} p(M-\tfrac{\Gamma}{2}) &= -\tfrac{\pi}{2} \\ p(M+\tfrac{\Gamma}{2}) &= +\tfrac{\pi}{2} \\ p(M) &= 0 \\ p'(M-\tfrac{\Gamma}{2}) &= 0 \\ p'(M+\tfrac{\Gamma}{2}) &= 0 \\ p''(M) &= 0\,. \end{aligned}$$

A shift of the coordinate system such, that the resonance is located at $x = 0$, reduces the number of conditions:

$$\begin{aligned} p(\Gamma) = -p(-\Gamma) &= \tfrac{\pi}{2} \\ p'(\Gamma) = p'(-\Gamma) &= 0 \\ p(0) = p''(0) &= 0\,. \end{aligned} \tag{A.14}$$

These properties are fulfilled by any centrally symmetric function. In this case, polynomials of degrees three and five will be considered.

A.5.1 Polynomial of Degree 3

For a centrally symmetric polynomial of degree 3

$$p(x) = ax^3 + bx\,, \tag{A.15}$$

the given conditions (A.14) can be directly used. For simplification $\gamma \equiv \frac{\Gamma}{2}$ will be used, which leads to

$$\begin{aligned} p(\gamma) &= a\gamma^3 + b\gamma = \frac{\pi}{2} \\ p'(\gamma) &= 3a\gamma^2 + b = 0\,. \end{aligned} \tag{A.16}$$

Solving for a and b, one obtains

$$p(x) = -\frac{\pi}{4\gamma^3}x^3 + \frac{3\pi}{4\gamma}x\,, \tag{A.17}$$

or, using the original coordinate system,

$$p_3(x) = -\frac{2\pi}{\Gamma^3}(x-M)^3 + \frac{3\pi}{2\Gamma}(x-M)\,. \tag{A.18}$$

A.5.2 Polynomial of Degree 5

For a centrally symmetric polynomial of degree 5

$$p(x) = ax^5 + bx^3 + cx\,, \tag{A.19}$$

an additional condition can be imposed, which is chosen to be the slope at $x = M$. Thus, one obtains

$$\begin{aligned} p(\gamma) &= a\gamma^5 + b\gamma^3 + c\gamma = \frac{\pi}{2} \\ p'(\gamma) &= 5a\gamma^4 + 3b\gamma^2 + c = 0 \\ p'(0) &= c = K\,, \end{aligned} \tag{A.20}$$

where K is the slope at the resonance and has to be fixed later. Solving for $a,\ b,\ c$ yields

$$p(x) = \left(\frac{K}{\gamma^4} - \frac{3\pi}{4\gamma^5}\right)x^5 + \left(\frac{5\pi}{4\gamma^3} - \frac{2K}{\gamma^2}\right)x^3 + Kx\,, \tag{A.21}$$

or

$$p_5(x) = \left(\frac{16K}{\Gamma^4} - \frac{24\pi}{\Gamma^5}\right)(x-M)^5 + \left(\frac{10\pi}{\Gamma^3} - \frac{8K}{\Gamma^2}\right)(x-M)^3 + K(x-M)\,. \tag{A.22}$$

The function $p_5(x)$ has four extrema at $x = \pm\frac{\Gamma}{2}$ and $x = \pm\frac{K\Gamma^3}{20K\Gamma - 30\pi}$. The first ones are wanted and imposed by (A.14), the latter ones are not wanted and can lie inside of the interval of the resonance. To avoid this behaviour, the value of the slope K has to be chosen such, that

$$\frac{K\Gamma^3}{20K\Gamma - 30\pi} \geqslant \left(\frac{\Gamma}{2}\right)^2\,. \tag{A.23}$$

Solving for K yields

$$K \leqslant \frac{15\pi}{8\Gamma}\,. \tag{A.24}$$

Choosing the lower bound for K in (A.24), the final form for $p_5(x)$,

$$p_5(x) = \frac{6\pi}{\Gamma^5}(x-M)^5 - \frac{5\pi}{\Gamma^3}(x-M)^3 + \frac{15\pi}{8\Gamma}(x-M)\,, \tag{A.25}$$

is obtained In figure A.3 the two solutions $p_3(x)$ (blue) and $p_5(x)$ (red) are shown.

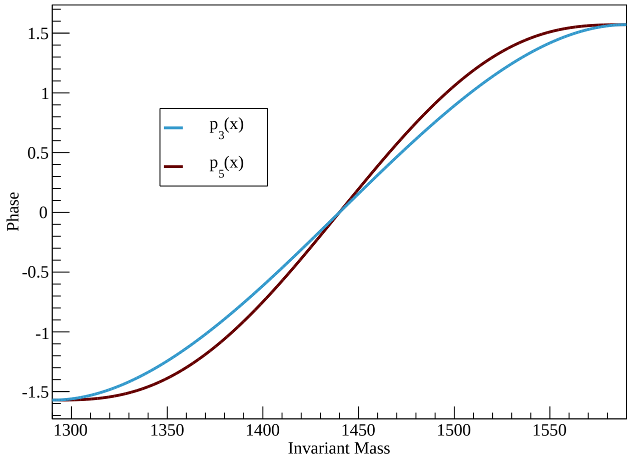

Figure A.3: The two possible solutions for the phase shift.

A.6 ERROR PROPAGATION OF COHERENT SUMS

We want to calculate the error of the coherent sum

$$\mathcal{S} = \left|\sum_i \mathcal{A}_i\right| = \left|\sum_i A_i e^{i\alpha_i}\right| \tag{A.26}$$

of fitted amplitudes $\mathcal{A}_i$, which have errors on their strengths A_i and phases α_i. For the calculation of errors we use

$$\mathcal{S} = \sqrt{\mathcal{S}^2}\,, \tag{A.27}$$

and thus

$$\Delta\mathcal{S} = \frac{1}{2\mathcal{S}}(\Delta\mathcal{S}^2)\,, \tag{A.28}$$

where

$$\mathcal{S}^2 = \left(\sum_i \mathfrak{Re}\mathcal{A}_i\right)^2 + \left(\sum_i \mathfrak{Im}\mathcal{A}_i\right)^2 \equiv (\mathfrak{Re}\Sigma)^2 + (\mathfrak{Im}\Sigma)^2 \tag{A.29}$$

and

$$(\Delta\mathcal{S}^2) = \sqrt{\left[2(\mathfrak{Re}\Sigma)(\Delta\mathfrak{Re}\Sigma)\right]^2 + \left[2(\mathfrak{Im}\Sigma)(\Delta\mathfrak{Im}\Sigma)\right]^2}\,. \tag{A.30}$$

The errors of the real and imaginary part of $\Sigma = \sum_i \mathcal{A}_i$ is given as the sum of the errors of the real and imaginary part of the single amplitudes

$$\begin{aligned}(\Delta\mathfrak{Re}\Sigma) &= \sqrt{\sum_i (\Delta\mathfrak{Re}A_i)^2} \\ (\Delta\mathfrak{Im}\Sigma) &= \sqrt{\sum_i (\Delta\mathfrak{Im}A_i)^2}\,.\end{aligned} \tag{A.31}$$

Finally, using $\mathfrak{Re}A_i = A_i\cos(\alpha_i)$ and $\mathfrak{Re}A_i = A_i\sin(\alpha_i)$, we obtain

$$\begin{aligned}(\Delta\mathfrak{Re}A_i) &= \sqrt{(\cos(\alpha_i)\Delta A_i)^2 + (A_i\sin(\alpha_i)\Delta\alpha_i)^2} \\ (\Delta\mathfrak{Im}A_i) &= \sqrt{(\sin(\alpha_i)\Delta A_i)^2 + (A_i\cos(\alpha_i)\Delta\alpha_i)^2}\,.\end{aligned} \tag{A.32}$$

B

ADDITIONAL FIGURES FOR CHAPTER 4

In this chapter, the probability and likelihood distributions, which were not shown in chapter 4, will be presented.

B.1 PROBABILITY DISTRIBUTIONS

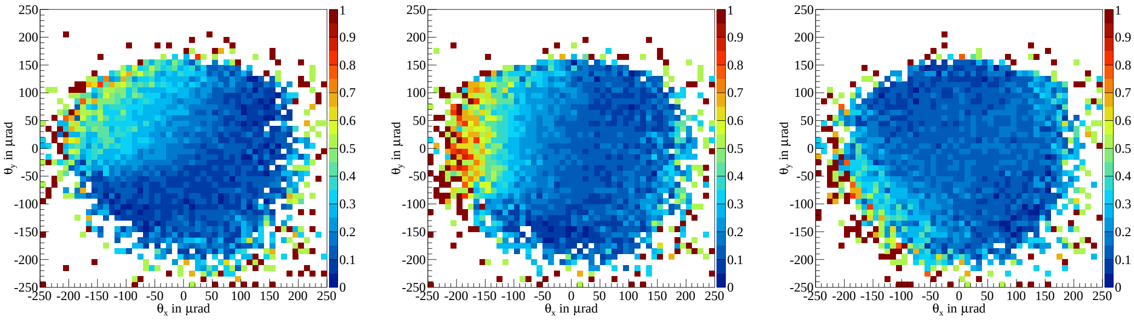

(a) PMT 1 (b) PMT 2 (c) PMT 3

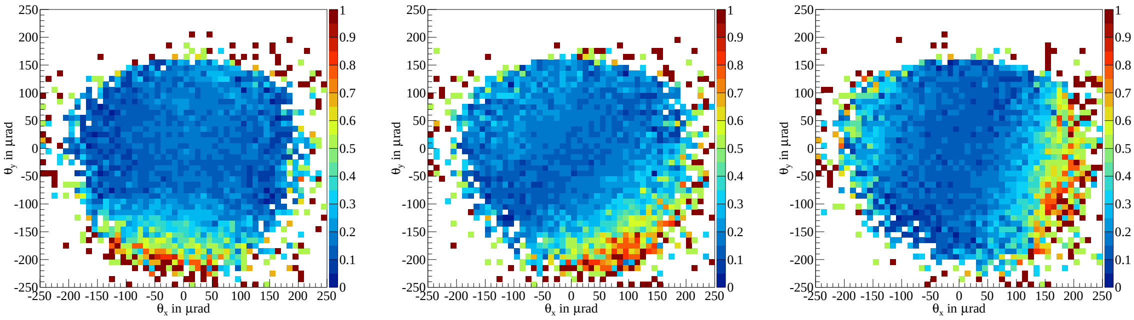

(d) PMT 4 (e) PMT 5 (f) PMT 6

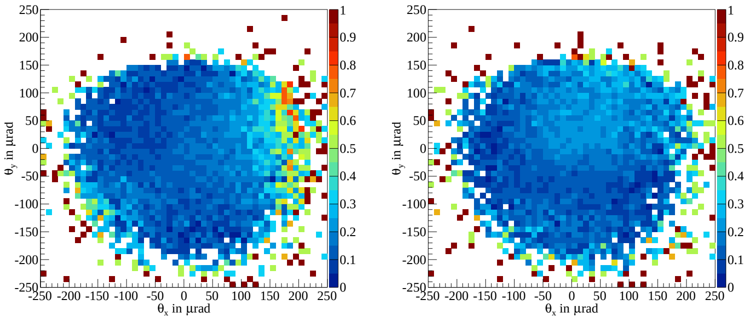

(g) PMT 7 (h) PMT 8

Figure B.1: Probability distribution $P^{i}_{(\theta_x,\theta_y)}(\overline{\text{signal}}|\text{kaon})$ for having no signal in the different PMTs with the kaon sample.

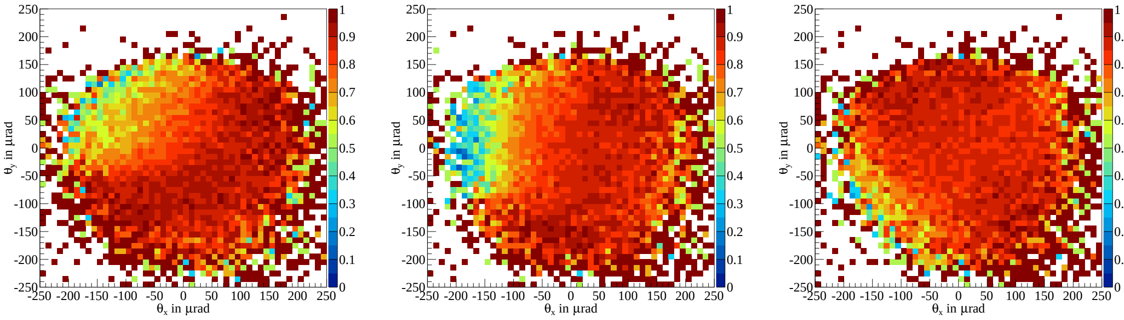

(a) PMT 1 (b) PMT 2 (c) PMT 3

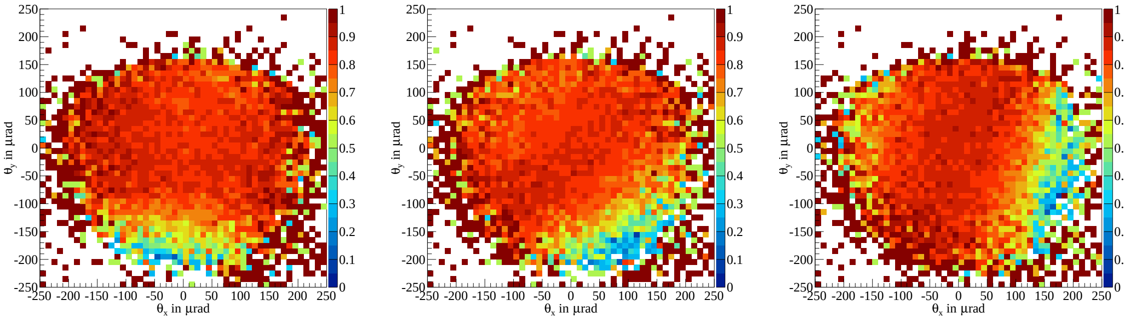

(d) PMT 4 (e) PMT 5 (f) PMT 6

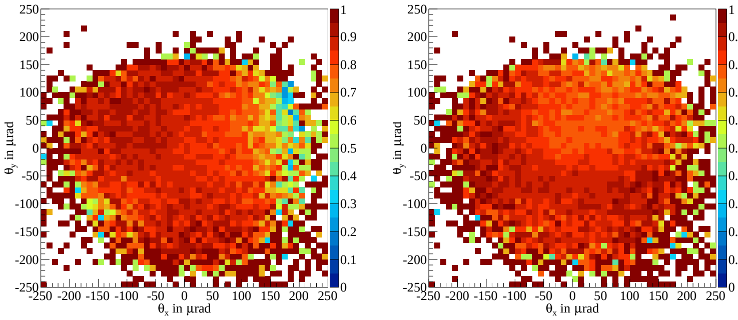

(g) PMT 7 (h) PMT 8

Figure B.2: Probability distribution $P^{i}_{(\theta_x,\theta_y)}(\mathrm{signal}|\mathrm{kaon})$ for having a signal in the different PMTs with the kaon sample.

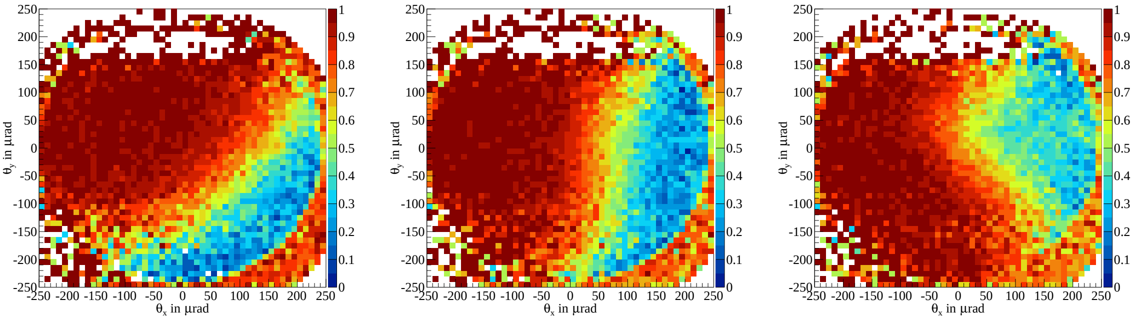

(a) PMT 1

(b) PMT 2

(c) PMT 3

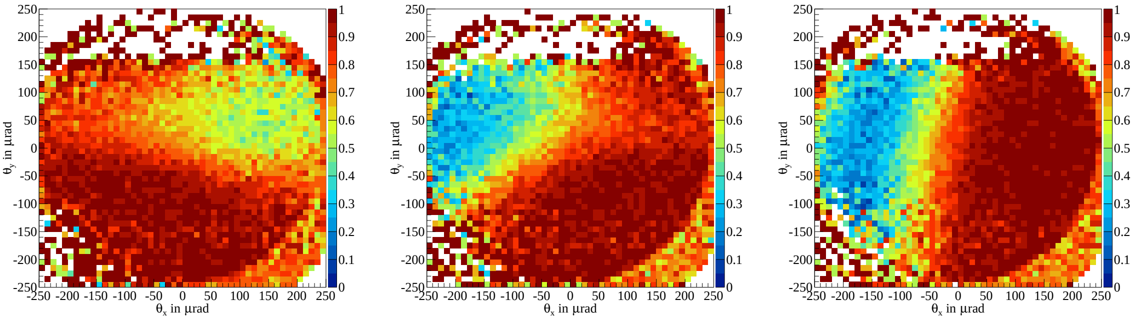

(d) PMT 4

(e) PMT 5

(f) PMT 6

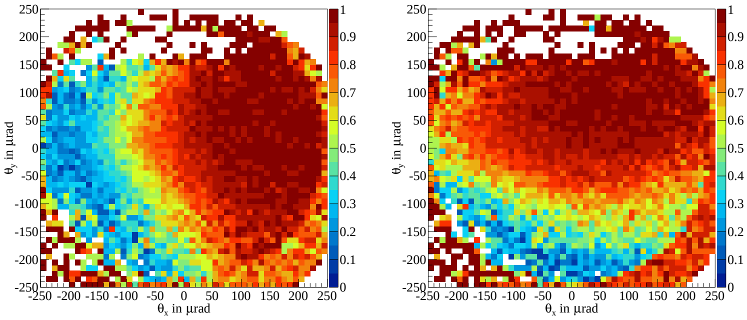

(g) PMT 7

(h) PMT 8

Figure B.3: Probability distribution $P^{i}_{(\theta_x,\theta_y)}(\overline{\text{signal}}|\text{pion})$ for having no signal in the different PMTs with the pion sample.

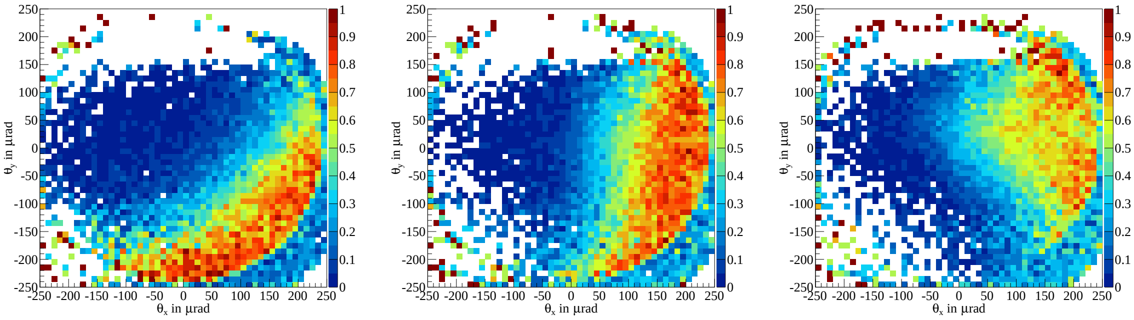

(a) PMT 1 (b) PMT 2 (c) PMT 3

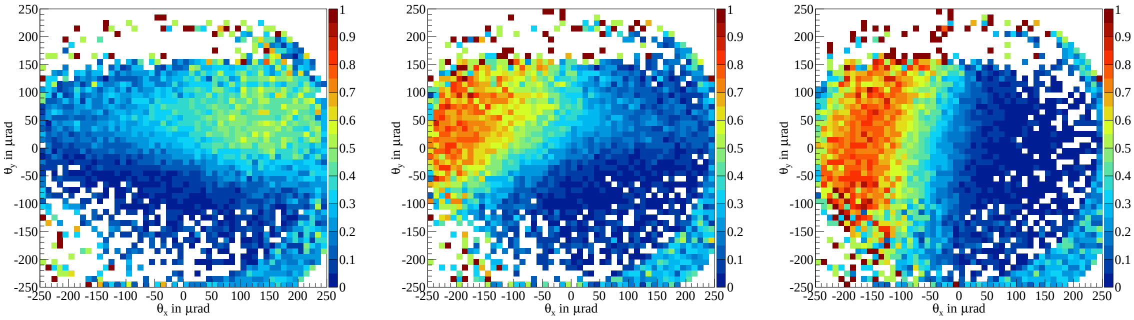

(d) PMT 4 (e) PMT 5 (f) PMT 6

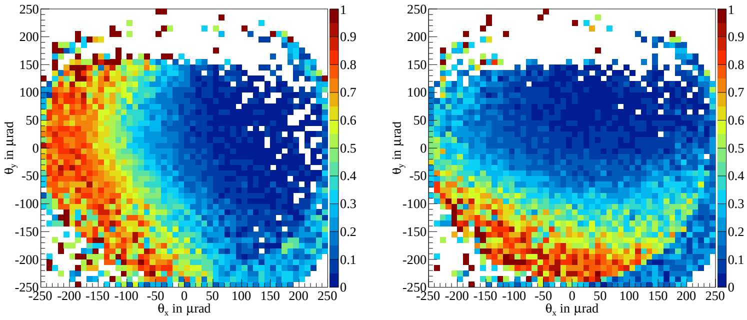

(g) PMT 7 (h) PMT 8

Figure B.4: Probability distribution $P^{i}_{(\theta_x,\theta_y)}(\text{signal}|\text{pion})$ for having a signal in the different PMTs with the pion sample.

B.2 LIKELIHOOD DISTRIBUTIONS

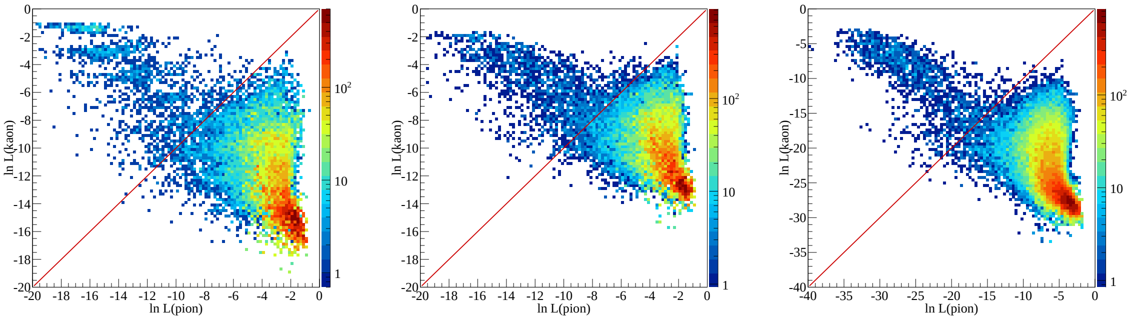

(a) CEDAR 1 (b) CEDAR 2 (c) 16 PMT

Figure B.5: Likelihoods for the beam sample using cut200 for both CEDARs and using all 16 photomultipiers together.

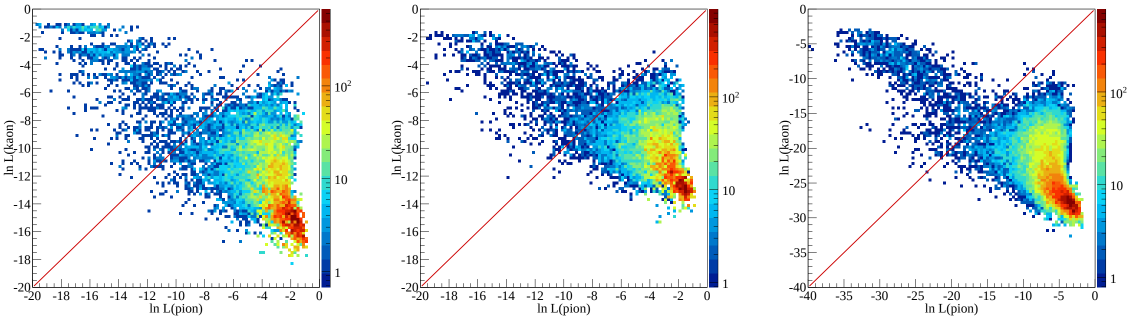

(a) CEDAR 1 (b) CEDAR 2 (c) 16 PMT

Figure B.6: Likelihoods for the beam sample using cut01 for both CEDARs and using all 16 photomultipiers together.

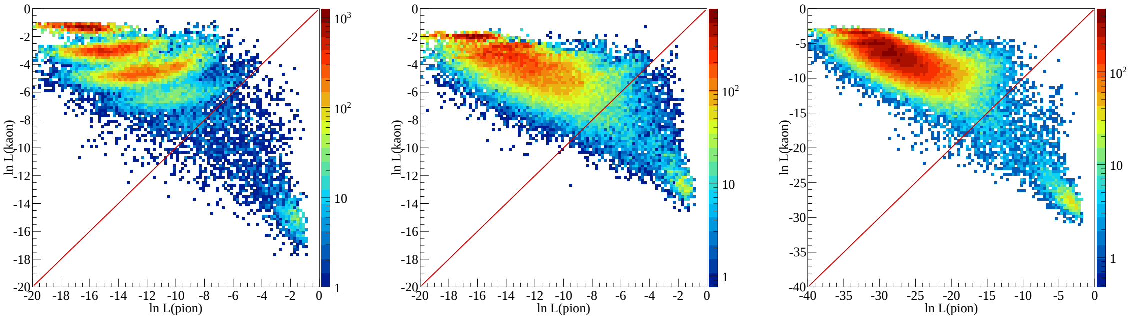

(a) CEDAR 1 (b) CEDAR 2 (c) 16 PMT

Figure B.7: Likelihoods for the kaon sample using cut200 for both CEDARs and using all 16 photomultipiers together.

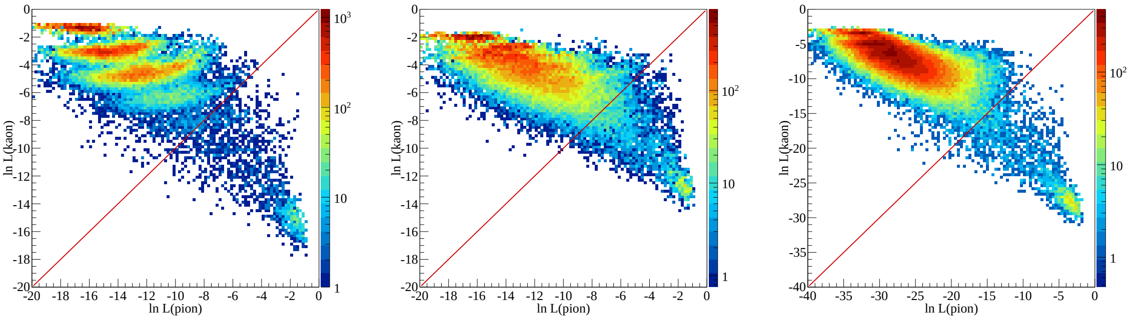

(a) CEDAR 1 (b) CEDAR 2 (c) 16 PMT

Figure B.8: Likelihoods for the kaon sample using cut01 for both CEDARs and using all 16 photomultipiers together.

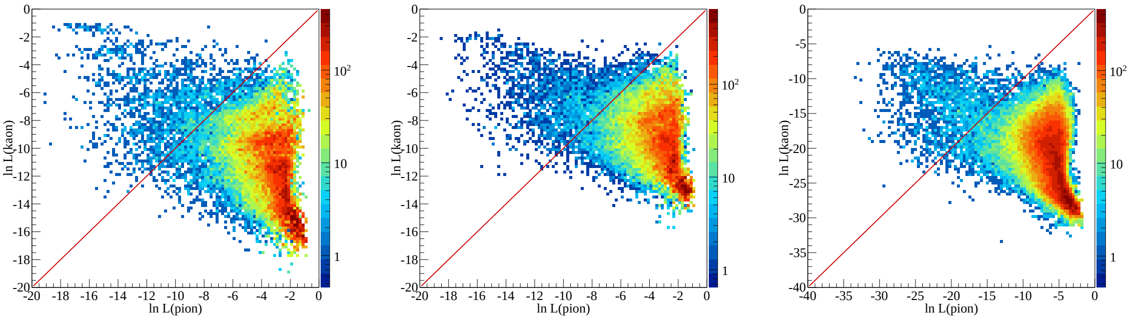

(a) CEDAR 1 (b) CEDAR 2 (c) 16 PMT

Figure B.9: Likelihoods for the pion sample using cut200 for both CEDARs and using all 16 photomultipiers together.

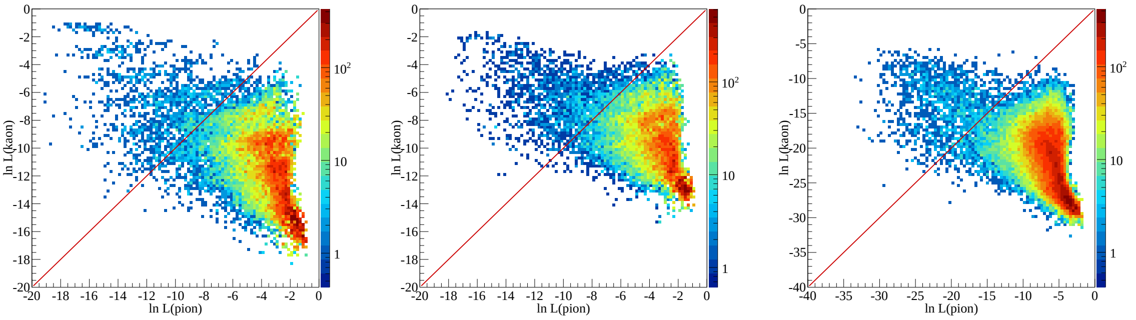

(a) CEDAR 1 (b) CEDAR 2 (c) 16 PMT

Figure B.10: Likelihoods for the pion sample using cut01 for both CEDARs and using all 16 photomultipiers together.

C

ADDITIONAL FIGURES FOR CHAPTER 8

In this chapter additional kinematic distributions are shown, which were omitted in chapter 8.

C.1 ANGULAR DISTRIBUTIONS FOR $pp \to pp\eta$

The Gottfried-Jackson angle $\cos(\theta)$ for $pp \to pp\eta$ is shown in the left panel of figure C.1. As for $pp \to pp\pi^0$, the distribution is dominated by a backward peak, which is broader in this case. Due to the acceptance correction, which is shown in the right panel of figure C.1 the peak height is reduced compared with the rest of the distribution. This was already observed in the pion case.

The distribution of the angle φ is given in the right panel of figure C.2. In contrast to the pion case, where the distribution was peaked around $\varphi = 0$ (and $\varphi = \pi$), the distribution for the η case is peaked around $\varphi = \pm\frac{1}{2}$, i. e. the decay plane is dominantly perpendicular to the production plane in this reaction. Due to acceptance correction, the structures are broadened a bit compared to the uncorrected distribution. This can be seen in the right panel of figure C.2.

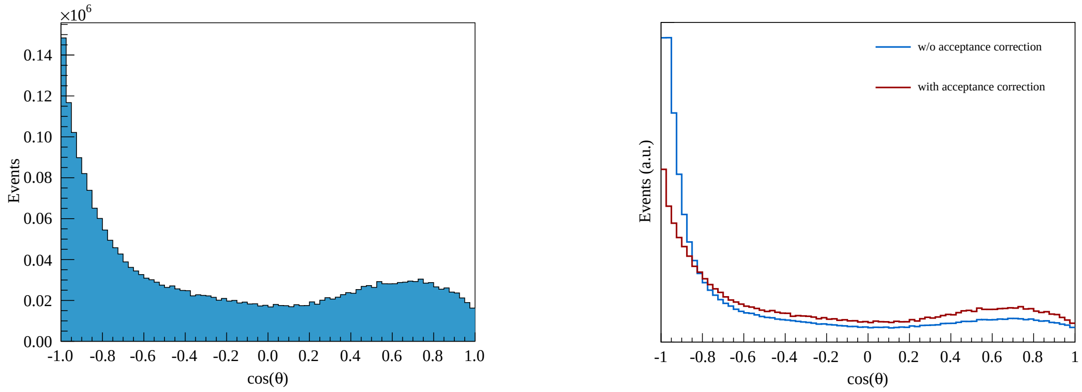

Figure C.1: Gottfried-Jackson angle $\cos(\theta)$ for $p\eta$. The left plot shows the distribution with applied acceptance correction, the right plot shows the comparison of corrected and uncorrected data normalised to each other.

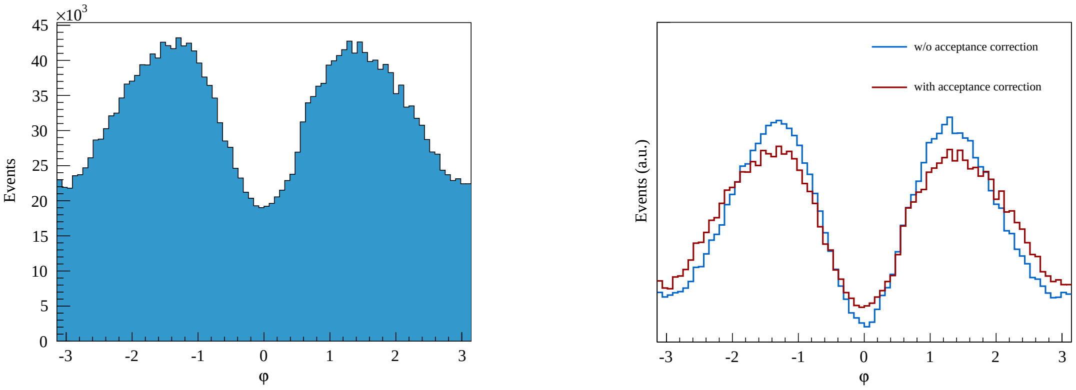

Figure C.2: Gottfried-Jackson angle φ for $p\eta$. The left plot shows the distribution with applied acceptance correction, the right plot shows the comparison of corrected and uncorrected data normalised to each other.

C.2 PION PAIR PRODUCTION

For the channel $pp \to pp\pi^+\pi^-$, there are no acceptance corrections available and only the uncorrected spectra are shown. Nevertheless, it can be assumed[1] that the acceptance correction for this channel is flat and does not change the distributions too much.

In this channel with three outgoing particles, it is interesting to look at the two-particle subsystems ($p\pi^+$, $p\pi^-$ and $\pi^+\pi^-$) to get information on sequential decays such as $pp \to \Delta^0\pi^+p$ with $\Delta^0 \to p\pi^-$. These kind of sequential decays are used in the so-called isobar model for meson spectroscopy in $\pi^-p \to \pi^-\pi^+\pi^-p$ [175, 176].

In figure C.3 the invariant mass spectra of the outgoing three-particle system $p\pi^+\pi^-$ and the spectra of the three different sub-systems, namely $\pi^+\pi^-$, $p\pi^+$ and $p\pi^-$, are shown.

The three-particle system exhibits a large structure around 1700 MeV/c^2 and a smaller one around 1500 MeV/c^2 similar to the $p\pi^0$ system. The $\pi^+\pi^-$ spectrum contains structures which should be contributions from $\rho(770)$, $f_0(980)$ and $f_2(1270)$. In the $p\pi^+$ and $p\pi^-$ spectrum the $\Delta(1232)$ and some further features from higher Δ states are visible. These different contributions in the single distributions have to be addressed by a partial wave analysis which is not done in this thesis. A first idea of the involved decays can be seen in figure C.4 where we show the invariant mass of the 3-particle system as a function of the masses of the $p\pi^+$ and $p\pi^-$ system. The structure around 1500 MeV/c^2 seems do decay via $\Delta(1232)^{++}\pi^-$ and $\Delta(1232)^0\pi^+$, while the larger 1700 MeV/c^2 structure also decays via $\Delta(1232)^{++}\pi^-$ but in the second channel dominantly via $\Delta^*\pi^+$.

---

[1] The acceptance distributions of the very similar channel $\pi^-p \to \pi^-\pi^+\pi^-p$ are known to be flat.

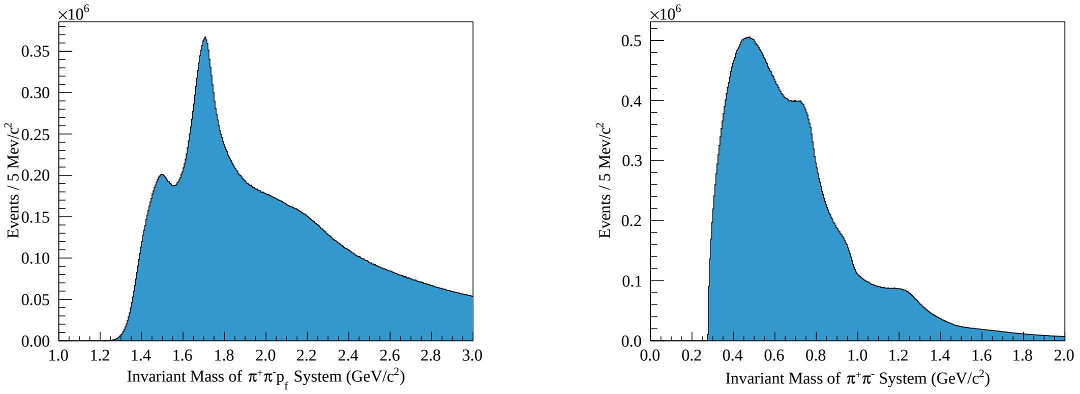

(a) $p\pi^+\pi^-$

(b) $\pi^+\pi^-$

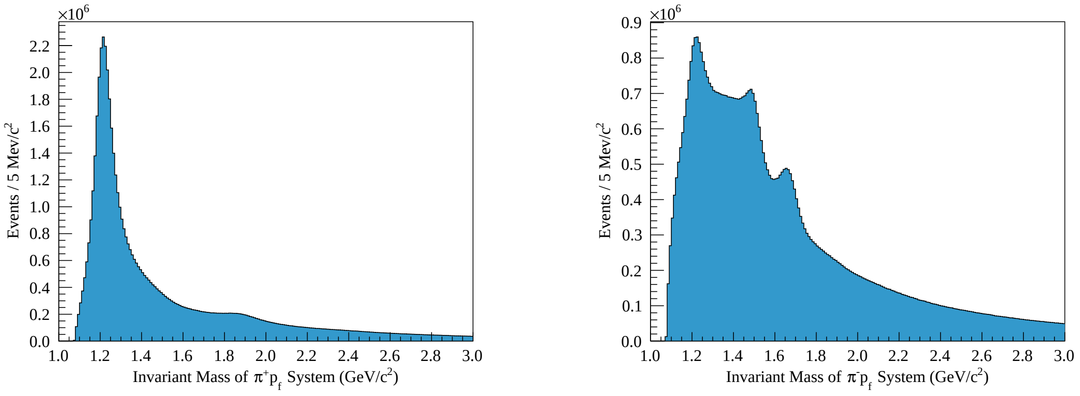

(c) $p\pi^+$

(d) $p\pi^-$

Figure C.3: Invariant mass spectra for $pp \to pp\pi^+\pi^-$.

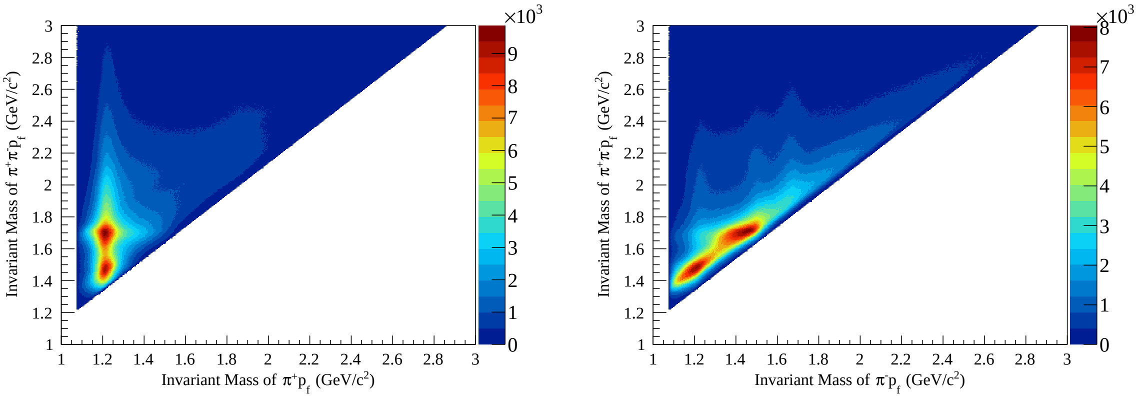

(a) $p\pi^+\pi^-$ vs. $p\pi^+$

(b) $p\pi^+\pi^-$ vs. $p\pi^-$

Figure C.4: Invariant mass of $p\pi^+\pi^-$ against the masses of the 2-particle states.

D

ADDITIONAL FIGURES FOR CHAPTER 9

In figures D.1 and D.2 the fits of the ω and ϕ peaks in the single bins of x_F are shown. These fits are used for the event yields plotted in figure 9.8.

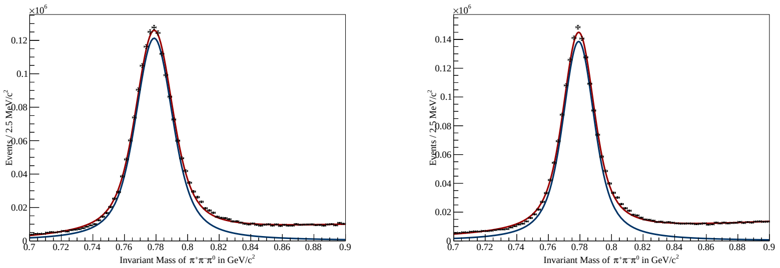

(a) $0.1 < x_F < 0.2$ (b) $0.2 < x_F < 0.3$

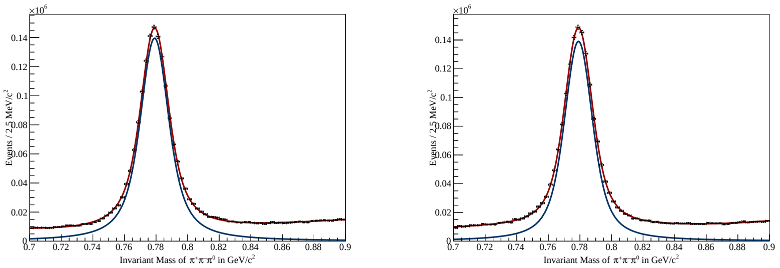

(c) $0.3 < x_F < 0.4$ (d) $0.4 < x_F < 0.5$

Figure D.1: Fits of ω mass in bins of x_F.

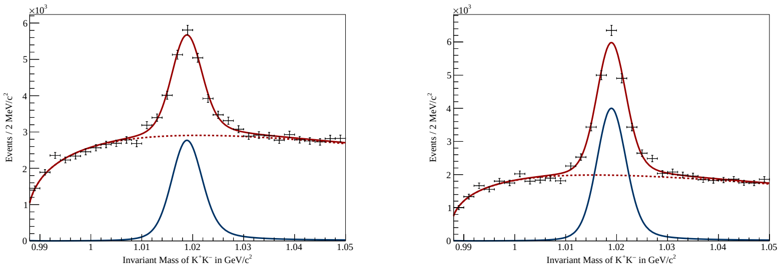

(a) $0.1 < x_F < 0.2$ (b) $0.2 < x_F < 0.3$

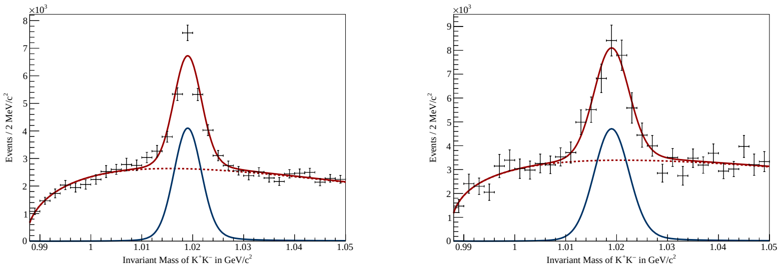

(c) $0.3 < x_F < 0.4$ (d) $0.4 < x_F < 0.5$

Figure D.2: Fits of ϕ mass in bins of x_F.

E

ADDITIONAL FIGURES FOR CHAPTER 12

In this chapter all results for the fit in mass bins for the single waves are shown for the different tests, which were done in chapter 12. This is the complete list of fits, some of these have already been shown before.

E.1 FITS TO THE MODEL

E.1.1 Resonances with $J^{\mathcal{P}} = \frac{1}{2}^{\pm}$

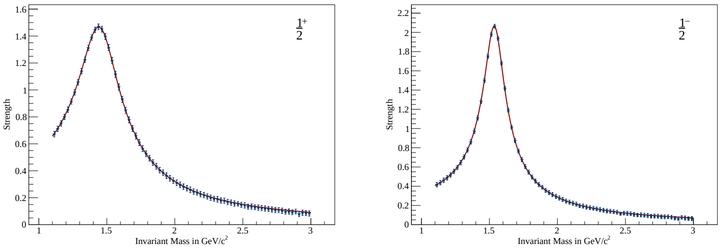

Figure E.1: The fit results (blue points) together with the model (red line) for the single waves in the model.

E.1.2 Resonances with $J^{\mathcal{P}} = \frac{1}{2}^{\pm}$ and $\frac{3}{2}^{\pm}$

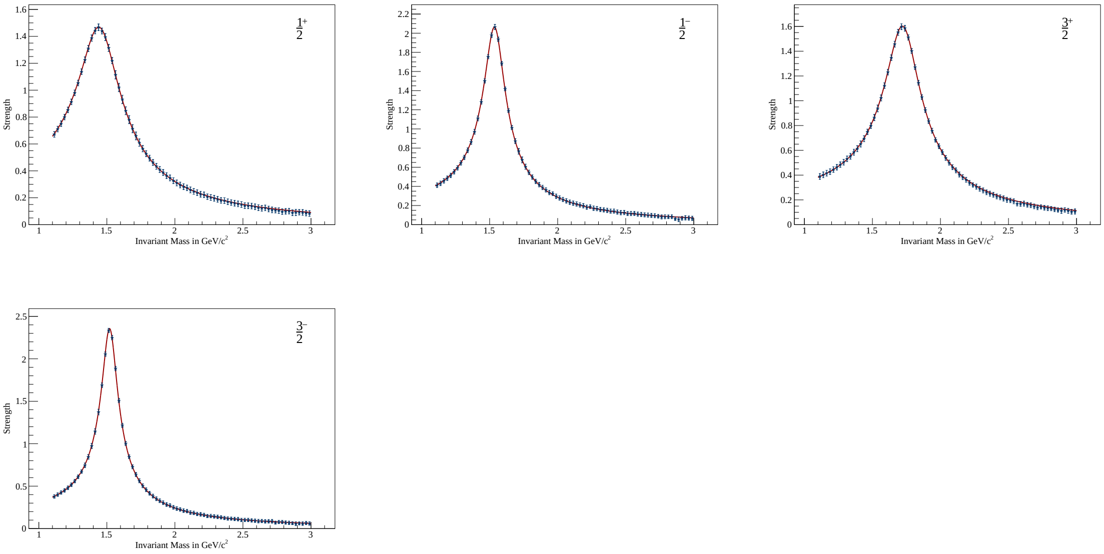

Figure E.2: The fit results (blue points) together with the model (red line) for the single waves in the model.

E.1.3 Full set of waves

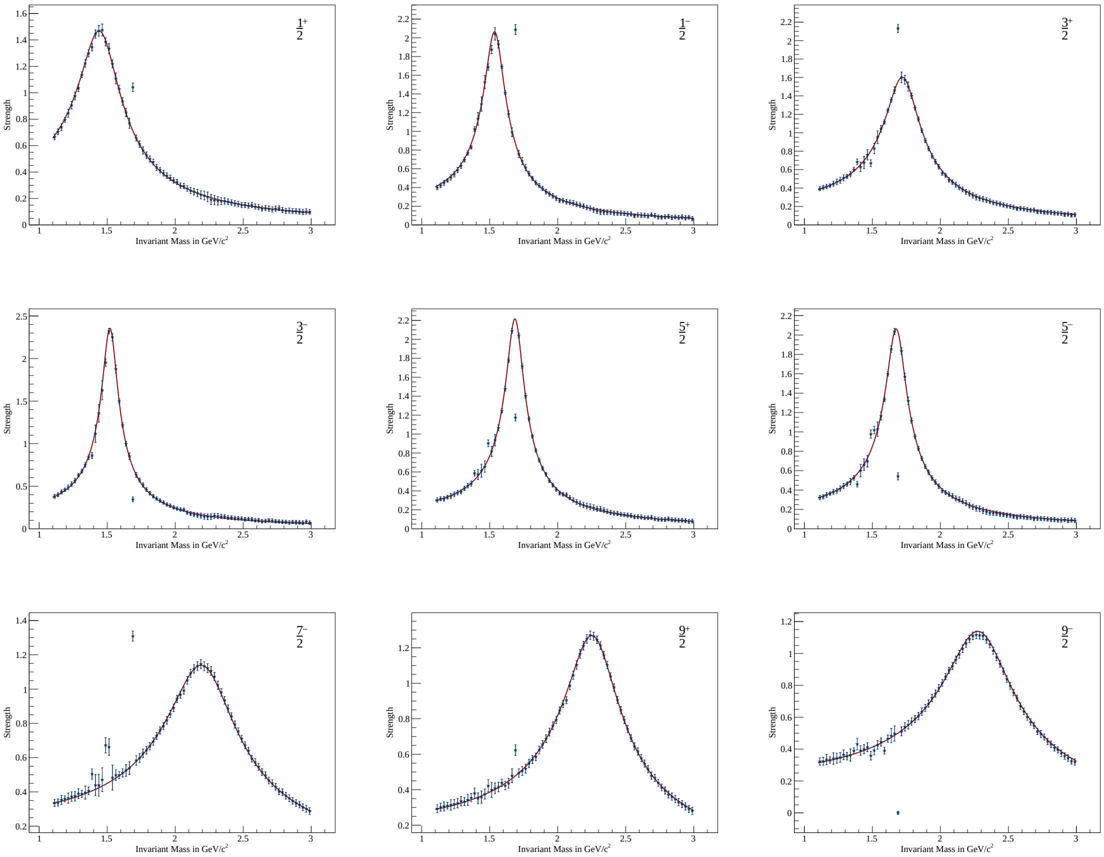

Figure E.3: The fit results (blue points) together with the model (red line) for the single waves in the model.

E.1.4 Two resonances with the same $J^{\mathcal{P}}$

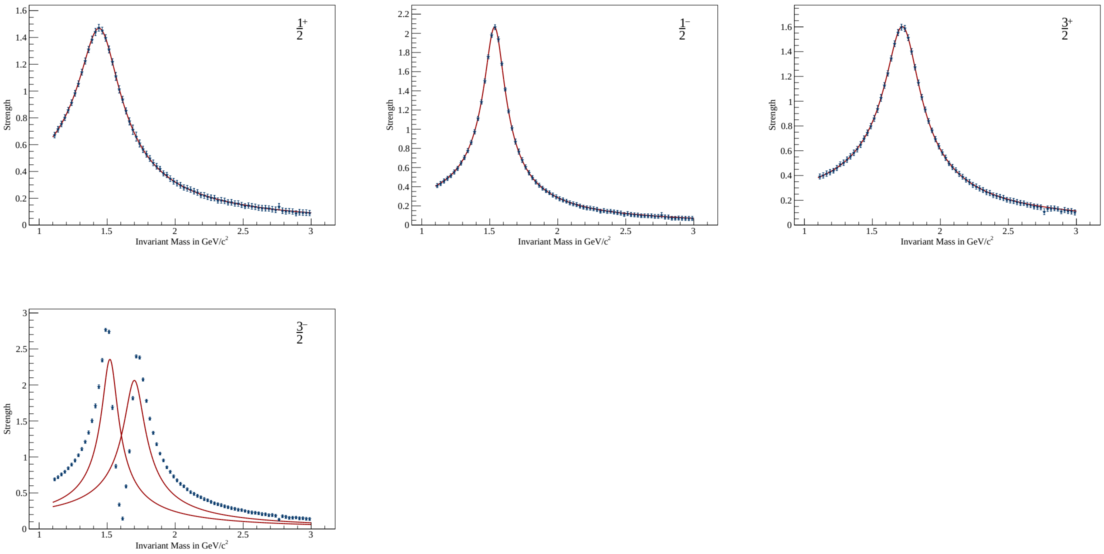

Figure E.4: The fit results (blue points) together with the model (red line) for the single waves in the model.

E.1.5 Fitting with too many resonances

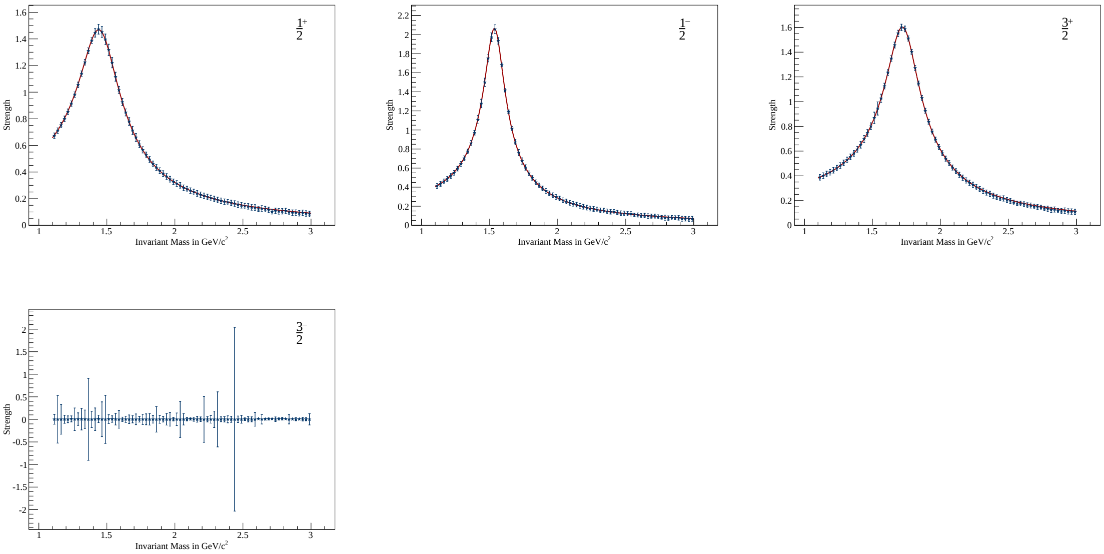

Figure E.5: The fit results (blue points) together with the model (red line) for the single waves in the model.

E.1.6 Fitting with too few resonances

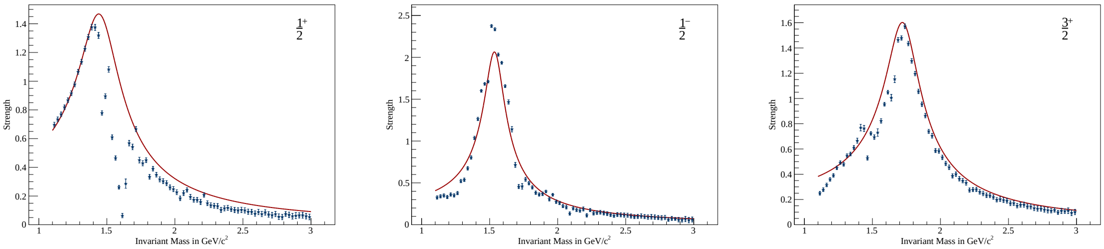

Figure E.6: The fit results (blue points) together with the model (red line) for the single waves in the model.

E.2 FITS ON REAL DATA

E.2.1 Full model without cuts

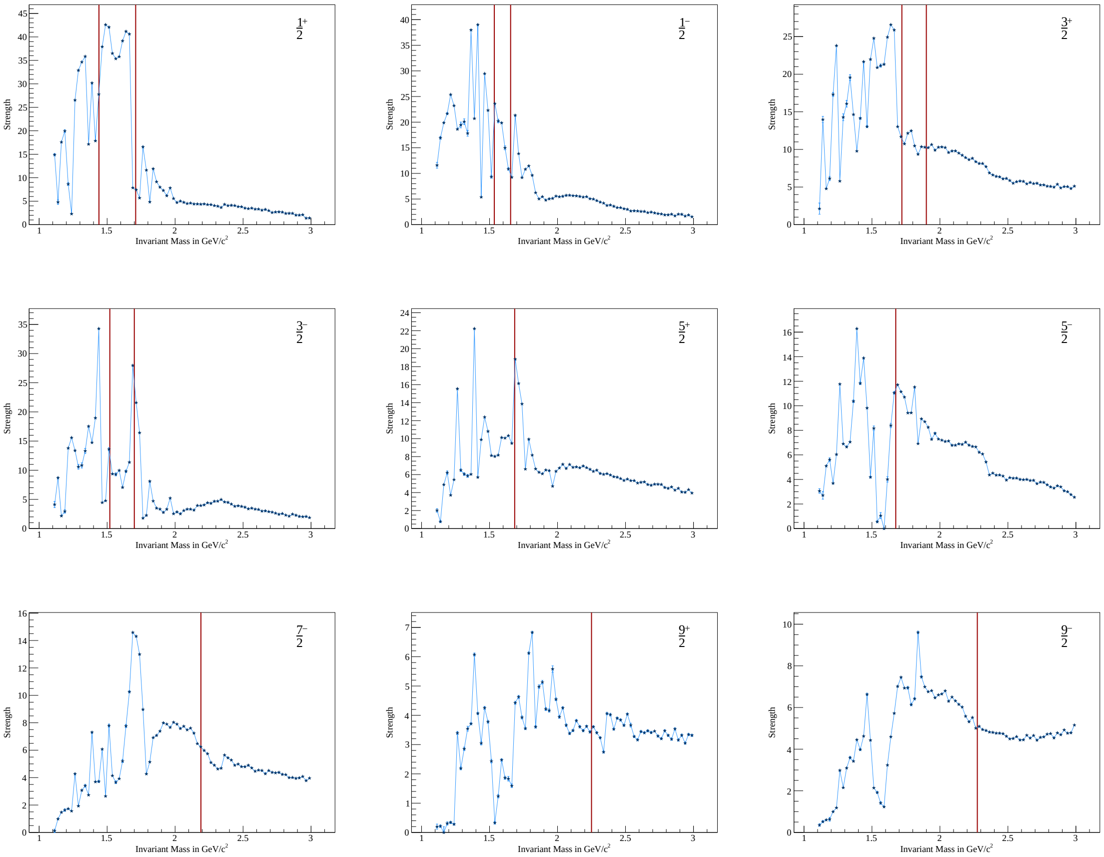

Figure E.7: The fit results (blue points) connected by a line to better guide the eye for the single waves in the model. The red lines denote the nominal position of resonances.

E.2.2 Only waves up to $\frac{5}{2}^{\pm}$ without cuts

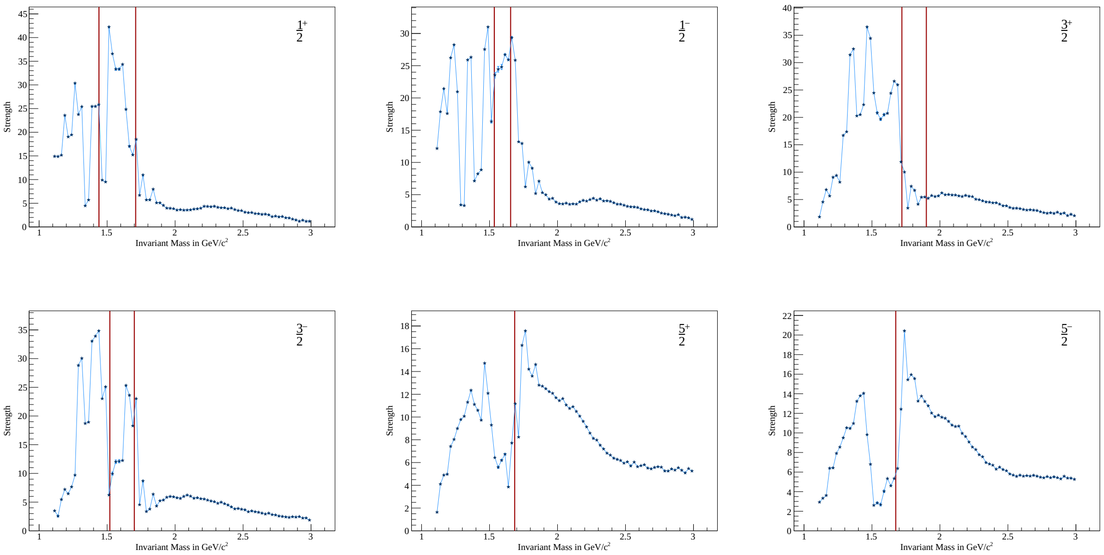

Figure E.8: The fit results (blue points) connected by a line to better guide the eye for the single waves in the model. The red lines denote the nominal position of resonances.

E.2.3 Fit in 38 mass bins

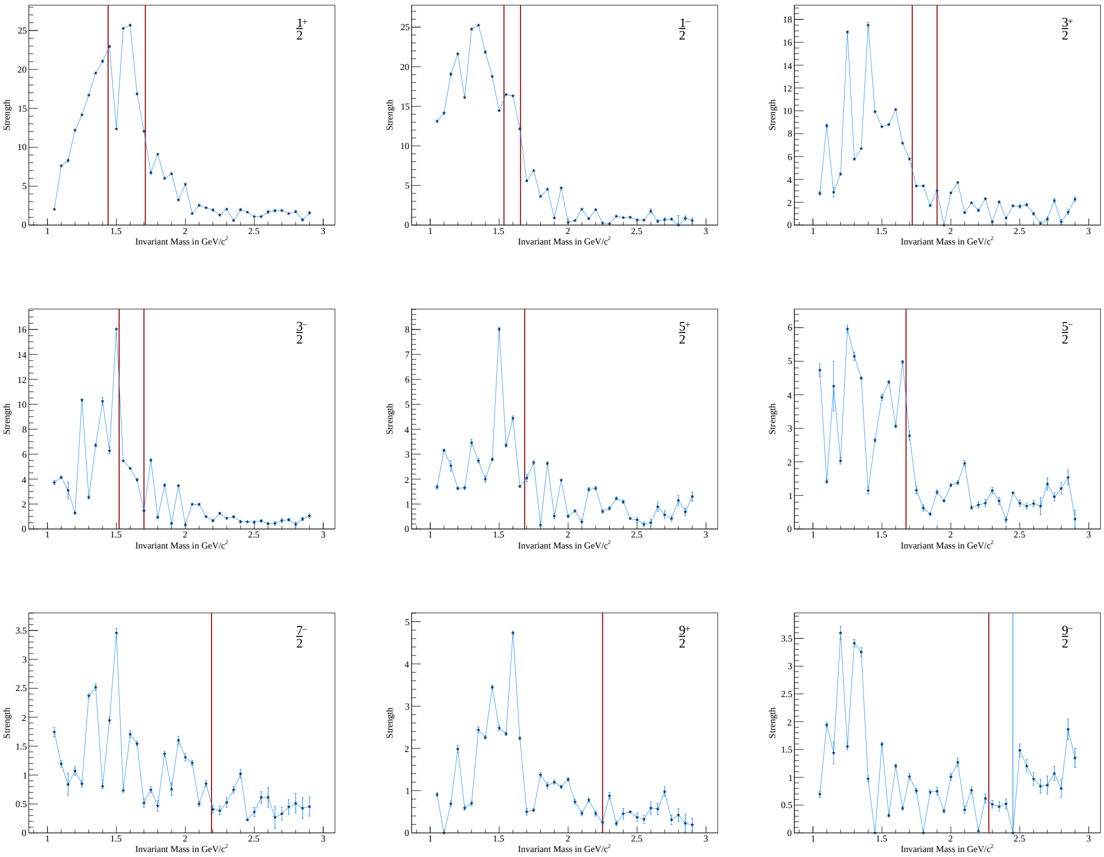

Figure E.9: The fit results (blue points) connected by a line to better guide the eye for the single waves in the model. The red lines denote the nominal position of resonances.

E.2.4 Cut on proton momentum

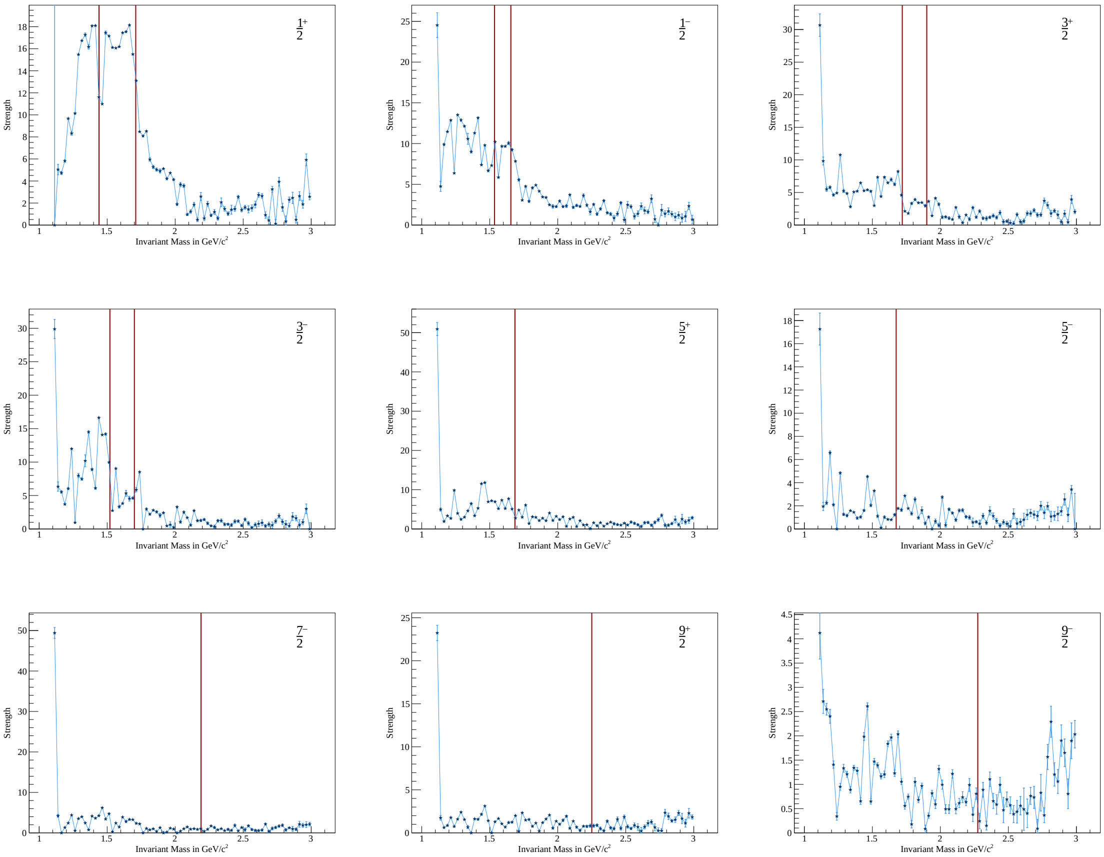

Figure E.10: The fit results (blue points) connected by a line to better guide the eye for the single waves in the model. The red lines denote the nominal position of resonances.

E.2.5 Exclusion of the backward peak

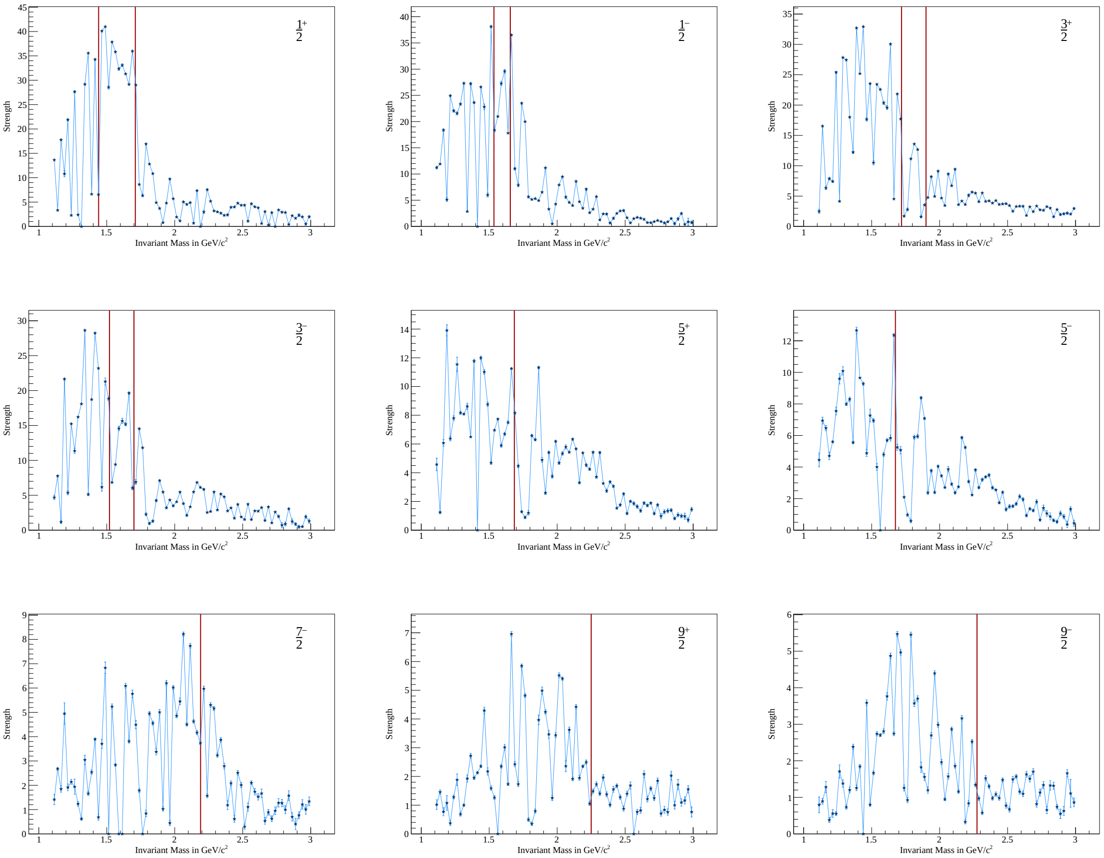

Figure E.11: The fit results (blue points) connected by a line to better guide the eye for the single waves in the model. The red lines denote the nominal position of resonances.

E.2.6 Momentum cut and exclusion of backward peak

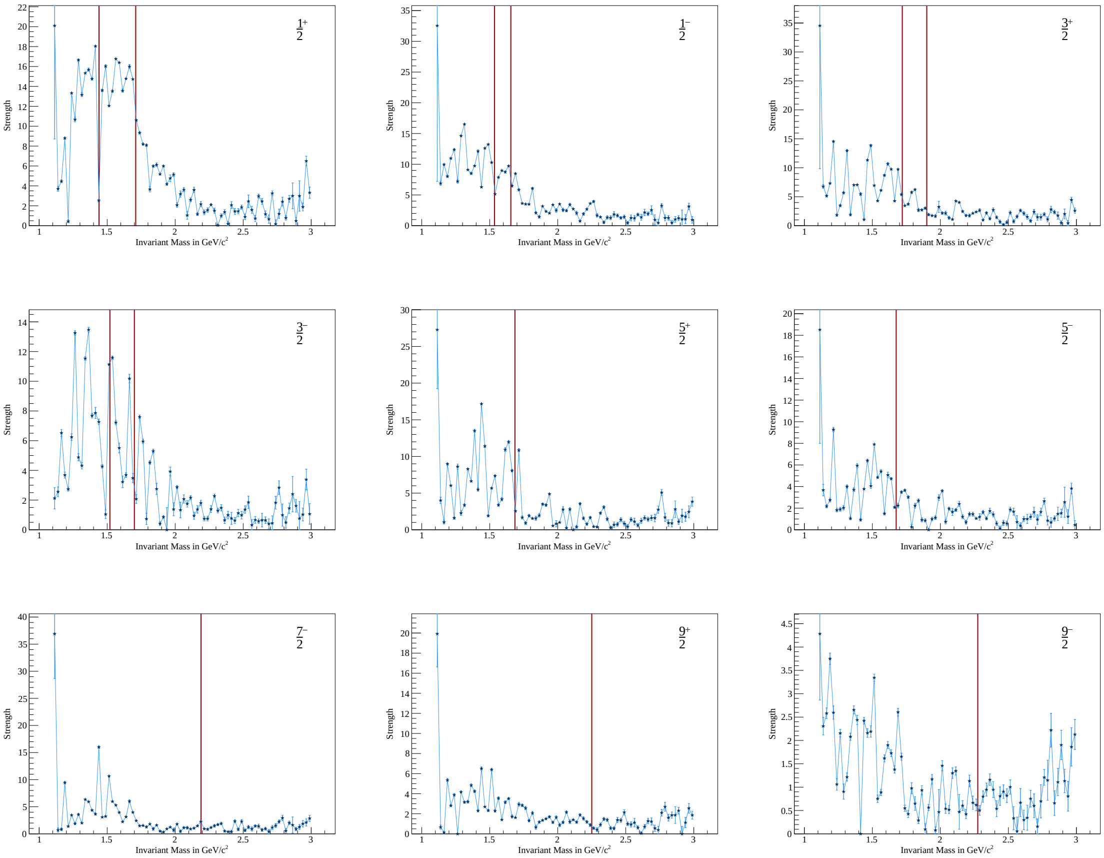

Figure E.12: The fit results (blue points) connected by a line to better guide the eye for the single waves in the model. The red lines denote the nominal position of resonances.

F

ADDITIONAL FIGURES FOR CHAPTER 13

Figure F.1 shows the different fits of the background contribution in $pp \to pp\pi^0$ in nine bins of the momentum transfer t', which are used to calculate the ratios given in figure 13.7.

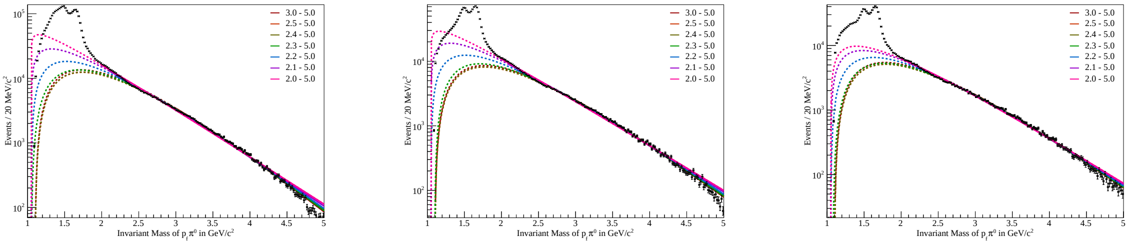

(a) $0.1 < t' < 0.2\,\mathrm{GeV}^2/c^2$ (b) $0.2 < t' < 0.3\,\mathrm{GeV}^2/c^2$ (c) $0.3 < t' < 0.4\,\mathrm{GeV}^2/c^2$

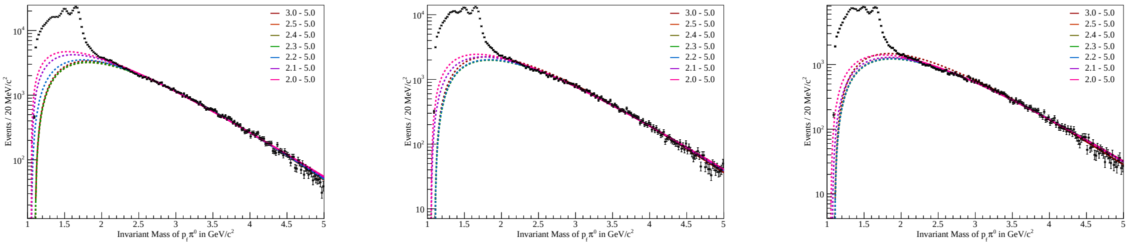

(d) $0.4 < t' < 0.5\,\mathrm{GeV}^2/c^2$ (e) $0.5 < t' < 0.6\,\mathrm{GeV}^2/c^2$ (f) $0.6 < t' < 0.7\,\mathrm{GeV}^2/c^2$

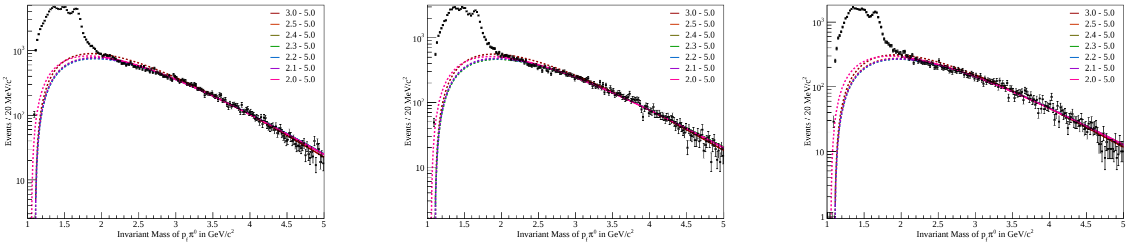

(g) $0.7 < t' < 0.8\,\mathrm{GeV}^2/c^2$ (h) $0.8 < t' < 0.9\,\mathrm{GeV}^2/c^2$ (i) $0.9 < t' < 1.0\,\mathrm{GeV}^2/c^2$

Figure F.1: Fits of the non-resonant background contribution to the invariant mass spectrum of $p\pi^0$ in bins of the momentum transfer t'. Different colours denote different fit ranges in the invariant mass.

G

USER'S MANUAL FOR BAYESIAN LIKELIHOODS IN THE CEDAR HELPER

The full likelihood method introduced in chapter 4 including all five steps is implemented in the CEDAR helper class available in the COMPASS hadron tools [70]. To successfully use this class inside phast the following files have to be made available during compilation:

- The source file `CEDAR_Helper.cc` and the corresponding header file,
- the file `cedar_time_corr.h` containing corrections for PMT timings for certain runs,
- the folder `CEDAR_DB` containing the hit maps[1].

G.1 GETTING THE PID

To get the PID for the beam particle in an event, the function

```
int CEDAR::LikeID_bayes
   (const PaEvent& e, const int iv, double A, double B)
```

is called, which determines the likelihood for the OR combination of the CEDARs as described in 4.4. `const PaEvent& e` is the current event and `const int iv` the index of the primary vertex. The values for `A` and `B` of the log likelihood differences (compare eq. (4.9b) and (4.10b)) are set to default values of $A = B = 1$ and thus do not have to be specified. To access the PID information of a single CEDAR or the combination of all 16 photomultipliers the method

```
int CEDAR::LikeID_bayes
   (const PaEvent& e, const int iv, int cedar, double A, double B)
```

is used. `int cedar` has to be chosen as

- `cedar=1`: CEDAR 1 (8 photomultipliers)
- `cedar=2`: CEDAR 2 (8 photomultipliers)
- `cedar=3`: CEDARs combined (16 photomultipliers)

In this case the values of `A` and `B` have to be specified (there is no default).
In both cases the PID uses the following convention (same as RICH):

value	PID
-1	no ID
0	π
1	K

---

[1] Also other files are included in this folder which are not needed by the likelihood method but are essential for other parts of the CEDAR helper class to work.

G.2 TOOLS FOR FURTHER STUDIES

For more detailed analyses also the likelihoods from the different CEDARs (and the combination of the 16 PMTs) can be obtained using the methods

```
double CEDAR::GetLikes_Pion
   (const PaEvent& e, const int iv, int cedar)
double CEDAR::GetLikes_Kaon
   (const PaEvent& e, const int iv, int cedar)
```

where all arguments are chosen as in the case of PID.
Using

```
double CEDAR::GetTheta_X
   (const PaEvent& e, const int iv, int cedar)
double CEDAR::GetTheta_Y
   (const PaEvent& e, const int iv, int cedar)
```

the corrected values for the beam divergence – θ_x and θ_y – for both CEDARs can be accessed. The information whether a certain photomultiplier registered a photon can be accessed through

```
bool CEDAR::Hit_in_PMT
   (const PaEvent& e, const int iv, int cedar, int pmt)
```

which will be `true` if photomultiplier `pmt` $(0-7)$ in CEDAR `cedar` $(1,2)$ has a hit.

G.3 HOW TO PRODUCE HIT MAPS

In the CEDAR folder of the hadron tools repository there is a phast user event (`UserEvent493677.cc`) which is used to produce hit maps. To use this user event a calibration sample (kaon or pion) is needed with as little background as possible. Running `UserEvent493677` over this sample will produce the needed histograms. After specifying the type of sample new hit maps `probKxy.db` or `probPxy.db` are automatically produced. These files have to be moved to the `CEDAR_DB` folder. After a recompilation of phast the new hit maps are ready to use.
Caveat: If you want to use the likelihood method for Primakoff data taking the hit maps have to be renamed `probKxy_2009.db` and `probPxy_2009.db`!
Caveat 2: Up to now (August 30, 2015) no hit maps have been produced for Primakoff data taking. The available hit maps are just dummy files!

G.4 ADAPTING THE METHOD TO PRIMAKOFF DATA

The method is more or less ready to use for 2009 and 2012 Primakoff data taking. Nevertheless some adaptions have to be made. At first the zero corrections for the beam divergence (see chapter 4.1) have to be set to the correct values obtained from Primakoff data. The values have to be set in the variables `double x_cent_20XX[2]` and `double y_cent_20XX[2]` (where `XX=09/12`) in `CEDAR_Helper.cc`.
Having set the divergence corrections new hit maps have to be produced using appropriate calibration samples. After that at least the values for the log likelihood differences A and B should be checked.

ACRONYMS

BEPC	Beijing Electron Positron Collider
BES	BEijing Spectrometer
BNL	Brookhaven National Laboratory
BT	Beam Trigger
CEBAF	Continuous Electron Beam Accelerator Facility
CEDAR	ChErenkov Differential Counter with Acromatic Ring focus
CERN	Conseil Européen pour la Recherche Nucléaire, European Organization for Nuclear Research
CLAS	CEBAF Large Acceptance Spectrometer
CMS	Centre-of-Mass System
COMGEANT	COMPASS GEANT
COMPASS	COmmom Muon and Proton Apparatus for Structure and Spectroscopy
CORAL	COMPASS Reconstruction ALgorithms
DC	Drift Chamber
DESY	Deutsches Elektronen-SYnchrotron
DST	Data Summary Tree
ECAL	Electromagnetic CALorimeter
ELSA	Elektronen-Stretcher-Anlage
GEANT	GEometry ANd Tracking
GEM	Gas Electron Multiplier
HCAL	Hadronic CALorimeter
ISR	Intersecting Storage Rings
LAS	Large Angle Spectrometer
LASS	Large Aperture Superconducting Solenoid
LHC	Large Hadron Collider

MAMI	MAinzer MIkrotron
MAPMT	Multi-Anode PhotoMultiplier Tube
mDST	mini Data Summary Tree
MWPC	MultiWire Proportional Chamber
PDG	Particle Data Group
PHAST	PHysics Analysis Software Tools
PMT	PhotoMultiplier Tube
PT	Proton Trigger
QCD	Quantum Chromo Dynamics
RICH	Ring Imaging CHrenkov detector
RHIC	Relativistic Heavy Ion Collider
RPD	Recoil Proton Detector
SAS	Small Angle Spectrometer
SciFi	Scintillating Fibre
SLAC	Stanford Linear Accelerator Center
SM	Spectrometer Magnet
SPS	Super Proton Synchrotron

BIBLIOGRAPHY

[1] K. A. Olive et al. Review of Particle Physics. *Chin.Phys.*, C38:090001, 2014. (Cited on pages 4, 7, 16, 18, 38, 83, 103, and 111.)

[2] P. W. Higgs. Broken symmetries and the masses of gauge bosons. *Phys. Rev. Lett.*, 13: 508–509, Oct 1964. (Cited on page 3.)

[3] F. Englert and R. Brout. Broken symmetry and the mass of gauge vector mesons. *Phys. Rev. Lett.*, 13:321–323, Aug 1964.

[4] G. S. Guralnik, C. R. Hagen, and T. W. B. Kibble. Global conservation laws and massless particles. *Phys. Rev. Lett.*, 13:585–587, Nov 1964. (Cited on page 3.)

[5] G. Aad et al. Observation of a new particle in the search for the Standard Model Higgs boson with the ATLAS detector at the LHC. *Phys.Lett.*, B716:1–29, 2012, 1207.7214. (Cited on page 3.)

[6] S. Chatrchyan et al. Observation of a new boson at a mass of 125 GeV with the CMS experiment at the LHC. *Phys.Lett.*, B716:30–61, 2012, 1207.7235. (Cited on page 3.)

[7] S. L. Glashow. Partial Symmetries of Weak Interactions. *Nucl.Phys.*, 22:579–588, 1961. (Cited on page 4.)

[8] A. Salam. Weak and Electromagnetic Interactions. *Conf.Proc.*, C680519:367–377, 1968.

[9] S. Weinberg. A Model of Leptons. *Phys.Rev.Lett.*, 19:1264–1266, 1967. (Cited on page 4.)

[10] G. Aad et al. Combined Measurement of the Higgs Boson Mass in pp Collisions at $\sqrt{s} = 7$ and 8 TeV with the ATLAS and CMS Experiments. 2015, 1503.07589. (Cited on page 5.)

[11] J. D. Bjorken. Asymptotic sum rules at infinite momentum. *Phys. Rev.*, 179:1547–1553, Mar 1969. (Cited on page 6.)

[12] C. G. Callan and D. J. Gross. High-energy electroproduction and the constitution of the electric current. *Phys. Rev. Lett.*, 22:156–159, Jan 1969. (Cited on page 6.)

[13] M. Gell-Mann and Y. Ne'eman. The Eightfold way: a review with a collection of reprints. 1964. (Cited on pages 8 and 145.)

[14] W. Heisenberg. On the structure of atomic nuclei. *Z.Phys.*, 77:1–11, 1932. (Cited on page 9.)

[15] E. Wigner. On the Consequences of the Symmetry of the Nuclear Hamiltonian on the Spectroscopy of Nuclei. *Phys.Rev.*, 51:106–119, 1937. (Cited on page 9.)

[16] M. Gell-Mann. The interpretation of the new particles as displaced charge multiplets. *Il Nuovo Cimento*, 4(2):848–866, 1956. ISSN 0029-6341. (Cited on page 9.)

[17] T. Nakano and K. Nishijima. Charge Independence for V-particles. *Prog.Theor.Phys.*, 10: 581–582, 1953. (Cited on page 9.)

[18] W. Pauli. The Connection Between Spin and Statistics. *Phys.Rev.*, 58:716–722, 1940. (Cited on page 10.)

[19] V. E. Barnes et al. Observation of a hyperon with strangeness minus three. *Phys. Rev. Lett.*, 12:204–206, Feb 1964. (Cited on page 10.)

[20] S. K. Choi et al. Observation of a narrow charmonium-like state in exclusive $B^{\pm} \to K^{\pm}\pi^{+}\pi^{-}J/\psi$ decays. *Phys.Rev.Lett.*, 91:262001, 2003, hep-ex/0309032. (Cited on page 11.)

[21] L. Maiani, F. Piccinini, A. D. Polosa, and V. Riquer. Diquark-antidiquarks with hidden or open charm and the nature of X(3872). *Phys.Rev.*, D71:014028, 2005, hep-ph/0412098. (Cited on page 11.)

[22] A. Ali, C. Hambrock, and M. J. Aslam. Tetraquark interpretation of the belle data on the anomalous $\upsilon(1s)\pi^{+}\pi-$ and $\upsilon(2s)\pi^{+}\pi^{-}$ production near the $\upsilon(5s)$ resonance. *Phys. Rev. Lett.*, 104:162001, Apr 2010. (Cited on page 11.)

[23] Z. Q. Liu et al. Study of $e^{+}e^{-} \to \pi^{+}\pi^{-}j/\psi$ and observation of a charged charmonium-like state at belle. *Phys. Rev. Lett.*, 110:252002, Jun 2013. (Cited on page 11.)

[24] C. Adolph et al. Search for exclusive photoproduction of $Z_c^{\pm}(3900)$ at COMPASS. 2014, 1407.6186. (Cited on page 11.)

[25] M. G. Alekseev et al. Observation of a $J^{PC} = 1^{-+}$ Exotic Resonance in Diffractive Dissociation of 190 GeV/c π^{-} into $\pi^{-}\pi^{-}\pi^{+}$. *Phys. Rev. Lett.*, 104:241803, Jun 2010, hep-ex/0910.5842. (Cited on page 11.)

[26] E. Klempt and A. Zaitsev. Glueballs, Hybrids, Multiquarks. Experimental facts versus QCD inspired concepts. *Phys.Rept.*, 454:1–202, 2007, 0708.4016. (Cited on page 11.)

[27] J. R. Forshaw and A. D. Ross. *Quantum Chromo Dynamics and the Pomeron*. Cambridge Lecture Notes in Physics, 1997. ISBN 978-0-521-56880-7. (Cited on page 11.)

[28] S. Mandelstam. Determination of the pion - nucleon scattering amplitude from dispersion relations and unitarity. General theory. *Phys.Rev.*, 112:1344–1360, 1958. (Cited on page 12.)

[29] R. E. Cutkosky. Singularities and discontinuities of Feynman amplitudes. *J.Math.Phys.*, 1:429–433, 1960. (Cited on page 12.)

[30] T. Regge. Introduction to complex orbital momenta. *Nuovo Cim.*, 14:951, 1959. (Cited on page 13.)

[31] T. Regge. Bound states, shadow states and Mandelstam representation. *Nuovo Cim.*, 18: 947–956, 1960. (Cited on page 13.)

[32] G. N. Watson. *Proc. Roy. Soc.*, 95:83, 1918. (Cited on page 14.)

[33] A. Sommerfeld. *Partial Differential Equations in Physics*. Academic Press, 1949. ISBN 978-0-126-54656-9. (Cited on page 14.)

[34] F. Carlson. *Sur une classe de séries de Taylor*. PhD thesis, Upsala, 1914. (Cited on page 14.)

[35] G. F. Chew and S. C. Frautschi. Principle of Equivalence for All Strongly Interacting Particles Within the S Matrix Framework. *Phys.Rev.Lett.*, 7:394–397, 1961. (Cited on page 16.)

[36] G. F. Chew and S. C. Frautschi. Regge Trajectories and the Principle of Maximum Strength for Strong Interactions. *Phys.Rev.Lett.*, 8:41–44, 1962. (Cited on page 16.)

[37] I. Y. Pomeranchuk. *Sov. Phys.*, 3:306, 1956. (Cited on page 16.)

[38] I. Y. Pomeranchuk. *Sov. Phys.*, 7:499, 1958. (Cited on page 16.)

[39] L. L. Foldy and R. F. Peierls. Isotopic Spin of Exchanged Systems. *Phys.Rev.*, 130: 1585–1589, 1963. (Cited on page 16.)

[40] A. Donnachie and P. V. Landshoff. Elastic Scattering and Diffraction Dissociation. *Nucl.Phys.*, B244:322, 1984. (Cited on pages 16 and 17.)

[41] A. Donnachie and P. V. Landshoff. Elastic Scattering at Large t. *Z.Phys.*, C2:55, 1979. (Cited on page 17.)

[42] A. Donnachie and P. V. Landshoff. Multi - Gluon Exchange in pp Elastic Scattering. *Phys.Lett.*, B123:345, 1983.

[43] A. Donnachie and P. V. Landshoff. p p and anti-p p Elastic Scattering. *Nucl.Phys.*, B231: 189, 1984. (Cited on page 17.)

[44] P. Abbon et al. The COMPASS experiment at CERN. *Nucl.Instrum.Meth.*, A577:455–518, 2007, hep-ex/0703049. (Cited on pages 21 and 27.)

[45] P. Abbon et al. The COMPASS Setup for Physics with Hadron Beams. *Nucl.Instrum.Meth.*, A779:69–115, 2015, 1410.1797. (Cited on pages 21, 25, 28, 37, 45, and 191.)

[46] L. Gatignon and M. Leberig. The M2 Beam Line, July 2004. URL `http://wwwcompass.cern.ch/compass/open_meetings/pre_villars_040702/Leberig_02-07-04.pdf`. last call: August 30, 2015. (Cited on page 22.)

[47] P. Atherton et al. Precise measurements of particle production by 400 gev/c protons on beryllium targets. *CERN Yellow Report*, CERN 80-07, 1980. (Cited on page 22.)

[48] J. Bernhard. *Exclusive Vector Meson Production in pp Collisions at the COMPASS Experiment*. PhD thesis, Johannes Gutenberg-Universität Mainz, January 2014. (Cited on pages 23, 74, 87, and 89.)

[49] E. Albrecht et al. Status and characterisation of COMPASS RICH-1. *Nucl.Instrum.Meth.*, A553:215–219, 2005. (Cited on page 24.)

[50] E. Albrecht et al. The radiator gas and the gas system of COMPASS RICH-1. *Nucl.Instrum.Meth.*, A502:266–269, 2003. (Cited on page 24.)

[51] E. Albrecht et al. The mirror system of COMPASS RICH-1. *Nucl.Instrum.Meth.*, A502: 236–240, 2003. (Cited on page 24.)

[52] P. Abbon et al. Design and construction of the fast photon detection system for COMPASS RICH-1. *Nucl.Instrum.Meth.*, A616:21–37, 2010. (Cited on page 24.)

[53] F. G. Binon et al. HODOSCOPE MULTI - PHOTON SPECTROMETER GAMS-2000. *Nucl.Instrum.Meth.*, A248:86, 1986. (Cited on page 25.)

[54] M. Adamovich et al. WA92: A Fixed target experiment to trigger on and identify beauty particle decays. *Nucl.Instrum.Meth.*, A379:252–270, 1996. (Cited on page 25.)

[55] P. Astbury et al. Measurement of Deep Inelastic Compton Scattering of High-energy Photons. *Phys.Lett.*, B152:419, 1985. (Cited on page 25.)

[56] T. Schlüter et al. Large-Area Sandwich Veto Detector with WLS Fibre Readout for Hadron Spectroscopy at COMPASS. *Nucl.Instrum.Meth.*, A654:219–224, 2011, 1108.4587. (Cited on page 27.)

[57] C. Bernet et al. The COMPASS trigger system for muon scattering. *Nucl.Instrum.Meth.*, A550:217–240, 2005. (Cited on page 27.)

[58] C. Adolph et al. Measurement of the charged-pion polarisability. 2014, 1405.6377. (Cited on page 28.)

[59] C. Bovet et al. *The CEDAR counters for particle identification in the SPS secondary beams: a description and an operation manual*. CERN, Geneva, 1982. (Cited on pages 31 and 34.)

[60] C. Bovet et al. CErenkov Differential counters with Acromatic Ring focus. CERN-Lab-2-EA-74-4, 1975. (Cited on page 31.)

[61] L. Gatignon. The M2 beam for COMPASS, March 2006. URL `http://jwenning.home.cern.ch/jwenning/documents/TrainingOP/ShutdownLectures06-M2.ppt`. last call: August 30, 2015. (Cited on page 31.)

[62] L. Lorenz. Über die Refractionskonstante. *Ann. Phys.*, 9:641–665, 1880. (Cited on page 32.)

[63] H. A. Lorentz. Über die Beziehung zwischen der Fortpflanzungsgeschwindigkeit des Lichtes und der Körperdichte. *Ann. Phys.*, 11:70–103, 1880. (Cited on page 32.)

[64] P. Jasinski. *Analysis of diffractively dissociation of* K^- *into* $K^-\pi^+\pi^-$ *on a liquid hydrogen target at the COMPASS spectrometer*. PhD thesis, Johannes Gutenberg-Universität Mainz, January 2012. (Cited on pages 32, 33, and 49.)

[65] T. Bayes. An Essay towards solving a Problem in the Doctrine of Chances. *Philosophical Transactions of the Royal Society of London*, 53:370–418, 1763. (Cited on page 40.)

[66] T. Schlüter, 2011. private communication. (Cited on page 51.)

[67] URL `http://coral.web.cern.ch/coral`. (Cited on page 60.)

[68] S. Gerassimov et al., 2003-2013. URL `http://ges.home.cern.ch/ges/phast/index.html`. (Cited on page 60.)

[69] Phast class list. URL `http://ges.web.cern.ch/ges/phast/doxygen-html/annotated.html`. (Cited on page 60.)

[70] Hadrontools. URL `http://wwwcompass.cern.ch/twiki/bin/view/HadronAnalysis/AdditionalSoftware`. COMPASS internal. (Cited on pages 61 and 177.)

[71] S. U. Chung, J. M. Friedrich, S. Paul, and Q. Weitzel. Diffractive dissociation for COMPASS, version III. `http://wwwcompass.cern.ch/twiki/pub/HadronAnalysis/WebHome/ab2cdn2.pdf`, March 2011. (Cited on pages 61, 64, and 66.)

[72] URL `http://rarfit.sourceforge.net/html/classRooRelBreitWigner.html`. last called August 30, 2015. (Cited on page 68.)

[73] B. Grube et al. Rootpwa. URL `http://sourceforge.net/projects/rootpwa/`. (Cited on page 72.)

[74] Geant detector description and simulation tool. URL `http://wwwasdoc.web.cern.ch/wwwasdoc/pdfdir/geant.pdf`. CERN Program Library Long Writeup W5013. (Cited on page 72.)

[75] K. Schoening. Option cards for mc simulations of hadron data. URL `/afs/cern.ch/compass/HadronGroup/HadronAnalysis/20101115/schoenning_MC_101115.pdf`. Talk in COMPASS hadron analysis meeting, 2010. (Cited on page 72.)

[76] URL `http://root.cern.ch/root/html/TEfficiency.html`. ROOT TEfficiency Class. (Cited on page 73.)

[77] C. J. Clopper and E. S. Pearson. The use of confidence or fiducial limits illustrated in the case of the binomial. *Biometrika*, 26:404–413, 1934. (Cited on page 73.)

[78] R. Koniuk and N. Isgur. Where Have All the Resonances Gone? An Analysis of Baryon Couplings in a Quark Model With Chromodynamics. *Phys.Rev.Lett.*, 44:845, 1980. (Cited on pages 77 and 97.)

[79] C. Adolph et al. Spin alignment and violation of the OZI rule in exclusive ω and ϕ production in pp collisions. *Nucl.Phys.*, B886:1078–1101, 2014, 1405.6376. (Cited on pages 83, 87, 88, and 91.)

[80] R. P. Feynman. Very high-energy collisions of hadrons. *Phys.Rev.Lett.*, 23:1415–1417, 1969. (Cited on page 83.)

[81] D. Barberis et al. A study of pseudoscalar states produced centrally in pp interactions at 450 GeV/c. *Physics Letters B*, 427(3-4):398 – 402, 1998. ISSN 0370-2693. (Cited on page 85.)

[82] D. Alde et al. Production of Pseudoscalar Mesons in 300 GeV Central $\pi^{-}N$ Collisions. *Z.Phys.*, C43:541, 1989. (Cited on page 85.)

[83] T. Åkesson et al. A comparison of direct photon, π^0, and η production in $p\overline{p}$ and pp interactions at the CERN ISR. *Phys. Lett. B*, 158:282–288. 16 p, Apr 1985. (Cited on page 85.)

[84] S. Okubo. Phi meson and unitary symmetry model. *Phys.Lett.*, 5:165–168, 1963. (Cited on page 88.)

[85] G. Zweig. An SU(3) model for strong interaction symmetry and its breaking. Version 1. 1964.

[86] G. Zweig. An SU(3) model for strong interaction symmetry and its breaking. Version 2. pages 22–101, 1964.

[87] J. Iizuka. Systematics and phenomenology of meson family. *Prog.Theor.Phys.Suppl.*, 37: 21–34, 1966. (Cited on page 88.)

[88] E. Klempt and J. Richard. Baryon spectroscopy. *Rev.Mod.Phys.*, 82:1095–1153, 2010, 0901.2055. (Cited on page 95.)

[89] A.V. Anisovich et al. Properties of baryon resonances from a multichannel partial wave analysis. *Eur.Phys.J.*, A48:15, 2012, 1112.4937. (Cited on page 95.)

[90] V. Shklyar, H. Lenske, and U. Mosel. Eta-meson production in the resonance energy region. *Phys.Rev.*, C87:015201, 2013, 1206.5414. (Cited on page 95.)

[91] J.-M. Richard. An introduction to the quark model. 2012, 1205.4326. (Cited on page 95.)

[92] A. J. G. Hey and R. L. Kelly. Baryon Spectroscopy. *Phys.Rept.*, 96:71, 1983. (Cited on page 95.)

[93] M. Battaglieri et al. Analysis Tools for Next-Generation Hadron Spectroscopy Experiments. *Acta Phys.Polon.*, B46(2):257, 2015, 1412.6393. (Cited on page 95.)

[94] R. E. Cutkosky et al. Pion - Nucleon Partial Wave Amplitudes. *Phys.Rev.*, D20:2839, 1979. (Cited on page 96.)

[95] R. E. Cutkosky et al. 4th International Conference on Baryon Resonances, Toronto, Canada, 1980 (University of Toronto, Toronto). (Cited on page 97.)

[96] G. Höhler et al. Physics Data 12-1, 1, 1979. (Cited on pages 96 and 97.)

[97] D. M. Manley and E. M. Saleski. Multichannel resonance parametrization of pi N scattering amplitudes. *Phys.Rev.*, D45:4002–4033, 1992. (Cited on page 96.)

[98] R. A. Arndt, W. J. Briscoe, I. I. Strakovsky, and R.L. Workman. Extended partial-wave analysis of piN scattering data. *Phys.Rev.*, C74:045205, 2006, nucl-th/0605082. (Cited on pages 96 and 97.)

[99] D. Aston et al. A Summary of the Results from LASS and the Future of Strange Quark Spectroscopy. 1990. (Cited on page 96.)

[100] D. Aston, N. Awaji, T. Bienz, F. Bird, J. D'Amore, et al. Observation of a New Ω^*- at 2.47-GeV/c^2 in K^-p Interactions at 11-GeV/c. *Phys.Lett.*, B215:799, 1988. (Cited on page 96.)

[101] A. M. Wright et al. in 7th International Conference on the Structure of Baryons, Santa Fe, New Mexico, 1995, edited by B. F. Gibson (World Scientific, Singapore). (Cited on page 96.)

[102] D. M. Manley et al. An Isobar Model Partial Wave Analysis of $\pi N \to \pi\pi N$ in the Center-of-mass Energy Range 1320-MeV to 1930-MeV. *Phys.Rev.*, D30:904, 1984. (Cited on page 96.)

[103] N. G. Kozlenko et al. Measurement of the total and differential cross-sections for the reaction $\pi^- p \to \eta n$ with the Crystal Ball detector. *Phys.Atom.Nucl.*, 66:110–113, 2003. (Cited on page 97.)

[104] S. Prakhov et al. Measurement of $\pi^- p \to \eta n$ from threshold to $p(\pi-) = 747$ MeV/c. *Phys.Rev.*, C72:015203, 2005. (Cited on page 97.)

[105] R. A. Arndt, I. I. Strakovsky, and R. L. Workman. The SAID PWA program. *Int.J.Mod.Phys.*, A18:449–455, 2003. (Cited on page 97.)

[106] R. A. Arndt et al. Low-energy eta N interactions: Scattering lengths and resonance parameters. *Phys.Rev.*, C72:045202, 2005, nucl-th/0507024. (Cited on page 97.)

[107] A. Starostin et al. Measurement of $\pi^- p \to \pi^0 n$ in the vicinity of the eta threshold. *Phys.Rev.*, C72:015205, 2005. (Cited on page 97.)

[108] M. E. Sadler et al. Differential cross-section of the charge exchange reaction $\pi^- p \rightarrow \pi^0 n$ in the momentum range from 148 MeV/c to 323 MeV/c. *Phys.Rev.*, C69:055206, 2004, nucl-ex/0403040. (Cited on page 97.)

[109] D. M. Asner et al. Physics at BES-III. *Int.J.Mod.Phys.*, A24:S1–794, 2009, 0809.1869. (Cited on page 97.)

[110] B. S. Zou. Baryon Resonances Observed at BES. *eConf*, C070910:112, 2007, 0802.0087. (Cited on page 97.)

[111] B. Liu. Baryon spectroscopy at BESIII. *PoS*, Hadron2013:115, 2013. (Cited on page 97.)

[112] D. Drechsel and T. Walcher. Hadron structure at low Q^2. *Rev.Mod.Phys.*, 80:731–785, 2008, 0711.3396. (Cited on page 97.)

[113] Aachen-Berlin-Bonn-Hamburg-Heidelberg-Munich Collaboration. Photoproduction of meson and baryon resonances at energies up to 5.8 GeV. *Phys.Rev.*, 175:1669–1696, 1968. (Cited on page 98.)

[114] J. Ballam et al. Bubble Chamber Study of Photoproduction by 2.8 GeV and 4.7 GeV Polarized Photons. 1. Cross-Section Determinations and Production of ρ^0 and Δ^{++} in the Reaction $\gamma p \rightarrow p\pi^+\pi^-$. *Phys.Rev.*, D5:545, 1972. (Cited on page 98.)

[115] J. Ballam et al. Vector Meson Production by Polarized Photons at 2.8 GeV, 4.7 GeV, and 9.3 GeV. *Phys.Rev.*, D7:3150, 1973. (Cited on page 98.)

[116] D. P. Barber et al. A Study of Elastic Photoproduction of Low Mass K^+K^- Pairs From Hydrogen in the Energy Range 2.8 GeV to 4.8 GeV. *Z.Phys.*, C12:1, 1982. (Cited on page 98.)

[117] D. P. Barber et al. A Study of the Reactions $\gamma p \rightarrow \omega p$ and $\gamma p \rightarrow \omega\Delta^+$. *Z.Phys.*, C26: 343–351, 1984. (Cited on page 98.)

[118] K. I. Blomqvist et al. The three-spectrometer facility at the Mainz microtron MAMI. *Nucl.Instrum.Meth.*, A403:263–301, 1998. (Cited on page 98.)

[119] A. R. Gabler et al. Response of TAPS to monochromatic photons with energies between 45 MeV and 790 MeV. *Nucl.Instrum.Meth.*, A346:168–176, 1994. (Cited on page 98.)

[120] E. Aker et al. The Crystal Barrel spectrometer at LEAR. *Nucl.Instrum.Meth.*, A321: 69–108, 1992. (Cited on page 98.)

[121] B. A. Mecking et al. The CEBAF Large Acceptance Spectrometer (CLAS). *Nucl.Instrum.Meth.*, A503:513–553, 2003. (Cited on page 98.)

[122] D. Drechsel and L. Tiator. Threshold pion photoproduction on nucleons. *J.Phys.*, G18: 449–497, 1992. (Cited on page 98.)

[123] D. Drechsel, O. Hanstein, S. S. Kamalov, and L. Tiator. A Unitary isobar model for pion photoproduction and electroproduction on the proton up to 1-GeV. *Nucl.Phys.*, A645: 145–174, 1999, nucl-th/9807001. (Cited on pages 98 and 100.)

[124] R. A. Arndt et al. Nucleon-Nucleon Partial Wave Analysis to 1-GeV. *Phys.Rev.*, D28:97, 1983. (Cited on page 98.)

[125] A. Anisovich, E. Klempt, A. Sarantsev, and U. Thoma. Partial wave decomposition of pion and photoproduction amplitudes. *Eur.Phys.J.*, A24:111–128, 2005, hep-ph/0407211. (Cited on page 98.)

[126] A. V. Anisovich and A. V. Sarantsev. Partial decay widths of baryons in the spin-momentum operator expansion method. *Eur.Phys.J.*, A30:427–441, 2006, hep-ph/0605135. (Cited on page 98.)

[127] T. Feuster and U. Mosel. Photon and meson induced reactions on the nucleon. *Phys.Rev.*, C59:460–491, 1999, nucl-th/9803057. (Cited on page 98.)

[128] G. Penner and U. Mosel. Vector meson production and nucleon resonance analysis in a coupled channel approach for energies $m_N < \sqrt{s} < 2\,\text{GeV}$. II. Photon induced results. *Phys.Rev.*, C66:055212, 2002, nucl-th/0207069. (Cited on page 98.)

[129] G. F. Chew, M. L. Goldberger, F. E. Low, and Y. Nambu. Relativistic dispersion relation approach to photomeson production. *Phys.Rev.*, 106:1345–1355, 1957. (Cited on page 99.)

[130] E. Amaldi, S. Fubini, and G. Furlan. *Pion-Electroproduction: Electroproduction at Low Energy and Hadron Form Factors (Springer Tracts in Modern Physics)*. Springer, 1 edition, 7 1979. ISBN 9783540089988. (Cited on page 99.)

[131] K. M. Watson. Some general relations between the photoproduction and scattering of pi mesons. *Phys.Rev.*, 95:228–236, 1954. (Cited on pages 99 and 100.)

[132] F. A. Berends, A. Donnachie, and D.L. Weaver. Photoproduction and electroproduction of pions. 1. Dispersion relation theory. *Nucl.Phys.*, B4:1–53, 1967. (Cited on page 99.)

[133] G. Knochlein, D. Drechsel, and L. Tiator. Photoproduction and electroproduction of eta mesons. *Z.Phys.*, A352:327–343, 1995, nucl-th/9506029. (Cited on page 100.)

[134] I. Blomqvist and J. M. Laget. A Nonrelativistic Operator Convenient for Analysis of Pion Photoproduction on Nuclei in the Delta (1236) Region. *Nucl.Phys.*, A280:405–428, 1977. (Cited on page 100.)

[135] R. L. Walker. Phenomenological analysis of single pion photoproduction. *Phys.Rev.*, 182:1729–1748, 1969. (Cited on page 100.)

[136] A. I. L'vov, V. A. Petrun'kin, and M. Schumacher. Dispersion theory of proton Compton scattering in the first and second resonance regions. *Phys.Rev.*, C55:359–377, 1997. (Cited on page 100.)

[137] O. Hanstein, D. Drechsel, and L. Tiator. Multipole analysis of pion photoproduction based on fixed t dispersion relations and unitarity. *Nucl.Phys.*, A632:561–606, 1998, nucl-th/9709067. (Cited on page 100.)

[138] J. Beringer et al. Review of particle physics. *Phys. Rev. D*, 86:010001, Jul 2012. (Cited on page 101.)

[139] N. Isgur and G. Karl. Positive Parity Excited Baryons in a Quark Model with Hyperfine Interactions. *Phys.Rev.*, D19:2653, 1979. (Cited on page 102.)

[140] D. Gromes and I. O. Stamatescu. Baryon Spectrum and the Forces Between Quarks. *Z.Phys.*, C3:43, 1979.

[141] J.-M. Richard and P. Taxil. The Ordering of Low Lying Bound States of Three Identical Particles. *Nucl.Phys.*, B329:310, 1990. (Cited on page 102.)

[142] Y. Suzuki and K. Varga. *Stochastic Variational Approach to Quantum-Mechanical Few-Body Problems*. Lecture Notes in Physics Monographs, M 54. Springer, 1998. ISBN 978-3-540-65152-9. (Cited on page 102.)

[143] E. Hiyama, Y. Kino, and M. Kamimura. Gaussian expansion method for few-body systems. *Prog.Part.Nucl.Phys.*, 51:223–307, 2003. (Cited on page 102.)

[144] B. Silvestre-Brac and C. Gignoux. Study of Light Baryons in the Three Quark Cluster Model: Exact Calculations. *Phys.Rev.*, D32:743–754, 1985. (Cited on page 102.)

[145] A. B. Giumaraes, H.T. Coelho, and R. Chanda. Quark Model for Heavy Baryons. *Phys.Rev.*, D24:1343–1346, 1981. (Cited on page 102.)

[146] P. Hasenfratz, R. R. Horgan, J. Kuti, and J. M. Richard. Heavy Baryon Spectroscopy in the QCD Bag Model. *Phys.Lett.*, B94:401, 1980. (Cited on page 102.)

[147] S. Capstick and W. Roberts. Quasi two-body decays of nonstrange baryons. *Phys.Rev.*, D49:4570–4586, 1994, nucl-th/9310030. (Cited on pages 102 and 103.)

[148] K. G. Wilson. Confinement of Quarks. *Phys.Rev.*, D10:2445–2459, 1974. (Cited on page 102.)

[149] H.-W. Lin and H. B. Meyer. *Lattice QCD for Nuclear Physics*. Lecture Notes in Physics. Springer, 2015. ISBN 978-3-319-08021-5. (Cited on page 102.)

[150] S. Durr et al. Ab-Initio Determination of Light Hadron Masses. *Science*, 322:1224–1227, 2008, 0906.3599. (Cited on pages 102 and 103.)

[151] S. U. Chung. Spin formalisms – updated version. URL `http://suchung.web.cern.ch/suchung/spinfm1.pdf`. 2007. (Cited on pages 105 and 108.)

[152] J. D. Richman. An Experimenter's Guide to the Helicity Formalism. 1984. (Cited on page 105.)

[153] L. Euler. Formulae generales pro translatione quacunque corporum rigidorum. *Novi Commentarii academiae scientiarum Petropolitanae*, 20:189–207, 1776. URL `https://math.dartmouth.edu/~euler/docs/originals/E478.pdf`. (Cited on page 105.)

[154] E. P. Wigner. *Gruppentheorie und ihre Anwendungen auf die Quantenmechanik der Atomspektren*. Vieweg Verlag, 1931. ISBN 978-3-663-00642-8. (Cited on page 106.)

[155] V. K. Khersonskii D. A. Varshalovich, A. N. Moskalev. *Quantum Theory of Angular Momentum*. World Scientific, 1988. ISBN 9971-50-107-4. (Cited on page 106.)

[156] M. Jacob and G. C. Wick. On the general theory of collisions for particles with spin. *Annals Phys.*, 7:404–428, 1959. (Cited on page 106.)

[157] J. M. Blatt and V. F. Weisskopf. *Theoretical Nuclear Physics*. Springer New York, 1979. ISBN 978-1-461-29961-5. (Cited on pages 110 and 147.)

[158] F. von Hippel and C. Quigg. Centrifugal-barrier effects in resonance partial decay widths, shapes, and production amplitudes. *Phys. Rev. D*, 5:624–638, Feb 1972. (Cited on page 147.)

[159] S. U. Chung. Formulas for partial-wave analysis (version v). URL `http://wwwcompass.cern.ch/twiki/pub/HadronAnalysis/PWAWorkshop/pwaform1.pdf`. 2010. (Cited on pages 110 and 147.)

[160] S. U. Chung and T. L. Trueman. Positivity conditions on the spin density matrix: A simple parametrization. *Phys. Rev. D*, 11:633–646, Feb 1975. (Cited on page 110.)

[161] G. Breit and E. Wigner. Capture of slow neutrons. *Phys. Rev.*, 49:519–531, Apr 1936. (Cited on page 111.)

[162] URL `http://lcgapp.cern.ch/project/cls/work-packages/mathlibs/minuit/index.html`. last call: August 30, 2015, . (Cited on page 112.)

[163] URL `http://root.cern.ch/drupal/content/numerical-minimization`. last call: August 30, 2015, . (Cited on page 112.)

[164] A. Austregesilo. *Central Production of Two-Pseudoscalar Meson Systems at the COMPASS Experiment at CERN*. PhD thesis, TU München, October 2014. (Cited on page 122.)

[165] P. Lebiedowicz and A. Szczurek. Exclusive $pp \to pp\pi^0$ reaction at high energies. *Phys.Rev.*, D87(7):074037, 2013, 1303.2882. (Cited on pages 127, 128, 129, 130, and 132.)

[166] L. Łukaszuk and B. Nicolescu. A possible interpretation of pp rising total cross-sections. *Nuovo Cimento Lett.*, 8:405, 1973. (Cited on page 127.)

[167] S. D. Drell and K. Hiida. Quasi-Elastic Peak in High-Energy Nucleon-Nucleon Scattering. *Phys.Rev.Lett.*, 7:199–202, 1961. (Cited on page 127.)

[168] R. T. Deck. Kinematical interpretation of the first pi - rho resonance. *Phys.Rev.Lett.*, 13: 169–173, 1964. (Cited on page 127.)

[169] L. L. Jenkovszky, O. E. Kuprash, J. W. Lamsa, V. K. Magas, and R. Orava. Dual-Regge Approach to High-Energy, Low-Mass Diffraction Dissociation. *Phys.Rev.*, D83:056014, 2011, 1011.0664. (Cited on page 131.)

[170] Laszlo Jenkovszky, Oleg Kuprash, Risto Orava, and Andrii Salii. Low missing mass, single- and double diffraction dissociation at the LHC. *Phys.Atom.Nucl.*, 77(12):1463–1474, 2014, 1211.5841. (Cited on page 131.)

[171] A.I. Fiks. Partial wave analysis of isobar production in $pp \to \pi^0 pp$. private communication. (Cited on page 133.)

[172] R. J. Barlow. Extended maximum likelihood. *Nucl.Instrum.Meth.*, A297:496–506, 1990. (Cited on page 136.)

[173] T. Schlüter. *The $\pi^-\eta$ and $\pi^-\eta'$ Systems in Exclusive 190 GeV π^-p Reactions at COMPASS (CERN)*. PhD thesis, LMU München, June 2012. (Cited on page 137.)

[174] L. C. Biedenharn and J. D. Louck. *Angular Momentum in Quantum Mechanics*. Encyclopedia of Mathematics and its Applications. Addison-Wesley, 1981. ISBN 978-0-521-30228-9. (Cited on page 146.)

[175] C. Adolph et al. Observation of a new narrow axial-vector meson $a_1(1420)$. 2015, 1501.05732. (Cited on page 162.)

[176] C. Adolph et al. Diffractive Resonance Production in $\pi^- + p \to \pi^-\pi^-\pi^+ + p_{\text{recoil}}$ at $190\,\text{GeV}/c$ with COMPASS and Observation of Strong Dynamical Effects, 2015. To be submitted to PhysRevD. (Cited on page 162.)

PUBLICATIONS

Some ideas and figures have appeared previously in the following publications:

- The likelihood method for the CEDAR detectors was presented at the SPIN-Praha-2012 conference and submitted as proceedings, which – up to now – have not been published.
- The likelihood method for the CEDAR detectors and some details and figures of the $pp \to pp\pi^0/\eta$ channel are included in the spectrometer description for the hadron beam set-up in [45].
- The likelihood method for the CEDAR detectors is described in the COMPASS internal note 2013-8.
- The event selection and kinematic distributions for $pp \to pp\pi^0/\eta$ as well as $pp \to pp\pi^+\pi^-(K^+K^-)$ are shown in COMPASS internal release notes.

PRESENTATIONS

The status and results of this thesis have been presented at several conferences:

- DPG-Frühjahrstagung 2012, Mainz, Germany, March 19 – 23, 2012:
  Neue Ansätze bei der Strahlteilchenidentifikation im COMPASS Experiment
- Advanced Studies Institute: Symmetries and Spin (SPIN-Praha-2012), Prague, Czech Republic, July 1 – 8, 2012:
  Likelihood methods for beam particle identification at the COMPASS experiment
- DPG-Frühjahrstagung 2013, Dresden, Germany, March 4 – 8, 2013:
  Baryon Spectroscopy at COMPASS
- International Workshop on New Partial-Wave Analysis Tools for Next Generation Hadron Spectroscopy Experiments (ATHOS 2013), Seeon, Germany, May 21 – 24, 2013:
  Baryon Spectroscopy at COMPASS
- DPG-Frühjahrstagung 2014, Frankfurt a. M., Germany, March 17 – 21, 2014:
  Baryon Spectroscopy at COMPASS
- DPG-Frühjahrstagung 2015, Heidelberg, Germany, March 23 – 27, 2015:
  Produktion neutraler Mesonen in Proton-Proton Streuung bei COMPASS